Lehrstuhl für Thermodynamik
Technische Universität München

On the Mechanisms of Combustion Driven Low-Frequency Oscillations in Aero-Engines

Johannes Eckstein

Vollständiger Abdruck der von der Fakultät für Maschinenwesen
der Technischen Universität München
zur Erlangung des akademischen Grades eines
DOKTOR – INGENIEURS
genehmigten Dissertation.

Vorsitzender:		Univ.-Prof. Dr.-Ing. Hans-Peter Kau
Prüfer der Dissertation:	1.	Univ.-Prof. Dr.-Ing. Thomas Sattelmayer
	2.	Univ.-Prof. Dr.-Ing. Hans-Jörg Bauer, Universität Karlsruhe (TH)

Die Dissertation wurde am 20.10.2004 bei der Technischen Universität München eingereicht und durch die Fakultät für Maschinenwesen am 20.12.2004 angenommen.

„Macht *ihr* hier wieder so einen Krach?“
(Kollegenzitat)

Danksagung/Acknowledgements

Diese Arbeit entstand am Lehrstuhl für Thermodynamik der Technischen Universität München im Rahmen des europäischen GROWTH-Programms „Instability Control of Low-Emission Aeroengine Combustors“(ICLEAC), Vertrag Nr. G4RD-CT2000-0215.
Mein erster und besonderer Dank gilt meinem Doktorvater, Herrn Professor Dr.–Ing. Thomas Sattelmayer, für die fachliche Betreuung und das in mich gesetzte Vertrauen. Sein reiches Erfahrungswissen sowie seine Begeisterung für die Verbrennungsforschung haben in unseren Fachgesprächen stets den Funken überspringen lassen.
Ich freue mich, dass Herr Professor Dr.–Ing. Hans-Jörg Bauer das Co-Referat übernommen hat. Als Leiter der Brennerkammerentwicklung bei Rolls-Royce Deutschland hat er unsere Projektarbeit stets mit Interesse verfolgt und unbürokratisch unterstützt.
Herrn Professor Dr.-Ing. Hans-Peter Kau vom benachbarten Lehrstuhl für Flugantriebe danke ich für die freundliche Übernahme des Prüfungsvorsitzes.
I want to address my personal thanks to Professor R. I. Sujith of the Indian Institute of Technology Madras, whom I had the pleasure to meet during his stay at the chair. He took care of reviewing the English draft version of this thesis.
Was wäre der Lehrstuhl ohne Dr.–Ing. Christoph Hirsch? Seine Motivationsgabe, gepaart mit einem beneidenswerten praktischen Know-How haben dem Projekt immer wieder neue Perspektiven erschlossen.
Mit meinem Bürokollegen Dipl.–Ing. Ewald Freitag habe ich die Höhen und auch die Klippen dieses europäischen Forschungsvorhabens gemeinsam gemeistert. Ihm verdanke ich nicht nur vier Jahre konstruktiv-kritische Fachdiskussion, sondern auch erstaunliche Ein-

blicke in die burgenländische Weinbaukunst.
In den Dank schliesse ich auch den gesamten Kollegenkreis am Lehrstuhl für Thermodynamik mit ein. Von der produktiven Arbeitsatmosphäre, dem offenen Erfahrungsaustausch sowie dem freundschaftlichen Miteinander habe ich sehr profitiert.
Ohne die tatkräftige Unterstützung meiner studentischen Hilfskräfte, Semestranden und Diplomanden würde manche wissenschaftliche Einsicht dieser Arbeit noch auf sich warten lassen. Vielen Dank für Eure motivierte und zuverlässige Mitarbeit.
Mein spezieller Dank gilt unserer mechanischen und elektrischen Werkstatt unter der meisterlichen Leitung von Erich Sieber, Bernhard Strobl und Jens Hümmer. Ohne sie wäre der Versuchsstand immer noch ein Konstrukt im Kopf des Doktoranden.
Unserem Industriepartner, Rolls-Royce Deutschland GmbH & Co. KG, sei herzlich gedankt für die Bereitstellung der Injektoren sowie für die Hilfe in allen Praxisfragen.
Meine Eltern haben meine Arbeit im fernen München immer mit aufrichtigem Interesse verfolgt. Ohne ihren persönlichen Rückhalt wie auch ihre finanzielle Unterstützung während meines vorangegangenen Maschinenbaustudiums im In- und Ausland wäre dieses Forschungsprojekt wahrscheinlich von jemand anderem bearbeitet worden. Vielen Dank an Euch.
Last, but not least, ein ganz persönliches Dankeschön an Christiane, meiner Lebenspartnerin, mit der ich glücklich bin und immer wieder erfahren darf, wie reizvoll das Leben auch jenseits der Technik ist.

München, im August 2004 Johannes Eckstein

Contents

Nomenclature

Latin Characters

a	m^2/s	thermal diffusivity
A	m^2	area
c	m/s	speed of sound
c	J/(kg·K)	specific heat
c_p	J/(kg·K)	isobaric specific heat
c_D	–	drag coefficient
d	m	diameter
D_{32}	μm	Sauter mean diameter
E	J	energy
f	Hz	frequency
f	m/s	Riemann invariant in downstream direction
g	m/s	Riemann invariant in upstream direction
h	J/kg	specific enthalpy
I	W/m^2	intensity
K	m^2/s	burning rate constant
k	1/m	wave number
l	m	length
m	kg	mass
N	$1/m^3$	droplet number density
p	Pa	pressure
$\dot{q}$	W/kg	specific heat release rate
$\dot{Q}$	W	heat release rate
$\dot{Q}_A$	W/m^2	heat release rate per unit area
s	J/(kg·K)	specific entropy
t	s	time
T	s	oscillation period
T	K	temperature
u	m/s	axial velocity
v	m/s	radial velocity
x	m	axial coordinate
Y	m·s/kg	admittance
Z	kg/(m·s)	impedance

Greek Characters

α	$W/(m^2 \cdot K)$	heat transfer number
γ	–	ratio of specific heats
ε	–	emissivity
ζ	–	pressure loss coefficient
η	$kg/(m \cdot s)$	dynamic viscosity
λ	m	wavelength
λ	$W/(m \cdot K)$	thermal conductivity
ν	m^2/s	kinematic viscosity
Ξ	–	amplitude growth rate
φ	$^\circ$	phase angle
ϕ	–	equivalence ratio
ρ	kg/m^3	density
σ	N/m	surface tension
τ	s	characteristic timescale
ω	1/s	angular frequency

Indices

a	air
acc	(droplet) acceleration
ad	adiabatic
b	burning
c	corner
cc	combustion chamber
crit	critical
d	droplet
down	downstream
dil	dilution zone
e	eigenfrequency
eff	effective
Eth.	ethanol, surrogate fluid
f	fuel
fl	flame
front	combustor front panel

g	gas phase
hs	heat shield
inj	injector
Ker.	kerosene
l	liquid phase
mix	mixing
prim	primary zone
r	by radiation
rel	relative (between gas and droplet)
t	thermocouple
tot	total
up	upstream
w	wall
0	reference
+	in downstream direction
–	in upstream direction

Superscripts

$(')$	perturbation
$(\bar{})$	average value
$(\dot{})$	time derivative

Universal Constants

h	=	$6.626 \cdot 10^{-34}$ Js	Planck constant
R	=	8.314 J/(mol·K)	molar gas constant
σ_B	=	$5.67 \cdot 10^{-8}$ W/(m^2·K^4)	Boltzmann constant

Non-Dimensional Numbers

Bi	=	$\alpha d/\lambda_t$	Biot number
M	=	u/c	Mach number
Nu	=	$\alpha d/\lambda_a$	Nusselt number
Oh	=	$\nu/(\rho\sigma d)^{0.5}$	Ohnesorge number

Pr	$=$	ν/a	Prandtl number
Sr	$=$	fd/u	Strouhal number
Re	$=$	ud/ν	Reynolds number
We	$=$	$\rho u^2 d/\sigma$	Weber number

Abbreviations

AFR	Air-Fuel-Ratio
AMF	Air Mass Flow
CFD	Computational Fluid Dynamics
FFT	Fast Fourier Transformation
FMF	Fuel Mass Flow
l.h.s.	left hand side
LPP	Lean Premixed Prevaporized
PIV	Particle Image Velocimetry
r.h.s.	right hand side
RQL	Rich-burn Quick-quench Lean-burn
SMD	Sauter Mean Diameter
TM	Transfer Matrix

Abstract

"Rumble" is a self-excited combustion instability, usually occurring during the start-up of aero-engines with fuel-spray atomisers at sub-idle and idle conditions and exhibiting low limit frequencies in the range of 50 Hz to 150 Hz. Entropy waves at the (nearly) choked combustor outlet are commonly supposed to be the key feedback-mechanism for the observed self-excited pressure oscillations. The study presented here aims to clarify the role of the entropy waves for the occurrence of rumble. For the experimental investigation, a generic air-blast atomiser with a design prone to self-excitation was incorporated into a thermoacoustic test rig featuring a single-sector staged combustor with variable outlet conditions.

As a first step, the role of the atomiser was investigated with respect to its acoustic response and the generated droplet size distributions. The atomisation process was separated from the complex instability mechanism of rumble by using sinusoidal forcing of the air mass flow rate in the absence of combustion. The pressure drop across the burner and the fluctuations of the acoustic velocity at the burner exit were investigated by a set of microphones and a hot wire anemometer. Phase-resolved Particle Image Velocimetry (PIV) was used to determine the forced velocity field of the burner. The recorded Mie-scattering intensities from the fuel droplets, obtained from the application of the PIV light sheet, were used to determine the geometry of the spray cone. Particle sizing by Fraunhofer diffraction was employed to measure the droplet size distributions for different air and fuel flow rates. The measurements were performed both under steady conditions and under forcing. Comparison of the dynamic data with the steady atomiser characteristics showed very good agreement, indicating a quasi-steady response of the burner in the low-frequency regime.

In the following, the combustor was investigated under self-excitation in the limit cycle. The combustor thermoacoustics was characterised by recording the OH*-chemiluminescence, the dynamic pressures and

PIV. A novel method has been developed for reconstructing the dynamic temperature fluctuations in the combustor. The temperature measurements have been used to monitor the generation of entropy waves by the flame and their propagation in the combustor. Experiments have been performed with choked exit nozzle and with an open-ended quarter-wave resonance tube to vary the combustor exit conditions. With the resonance tube, it was possible to eliminate the impact of entropy waves on self-excitation. An alternate injector design featuring a higher effective swirl in the primary zone, was used to assess the influence of the fuel transport into the flame on the instability.

A low order model of the staged combustor was developed to reproduce the general instability behaviour encountered during the experiments. To formulate the network model, a simple transfer function for a spray flame had to be developed, based on the experimental findings. The model also incorporates the characteristics of the respective atomiser, as determined by the preceding measurements. The modelling results agreed well with the measurements and showed that low-frequency self-excitation can also be obtained in the absence of entropy waves.

1 Introduction

1.1 Technological Background

Growing airline passenger numbers and a rising environmental awareness of the public have raised the demand for significant reductions of pollutant emissions from gas turbine aero-engines. Technological progress and the CAEP[1]-emission standards, imposed by the ICAO[2], have led to a continuous improvement of the combustion processes within the constraints of the aero-engine operation. As a result, the fuel efficiency per passenger-km of today's subsonic aircrafts has been increased by about 70% compared to 40 years ago [PLG+99].

Even though the contribution of civil aviation is relatively small compared to the global anthropogenic global pollution (3% in 1990), aero-engines at cruising altitude directly emit a number of chemically active species into the upper troposphere and lower stratosphere, which are suspect to alter the concentration of atmospheric ozone. The species with the greatest impact are nitric oxide (NO), nitrogen dioxide (NO_2) and soot. Calculated estimates show that such aircraft-related emissions have increased the concentration of NO_x at cruise altitudes in the northern mid-latitudes by approximately 20% [PLG+99].

Despite good success in reducing CO_2, CO and Unburned Hydrocarbons (UHC), the emission rates for NO_x have remained fairly unaffected by the recent advances in combustion efficiency [Zar97]. New concepts of fuel atomisation, pre-vaporisation and staged injection, that are currently being developed and tested for their airworthiness, therefore focus on Low-NO_x combustion [Lef95, Bau04].

The single most important factor affecting the NO_x-formation rates is known to be the flame temperature, exhibiting an exponential influence [Cor92]. Furthermore, NO_x production is shown to li-

[1] Committee on Aviation Environmental Protection
[2] International Civil Aviation Organization

nearly increase with rising combustor residence times. However, as shown in Figure 1.1, a great deal of compromise has to be involved in design, since operating conditions which usually suppress the NO_x-formation, like low temperatures and low combustor residence times, tend to exacerbate the problems related to CO and UHC. Strategies for optimised Low-NO_x-combustion therefore predominantly strive to lower the temperatures in the primary-zone while maintaining the combustion zone(s) within a fairly narrow temperature band within 1670 K and 1900 K over the entire projected power range of the engine [TH96, Lef99].

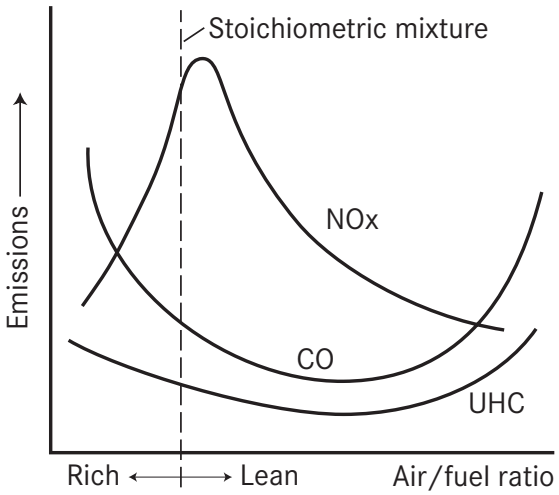

Fig. 1.1: Emission characteristics as a function of the air-fuel-ratio [CRS01].

For the *dry low NO_x* (DLN) approach, the temperature decrease in the primary zone is achieved without injecting water or steam, but by operating the flame reasonably far away from stoichiometric air/fuel mixtures. Depending on whether the regime under which combustion takes place is lean or rich, the Rich-burn/Quick-quench/Lean-burn-(RQL) and the Lean-Premix-Prevaporised (LPP) combustion concept have emerged as the most promising solutions.

Rich-burn/Quick-quench/Lean-burn (RQL) combustion: In RQL-combustors, the combustion zone is divided into two stages: a rich primary stage and a lean burn-out stage. Air staging in the quen-

ching zone effects the transition from rich to lean burning conditions. The RQL-technology relies on an adequate mixing zone design with effective injection of the quenching air in order to minimise the residence times under stoichiometric conditions. [BKHD99, HCF+98]. Laboratory-scale tests have yielded a 57% lower production of NO_x [Zar97]. A sector of an annular RQL-combustor is shown in Figure 1.2. This type of staged combustion is commonly found in modern

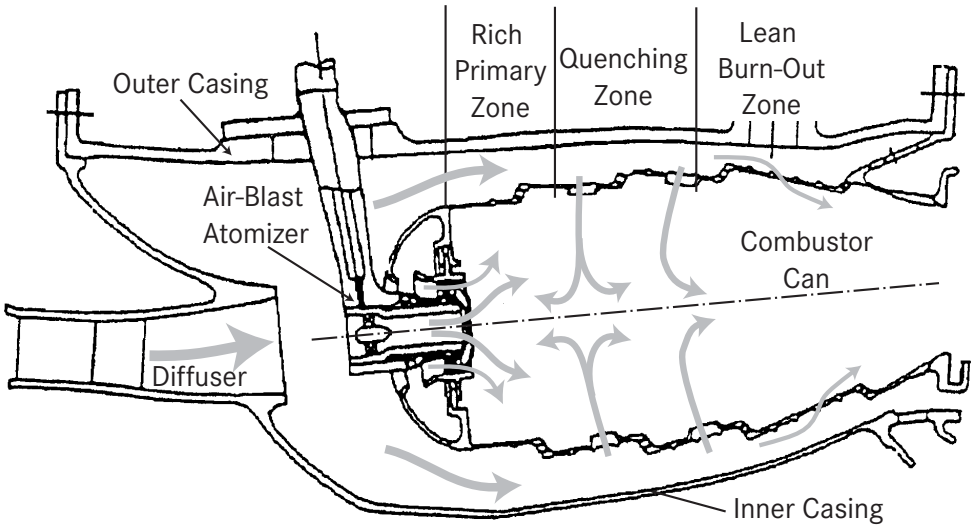

Fig. 1.2: Typical RQL-combustor [KBK+98].

combustor designs. However, the potential of NO_x-reduction is limited in practice due to the increased formation of soot [Bau04].

Lean-Premixed-Prevaporised (LPP) combustion: Compared to the RQL-technology, LPP-combustion offers a higher potential for NO_x-reduction due to the absence of stoichiometric burning conditions in the combustor [vdBS03]. The combustion process takes entirely place in the lean regime. The attainment of near-perfect mixture homogeneity before combustion and sufficiently large autoignition delay times are prerequisites for low NO_x-formation rates [PHW98, Fin01, CMF+04]. LPP-burner design therefore strives for intense air-fuel mixing and prevaporisation within an additional premixing section being part of the injector. The premixer has however

to be kept short enough in order to avoid auto-ignition of the combustible mixture in the duct. A characteristic LPP-burner design is shown in Figure 1.3.

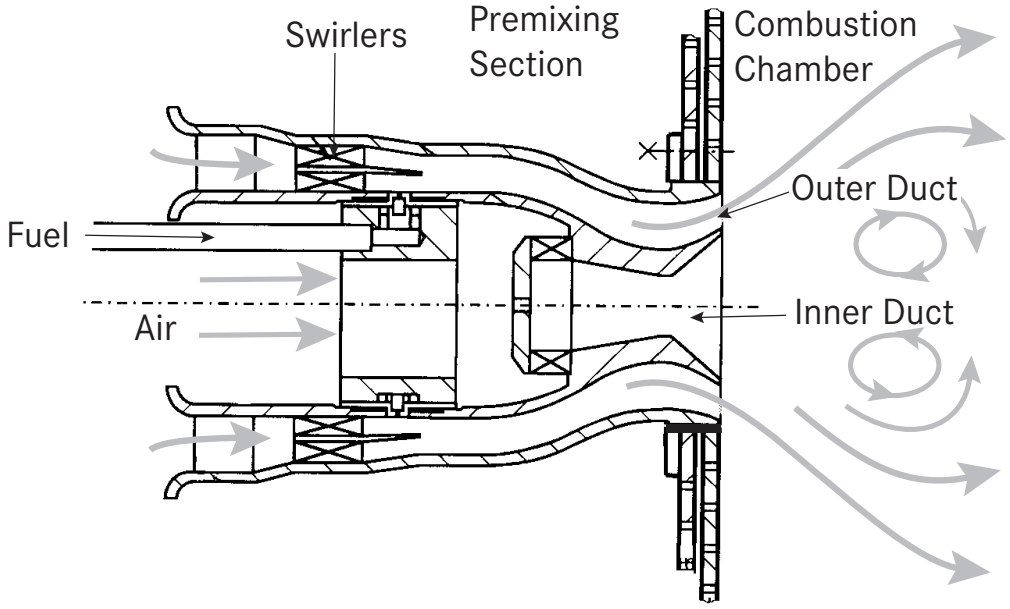

Fig. 1.3: Generic LPP-injector design [Fin01].

With the improvements achieved, thermoacoustic combustion instabilities known and feared for their destructive potential in stationary gas turbines have adversely become more prominent in aero-engines. During recent years, intense scientific efforts were undertaken to identify the underlying physical driving mechanisms and to investigate the sensitivity between combustor geometries, oscillation frequencies and emission figures, e.g. [CHP+00]. Yet, a standard procedure to predict and to assess the engine's susceptibility to combustion instability in an early design stage does still not exist. This thesis aims to provide further knowledge to support the setting-up of predictive design tools which will lower engine development times and costs, avoid test facility failure and reduce the number of hardware tests to be carried out. With "rumble" a particular combustion instability is focussed on, which is characteristic for the start-up of aero-engines, producing limit frequencies between 50 Hz and 150 Hz.

1.2 Combustion Instabilities

Combustion instabilities are self-sustained large amplitude oscillations of the pressure and the velocity in combustors with the flame acting as acoustic actuator and the combustor hardware as acoustic resonator. The underlying flame-acoustics interaction is complex and can be regarded as an energy transfer problem: If the energy balance of the acoustic system results in a surplus of energy addition by the flame, the oscillation amplitude will grow. If dissipating mechanisms are dominating, the self-excited oscillation will decay and the system will stabilise. The limiting amplitude of the instability is obtained whenever the exciting and the dissipating mechanisms are balanced out. The limit cycle of the instability will always be accompanied with the occurrence of non-linear effects.

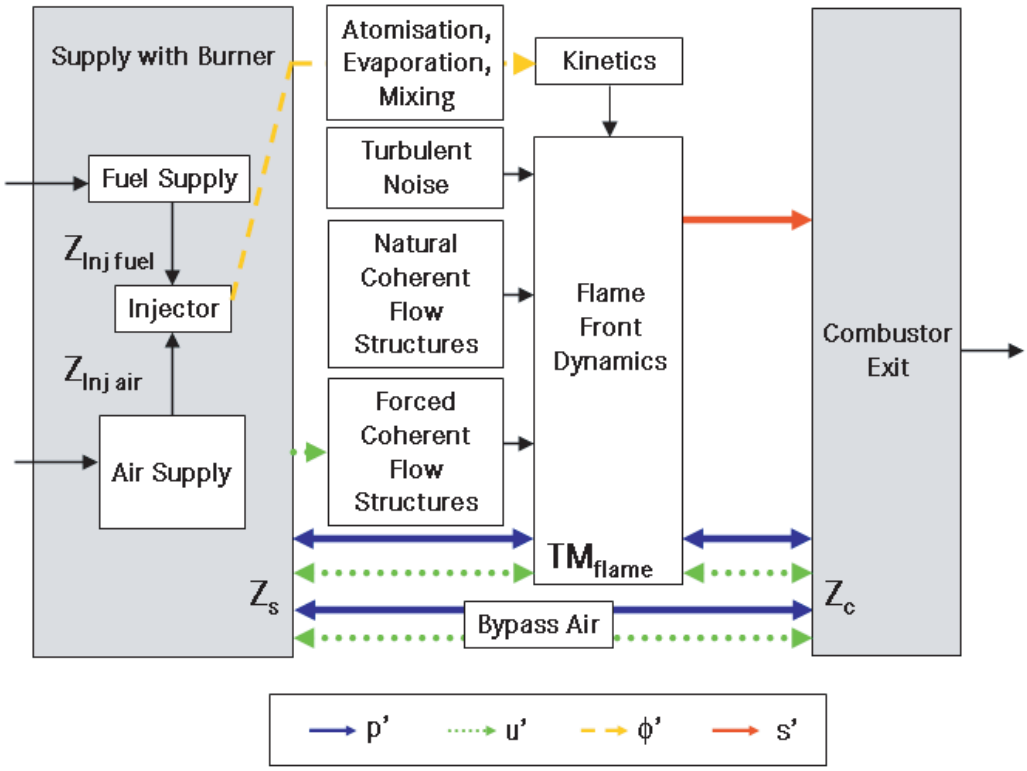

Fig. 1.4: Drivers for combustion instabilities [Sat03].

The combustor can be understood as acoustic system and can be

decomposed in single components for the purpose of stability analysis. Figure 1.4 shows a simple combustor model with the main components being the injector with fuel and air supply, the combustion chamber with the flame and the combustor exit. Usually, a fraction of the supplied air bypasses the flame, being used for staged combustion or for dilution. The combustion performance of the flame will be influenced by atomisation, evaporation, mixing and the reaction kinetics, depending on the injector technology and the fuel type used. The combustor outlet and the supply section, containing the fuel and the air duct with the injector, can be characterised by appropriate boundary conditions, such as the impedances Z. The acoustic properties of the flame are contained in the flame transfer matrix (TM), which relates the acoustic variables (acoustic pressure p' and velocity u') up- and downstream of the flame. These and further acoustic terms will be introduced in detail in section 2.

From literature, five mechanisms can be discerned as stimuli for acoustic instabilities, shown in Figure 1.4:

- **Turbulent noise**: Turbulent background noise is an inevitable result of the air injection and the combustion process. Turbulent noise has a random broad-band character which can be selectively amplified by combustor resonance. The distinct peaks in the noise spectrum can then alter the flame dynamics. Turbulent noise is an autonomous source of sound, i.e., it takes place independently from possible oscillations of the combustor pressure, e.g. [Sta71, CS91].

- **Natural and forced coherent flow structures**: Coherent flow structures imply effects like vortex shedding or other periodic instabilities of the flow. Coherent flow structures provoke heat release fluctuations of the flame by changing the conditions for local turbulent mixing of the combustible mixture with the hot combustion gases. While for forced coherent flow structures, the acoustic velocity and pressure perturbations act as pacemaker for their development and their propagation, natural

structures are largely independent of any acoustic forcing. Natural coherent flow structures and the subsequent response of the flame rather follow characteristic Strouhal numbers, connected with the features of the cold flow, e.g. [PGW98, SG92, PTV+87].

- **Equivalence ratio waves**: Acoustic disturbances alter the supply conditions of the injector. If the fuel and/or the air flow rate in the combustor is changed under the influence of acoustic oscillations, periodic mixture fluctuations, so-called equivalence ratio waves ϕ' are obtained which are convected to the flame. Equivalence ratio waves will impact the heat release of the flame and the flame speed by changing the chemical reaction rate. In the particular case of fuel-spray atomisers, the modulation of the combustor pressure will periodically alter the atomiser performance. A fluctuating droplet size distribution will be obtained with associated changes in the evaporation and burning rates, e.g. [Sat03, HZGV95, HV02, LZ98].

- **Entropy waves**: Entropy waves s' essentially are periodic temperature patterns in the flow originating from the fluctuating heat release of the flame and/or a fluctuating mass flow of the gas. In the presence of strong area contractions, such as nozzles or turbine guide vanes, entropy waves effect the reflection of pressure waves which influence combustor stability, e.g. [PPD99, KEH85, CM77].

Forced flow structures, equivalence ratio and entropy waves lead to a selective amplification of sound by the flame and are of particular interest with respect to sustaining combustion instabilities. Even relatively small disturbances can drive oscillations producing unacceptably large amplitudes. Section 1.3 is therefore dedicated to provide a more detailed literature review.

On the other hand, the attenuating processes are relatively weak and gain relative strength rather slowly with increasing amplitude, which explains the prevalence of acoustic instabilities in combustors.

The following mechanisms are known to attenuate acoustic oscillations [Kel95]:

- **Acoustic radiation, viscous and structural damping**: These effects comprise acoustic losses by radiated sound, sound absorption by non-rigid combustor walls, effects of friction and heat conduction in shear-layers and in the oscillating medium itself. However, for closed combustion chambers the effective attenuation obtained by these mechanisms is usually too weak to limit the oscillation amplitude. An impact on the stability limits of the oscillation is nevertheless observed.

- **Acoustic-vorticity interaction**: In rotational mean flows, i.e. in areas of mean velocity gradient, the irrotational acoustic field is coupled with the vorticity field of the flow [Pan04]. Energy is transferred between the acoustic mode and vorticity mode, being mediated by the mean flow. In particular, an acoustic particle oscillating in a non-uniform flow field generates vortices, which are convected downstream with the flow. This mechanism is particularly relevant for acoustic losses occurring in recirculation zones or shear layers.

- **Altered fuel supply**: Large-scale oscillations of the acoustic pressure in the combustor will alter the effective pressure drop over the burner. The air flow rate of the burner and the respective air velocities in the primary zone can then become subject to strong modulations. Depending on the injector type, this will either lead to restricted fuel transport to the flame or to fuel enrichment, both impeding a stable combustion.

- **Nonlinear self-detuning of the combustor**: Culick [Cul94] has shown that the non-linear behaviour in the limit cycle can promote the transfer of acoustic energy to higher oscillation modes. As a result, amplitude dispersion in the frequency regime is obtained with the response amplitude at the excitation frequency being lower than the respective excitation. Non-linear

amplitude saturation is thus reached as soon as the energy transfer to the higher harmonic balances the energy input by lower-frequency excitation.

- **Shock wave formation**: In extreme cases, excessive acoustic oscillations can result in the formation of shock waves due to the interaction between fluid-dynamics and shock-kinetics. This effect was particularly studied in the context of unstable liquid-propellant rockets combustors [Cro65], but is irrelevant for gas turbine applications.

1.3 Instability Mechanisms

1.3.1 Rayleigh's Criterion

In the year 1878, as a result of his studies on the interaction of acoustic waves and heat release, Lord Rayleigh stated that

> "*If heat be communicated to, and abstracted from, a mass of air vibrating (for example) in a cylinder bounded by a piston, the effect produced will depend upon the phase of the vibration at which the transfer of heat takes place. If heat be given to the air at the moment of greatest condensation, or be taken from it at the moment of greatest rarefaction, the vibration will be encouraged. On the other hand, if heat will be given at the moment of greatest rarefaction, or abstracted at the moment of greatest condensation, the vibration will be discouraged.*" [Ray26]

This statement, known as *Rayleigh's criterion*, can be expressed more generally in mathematical terms by

$$\int_0^T \dot{Q}'(t) \cdot p'(t) dt > 0 \tag{1.1}$$

where T corresponds to a period of the oscillation and p' and $\dot{Q}'$ to the respective pressure and heat release oscillations. The tendency for

acoustic instabilities will be highest, if the pressure and heat release oscillate in phase.

In practice, as discussed in the preceding section, the heat release will respond to the pressure perturbations and $\dot{Q}'$ will lag p' by a time interval τ. Assuming a sinusoidal variation of the combustor pressure and heat release

$$p'(t) = \hat{p} \sin \omega t \tag{1.2}$$

$$\dot{Q}'(t) = \hat{\dot{Q}} \sin \omega (t - \tau) \tag{1.3}$$

the application of Eq. (1.1) with $T = \frac{1}{f} = \frac{2\pi}{\omega}$ leads to

$$\hat{p}\, \hat{\dot{Q}} \int_t^{t+2\pi/\omega} \sin \omega t \sin \omega (t - \tau) dt = \hat{p}\, \hat{\dot{Q}} \frac{\pi}{\omega} \cos \omega \tau > 0 \tag{1.4}$$

In order to obtain self-excitation according to the Rayleigh criterion, the time-lag τ must lie within the ranges

$$0 < \tau < \frac{T}{4} \qquad \frac{3T}{4} < \tau < \frac{5T}{4} \qquad \text{... etc.} \tag{1.5}$$

The time-lag explanation was first given by Summerfield [Sum51] for the occurrence of low-frequency "chugging" in liquid rockets. Since then, it has inspired many scientific interpretations for thermoacoustic instability phenomena observed. However, Rayleigh's criterion has shown to be a necessary, but not a sufficient condition for the occurrence of thermoacoustic instabilities. Acoustic losses occurring in the system might exceed the energy input by the flame.

1.3.2 Equivalence Ratio Waves

The impact of acoustic waves on the formation of mixture inhomogeneities has been studied by many authors, particularly in context of premixed combustion. The driving mechanism can be outlined on the basis of the experimental investigations of Hermann et al. [HZGV95]: The pressure perturbations in the combustion chamber

alter the pressure drop over the mixing device/injector. The air and the fuel duct will respond differently to these changes which impacts the fuel and the air mass flow rates and results in fluctuations of the local fuel-air-ratio. These equivalence ratio fluctuations are convected with the flow to the flame and result in oscillations of the heat release. As a secondary effect, the unsteady flow field in the primary zone due to the superimposed acoustic velocity perturbations may enhance or reduce the convection times of the combustible mixture. Unstable behaviour of a given burner configuration can be related to a total delay time, being impacted by mixture formation, convection and reaction, which fulfills the conditions of Eq. (1.5).

The scientific challenges which arise for an appropriate description of unstable systems is twofold: First, the relevant sub-processes in the thermoacoustic feedback loop have to be identified and their relative contribution to the total delay time has to be determined. Second, engine-specific flame response models have to be formulated to address the issue of time delays due to interaction between acoustics and the flame, e.g. [Lie03].

Like several other authors, Lieuwen et al. [LZ98], and Hubbard et al. [HD98] focus on the convective time lag of the reactive mixture from the nozzle to the flame tip as the determining contribution for the oscillation frequencies obtained. Characteristic ratios of convective time delay and oscillation period were found to sufficiently describe the instability behaviour of the investigated combustor designs.

As a consequence of experimental results, the model proposed by Straub et al. [SRBS01] also includes a variable effective flame length due to non-negligible combustion time scales, which are a function of the local equivalence ratio.

In parallel to the modelling work, measurement techniques were further developed to capture the local air-fuel ratio in premix ducts, e.g. [MDL98]. However, most approaches, such as laser absorption, are bound to specific fuels and are thus not universally applicable.

For spray flames, only very few publications about equivalence ratio waves as driver for instability have been found. This seems due to two reasons: First, the sub-processes that impact the combustion delay time are highly complex, containing aspects of droplet injection, atomisation, transport, evaporation, mixing, and chemical kinetics [Dip72, Cul88]. In addition, it is commonly assumed that equivalence ratio waves become particularly important for elevated degrees of premixedness; i.e., LPP-flames, while for conventional combustors, the impact of entropy waves are considered to prevail [Kel95].

1.3.3 Forced Coherent Flow Structures

In the context of large-scale coherent structures, vortex shedding is the most common form of flow instability. It is often observed in the wake of rearward facing steps or of bluff bodies. Vortex-flame interaction has been studied first with instability phenomena occurring in afterburners and ramjets, e.g. [RM56]. In the special case of forced coherent flow structures, the acoustic velocity perturbations act as pacemaker for the periodic development, propagation and break-down of vortices [SZ85]. Vortices usually originate from shear layer instabilities which are amplified and lead to vortex roll-up when a specific energy level is reached. The vortices are convected downstream, interact and merge together to produce new larger structures before breaking down into small scale turbulence [PTV$^+$87]. The vortex roll-up and the vortex merging takes place at discrete Strouhal numbers, which are specific to the set-up used. Acoustic forcing can selectively amplify the processes of vortex shedding or vortex pairing when the excitation frequency approaches the respective vortex shedding frequency or the preferred mode frequency [SG92], thereby influencing the vortex shedding rate and the vortex size obtained.

Vortex-induced heat release pulsations occur since [Cul88]:

- the roll-up of the mixing-layer between hot combustion gases and reactants leads to the formation of large-scale vortices with

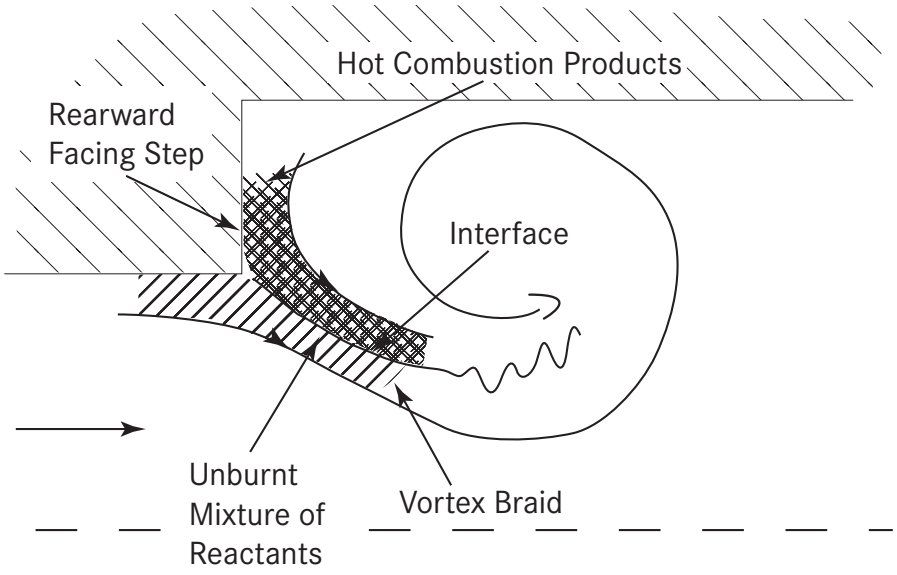

Fig. 1.5: Vortex roll-up in a dump combustor [SG92].

combustion in the vortex (e.g. [PGW00]), as shown in Figure 1.5.

- combustion is enhanced by the periodic increase of turbulent fine-scale mixing during vortex pairing and wall-impingement due to high local strain rates obtained (e.g. [SZ85, SZ87]).

- convected vortices periodically distort the flame surface area.

Poinsot et al. [PTV+87] experimentally investigated the time-delay characteristics for a vortex-driven instability at a multiple flame-holder dump combustor during an oscillation cycle. In correspondence to the instability mechanism related to equivalence ratio waves, they have shown that the phase relationship between heat release and pressure maximum was determined by time-delays due to vortex formation, vortex growth/convection and combustion. The overall phase did satisfy the Rayleigh criterion Eq. (1.5). Vortex shedding was obtained for maximum velocity phase at the combustor inlet plane. The acoustic field did accelerate the initial vortex growth.

Yu et al. [YPW+96] have shown the extent to which the droplet-

vortex interaction in practical liquid-fuelled combustors can alter the features of the flame. When fuel injection was synchronised with the vortex shedding phase, a higher droplet dispersion along the vortex perimeter and shorter flames of higher combustion intensity were obtained. Out-of phase or non-synchronised fuel injection led to long flames with the burning droplets being bound inside the jet core. Phase-related injection of fuel could then be used to actively control combustion. However, the control effect is bound to small droplets with Stokes numbers near unity.

1.3.4 Entropy Waves

Entropy waves, or "hot spots", are deviations from the isentropic state of a flow, which originate from varying specific heat release rates, e.g. from an oscillating flame. The temperature non-uniformities of the flow result in local density changes which can interact with the acoustic field. As material waves, the propagation of entropy waves is bound to the combustor flow.

The presence of entropy waves can profoundly alter the stability profile of a combustor. Being convected across strong area contractions, they effect a rearward pressure feedback [MC77, CM77], which can alter the combustor acoustics in the case of choked combustor boundaries. As a consequence of their moderate propagation speed, entropy waves are predominantly made responsible for the occurrence of low-frequency instabilities [KEH85]. A mathematical description of entropy waves is given in section 2.4.

Polifke et al. [PPD01] formulated a linear 1D-model with choked exit to demonstrate the coupling between entropy waves and combustor acoustics. They showed that entropy and acoustic waves can interfere both constructively and destructively, depending on their relative phase. The combustor response is even altered at higher frequencies, exceeding the frequencies associated with the characteristic time scales of entropy convection.

The premixed flame model of HUBBARD [HD98] produced narrow bands of instability also for cases with constant heat release rates due to the destabilising effect of entropy waves on the in- and outflow of the combustor. Comparable results were obtained by the theoretical analysis of UMURHAN [Umu99] for spray combustion.

However, SATTELMAYER [Sat03] has shown that the aerodynamic dispersion due to a non-uniform combustor flow can significantly reduce the impact of entropy waves as potential driver for instabilities. His model of a premixed combustor accounts for dispersion acting on equivalence ratio and entropy waves. The destabilising effect of entropy waves was found to be bound to small dispersion rates of the entropy waves and to the low-frequency domain below 200 Hz. The assessment of overall system stability revealed to critically depend on the appropriate description of the equivalence ratio waves in the primary combustion zone.

1.4 Rumble

Rumble is a specific form of an audible, self-excited combustion instability in aero-engine combustors exhibiting limit frequencies which typically range between 50 Hz and 150 Hz. Rumble was observed in context with liquid-fuelled diffusion burners being operated under low inlet temperatures $T_{30} < 500$ K and low combustor pressures $p_{30} < 4$ bar. Such operating conditions are commonly found in the start-up cycle of conventional aero-engines at idle and sub-idle conditions.

Experimental work with rumble-prone spray atomisers has been conducted by KONRAD ET AL. [KBK+98], who detected a strong coherence between the occurrence of rumble and an unstable fuel delivery by the injector. Modifications of the fuel atomiser design, especially a modified swirler aerodynamics and geometrical changes inside the fuel duct, led to an improvement of the atomisation quality and the elimination of rumble. The design of the combustor chamber proved

to be less relevant.

Aspects of fuel duct design have also been addressed by the work of Jermy et al. [JDG02], who have investigated airblast nozzles under external forcing with regard to the fuel distribution on the prefilmer lip. The injection device which encouraged instability showed a significantly increased fuel response to acoustic forcing, peaking at those frequencies at which the self-excited combustion oscillation was observed.

Zhu et al. [ZDB99, ZDB00] numerically investigated a 2-D staged model combustor accommodating an airblast atomiser to simulate the flame response to fuel and air forcing as well as the onset of self-excited rumble oscillations. Here, the sensitivity of the atomiser to changing air flow rate proved to be of particular importance for the occurrence of patterns of unmixedness and for instability. The limit frequencies of the rumble oscillations were essentially determined by the process of entropy convection inside the combustor. The effects of entropy dispersion in the dilution zone of the combustor has however not been shown in detail, but is expected to lead to a decreased magnitude of the pressure feedback at the choked nozzle.

1.5 Goals of the Work

On the basis of the current knowledge in combustion instability research, the following scenario for the occurrence of rumble in aero-engines with airblast atomisers can be postulated:

Airblast atomisers, featuring very low acoustic impedance[3] on the air side, primarily respond to periodic changes in air velocity. The air velocity modulations will impact the atomisation process and the characteristic droplet sizes $d(t)$ obtained. The droplet patterns, when being convected into the flame, are subject to dispersion and mixing induced by turbulence and shear layer effects of the swirling flow. In the flame, the droplet size dependent evaporation and combustion

[3] see section 2.2.3

time scales will result in periodic variations of fuel consumption and heat release $\dot{q}(t)$. Self-excitation is possible, if the convective time delay of the droplets in the primary zone is such that Rayleigh's criterion Eq. (1.1) is fulfilled. A purely thermoacoustic instability mode is then produced, according to Figure 1.6 below. The oscillating heat release further drives entropy waves $s(t)$ that are convected downstream to the combustor exit. On their way to the combustor outlet, the entropy waves are subject to dispersion whose strength will be considerably influenced by the injection of primary and secondary air in the quenching zone. Choked or nearly-choked outlet conditions potentially cause a reflection of the entropy wave as pressure waves which will alter the effective pressure drop over the injector and thus the local air velocities. If the impinging entropy wave is strong enough, entropy reflection at the nozzle could thus act as an alternative pacemaker for self-excitation.

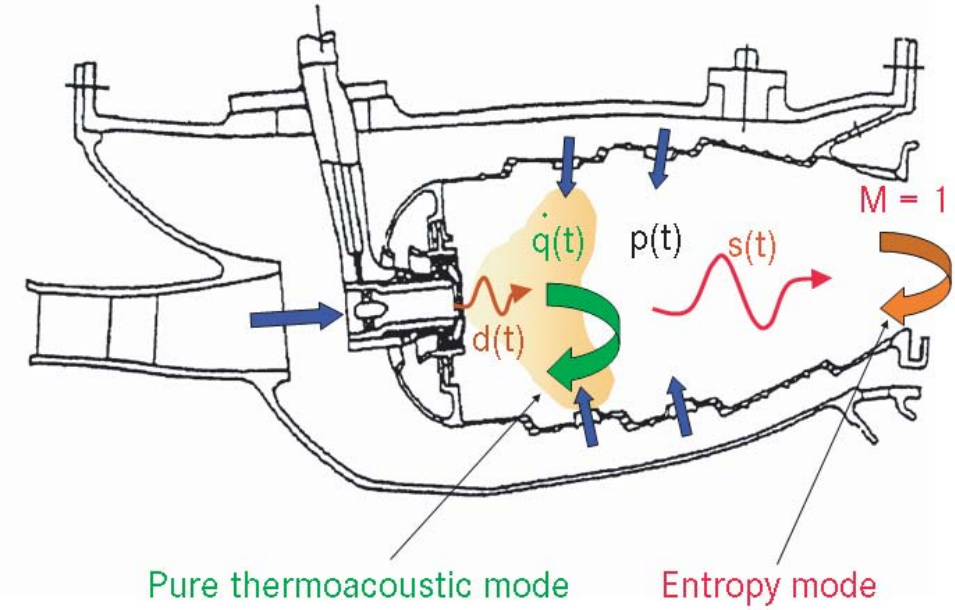

Fig. 1.6: Potential feedback mechanisms in a RQL-combustor.

The relative contribution of the thermoacoustic and the entropy mode for developing and sustaining low-frequency combustion oscillati-

ons is not obvious. In this context, the experimental and theoretical work of this thesis aims at answering the following questions:

- What is the contribution of the entropy waves on promoting rumble? What are the typical operating conditions of the atomiser for the entropy inhomogeneities in the combustor becoming important?
- What is the influence of time-delay effects in the primary zone, due to droplet acceleration and convection from the atomiser lip to the flame?
- What is the impact of the atomiser performance? How do varying air velocities alter the generated droplet sizes? How do the droplet size fluctuations influence the heat release of the flame?

Experiments conducted on a generic single liner test rig and subsequent low order modelling of the system are used to address these questions.

A brief introduction of the basic equations of thermoacoustics is given in **chapter 2**.

In **chapter 3**, a description of the test rig is presented. The setup accommodates a generic Rich-Quench-Lean (RQL) combustion chamber, featuring staged mixing air injection comparable to a Low-NOx can design. The combustor can be flexibly equipped with different generic airblast injectors.

The measurement methods applied for the experiments are introduced in **chapter 4**. Besides the use of rather well-established measurement methods (Particle Image Velocimetry (PIV), Malvern sizer, microphone and hot wire anemometry), a particular challenge consists in measuring the steady and the dynamic gas temperatures inside the combustor. For this purpose, the double thermocouple method, which has already been used for measuring the steady temperature [Hei02] and very-low frequency perturbations ($f < 15$ Hz [Bra91]),

has been further improved to account for the extended frequency range of rumble ($f < 150$ Hz).

The experimental results are presented in **chapters 5** and **6**. In chapter 5, the response of a rumble-prone airblast atomiser to forced acoustic perturbations is evaluated. The spray produced by the atomiser is analysed and first conclusions are drawn with respect to the tendency to promote instabilities. The data obtained are used to provide the upstream boundary condition for the low order model.

In chapter 6, the injector performance is presented under self-excited conditions with flame. The parameters impacting the limit cycle are discussed. Comparative measurements with a different burner design are presented to assess the influence of the injector aerodynamics.

A linear stability analysis of the conditions for low-frequency combustion instabilities closes this thesis (**chapter 7**). A low-order model has been developed to account for spray combustion in the staged RQL-setup investigated. The low-order results are compared with the experimental findings.

The conclusions and recommendations for future work are presented in **chapter 8**.

2 Acoustics

2.1 Linear Acoustics

Sound consists of mechanical oscillations propagating in continua. In context of aero-engine applications, thermoacoustic research is focussed on sound propagation in gaseous media (air, flue gases in the combustor). Here, a sound wave leads to disturbances of the flow variables pressure p, density ρ and particle velocity $\mathbf{u}$ from their mean state. For the pressure and temperature range found in gas turbine combustors, the interdependency of the acoustic variables is appropriately described by the thermodynamic state equations for a perfect gas. The sound-induced fluctuations of the thermodynamic variables p and ρ are usually very small compared to the corresponding mean values

$$\frac{p'}{\bar{p}} \ll 1 \qquad \frac{\rho'}{\bar{\rho}} \ll 1. \tag{2.1}$$

The prime denotes the fluctuation of the acoustic quantity while the overbar refers the mean value. Equation (2.1) imposes the formal restriction for the application of linear acoustics which permits the decomposition of the time-dependent local flow variables into a stationary mean value and a superposed perturbation:

$$\begin{aligned} p(\mathbf{x},t) &= \bar{p} + p'(\mathbf{x},t) + p''(\mathbf{x},t) && (2.2)\\ \rho(\mathbf{x},t) &= \bar{\rho} + \rho'(\mathbf{x},t) + \rho''(\mathbf{x},t) && (2.3)\\ \mathbf{u}(\mathbf{x},t) &= \bar{\mathbf{u}} + \mathbf{u}'(\mathbf{x},t) + \mathbf{u}''(\mathbf{x},t). && (2.4) \end{aligned}$$

$\mathbf{x}$ is the local coordinate, $\bar{\mathbf{u}}$ and $\mathbf{u}'$ are the corresponding vectors of the mean and the acoustic velocities. The local fluctuations imposed by turbulence, denoted above by the double prime, are not considered hereafter due to their non-deterministic nature.

Since the oscillation amplitudes are small, the influence of viscous shear stresses is small compared to the stresses induced by the acoustic pressure. Sound can therefore be regarded as weak motion of an inviscid fluid.

2.2 Acoustic Equations for the Non-Reacting Flow

In a first step, in order to establish the basic equations of sound propagation, heat addition by combustion is neglected and only *non-reacting flows* are regarded. For inviscid fluids, the conservation of mass, momentum and energy are given by the Euler equations [Spu87]:

Conservation of mass:

$$\frac{D\rho}{Dt} + \rho(\nabla \cdot \mathbf{u}) = 0 \quad [4] \tag{2.5}$$

Conservation of momentum (neglecting body forces):

$$\rho\frac{D\mathbf{u}}{Dt} + \nabla p = 0 \tag{2.6}$$

Conservation of energy ($\dot{q} \equiv 0$):

$$\rho\frac{D}{Dt}\left(\frac{\mathbf{u}\cdot\mathbf{u}}{2} + h\right) = \frac{\partial p}{\partial t} \tag{2.7}$$

The term $\frac{D}{Dt} = \frac{\partial}{\partial t} + \mathbf{u}\cdot\nabla$ is the material derivative. Since the compression in a sound wave occurs too rapidly for a considerable exchange of heat, sound propagation can be assumed isentropic in the absence of significant heat sources. The entropy conservation reduces to

$$\frac{Ds}{Dt} = 0. \tag{2.8}$$

[4] This is not strictly correct for the presence of evaporating sprays, which will introduce a source term into the continuity equation [Cul88]. However, for the present considerations, this effect is weak and will be neglected.

From the first law of thermodynamics, the change of state for a perfect gas under isentropic conditions can be derived as [Spu87]:

$$p = C\rho^{\gamma} \tag{2.9}$$

C is a constant and depends on the reference state. γ is the ratio of specific heats $\gamma = c_p/c_v$.

The conservation equations for the acoustic perturbations are derived from Eqs. (2.5) and (2.6) by replacing p, ρ and $\mathbf{u}$ by their decomposed formulations Eqs. (2.2), (2.3), (2.4), subtracting the respective conservation equation for the mean flow and neglecting products of small quantities:

Mass:

$$\frac{\partial \rho'}{\partial t} + \nabla \cdot (\bar{\rho}\mathbf{u}') + \nabla \cdot (\rho'\bar{\mathbf{u}}) = 0 \tag{2.10}$$

Momentum:

$$\frac{\partial \mathbf{u}'}{\partial t} + (\bar{\mathbf{u}} \cdot \nabla)\mathbf{u}' + (\mathbf{u}' \cdot \nabla)\bar{\mathbf{u}} + \frac{\rho'}{\bar{\rho}}(\bar{\mathbf{u}} \cdot \nabla)\bar{\mathbf{u}} + \frac{1}{\bar{\rho}}\nabla p' = 0 \tag{2.11}$$

The set of equations is completed by a relation between acoustic pressure and density that can be obtained from the state equation Eq. (2.9). Equation (2.9) implies that for isentropic flows p is a function of ρ only. Neglecting terms of higher order, a Taylor expansion of p around $\bar{p}$ leads to

$$p(\mathbf{x}, t) = \bar{p} + \left(\frac{\partial p}{\partial \rho}\right)_s \rho' + \mathcal{O}(\rho'^2) \tag{2.12}$$

By defining

$$c^2 \equiv \left(\frac{\partial p}{\partial \rho}\right)_s \tag{2.13}$$

the following dependency is obtained

$$p' = c^2 \rho' \tag{2.14}$$

It will be shown in section 2.2.1 that c is the *speed of sound*. From the derivative of Eq. (2.9)

$$\frac{dp}{d\rho} = C\gamma\rho^{\gamma-1} = \gamma\frac{p}{\rho} \tag{2.15}$$

c is calculated for the perfect gas, using Eq. (2.13),

$$c = \sqrt{\gamma\frac{p}{\rho}} = \sqrt{\gamma RT}. \tag{2.16}$$

R is the specific gas constant. c is thus a variable of state, depending on the specific gas composition and on the gas temperature. For air at 300 K, c becomes 348 m/s.

For constant $\bar{\rho}$, the *convective wave equation for the non-reacting flow* is obtained by differentiating Eq. (2.10) with respect to t, subtracting the divergence of Eq. (2.11) and using Eq. (2.14)

$$\frac{D^2 p'}{Dt^2} - c^2 \nabla^2 p' = 0. \tag{2.17}$$

Equation (2.17) describes the propagation of the pressure waves with the propagation speed c in an isentropic medium moving with the convective speed $\bar{\mathbf{u}}$. The direction of wave propagation is normal to the wave front, being defined as the connecting surface of all points where p features the same amplitude and phase.

The acoustic velocity $\mathbf{u}'$ can be obtained from the linearised momentum equation Eq. (2.11), which reduces for constant mean flow $\nabla\bar{\mathbf{u}} \equiv 0$ to

$$\bar{\rho}\frac{D\mathbf{u}'}{Dt} + \nabla p' = 0. \tag{2.18}$$

With Eqs. (2.17), (2.18) and (2.14), the three dimensional acoustic field in a non-reacting moving medium is well-defined.

The solution of Eq. (2.17) shows that the occurrence of multi-dimensional wave fields in slender ducts is bound to high oscillation frequencies [Mun87]. Combustion instabilities in gas turbines typically feature frequencies less than 1000 Hz, which leads to the necessity to consider multi-dimensional wave fields in annular combustion chambers, where the circumferential dimension of the combustor is of the order of the occurring wavelengths [WKHJ99, PS02, Kun04]. For the liner geometry investigated, the radial dimensions are small and only one-dimensional, plane waves have to be taken into account. The wave equation Eq. (2.17) can therefore be simplified to the one-dimensional form

$$\left(\frac{\partial}{\partial t} + \bar{u}\frac{\partial}{\partial x}\right)^2 p' - c^2\frac{\partial^2 p'}{\partial x^2} = 0 \tag{2.19}$$

or

$$\frac{1}{c^2}\frac{\partial^2 p'}{\partial t^2} - (1-M^2)\frac{\partial^2 p'}{\partial x^2} + 2\frac{M}{c}\frac{\partial^2 p'}{\partial x \partial t} = 0. \tag{2.20}$$

x is the axial coordinate being oriented in main flow direction. M is the Mach-number of the flow, $M = \bar{u}/c$.

2.2.1 Sound Propagation in a Quiescent Medium

For low or vanishing Mach-numbers ($M \ll 1$), Eq. (2.20) further reduces to the following hyperbolic differential equation

$$\frac{\partial^2 p'}{\partial t^2} - c^2\frac{\partial^2 p'}{\partial x^2} = 0. \tag{2.21}$$

According to the method of D'Alembert, Eq. (2.21) can be solved by substitution of the variables: $\xi = x - ct$, $\eta = x + ct$ [MW70]. The

following general solution is obtained:

$$\frac{p'(x,t)}{\bar{\rho}c} = f(\xi) + g(\eta) = f(x - ct) + g(x + ct). \tag{2.22}$$

The *Riemann invariants* f and g are arbitrary functions, which are at least twice differentiable. f and g represent disturbances which travel undispersed with propagation speed c in positive and negative x-direction, respectively. The notation for the Riemann invariants is a pure matter of definition and broadly varies in literature. In the context of this thesis, the definition of f and g according to Eq. (2.22) is employed, being normalised by the factor $\bar{\rho}c$, such that the dimension of a velocity is obtained.

In order to express the acoustic velocity u' in terms of f and g, Eq. (2.22) must be evaluated in the one-dimensional formulation of Eq. (2.18) for the medium at rest

$$\bar{\rho}\frac{\partial u'}{\partial t} + \frac{\partial p'}{\partial x} = 0. \tag{2.23}$$

After application of the chain rule and integration with substitution of the variables, the following relation for u' is obtained

$$u' = f(x - ct) - g(x + ct). \tag{2.24}$$

With Eqs. (2.24) and (2.22), f and g can conversely be expressed by the acoustic variables p' and u':

$$f = \frac{1}{2}\left(\frac{p'}{\bar{\rho}c} + u'\right) \tag{2.25}$$

$$g = \frac{1}{2}\left(\frac{p'}{\bar{\rho}c} - u'\right). \tag{2.26}$$

As mentioned above, f and g are arbitrary functions in time. If the time dependence of the Riemann invariants is assumed to be of the exponential form $e^{i\omega t}$, the *harmonic solution* of the wave equation

Eq. (2.21) is obtained. The harmonic wave is one particular solution, however of practical importance, since all wave forms can be obtained by Fourier synthesis of harmonic functions. Rewriting Eqs. (2.22) and (2.24) yields

$$p'(x,t) = \bar{\rho}c\left(f \cdot e^{i\omega(t-x/c)} + g \cdot e^{i\omega(t+x/c)}\right) \quad (2.27)$$

$$u'(x,t) = f \cdot e^{i\omega(t-x/c)} - g \cdot e^{i\omega(t+x/c)} \quad (2.28)$$

with $\omega = 2\pi f$ being the angular frequency of the oscillation. Introducing the wave number

$$k = \frac{\omega}{c} = \frac{2\pi}{\lambda} \quad (2.29)$$

where λ is the wavelength $\lambda = \frac{c}{f}$, Eqs. (2.27) and (2.28) can be rewritten as

$$p'(x,t) = \bar{\rho}c\left[f \cdot e^{-ikx} + g \cdot e^{+ikx}\right] e^{i\omega t} \quad (2.30)$$

$$u'(x,t) = \left[f \cdot e^{-ikx} - g \cdot e^{+ikx}\right] e^{i\omega t}. \quad (2.31)$$

The complex notation in Eqs. (2.27)–(2.31) is commonly used to facilitate mathematical operations. For a harmonic time-dependency of the Riemann invariants, the resulting perturbation of the acoustic pressure and the acoustic velocity is harmonic, too, oscillating with the same frequency f.

With respect to Eq. (2.16), uniform sound propagation speeds in the duct are only obtained for vanishing temperature gradients in the medium, requiring homentropic flow conditions [SWZ95, SSL01]. For a homentropic flow, the entropy for each particle of the flow in space and time is uniform

$$\nabla s \equiv 0. \quad (2.32)$$

Equation (2.32) is thus a prerequisite for plane wave fronts keeping their shape. Non-homentropic flow conditions are obtained for example in the presence of a flame, under conditions of staged injection of

cooling air in a combustor or for non-negligible heat conduction at the walls of the duct.

2.2.2 Sound Propagation in a Moving Medium

For non-vanishing constant mean flow, the convective one-dimensional wave equation Eq. (2.19) can be solved by separation of the variables [Mun87]:

$$p'(x,t) = \alpha(x)\beta(t). \tag{2.33}$$

For harmonic waves $\beta(t) \equiv e^{i\omega t}$, the following general solution is found

$$p'(x,t) = \bar{\rho}c\left(f \cdot e^{-i\omega/(c+\bar{u})x} + g \cdot e^{+i\omega/(c-\bar{u})x}\right)e^{i\omega t} \tag{2.34}$$

$$u'(x,t) = \left(f \cdot e^{-i\omega/(c+\bar{u})x} - g \cdot e^{+i\omega/(c-\bar{u})x}\right)e^{i\omega t}. \tag{2.35}$$

In agreement with the case of quiescent medium, the solution can be interpreted as disturbance f travelling in downstream direction with the propagation speed $c + \bar{u}$ and a disturbance g travelling in opposite direction with $c - \bar{u}$, see Figure 2.1.

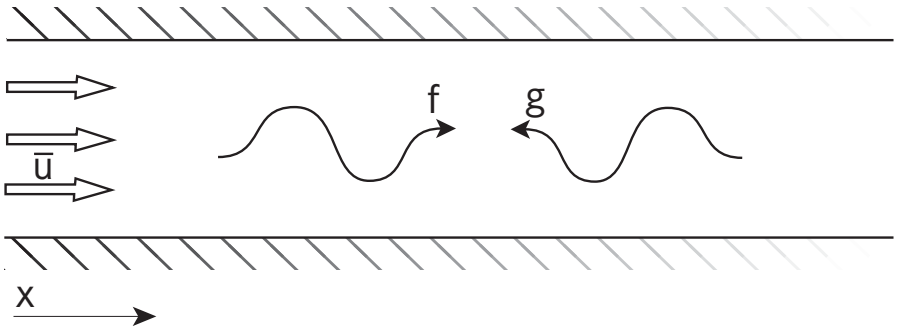

Fig. 2.1: Orientation of f and g in a duct.

By defining the convective wave number

$$k_{\pm} = \pm\frac{\omega/c}{1 \pm M} = \pm\frac{k}{1 \pm M} \tag{2.36}$$

the Eqs. (2.34), (2.35) can be written as

$$p'(x,t) = \bar{\rho}c \left[f \cdot e^{-ik_+x} + g \cdot e^{+ik_-x}\right] e^{i\omega t} \tag{2.37}$$

$$u'(x,t) = \left[f \cdot e^{-ik_+x} - g \cdot e^{+ik_-x}\right] e^{i\omega t}. \tag{2.38}$$

These results correspond to the steady case when regarding the sound propagation relative to the mean flow; i.e., for a x-coordinate which moves with $\bar{u}$.

2.2.3 Impedance and Reflection Coefficient

In analogy to electronics, where the impedance is obtained as complex ratio of electric potential and current, the *acoustic impedance* Z of the propagating acoustic wave is defined as the quotient of the acoustic pressure and velocity

$$Z(x,\omega) \equiv \frac{p'(x,\omega,t)}{u'(x,\omega,t)}. \tag{2.39}$$

Accordingly, the *admittance* Y is the inverse of Z:

$$Y(x,\omega) \equiv \frac{1}{Z(x,\omega)} = \frac{u'(x,\omega,t)}{p'(x,\omega,t)}. \tag{2.40}$$

With respect to Eqs. (2.30), (2.31), (2.37) and (2.38), it follows in presence as well as absence of convection that Z and Y are local complex quantities, depending on x and ω but being independent of t. The real part of Z is called *resistance* and its imaginary part *reactance*. The absolute value of Z varies between 0 at a pressure node and ∞ at a velocity node.

Correspondingly, changing to f and g notation, the acoustic *reflection coefficient* $r(x)$ is defined as the ratio of the upstream propagating wave $g(x)$ and the downstream propagating wave $f(x)$ at any location x

$$r(x) \equiv \frac{g(x)}{f(x)}. \tag{2.41}$$

r is suitable to specify acoustic boundary conditions, for example at the duct exits. For an *open duct exit*, say located at $x = L$, the pressure perturbation vanishes as a consequence of the surrounding plenum condition

$$p'(L,t) = 0. \tag{2.42}$$

On the other hand, a *closed exit* is characterised by zero velocity, if the confining wall is rigid

$$u'(L,t) = 0. \tag{2.43}$$

The evaluation of Eqs. (2.42), (2.43), (2.22) and (2.24) shows that a closed end is represented by $r = 1$, while r becomes -1 for an open end. Since both boundary conditions are idealised cases, the reflection coefficient of ducts will practically lie between $-1 \leq r \leq 1$. A special case is obtained for the *anechoic end* where the incident wave f is not reflected: $g \equiv 0$. For an anechoic end, r is zero.

Table 2.1 gives a short summary of the impedances and the reflection coefficients obtained for the respective exit conditions.

Exit Condition	Impedance	Reflection coefficient
open end	$Z = 0$	$r = -1$
closed end	$Z \to \infty$	$r = 1$
anechoic end	$Z = \bar{\rho}c$	$r = 0$

Tab. 2.1: Acoustic boundary conditions

The factor $\bar{\rho}c$ which has already been used for normalising the Riemann invariants in Eq. (2.22) is often referred to as the *characteristic impedance of the medium* since it determines the amplitude coupling between the pressure and velocity disturbance for the isolated waves f and g in the medium. Liquid media will thus yield higher characteristic impedances than gases, due to their higher density and speed of sound. For a given pressure perturbation, negligible velocity

fluctuation of the liquid is then obtained. As a consequence, the liquid fuel supply of combustors is usually assumed acoustically closed $Z_f \to \infty$.

2.3 The Flame as Deflagration Front

2.3.1 Rankine-Hugoniot Relations

Flames are potential sources of sound due to the volumetric expansion associated with the released heat. Momentary changes in heat release will alter the rate of volume production which couples with the system acoustics.

The equations of sound propagation, derived above for the special case $\dot{q} \equiv 0$, do not hold across flames, since the local conditions are highly non-isentropic. If the axial flame length l is small compared to the wavelength λ; i.e., if the following relation

$$\frac{\omega l}{c} = kl \ll 1 \tag{2.44}$$

holds, the flame is compact and can be treated as lumped element in a single plane. Equation (2.44) usually applies for rumble, since the acoustic wavelengths are several metres, by far exceeding the dimensions of aero-engines combustors.

The heat release of the compact flame, considered concentrated to the flame position $x = x_{fl}(t)$, can be expressed by

$$\dot{Q}_A(t) = \int_{x_{fl}^-}^{x_{fl}^+} \rho \dot{q}(x,t) dx = \rho q u \tag{2.45}$$

In Eq. (2.45), $\dot{Q}_A(t)$ is the rate of heat addition per unit area. The flame thus adopts the character of a discontinuity and the sections up- and downstream of the flame can further be assumed isentropic.

The analysis of the combustor acoustics is then carried out by separately regarding the sections upstream and downstream of the flame, being coupled by the jump conditions (1)-(2) imposed by the flame, as shown in Figure 2.2.

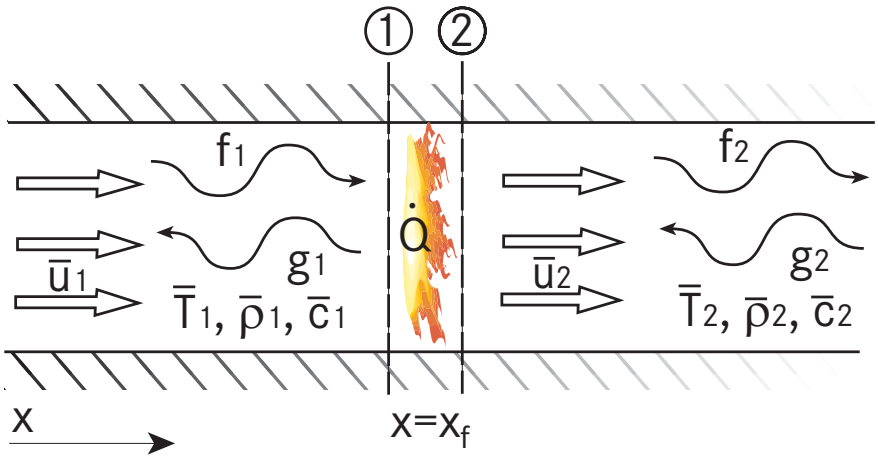

Fig. 2.2: Discontinuity induced by a flame in a duct.

The coupling conditions can be derived by integrating the conservation equations for mass and momentum, Eqs. (2.5) and (2.6), over the flame with negligible thickness $l \to 0$:

$$\rho_2 u_2 = \rho_1 u_1 \tag{2.46}$$

$$p_2 + \rho_2 u_2^2 = p_1 + \rho_1 u_1^2 \tag{2.47}$$

The conservation of energy can be immediately obtained from the first law of thermodynamics

$$u_2 \rho_2 (h_2 + \frac{u_2^2}{2}) = u_1 \rho_1 (h_1 + \frac{u_1^2}{2}) + \dot{Q}_A \tag{2.48}$$

where h is the enthalpy. Eq. (2.48) is a model simplification, since the entire combustion process is reduced to the addition of heat $\dot{Q}_A$, regardless of the chemical conversion in the mixture. In the particular case of spray combustion, Eq. (2.46) contains a further simplification, because the volume increase by the evaporating and burning fuel is

not accounted for. However, typical Air-Fuel-Ratios (AFR) encountered during engine operation are high. Stoichiometric conditions for kerosene combustion are obtained for AFR ≈ 14.67 [Rac98], resulting in a relative volume increase due to the liquid fraction by 6.8%, further decreasing for lean conditions. The contribution of the liquid fuel to the volume increase is thus small compared to the impact of the temperature rise over the flame $\bar{T}_2/\bar{T}_1$, which is 5 or more for start-up conditions.

For a perfect gas, the enthalpy h is

$$h = c_p T = \frac{\gamma}{\gamma - 1}\frac{p}{\rho}. \tag{2.49}$$

Eqs. (2.46)-(2.49) together with Eq. (2.16), are the five equations that determine the coupling of the five unknowns c, T, p, u, ρ over the flame. Assuming that the caloric properties of the gas, R and γ, do not change, the following relations can then be derived [Chu53, KEH85, PPD01]

$$\frac{u_2}{u_1} = \frac{\rho_1}{\rho_2} = 1 + \frac{\gamma - 1}{\gamma}\frac{\dot{Q}_A}{p_1 u_1} + \mathcal{O}(M^2) \tag{2.50}$$

$$\frac{T_2}{T_1} = \left(\frac{c_2}{c_1}\right)^2 = 1 + \frac{\gamma - 1}{\gamma}\frac{\dot{Q}_A}{p_1 u_1} + \mathcal{O}(M^2) \tag{2.51}$$

$$\frac{p_2}{p_1} = 1 + \mathcal{O}(M^2). \tag{2.52}$$

Eqs. (2.50)-(2.52) are known as the *Rankine-Hugoniot relations*. $\dot{Q}_A$ is the concentrated heat input of the flame per unit area according to Eq. (2.45).

By decomposing the quantities into mean value and perturbation, $\psi = \bar{\psi} + \psi'$, the *Rankine-Hugoniot relations for the acoustic fluctuations* can be derived from Eqs. (2.50)–(2.52), e.g. [PPD01]. The occurrence of rumble is bound to low air mass flows in aero-engines featuring Mach-numbers usually smaller than 0.1. Restricting our considerations to this special case of *low-speed reacting flows*, i.e. de-

flagration fronts where $M_1, M_2 \ll 1$, the Rankine-Hugoniot relations for the acoustic fluctuations are obtained from Eqs. (2.50), (2.52)

$$p_2' - p_1' = 0 \tag{2.53}$$

$$u_2' - u_1' = \frac{\gamma - 1}{\gamma \bar{p}_1} \dot{Q}_A' = \frac{\gamma - 1}{c_1^2 \bar{\rho}_1} \dot{Q}_A'. \tag{2.54}$$

2.3.2 Flame Transfer Functions and Transfer Matrices

With respect to Eqs. (2.53) and (2.54), the problem of acoustic coupling across flames is still unclosed. Additional information is required about the specific flame kinematics involved, or, more generally, about how perturbations of the supplying flow influence the heat release response of the flame. This dependency can be expressed in terms of

$$\dot{Q}' = f\left(u_1'\right) \qquad \text{or} \qquad \frac{\dot{Q}'}{\bar{\dot{Q}}} = f\left(\frac{u_1'}{\bar{u}_1}\right). \tag{2.55}$$

Functions of the type Eq. (2.55) are called *flame transfer functions*.

Flame transfer functions can be obtained either by analytical considerations, e.g. [KEH85, LZ00, PPD01], or by measurement [Len80, KK99, Kun04]. In the latter case, the determination of the heat release response of the flame is challenging, as it can not be measured directly. The chemiluminescence of the CH*-, C_2* or OH*-radical has emerged as viable indicator, particularly used in the context of premixed flames [LG81, KHS04, CSC+03].

With the flame transfer function of the respective flame being known, the Rankine-Hugoniot relations, Eqs. (2.53) and (2.54), can be employed for describing the coupling of the acoustic variables $p_{1,2}', u_{1,2}'$ over the flame. This coupling can be expressed in mathematical terms

by a flame transfer matrix $\hat{\mathbf{T}}_{pu}$

$$\begin{pmatrix} \frac{p'}{\bar{\rho}c} \\ u' \end{pmatrix}_2 \equiv \underbrace{\begin{pmatrix} T_{11} & T_{12} \\ T_{21} & T_{22} \end{pmatrix}}_{\hat{\mathbf{T}}_{pu}} \cdot \begin{pmatrix} \frac{p'}{\bar{\rho}c} \\ u' \end{pmatrix}_1 \quad . \tag{2.56}$$

The indices 1 and 2 refer to the boundaries of the flame zone x_{fl}^{+}, x_{fl}^{-}, according to Figure 2.2. Using transfer matrices, the flame is reduced to a "black-box"or an acoustic multi-port, comparable to Figure 2.3 [SP99, PP98, PFHS03]. The flame transfer function can be implemented into acoustic network models for performing stability analysis of acoustic systems, e.g. [SP03].

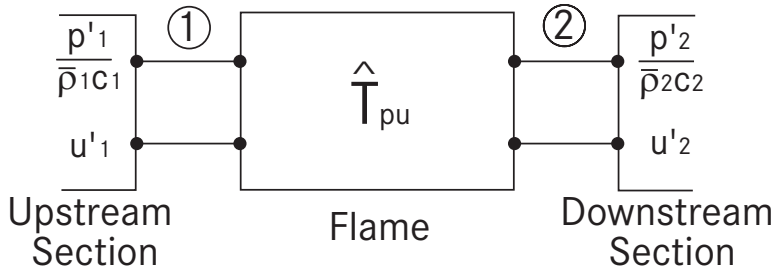

Fig. 2.3: The flame as acoustic two-port.

Besides using flame transfer functions, the flame transfer matrix can be determined by directly measuring the acoustic pressures and velocities in the combustor. This *pure acoustic approach* however is challenging with respect to the measurement uncertainties involved [PFHS03]. In addition, flame compactness and near-homentropic flow conditions downstream of the flame have to be achieved, which are indispensable for accurate measurement data.

2.4 Entropy Waves and Acoustics

2.4.1 Generation and Convection of Entropy Waves

The presence of a mean flow in the combustor not only alters the propagation speed of the sound waves, but also leads to the generation and to the propagation of entropy waves which originate at the flame and travel with the flow.

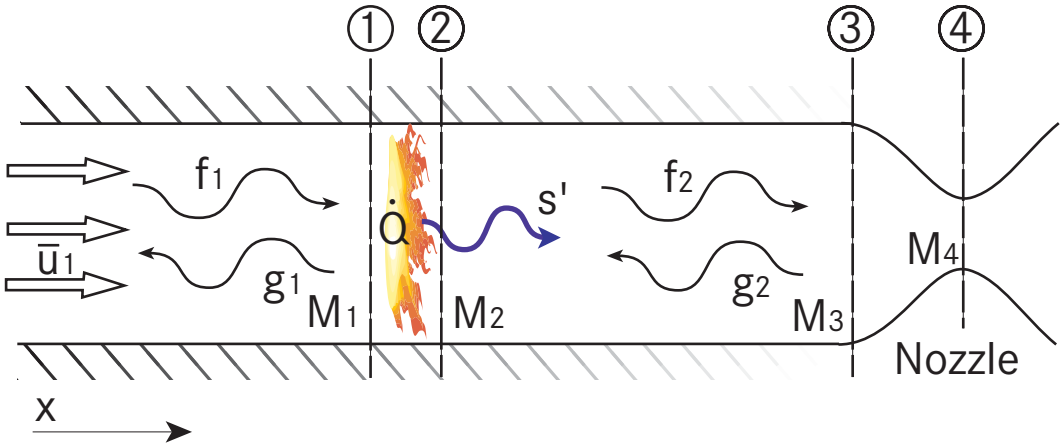

Fig. 2.4: Interaction of entropy waves and combustor acoustics.

Eqs. (2.52) and (2.53) indicate that the pressure drop over the flame is negligible. For a perfect gas under isobaric conditions, the entropy is a function of the temperature only:

$$s - s_0 = c_p \ln\left(\frac{T}{T_0}\right). \tag{2.57}$$

From Eq. (2.57), it follows for the entropy perturbation:

$$s_2' = (\bar{s}_2 + s_2') - \bar{s}_2 = c_p \ln\left(\frac{\bar{T}_2 + T_2'}{\bar{T}_2}\right) = c_p \ln\left(\frac{T_2'}{\bar{T}_2} + 1\right). \tag{2.58}$$

Linearising the logarithm by Taylor expansion yields

$$\ln(x+1) = x + \mathcal{O}(x^2). \tag{2.59}$$

The amplitude of the linearised perturbation of the specific entropy s_2' is then obtained as:

$$s' = \frac{\dot{q}'}{\bar{T}_2} = c_p \frac{T_2'}{\bar{T}_2}. \tag{2.60}$$

Taking into account the mean heat release of the flame $\bar{\dot{q}} = c_p(\bar{T}_2 - \bar{T}_1)$, Eq. (2.60) can now be re-written

$$s' = \frac{q'}{\bar{T}_2} = \underbrace{\frac{c_p(\bar{T}_2 - \bar{T}_1)}{\bar{\dot{q}}}}_{=1} \frac{q'}{\bar{T}_2} = c_p \left(1 - \frac{\bar{T}_1}{\bar{T}_2}\right) \frac{\dot{q}'}{\bar{\dot{q}}} \tag{2.61}$$

or, in terms of the absolute heat release $\dot{Q}$,

$$s' = c_p \left(1 - \frac{\bar{T}_1}{\bar{T}_2}\right) \frac{\dot{Q}'}{\bar{\dot{Q}}}. \tag{2.62}$$

Following Eqs. (2.60), (2.62), the amplitude of the entropy waves is thus proportional to the relative temperature oscillation $T_2'/\bar{T}_2$ in the downstream sector of the combustor and the relative heat release fluctuation of the flame $\dot{Q}'/\bar{\dot{Q}}$.

The presence of entropy waves impacts the acoustic variables in the dilution sector (2)-(3) of the combustor, as indicated in Figure 2.4. Linearising the density $\rho(p, s)$ around the mean value, the density perturbation ρ' is given by

$$\rho' = \left(\frac{\partial \rho}{\partial p}\right)_s p' + \left(\frac{\partial \rho}{\partial s}\right)_p s' \tag{2.63}$$

where the indices $()_p$, $()_s$ refer to isobaric and isentropic conditions. The first derivative is already known from Eq. (2.13) and equals per definition $1/c_2^2$.

$(\partial\rho/\partial s)_p$ can be derived by differentiating Eq. (2.57)

$$ds = c_p \frac{dT}{T}. \tag{2.64}$$

For $dp \equiv 0$, the thermal state equation of the ideal gas in differential formulation

$$\frac{dp}{p} - \frac{dT}{T} - \frac{d\rho}{\rho} = 0 \tag{2.65}$$

reduces to

$$\frac{dT}{\bar{T}} = -\frac{d\rho}{\bar{\rho}}. \tag{2.66}$$

Inserting Eq. (2.66) in (2.64) yields

$$ds = -\frac{c_p}{\bar{\rho}} d\rho. \tag{2.67}$$

and thus

$$\left(\frac{\partial\rho}{\partial s}\right)_p = -\frac{\bar{\rho}}{c_p}. \tag{2.68}$$

Equation (2.63), expressed in terms of linear perturbations in the downstream section of the combustor, finally becomes

$$\rho_2' = \frac{p_2'}{c_2^2} - \frac{\bar{\rho}_2 s'}{c_p} \tag{2.69}$$

or, using the identity $c_2^2 \rho_2 = \gamma \bar{p}_2$ from Eq. (2.16)

$$\frac{\rho_2'}{\bar{\rho}_2} = \frac{p_2'}{\gamma \bar{p}_2} - \frac{s'}{c_p}. \tag{2.70}$$

Following Eq. (2.70), the field of the local density fluctuations $\rho'(x,t)$ is a superposition of pressure and entropy waves. While the pressure waves propagate with the speed of sound, entropy waves are material waves, being convected with the combustor flow. Equation (2.61) indicates that harmonic fluctuations of the specific heat release $\dot{q}'(t) = \hat{\dot{q}} \cdot e^{i\omega t}$ generate harmonic entropy waves:

$$s'(x,t) = \hat{s} \cdot e^{i\omega(t-x/\bar{u}_2)}. \tag{2.71}$$

$\bar{u}_2$ is the mean flow velocity downstream of the flame. As a consequence of Eq. (2.71), a non-uniform flow velocity leads to dispersion of the entropy wave in the combustor. The density field in the dilution zone becomes with Eqs. (2.70), (2.71)

$$\rho'(x,t) = \frac{p'(x,t)}{c_2^2} - \frac{\hat{s}\bar{\rho}_2}{c_p} \cdot e^{i\omega(t-x/\bar{u}_2)}. \tag{2.72}$$

2.4.2 The Effect of Distributed Heat Release

The entropy wave number, which can in correspondence to Eq. (2.29) be defined as $k_s = \omega/\bar{u}_2$, is by the factor M_2 smaller than the wave number k for the acoustic waves

$$k_s = \frac{\omega}{\bar{u}_2} = M_2 \frac{\omega}{c_2} = M_2 k. \tag{2.73}$$

In section 2.3, the flame has been considered compact. This approach was justified with respect to the length of the flame zone being negligible compared to the occurring acoustic wavelengths. The assumption of negligible flame thickness is however critical in context with entropy waves, since a modified compactness criterion has to be used, corresponding to Eq. (2.44):

$$\frac{\omega l_{fl}}{\bar{u}} = k_s l \ll 1. \tag{2.74}$$

Eq. (2.74) is very restrictive. Typical engine start-up conditions, associated with the occurrence of rumble, are characterised by low air mass flows and rather long flames due to larger spray droplets with elevated evaporation and combustion time scales. A first estimate with typical values $f = 100\,\mathrm{Hz}$, $l_{fl} = 0.05\,\mathrm{m}$, $\bar{u} = 30\,\mathrm{m/s}$ yields $\omega l_{fl}/\bar{u} \approx 1.05$. The axial distribution of the heat input can therefore alter the impact of the entropy waves on the combustor acoustics.

The analysis of Dowling [Dow95] has shown that for a non-compact flame, the instability frequencies induced by entropy waves tend to rise. However, the spatial distribution of the heat input itself is less important. For the evaluation of the experimental results, it has therefore to be critically checked whether the effect of extended flames biases the entropy driven modes towards higher frequencies.

2.4.3 Compact Critical Nozzles

The coupling between entropy disturbances and the combustor acoustics is obtained under the influence of strong velocity gradients at varying cross-sections. In real combustors, the area blockage induced by the turbine guide vanes leads to a considerable flow acceleration at the combustor exit which can reach sonic outflow conditions.

For the length of the area contraction being small compared to the wavelength, the nozzle can be considered as lumped element. The details of the nozzle flow as well as the nozzle storage capacity between inlet and discharge can then be neglected and the nozzle can be replaced by appropriate boundary conditions. For an adiabatic and loss-free nozzle, where the entropy flux is constant, Marble and Candel [MC77] have shown that the following condition holds:

$$\frac{u'}{c} - \frac{\gamma M}{2}\frac{p'}{\gamma \bar{p}} + \frac{M}{2}\frac{\rho'}{\bar{\rho}} = 0. \tag{2.75}$$

Combining Eqs. (2.75) and (2.70), the following acoustic boundary

condition for the combustor exit (Pos. 3 in Figure 2.4) is obtained

$$u_3' = \frac{\gamma - 1}{2} M_3 \frac{p_3'}{\bar{\rho}_3 c_3} + M_3 \frac{c_3}{2} \frac{s'}{c_p}. \tag{2.76}$$

For the limiting case of vanishing Mach numbers, $M_3 \to 0$, the nozzle thus imposes closed end conditions $u_3' \to 0$. Depending on the critical Mach number in the throat, the response of the nozzle to acoustic and entropy disturbances will be different. For subsonic conditions in the nozzle throat ($M_4 < 1$), the acoustic waves downstream of the nozzle can propagate rearwards through the nozzle and thus interfere with the upstream acoustics of the combustor. For the choked nozzle ($M_4 = 1$), the back-passage through the nozzle is blocked and the upstream acoustics is decoupled. For this case, the increase of volume flux in the nozzle related to a temperature rise will generate an *expansion* wave propagating upstream. The contribution of entropy fluctuations to the reflected pressure wave can be quantified, using Eq. (2.76)

$$\frac{p_3'}{p_3} = -\frac{\gamma M_3}{2 + (\gamma - 1) M_3} \frac{T_3'}{\overline{T}_3}. \tag{2.77}$$

As a consequence, for a given entropy perturbation, the relative strength of the reflected pressure wave becomes weaker for decreasing M_3.

3 Test Rig Design

The experimental investigation of rumble was conducted on a single sector test rig. Two generic designs of a diffusion-type prefilming airblast atomiser were tested. Both injectors feature three concentric air streams with all air swirlers being oriented in the same direction. Fuel is supplied through the shaft and distributed on the annular prefilmer, which is located between the inner and the middle duct.

The injector, known to be prone to intense rumble, features a rather narrow spray cone angle and is used for most of the measurements. The second design, exhibiting different aerodynamics of the primary zone and particularly a wider cone angle of the injected air, was used as reference case (section 6.4).

The operating range of the test rig was chosen to closely meet the start-up conditions in real aero-engines. The test rig can be operated within the following boundary conditions:

- air mass flows $\dot{m}_a \leq 100$ g/s
- thermal power of the flame $\dot{Q} \leq 100$ kW
- static combustor pressure p: atmospheric (open combustor exit) up to 2 bar (choked operation with outlet nozzle)
- optional air preheating $T_a \leq 600$ K.

The fact that rumble is observed at low combustor pressures (1-4bar absolute) is favourable for the investigation at atmospheric pressure conditions [JHG03]. This permits maximum optical access into the primary combustion zone and a high degree of adaptability to the requirements of measurement techniques employed. A modular test rig design was realised, which provides the option of tuning the test rig acoustics [Aue99].

An overall view of the test facility is shown in Figure 3.1 and the corresponding infrastructure can be seen in Figure 3.2. The key com-

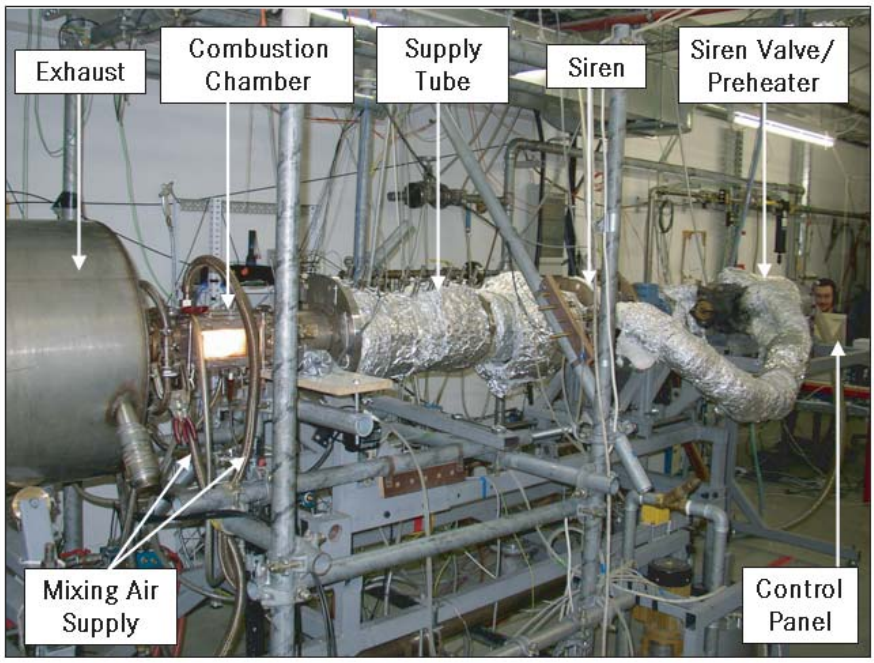

Fig. 3.1: Test facility.

ponents, which will be presented in more detail in the following subsections, are a siren/valve unit to effect acoustic forcing of the supplying air flow, a connecting supply tube, which acts as resonator, and the combustor module, accommodating the injector and the combustion chamber. An electrical air pre-heater[5] (32 kW) is placed upstream of the siren valve, capable of providing maximum air temperatures of 800 K. To fulfill the requirements of a RQL-combustor, additional mixing holes for secondary air injection were to be implemented into the combustion chamber at well defined locations. The air mass flow through these holes is not subject to external forcing. It is diverted from the main flow upstream of the siren valve and led through a separate bypass duct. The respective air mass flow is metered by a measurement orifice [Koc72] and can be controlled by a flow restrictor valve. Before entering the combustor, the bypass flow is divided evenly and directed to the upper and lower combustor side-plates.

[5]Type Leister 40000

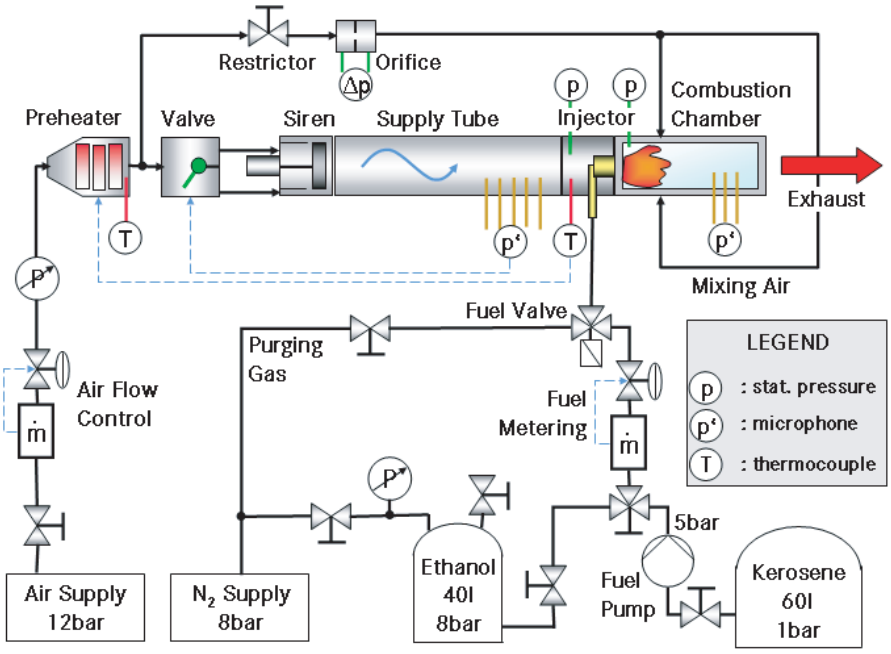

Fig. 3.2: Test facility infrastructure.

The mixing air can be optionally switched off. This is a helpful feature for measurements, where the impact of secondary air injection is undesirable, such as for the investigation of the atomiser performance in chapter 5. Thermocouples are located in the bypass duct and in the vicinity of the injector inlet to capture the air temperatures at the combustor front panel and of the mixing air. A third thermocouple located at the pre-heater exit monitors the pre-heater performance and prevents overheating. The mean and oscillating pressure losses over the injector are detected by pairs of pressure taps and microphone ports close to the burner in- and outlet. Optional microphone access is provided in the supply tube and in the combustion chamber for measuring the axial distribution of acoustic pressures.

The air is taken from the compressed air-supply (12 bar) being integral part of the lab infrastructure. The air used for combustion is filtered and the air mass flow is controlled by a thermal mass flow controller [6].

[6]Type Bronkhorst In-Flow F206BI-FBD-99V

For the experiments with combustion, kerosene Jet A-1 is used as fuel. The kerosene is stored in a 60 l tank. A fuel pump is used to boost the fuel pressure up to 5 bar. The fuel mass flow is measured using a Coriolis flow meter[7] and can be controlled by a metering valve[8]. In order to avoid coking of the injector, nitrogen is used for purging the fuel ducts of the atomiser after flame extinction or in case of emergency. The nitrogen is taken from the local supply and is connected to the fuel line by a set of magnetic valves.

For safety reasons, the kerosene is replaced by a mixture of 90% ethanol and 10% water (section 4.5.1) for experiments without combustion. The ethanol mixture is stored in a separate 40 l vessel. During the measurements, nitrogen is used to pressurise the vessel to 8 bar.

3.1 Siren

The test rig design features a siren to accomplish the acoustic excitation. Compared to speakers, which are also commonly used in thermoacoustic research, e.g. [PGW98], the attainable forcing amplitudes of sirens are particularly higher at low frequencies. This is relevant with respect to the intended experiments in the low-frequency regime including atomisation.

The siren excites an acoustic field by deterministically modulating the air supply of the combustor front panel containing the airblast injector. Its design is shown in Figure 3.3.

The excitation unit of the siren (green components in Figure 3.3) consists of a rotor-stator combination. Following the principle of hole sirens, the waveform of the generated acoustic perturbation is assumed to correlate with the open area of two shapes passing each other at a specified velocity. The velocity determines the excitation frequency obtained and can be set by the rotation speed of the siren shaft carrying the rotor blade. The siren features six rectangular

[7] Type Danfoss MASS2100 DI1.5
[8] Type Research Control Valves, RC200 1/4“

orifices, being equally distributed on the rotor, and six double sine shapes in the stator plate. The shapes have been adapted to account for the finite reference radii ($r = 30$ mm) of both the stator and the rotor disc. They are shown in Figure 3.4. The axial clearance between stator and rotor is approximately 0.3 mm. This configuration has shown to provide high signal quality with dominating ground mode and a low noise level.

Figure 3.5 shows the amplitude spectrum of the dynamic pressure obtained at the injector inlet for selected excitation frequencies of the siren in the low-frequency domain. It can be seen that the excitation is nearly sinusoidal with over 95% of the excitation energy being

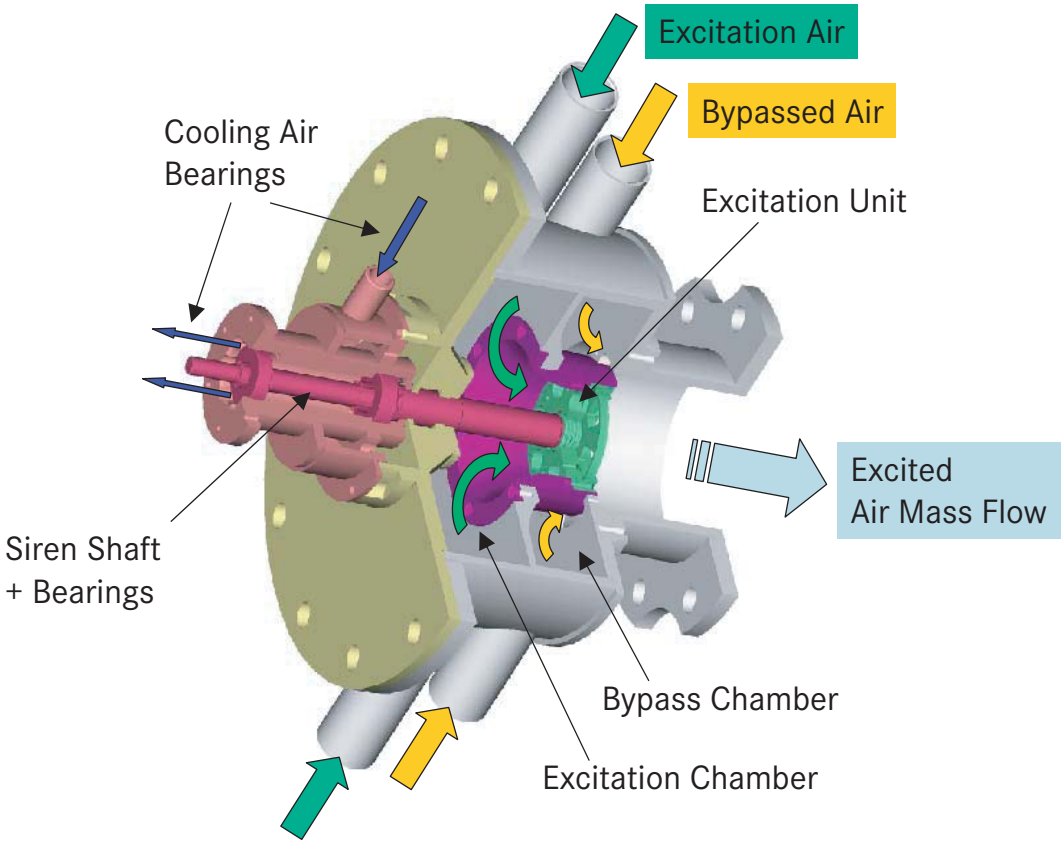

Fig. 3.3: Assembly drawing of the hot-air siren.

contained in the first harmonic. The attainable amplitudes vary being impacted by the acoustics of the connecting supply tube (see section 3.2).

Fig. 3.4: Siren outlet: The excited air flow leaves the siren through the double-sine shaped orifices in the centre, while the bypassed air is injected through the holes in the outer annulus.

Besides the effects of tube resonance, the achievable excitation amplitudes are also influenced by the air mass flux applied. Therefore, a two chamber siren design was developed to adjust the forcing amplitude in the case of need. By incorporating a separate bypass chamber, which directly feeds the siren outlet, the excitation unit of the siren can be bypassed. With a given mass flux of the air, it is now possible to reduce the amplitude of the acoustic forcing by increasing the air mass fraction being led through the bypass chamber. This air distribution through the siren is set using a siren valve, which is integrated upstream in the air supply. The valve and the siren are connected by four flexible tubes of stainless steel (two for the bypass chamber, two for the excitation chamber). The pressure loss induced by the flexible tubes and the buffer volumes of the two siren chambers provides an effective acoustic decoupling of the upstream infrastructure, in particular the air mass controller, for the frequency range of interest ($f \geq 50$ Hz).

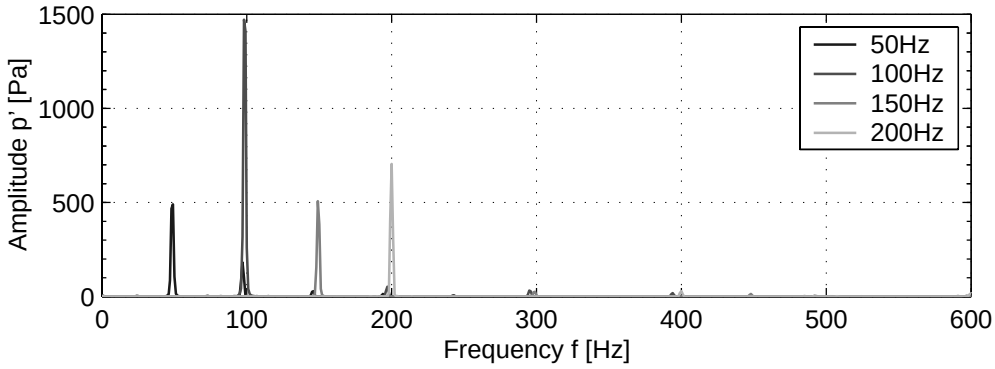

Fig. 3.5: Amplitude spectrum of the dynamic pressure oscillations obtained at the injector inlet for low-frequency excitation with the siren.

The siren is designed for operation under elevated air temperature conditions. In order to prevent overheating of the ball bearings suspending the siren shaft, they are air-cooled and located outside of the potentially hot siren chambers. The resulting cantilever design of the shaft is shown in Figure 3.3. The siren shaft is connected to a 1.1 kW three-phase A.C. motor with a nominal torque of 3.7 Nm[9]. The rotational speed is controlled by a frequency converter[10], able to produce effective excitation frequencies up to 800 Hz.

3.2 Supply Tube

The siren is connected to the combustor by a supply tube. The supply tube aims at establishing a well-defined one-dimensional acoustic state upstream of the burner inlet by homogenising the jet flow exiting the siren orifices. Furthermore, the supply tube can be used as a resonator to achieve higher excitation amplitudes.

The supply tube consists of a cylindrical duct with an inner diameter of 124 mm. In order to achieve an axial one-dimensional acoustic field inside the duct, the transverse modes must be suppressed. To

[9]Type HS-weg TE80-2, 3×230V/400V
[10]Type KIMO Motor Master MM215-EMC

achieve this, the diameter of the duct has to be small compared to the wavelength, as discussed in context of section 2.2. Higher order modes occur beyond specific "cut-off"-frequencies f_{cut}, which depend on the respective acoustic mode and the duct geometry. The cut-off frequencies can be calculated by solving the Eqs. (2.17) and (2.18) for the 3-D wave. In cylindrical ducts, modes which are not entirely axial start propagating at frequencies above

$$f_{cut,(1,0)} = \frac{1.84}{\pi d} c \tag{3.1}$$

depending on the duct diameter d and the speed of sound c [Mun87]. The critical cut-off frequency for the given duct geometry is obtained for ambient air temperatures (300 K) and becomes 1578 Hz, which exceeds the operating range of the siren by the factor 2. Hence, circumferential and radial modes are evanescent, which is essential for the interpretation of the acoustic single-point measurements to be performed in the supply tube.

Three exchangeable segments, shown in Figure 3.6, allow the flexible adaptation of the supply tube length. The length of two segments is fixed, measuring 200 mm and 400 mm, while the third module is adjustable in length between 650 mm and 850 mm. The overall length of the supply tube can thus be continuously varied from 850 mm to 1450 mm.

By adjustment of the supply duct length, tube resonance is another option to control the forcing amplitude obtained. Since the investigation is focussed on low-frequency domain (50-150 Hz), the maximum length of the tube was used (1450 mm) to take advantage of the first resonance mode of the tube at about 100 Hz (see Figure 3.5). The supply tube length was not changed during the measurements. The forcing amplitude has been fine-tuned using the siren valve.

Ten equally spaced microphone ports are welded to the tube in the far-field of the siren and can be used to determine the local acoustic pressures. The distance between adjacent ports was set to 60 mm,

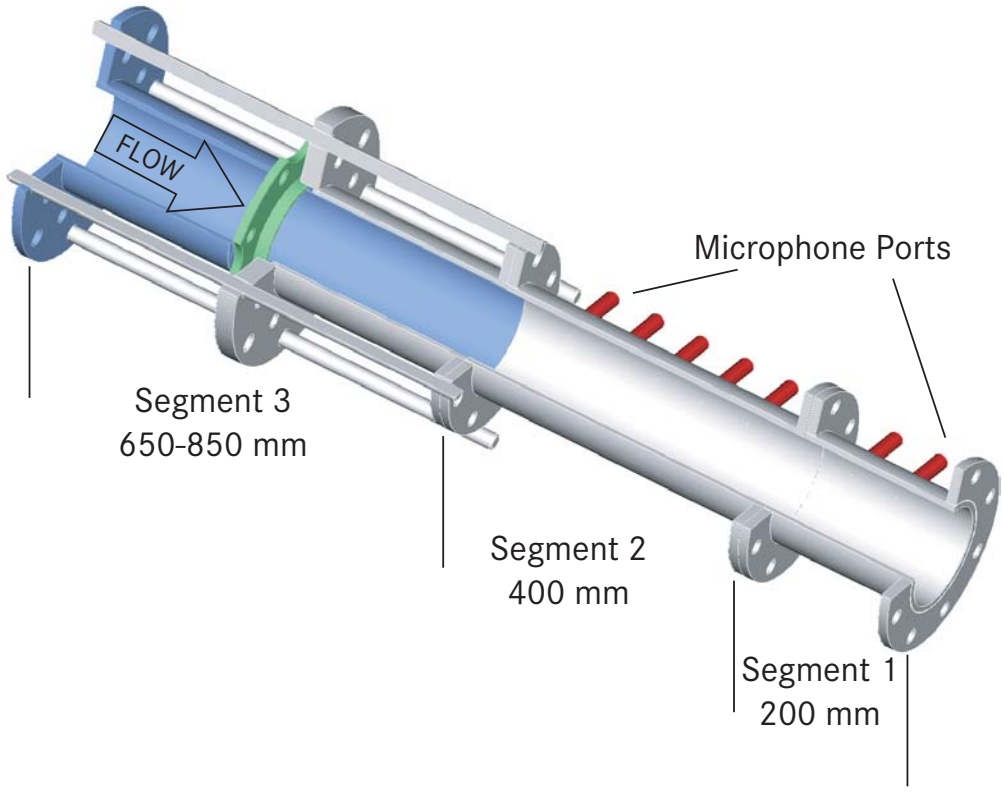

Fig. 3.6: Supply tube construction.

which is less than half of the smallest wavelength which the siren can excite. Nodes of the acoustic pressure thus can be avoided by an adequate choice of the microphone positions, and a sufficient number of pressure signals can be captured to reliably determine the acoustic state upstream of the injector.

3.3 RQL-Model Combustor

3.3.1 Design

The model combustor accommodates the injector, the front panel and the combustion chamber. It has a squared cross-section and measures 90 mm × 90 mm × 300 mm, which is comparable to the dimensions of a single sector in an annular aero-engine combustor. The construction consists of a fixed frame accommodating exchange-

able side plates, which allows the adaptation to the requirements of the measurement techniques applied. The primary combustion zone and the upstream section of the dilution zone are optically accessible by exchangeable quartz windows. The viewed area measures 150 mm × 80 mm. Pressure transducers and dynamic temperature probes can be located along the entire length of the combustor. Ignition is achieved using a high-performance spark plug[11].

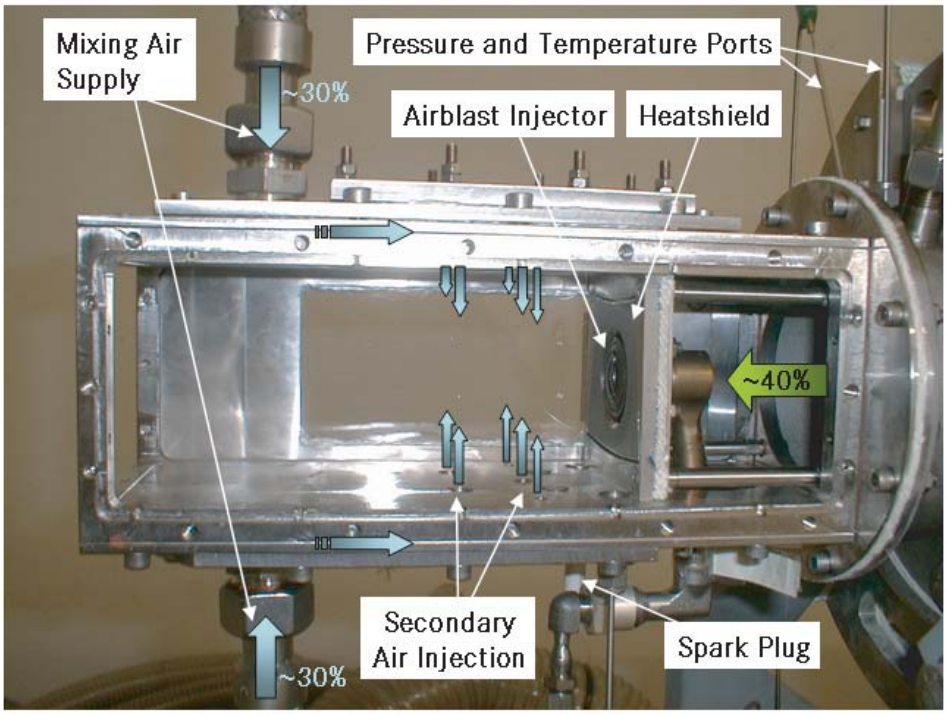

Fig. 3.7: RQL-model combustor with air distribution.

The generic combustor design is of the Rich-Quench-Lean-type. The internal air distribution in the combustor has been deduced from a typical Low-NOx can design comparable to that shown in [KBK+98]. In order to meet the aerodynamic and stoichiometric operating conditions, two rows of holes for secondary air injection were provided in the top and bottom plates of the combustion chamber as shown in Figure 3.7. The opposing jets obtained are the second source of

[11] Type Champion G54V

primary air and improve flame stabilisation by enhancing the recirculation in the primary zone.

In the generic setup used, about 60% of the overall air mass flow enters the combustion chamber as mixing air, being evenly distributed to the upper and the lower side plates of the combustor. These side plates are double-walled and the mixing air is directed inside the plates in counterflow direction to the mixing holes as indicated in Figure 3.7. By this, the mixing air is also used for cooling the combustor walls. The pattern and location of the mixing holes were derived from a real (annular) liner geometry. The hole diameters were determined on the basis of CFD to obtain a realistic air distribution. The grid of the injection holes of the model combustor is shown in Figure 3.8.

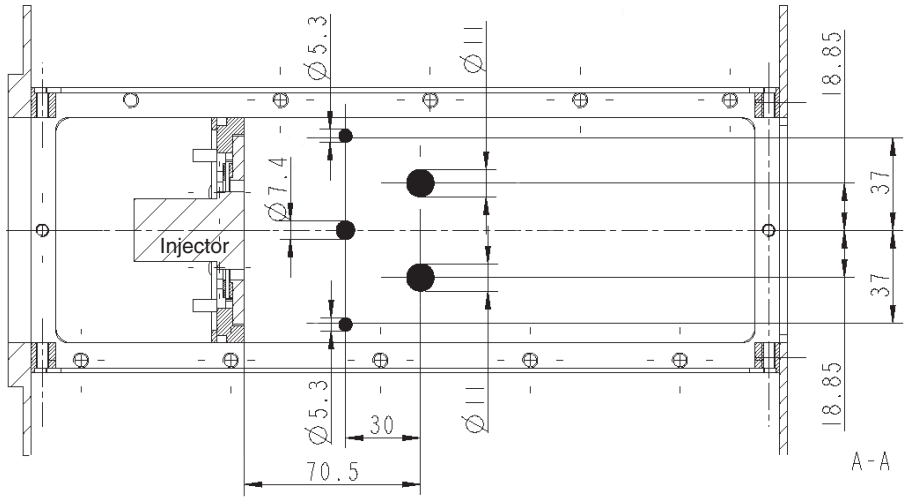

Fig. 3.8: Pattern and location of the mixing holes in the model combustor (in mm).

The injection air is not subject to acoustic forcing. The supply of the air injection is acoustically decoupled from the combustor using perforated plates, which impose acoustically closed end conditions, $Z_{mix} \rightarrow \infty$.

Dilution, film- and internal liner-cooling in the downstream part of the combustion chamber are omitted in the setup.

The front panel of the combustor consists of the generic airblast injector and a perforated heat shield as shown in Figure 3.7. The heat shield contains a set of 240 laser drilled cooling holes. The approximate diameter of each hole is 0.6 mm.

3.3.2 Air Flow Distribution

As shown in Figure 3.9, the air supply to the combustor consists of three parallel branches feeding the injector, the heat shield and the mixing air. The air flow distribution within the front panel (injector ↔ heat shield) and between the front panel and the secondary air injection has been determined for the model combustor on the basis of measurements of the static pressure drop.

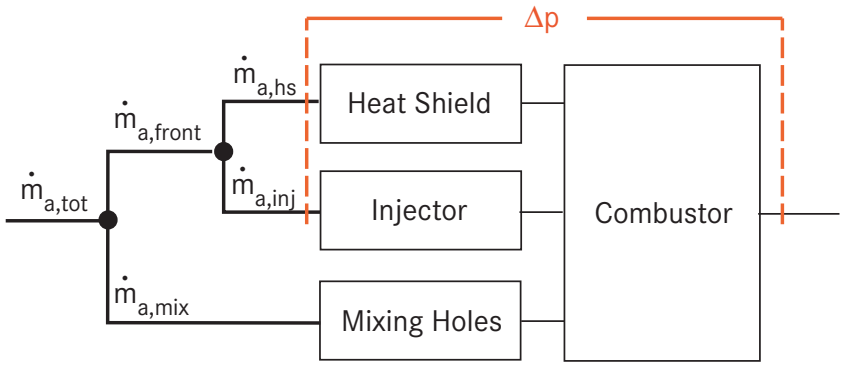

Fig. 3.9: Air flow distribution for the generic RQL-combustor and pressure loss measurements for the determination of the internal air distribution.

While the total air mass flow $\dot{m}_{a,tot}$ and the mixing air $\dot{m}_{a,mix}$ are explicitly known by flow metering, see Figure 3.2, the air split in the front panel between heat shield and injector is given by the intrinsic pressure loss characteristics of these devices. In order to obtain information about the internal air distribution of the front panel, cold-flow tests have been conducted with the injector, the heat shield and the mixing orifices selectively being blocked. By measuring the air-mass flows inducing identical cold pressure losses in the combustor, information about the air distribution in the front panel and

verification data for the measured $\dot{m}_{a,mix}$ can be gained. In this context, the upstream conditions were approximated as a plenum due to the comparatively low Mach number flows obtained in the supply tube (M < 0.05). The pressure loss Δp was then determined without acoustic forcing by comparing the static pressures upstream of the front panel and in the combustor.

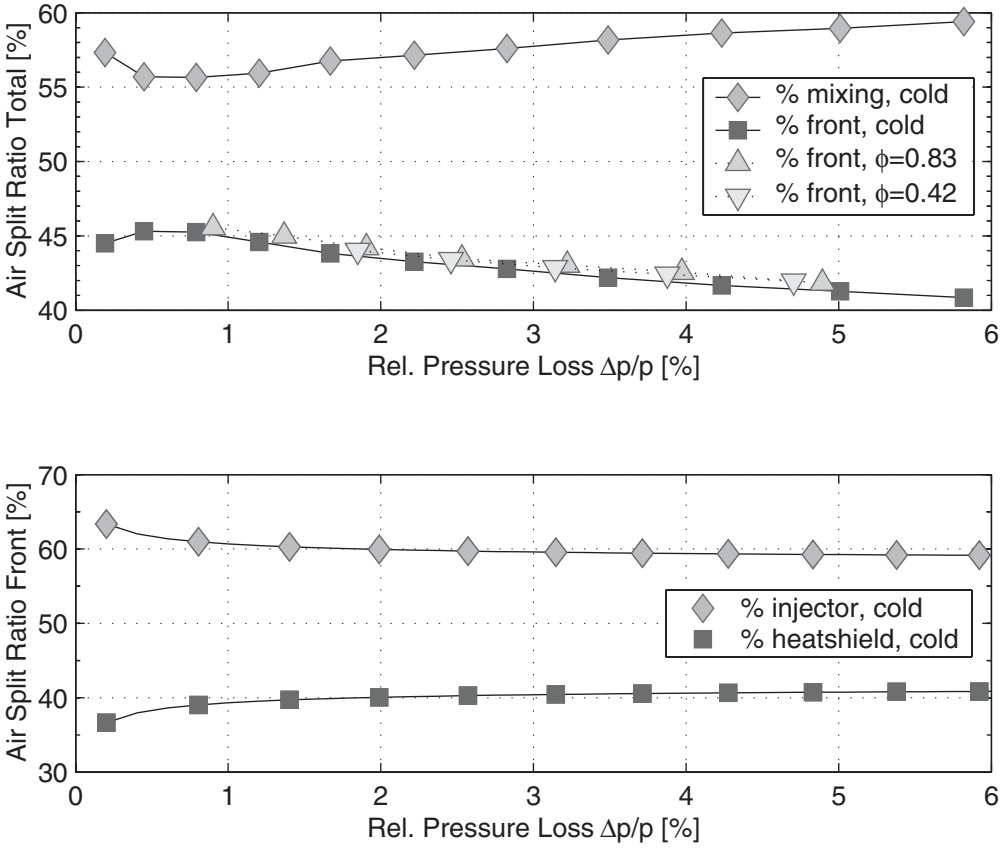

Fig. 3.10: Relative air flow distribution between bypass and main duct (upper graph) and between heat shield and injector (lower graph).

The air distribution was specified for the rumble-prone narrow-cone injector design. A cross-check was performed for the wide-cone design, exhibiting a qualitatively and quantitatively similar behaviour with deviations less than 2 percent points. The upper graph in Figure 3.10 shows the relative air mass distribution between the main duct ($\dot{m}_{a,front}/\dot{m}_{a,tot}$) and the mixing air ($\dot{m}_{a,mix}/\dot{m}_{a,tot}$) as a function of

the overall pressure drop over the combustor $\Delta p/p$. $\Delta p/p$ itself is a function of $\dot{m}_{a,tot}$. Figure 3.10 indicates that the ratio $\dot{m}_{a,mix}/\dot{m}_{a,front}$ is approximately 57/43 which is a realistic value for RQL-setups. The changes of the relative air distribution induced by varying $\dot{m}_{a,tot}$ are less than 5 percentage points with a tendency for increasing air mass flow through the mixing ducts for higher overall air mass flows. The internal air distribution on the combustor front panel, i.e., between heat shield and injector, is shown in the lower graph of Figure 3.10. Here, an air mass ratio $\dot{m}_{a,inj}/\dot{m}_{a,hs}$ of nearly 60/40 with respect to $\dot{m}_{a,front}$ is measured. The sensitivity to varying $\Delta p/p$ is even smaller. From the cold flow measurements, the following distribution is obtained, which can be assumed independent of $\Delta p/p$ with good accuracy:

$\dot{m}_{a,inj}$=26%	$\dot{m}_{a,hs}$=17%	$\dot{m}_{a,mix}$=57%

Comparative measurements were performed for conditions with combustion, exemplarily shown in the upper graph of Figure 3.10. The cold pressure losses are augmented by the fundamental thermodynamic loss induced by the flame, which increases the total pressure loss by about 20% for a given $\dot{m}_{a,tot}$ [CRS01]. As a consequence, the respective measurement points in Figure 3.10 tend towards higher $\Delta p/p$ in the presence of a flame. However, due to the flat dependency of the air mass distribution on the pressure loss, the distribution between mixing and front panel air is only little affected. The relative deviations induced by the flame do not exceed 1.5 percent points and are seen to be rather independent of the overall equivalence ratio ϕ applied.

3.3.3 Combustor Outlet

In regard to the timescales involved, engine start-up can be approximated as a sequence of quasi-steady operating conditions in the combustor. For this reason, the measurements were conducted under

steady conditions of the mean flow, under both external deterministic forcing with the siren and in the self-excited "rumble" mode. Depending on the measurement requirements, the combustor was operated with three different acoustic exit conditions.

Open-ended combustion chamber without extension: For the steady measurements and the measurements with siren, self-excitation must be suppressed, since the self-excited oscillation usually exceeds by far the forcing amplitude of the siren. For this purpose, the open-ended combustion chamber without extension has been used. Compared to the acoustic wavelengths in the low-frequency regime $f < 150$ Hz, the length of the combustion chamber is small, $l_{cc} \ll \lambda$. The low impedance at the open combustor exit, being imposed by the plenum conditions of the adjacent exhaust duct, therefore results in comparably low impedances at the injector outlet, $Z_{inj} \rightarrow 0$. The dynamic pressure amplitude p' at the injector exit is small. Upstream forcing by the siren, which alters the effective pressure drop across the burner, thus determines the injector response and is only marginally altered by the flame.

For investigating the self-excited rumble oscillations, two configurations of the combustion chamber exit were applied:

(Sub-)Critical nozzle: As it was shown in section 2.4.3, one possible explanation for the occurrence of rumble is the reflection of entropy waves at the (nearly) choked combustor outlet due to the presence of the turbine inlet guide vanes in real engines. To replicate these conditions, a critical nozzle was manufactured to be mounted at the combustion chamber exit. A drawing of the nozzle assembly is shown in Figure 3.11.

The nozzle is made of brass due to the good thermal conductivity and machinability of this material. To compensate the strongly increased heat flux due to high velocities at the throat, water cooling is applied. The nozzle was designed to accommodate exchangeable throats to adapt the critical diameters to the operating conditions. For the measurements, a critical throat diameter of 20 mm was selected. A

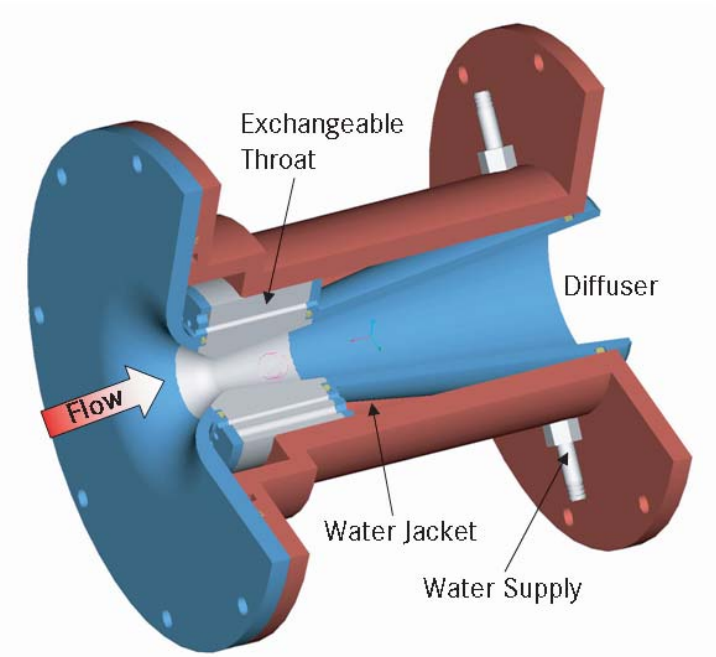

Fig. 3.11: Assembly drawing of the critical nozzle.

quick reduction of flow cross section at the nozzle inlet models the realistic engine conditions found at the turbine guide vanes. The low expansion angle of the diffuser aims at minimising flow separation and the large pressure losses associated with it. However, pressure losses could not completely be avoided and the static pressure in the combustion chamber was subject to variations, depending on the operating conditions. The maximum absolute pressures encountered inside the combustor did not exceed 1.8 bar.

Resonance tube: In order to investigate the impact of the primary zone aerodynamics for the excitation of the low-frequency combustion instabilities, an open-ended flame tube was designed. The open end eliminates the pressure feedback due to entropy waves, since critical outflow conditions are not attained.

The cylindrical tube, shown in Figure 3.12, measures 101 mm in diameter and thus matches the cross sectional area of the combustor. In order to comply with the low admittance imposed by a choked nozzle at the combustion chamber exit, a tube length of 1320 mm has been

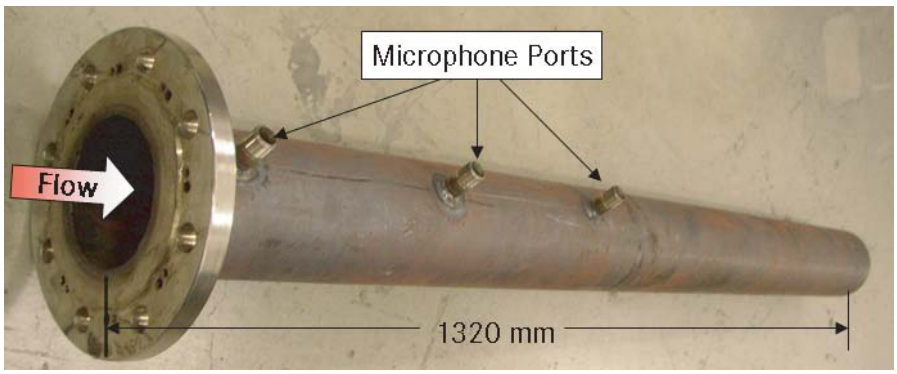

Fig. 3.12: Resonance tube.

chosen, corresponding to a typical $\lambda/4$-wavelength obtained during rumble.

The different combustor outlet conditions applied are summarised in Table 3.1.

Configuration	Impedance	Mach number
Open exit	$Z \to 0$	$M \to 0$
Nozzle	$Z \to \infty$	$M \to 1$
Resonance tube	$Z \to \infty$	$M \to 0$

Tab. 3.1: Outlet conditions of the combustion chamber.

4 Measurement Techniques

4.1 Single Point Measurements of the Acoustic Variables

4.1.1 Microphones

The dynamic pressure in the supply section of the rig was measured by means of G.R.A.S. 1/4" condenser microphones which are shown on the left hand side in Figure 4.1. The microphones were used in water-cooled adapters, shown in the centre of Figure 4.1, to prevent overheating when being in contact with preheated air or flue gas. The microphones were connected to a multi-channel conditioning amplifier[12]. The voltage sensitivities have been varied between 1 mV/Pa and 3.16 mV/Pa, depending on the dynamic pressure amplitudes.

Fig. 4.1: 1/4" condenser microphone (left) with cooling adapter (centre) and PCB piezo-transducer (right).

The tendency for soot deposition on the cooled microphone membra-

[12]Type Nexus 2692C by Brüel & Kjær

ne under highly oscillating conditions in the combustor showed to be a major reason of sensor degradation and measurement error. As a consequence, the condenser microphones in the combustion chamber were replaced by water-cooled pressure transducers of type PCB M106B. This acceleration-compensated piezo-type transducer is capable of measuring the dynamic pressure within a range of 0.7 Pa to 0.57 bar on a static head of up to 138 bar and is shown on the right hand side of Figure 4.1. It was usually operated at sensitivities of 450 μV/Pa.

To capture the difference of the dynamic pressure $\Delta p'$ over the burner, two microphones were placed in the immediate vicinity up- and downstream of the injector. The upstream position in the supply section coincides with the injector inlet. Pressure measurements in the combustor were performed at 6 mm downstream distance of the burner outlet to minimise contact with impinging fuel droplets and soot. The measurement positions are illustrated in Figure 4.2.

The absolute calibration of the condenser microphones was accomplished using a pistonphone[13]. Consistency and repeatability of the measured pressure amplitudes were high, producing a relative measurement error of less than $\pm 1.5\%$. Comparative measurements in the rig under siren forcing have shown that the error induced by the use of different microphone types is negligible, featuring a relative amplitude deviation of less than 2.5% and a phase drift below 2° for the frequency range of interest.

4.1.2 Hot Wire Anemometry

Hot wire measurements were conducted for the time-resolved determination of the acoustic velocity in the combustor and for local consistency checks with the PIV data (section 4.2). The measurements were performed at cold flow conditions without spray and flame. A Constant Temperature Anemometer (CTA)[14], equipped with

[13] Type G.R.A.S 42AA
[14] Type DISA 55D01

a 10 μm Pt-Ir hot-wire probe, was used for that purpose. For constant temperature anemometry, the hot wire is heated by electrical current, being connected to one arm of a Wheatstone bridge, which is part of the CTA. A servo amplifier keeps the bridge in balance by controlling the current to the sensor so that the resistance and wire temperature remain constant. The bridge voltage E is correlated with the convective heat transfer at the wire and thus a direct measure of the velocity. The local velocity u can be interpolated by a polynomial curve fit in fourth order [Jør02], according to

$$u = C_0 + C_1 \cdot E + C_2 \cdot E^2 + C_3 \cdot E^3 + C_4 \cdot E^4. \tag{4.1}$$

Calibration aims at the determination of the coefficients $C_0 \ldots C_4$ for the respective wire position.

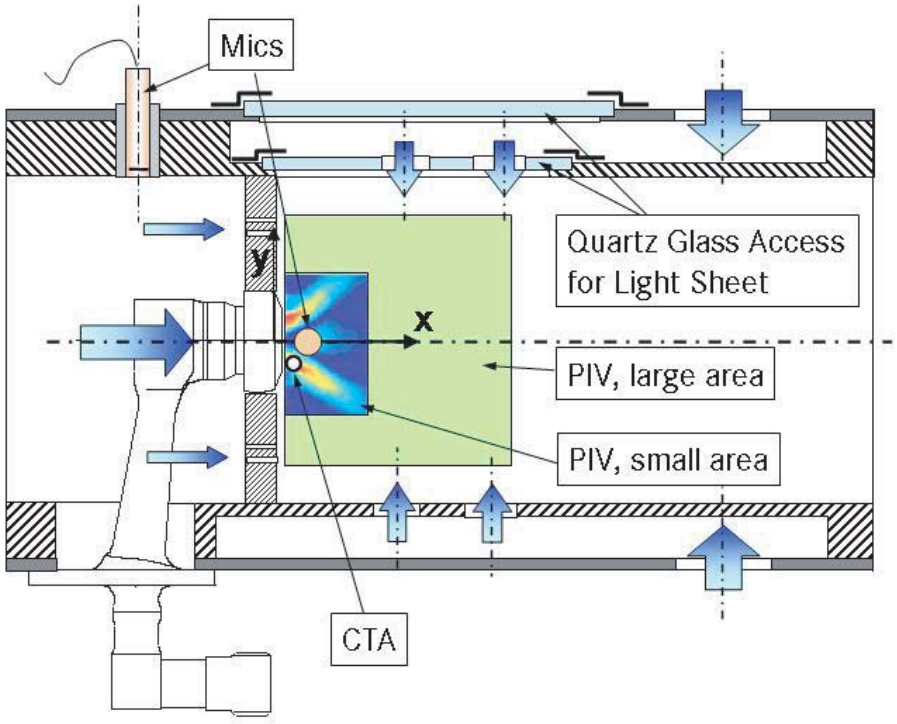

Fig. 4.2: Positioning of the hot wire, the microphones and the PIV light sheet in the combustor.

The hot wire probe was usually applied in the centre plane of the combustor, 3 mm downstream of the injector exit as shown in Figure 4.2. To make the measurement representative of the burner acoustic velocity, the probe was positioned directly in the exiting air jet of the injector, where maximum velocity and a low local turbulence level were obtained. Calibration in absolute terms was not performed. CTA data are given in relative amplitudes $u'/\bar{u}$, with the calibration being accomplished by varying the air mass flow over the injector for a given wire orientation and air temperature.

4.2 Particle Image Velocimetry (PIV)

Two-component (2C) PIV was employed to accomplish the following measurement tasks:

1. determination of the velocity field of the air flow under non-combusting conditions
2. determination of the velocity field of the spray droplets with combustion
3. visualisation of the spray cone and of the local fuel distribution in the primary zone.

The principle of 2C-PIV is illustrated in Figure 4.3 [Dan00]. A stroboscopic light sheet, being generated by a pulsed laser system with subsequent optical set-up, is used to illuminate the flow field in the measurement plane. The flow is seeded with small particles (e.g. TiO_2, SiO_2 or oil droplets), and the Mie scattered laser light is detected by a synchronised CCD-camera, which is oriented perpendicular to the laser light sheet. If the duration of the laser pulses is short enough, the movement of the seeding particles can be frozen. In order to obtain the instantaneous velocity field, two shots of the particle distribution are made within a well-defined time interval. The two recorded particle fields (=frames) are then compared to determine the

displacement vectors of the particles by cross-correlation. For that purpose, the camera images are usually sub-divided into smaller interrogation areas, within which the correlation and the determination of the average local displacement vectors is being performed. The displacement is obtained by calculating the shift of the correlation peak with respect to the origin of the interrogation window. Using an appropriate peak finding algorithm, sub-pixel accuracies down to 0.2 pixel can be achieved [RWK98]. The velocity field is finally obtained by dividing the displacement vectors with the selected pulse separation of the laser.

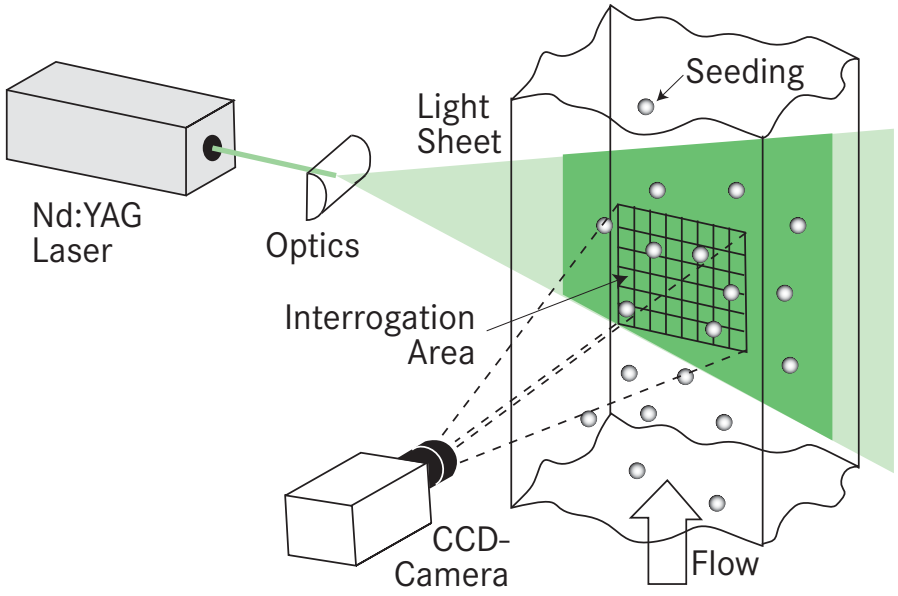

Fig. 4.3: PIV-setup.

The 2D-PIV system[15] used during the measurements consists of a double-cavity Nd:YAG laser system to establish short pulse separations at sufficiently high power output (max. 200 mJ). The frequency-doubled laser light at 532 nm is emitted in pulses of 10 ns. The pulse separation is varied between $3 - 15\ \mu s$, depending on the operating conditions, the size and the density of the seeding. The CCD chip of the camera contains 1028×1280 pixels with 8 bit resolution and allows storage of two individual frames for subsequent cross-correlation.

[15] Dantec FlowMap PIV

Two measurement areas in the combustor were investigated, shown in Figure 4.2, both coinciding with the central longitudinal section of the primary zone. The laser light sheet was directed from the top through the combustion chamber. To provide optical access to the combustion chamber, the upper side wall of the combustion chamber was equipped with quartz windows, as shown in Figure 4.2, the inner one containing the characteristic hole pattern for mixing air injection. The smaller region in the vicinity of the injector exit was chosen to collect detailed data in the near-field of the combustor outlet and measured 25 mm × 30 mm, beginning 1 mm downstream of the combustor front panel. The larger region measured 75 mm × 65 mm and was used to get a global view of the flow field throughout the primary zone.

PIV-recordings were made under stationary and oscillating flow conditions. The dynamic measurements were conducted phase-resolved applying phase angle intervals of 30° and 36°, respectively. The average flow field obtained at each phase angle is based on 180 single shots. Under stationary conditions, 100 recorded images proved to be sufficient for representative velocity averages.

For the air velocity measurements without combustion, oil droplets being supplied by a Laskin nozzle generator [RWK98] were used as tracer. For spray visualisation and determination of the droplet velocities, the external seeding was omitted and the fuel droplets themselves were recorded and correlated. Under the latter conditions, the velocity evaluation has shown to be biased by the following two effects:

- **Decreasing droplet concentration:** The droplet concentration varies strongly over the primary combustor zone which impacts the quality of the local velocity data obtained. Efforts were made to adapt the laser power to the droplet concentration encountered in most parts of the envisaged recording area. However, in the immediate vicinity of the atomiser exit, high spray density and effects of multiple scattering led to a local over-

exposure of the recorded image, which does not allow for the separation of individual droplets. As a result, underestimated or vanishing velocities are obtained in these regions, as shown in Figure 4.4. On the other hand, enhanced droplet evaporation and combustion in the flame resulted in a rapid decrease in droplet concentration, paired with a considerable rise in background noise, both making the determination of velocities in the flame zone erroneous.

- **Polydisperse spray:** PIV does not allow for the discrimination of the particle sizes for velocity evaluation. Since the average energy of the scattered light is known from Mie theory to be proportional to $(d/\lambda)^2$ [RWK98], the images of the larger droplets tend to dominate the PIV evaluation. In the case of the polydisperse spray of the injector, the measured velocities were therefore biased towards lower values, due to the increasing inertia of the larger droplets in the accelerating air flow of the primary zone.

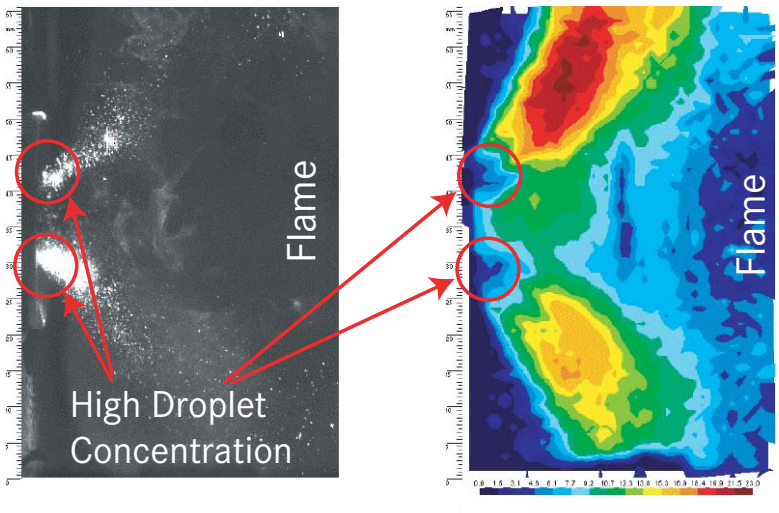

Fig. 4.4: Example for the measurement bias when the kerosene spray is used as seeding: Droplet scatter (l.h.s.) and evaluated velocity map (r.h.s).

4.3 OH*-Chemiluminescence

Photomultiplier

The time-resolved OH*-chemiluminescence of the flame was captured using a photomultiplier. To detect the OH*-chemiluminescence, which peaks at a wavelength of 308 nm, a DUG 11X-filter[16] was integrated into the optical path. The filter has a band-pass characteristics for wavelengths between 250 nm and 380 nm, which is plotted in Figure 4.5. The photomultiplier was positioned at 300 mm radial distance from the combustion chamber with a field of view covering its whole optically accessible part (90 mm × 150 mm) shown in Figure 4.6.

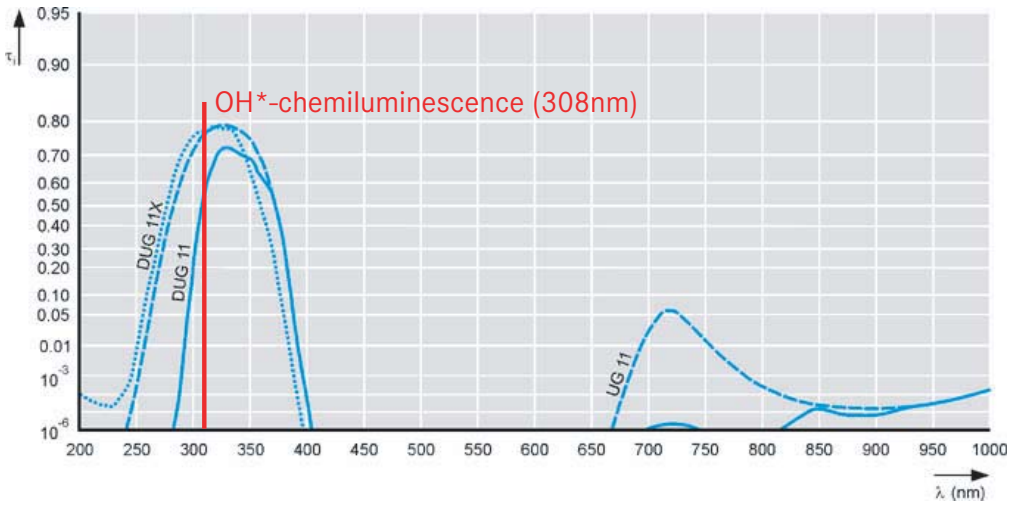

Fig. 4.5: Transmissivity characteristics of the DUG 11X filter.

ICCD High-Speed Video

Spatially-resolved flame recordings were performed using an intensified high-speed camera[17] being equipped with the above-mentioned DUG 11X-filter. The self-excited flame was recorded at an image resolution of 256 × 256 pixels. The sampling rate was 4500 Hz. Usually, a sequence of 400 camera images were acquired for each operating point, covering 6 to 10 oscillation periods of the flame. The camera

[16]Supplier: ITOS Gesellschaft für Technische Optik mbH
[17]Type Kodak EKTAPRO Motion Analyzer 4540

was focused on the central plane of the primary zone of the combustion chamber. The viewing area covers the entire height of the combustion chamber in the flame zone over a length of 113 mm, as shown in Figure 4.6.

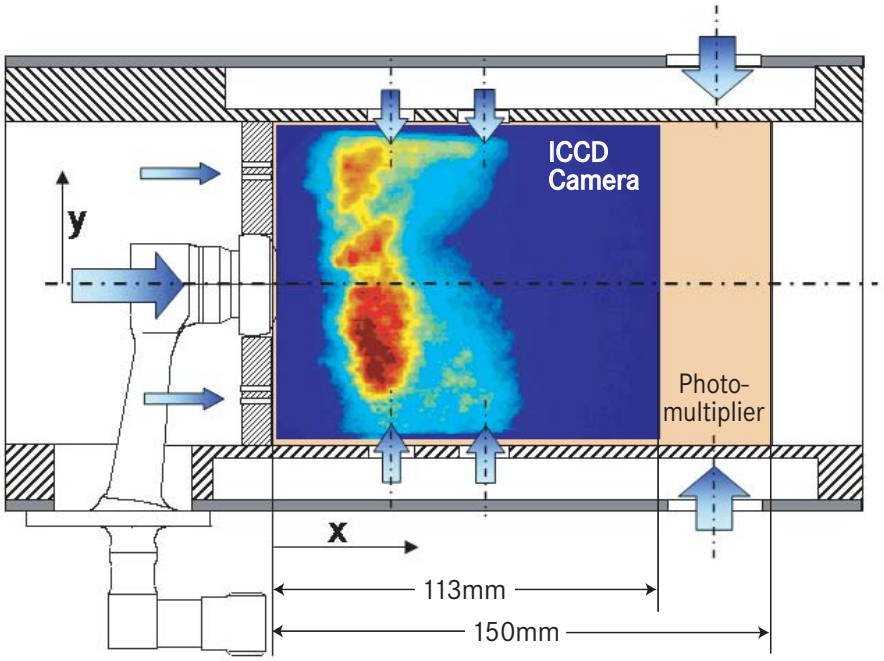

Fig. 4.6: Field of view for the high speed camera and the photomultiplier used for OH*-chemiluminescence recordings.

The recorded intensities were evaluated in relative units $I'/\bar{I}$. A comparison between the measured intensities of the photomultiplier and the spatially integrated images of the high-speed camera shows an excellent agreement with relative deviations below 2%. Thus, the differences related to the larger field of view of the photomultiplier in the dilution sector of the combustor are small.

4.3.1 Physics of OH*-Chemiluminescence

The term 'chemiluminescence' was introduced by Weidemann in 1888 and refers to the emission of light from a chemical reaction.

OH*-chemiluminescence consists of the radiation emitted from the electronically excited hydroxy radical[18] when returning to the energetic ground state through $^2\Sigma \rightarrow ^2\Pi$ transition [Gay74].

$$OH^* \rightarrow OH + hf \tag{4.2}$$

In Eq. (4.2), h is the Planck constant. The characteristic wavelengths of the emitted photons ($\lambda \approx 308$ nm) is thus proportional to the energy released by the radical during transition.

The intensity of the chemiluminescent radiation depends on the chemical kinetics involved in the combustion process [HV03, DV92] and is therefore related to the type of fuel used. The emitters commonly used for measurements in hydrocarbon flames are OH*, C_2*, CH* and CO_2*, of which the hydroxy radical OH* is of eminent practical significance due to its high emitted intensities.

The practical significance of the OH*-chemiluminescence and especially the relationship with the heat release is not evident. Since the instantaneous heat release cannot be measured directly, in-situ calibration of the chemiluminescent emissions with respect to the heat release is practically unfeasible. Modelling efforts therefore strive to theoretically determine the sources of chemiluminescent emissions and their relation with the heat released. However, due to the complexity of reaction kinetics and the number of subreactions involved, considerable practical success was obtained only for low-carbon fuels, such as methane.

The following simplified formation path for OH* was first postulated by Krishnamahari et al. [KB61] and is commonly used in literature, e.g. [DV92, Law00]

$$CH + O_2 \rightarrow CO + OH^*. \tag{4.3}$$

This formation path has shown to be particularly applicable for the

[18] the electronically excited state is usually denoted with *

interpretation of OH*-chemiluminescence for multi-carbon fuel combustion where CH-radicals can be found at elevated concentrations.

Haber [HV03] suggests an alternative formation mechanism between formyl radicals and atomic oxygen. It particularly accounts for the experimental observation that one-carbon fuels (CH_4, CH_3OH) exhibit a chemiluminescent intensity maximum under near-stoichiometric ($\phi \approx 0.9$) and near-adiabatic conditions, e.g. [Hab00, Büc92]:

$$HCO + O \rightarrow CO + OH^*. \tag{4.4}$$

Emission of photons according to Eq. (4.2) is one option for the destruction of OH*. Apart from the destruction of OH* by chemical reaction, which is less significant for technical flames [DV92], the excess energy of the OH* radical is also removed by collisional quenching with another molecule M according to

$$OH^* + M \rightarrow OH + M. \tag{4.5}$$

The calculations of Garland et al. [GC86] have shown that the quenching rates depend on the quenching cross section of the respective quencher M and considerably decrease with temperature. As a consequence, the OH*-chemiluminescence exhibits a strong temperature dependency, tending to increase for higher flame temperatures. This makes the interpretation of the chemiluminescent radiation challenging in context with non-premixed flames or non-adiabatic environments. The study of Najm et al. [NPMW98] has revealed that the significance of OH*-emissions must also be critically assessed for premixed configurations.

Most researchers refer to the work of Price et al. [PHS68] to justify the assumption of a proportional correlation between OH*-emissions and the local heat release rate. OH*-chemiluminescence has become widely used as practical measure for the heat released by premixed methane-air flames, such as for determining the thermoacoustic flame

response e.g. [HZGV95, PP98, SRBS01, Fis04]. Applications have also been extended to non-premixed configurations, e.g. [Kle00]. Morrell et al. [MSW+01] interpreted the chemiluminescent emissions in a n-heptane fuelled, non-premixed combustor. The study revealed that OH* was a reliable indicator for the volume-integrated heat release for overall lean combustion conditions ($0.64 < \phi < 0.9$). Residual OH*-intensities were encountered in the post-combustion zone, being thermally produced.

Despite the encouraging results by Morrell et al., it is in general not clear to what extent the OH*-chemiluminescence represents the heat release rate in the case of the kerosene spray flames under investigation. The fast thermocouple method, introduced in the following section, is therefore used to allow a critical assessment of the measured chemiluminescent emissions.

4.4 Dynamic Temperature Probe

The quantification of the local gas temperatures in the combustor is particularly instructive, since it provides information about

- the generation, propagation and dispersion of entropy waves in the combustor under different operating conditions
- asymmetries in the temperature distribution; e.g. due to the influence of the staged air injection
- the coupling between the OH*-chemiluminescence and the heat release for the spray flames investigated.

For this purpose, the double thermocouple method was further developed. It was already successfully applied under steady conditions [Hei02] and for measuring periodic temperature perturbations below $f < 15$ Hz [Bra91]. Within this thesis, it has been adapted to account for the extended frequency range of the rumble instability ($f < 150$ Hz). The associated challenges are twofold: Firstly, a probe

has to be developed which accommodates the thermocouples, being suitable for the use in the flame. Secondly, the frequency of the temperature fluctuations are considerably faster than the response of the thermocouples, which means that the temperature oscillations are captured with considerable attenuation and phase shift. The real gas temperature has therefore to be reconstructed from the measured signals, additionally taking into account the radiative heat losses of the thermocouples.

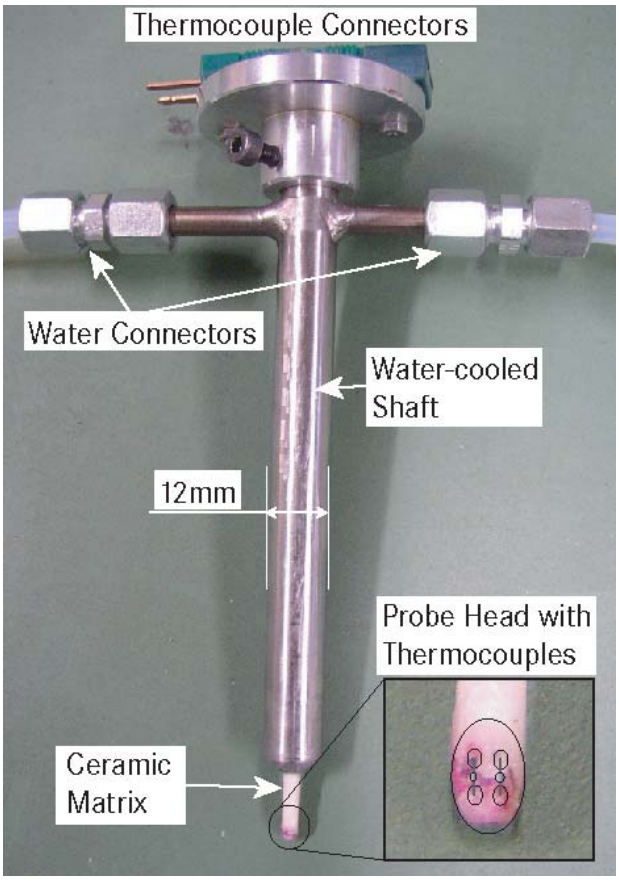

Fig. 4.7: Dynamic temperature probe.

The measurements were conducted using water-cooled probes of the type shown in Figure 4.7. The probes host two Pt/10%RhPt-thermocouples (type S) featuring different wire diameters (0.002" and 0.003") which are positioned with an 1 mm separation at the tip of a ceramic isolator. The thermocouples were connected to a cold-junction compensated amplifier.

The temperature change "felt" by each thermocouple is determined by the local energy balance of the convective and the radiative heat transfer according to Figure 4.8:

$$m_t c_t \frac{dT_t}{dt} = \underbrace{\alpha_t A_t (T_g - T_t)}_{\text{convection}} \underbrace{-\varepsilon \sigma_B A_t (T_t^4 - T_w^4)}_{\text{radiation}}. \tag{4.6}$$

The radiative heat losses of the thermocouples (index t) to the cooler combustor walls (index w) are approximated by Kirchhoff's law of radiation, assuming $A_w \gg A_t$. The applicability of Kirchhoff's law requires a local thermal equilibrium of the radiating body. The emissivity ε of a radiating grey body is known to be exclusively related to the intensity of spontaneous emission of the body [Bal76], being a function of its atomic structure and its temperature. The time scale of spontaneous emission is small compared to the oscillation period of the combustion instability. Furthermore, the Biot number Bi_t of the thermocouple alloy is small compared to the Nusselt number Nu_t, determining the convective heat transfer from the surrounding gas phase, since the thermal conductivity of the metal λ_t is considerably higher than that of the gas λ_a

$$Bi_t = \frac{\alpha_t d_t}{\lambda_t} = Nu_t \frac{\lambda_g}{\lambda_t} \Rightarrow \frac{Bi_t}{Nu_t} = 9.8 \cdot 10^{-4}. \tag{4.7}$$

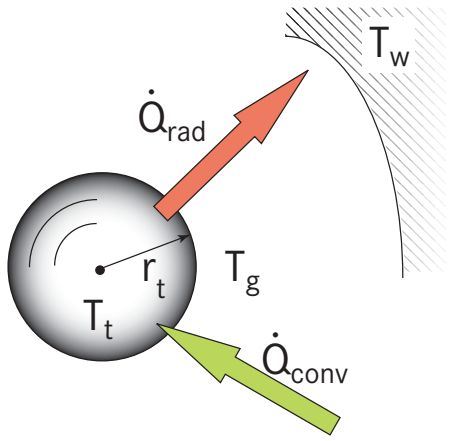

Fig. 4.8: Heat balance at the thermocouple tip.

As a consequence, effects of internal heat conduction in the thermocouple can be neglected and the thermocouples attain uniform temperature, immediately responding to the changes imposed by the temperature fluctuations of the gas. The assumption of a local thermal equilibrium is thus fulfilled and the thermocouples exhibit a quasi-steady grey body behaviour. Following [Koh88], the emissivity ε of platinum in hot ambiances can be calculated to

$$\varepsilon = 11 \cdot 10^{-5} T_t + 17 \cdot 10^{-3}, \quad T_t \in [1000\ \mathrm{K}, 2000\ \mathrm{K}]. \tag{4.8}$$

Soot deposition on the thermocouple was not observed during operation, such that Eq. (4.8) was applied to model the local radiative heat losses. For deriving the equations for the steady mean temperature $\bar{T}$ and the temperature perturbations T', it is assumed that the perturbation of the wall temperature is negligible $T'_w \equiv 0$ due to its high caloric capacity $m_w c_w \gg m_t c_t$. Furthermore, the welded thermocouple contacts are assumed to be spherical; i.e., $m_t/A_t = \rho_t d_t/6$. The temperature T is now linearised around the respective mean value $T = \bar{T} + T'$ assuming that $T' \ll \bar{T}$. In particular, the application of the binomial formula yields

$$(\bar{T} + T')^4 = \bar{T}^4 + 4\bar{T}^3 T' + \mathcal{O}(T'^2). \tag{4.9}$$

From Eq. (4.6), it is obtained after short manipulation

$$\bar{T_t} + \frac{\varepsilon\sigma_B}{\alpha_t}(\bar{T_t}^4 - \bar{T_w}^4) = \bar{T_g} \tag{4.10}$$

$$\underbrace{\frac{\rho_t}{6} d_t c_t \cdot \frac{1}{\alpha_t + 4\varepsilon\sigma_B \bar{T_t}^3}}_{\tau} \frac{dT'_t}{dt} + T'_t = \underbrace{\frac{\alpha_t}{\alpha_t + 4\varepsilon\sigma_B \bar{T_t}^3}}_{K} T'_g. \tag{4.11}$$

Equation (4.10) contains the energy balance for the mean temperature and Eq. (4.11) describes the linearised thermocouple response, being exposed to temperature perturbations T'_g. Eq. (4.11) represents

a first-order time-lag (P-T1) behaviour, featuring a low-pass characteristics for frequencies above the cut-off frequency f_c which is given by

$$f_c = \frac{1}{\tau} = \frac{6(\alpha_t + 4\varepsilon\sigma_B \bar{T}_t^3)}{\rho_t d_t c_t}. \tag{4.12}$$

The corresponding Bode diagram is shown in Figure 4.9.

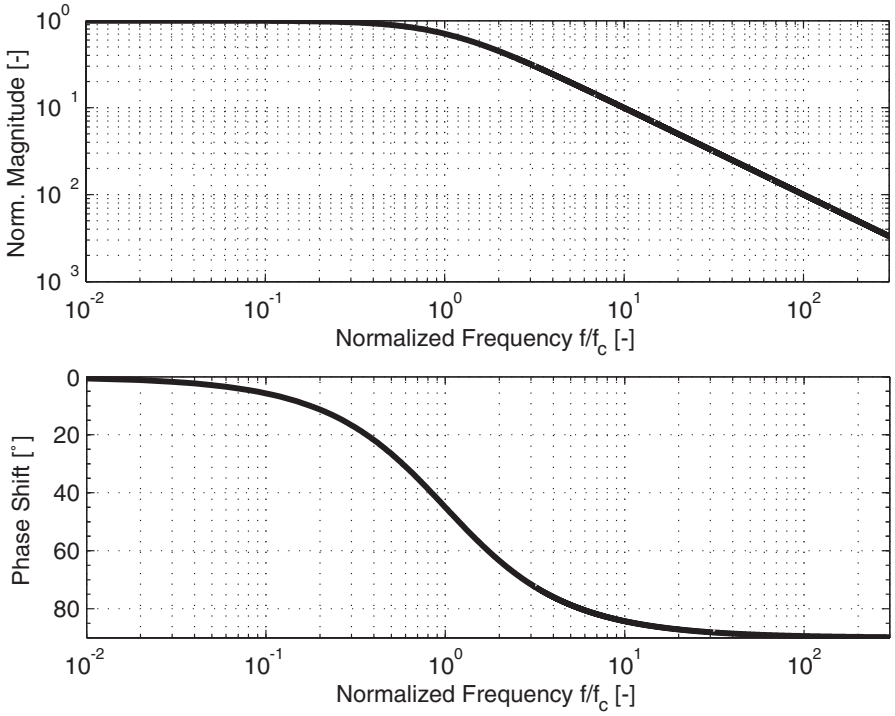

Fig. 4.9: Bode plot of the linearised P-T1 response behaviour of the thermocouples: Normalised magnitude $T_t'/(T_g' \cdot K)$ and phase shift over the normalised frequency f/f_c.

f_c is a function of the thermocouple diameter d_t and the convective heat transfer coefficient $\alpha_t = f(Nu)$. The initial gain K describes the step response of the thermocouple for $t \to \infty$

$$K = \frac{\alpha_t}{\alpha_t + 4\varepsilon\sigma_B \bar{T}_t^3} \tag{4.13}$$

K is lower than unity as a consequence of the radiative heat losses. In the frequency domain, the P-T1 behaviour in Eq. (4.11) is represented by the following complex transfer function

$$\hat{H}_t(i\omega) \equiv \frac{\mathscr{F}(T_t')}{\mathscr{F}(T_g')} = \frac{K}{1 + i\omega\tau}. \tag{4.14}$$

where $\mathscr{F}()$ denotes the Fourier transform and $\omega = 2\pi f$ the angular frequency of the excitation.

4.4.1 Mean Temperature Reconstruction

Applying Eq. (4.10) to both thermocouples on the probe, the steady gas temperature $\bar{T}_g$ can be calculated from the measured temperatures $\bar{T}_1$ and $\bar{T}_2$ with $Nu = \alpha_t d_t / \lambda_g$

$$\bar{T}_g = \bar{T}_1 + \frac{\bar{T}_1 - \bar{T}_2}{\frac{\alpha_1}{\alpha_2} \cdot \frac{\bar{T}_2^4 - \bar{T}_w^4}{\bar{T}_1^4 - \bar{T}_w^4} - 1} = \bar{T}_1 + \frac{\bar{T}_1 - \bar{T}_2}{\frac{Nu_1 d_2}{Nu_2 d_1} \cdot \frac{\bar{T}_2^4 - \bar{T}_w^4}{\bar{T}_1^4 - \bar{T}_w^4} - 1}. \tag{4.15}$$

$\bar{T}_g$ depends on the wall temperature, the thermocouple diameters d_1, d_2, and the characteristics of the convective heat transfer determining Nu_1/Nu_2. In the following, the index 2 indicates the larger thermocouple, $d_2 > d_1$.

4.4.1.1 Convective Heat Transfer

The key assumption of the double thermocouple approach is the identity of the relative air velocity determining the convective heat transfer $u_1 \equiv u_2$. This is justified by the close distance between the two thermocouples on the probe head (1 mm). Applying the Nusselt correlation $Nu = f(Re, Pr)$ for forced convection, the ratio of the local Nusselt numbers, Nu_1/Nu_2 can be re-written as a function of Re_1/Re_2, due to the identity $Pr_1 \equiv Pr_2$. For $u_1 \equiv u_2$, Re_1/Re_2 again is only a function of the diameter ratio d_1/d_2, which can be

measured. The ratio Nu_1/Nu_2 can therefore be determined without detailed knowledge of the local velocity according to

$$\frac{Nu_1}{Nu_2} = \left(\frac{d_1}{d_2}\right)^{\beta}. \tag{4.16}$$

The exponent β is given by the Nusselt correlation used. For the spherical thermocouple geometry considered, HEILOS [Hei02] employed $\beta = 0.5$ for his reconstructions. The Nusselt correlation derived by MCADAMS [Bee92] proposes an even higher value $\beta = 0.6$. Both values proved to be overestimated for the set-up used. The impact of β on the reconstructed gas temperature $\bar{T}_g$ was preliminarily assessed on the basis of temperature measurements in the combustor for varying overall equivalence ratios ϕ. The results are shown in Figure 4.10. For $\beta > 0.4$, the reconstructed temperatures are implausibly high, partly exceeding the adiabatic flame temperature for stoichiometric kerosene flames.

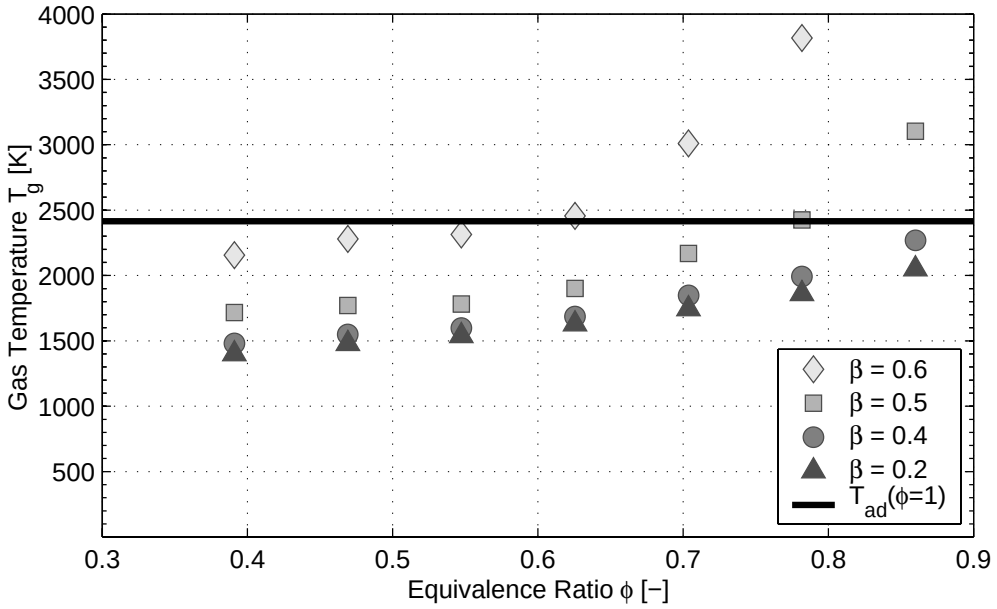

Fig. 4.10: Reconstructed gas temperature as a function of β.

Another Nusselt correlation is given by Whitaker [ID96]

$$Nu = 2 + \left(0.4Re^{\frac{1}{2}} + 0.06Re^{\frac{2}{3}}\right) Pr^{0.4} \left(\frac{\eta}{\eta_w}\right)^{\frac{1}{4}}. \qquad (4.17)$$

Equation (4.17) exhibits the disadvantage that β can not be directly obtained from the analytical expression, but has to be approximated numerically. In this case, assumptions had to be made for the range of Reynolds-numbers and for the gas temperatures which impact the gas viscosity η. The values for β obtained for the expected range of gas velocities and temperatures are given in Table 4.1. The exponents in Table 4.1 approximate the calculated data within an error margin of 4%.

		$\bar{u}$[m/s]		
		30	50	100
$\bar{T}_g$[K]	1200	0.257	0.294	0.346
	1800	0.205	0.243	0.294
	2400	0.171	0.208	0.257

Tab. 4.1: Approximated β for the operating range.

From Table 4.1, it can be seen that the calculated β ranges between 0.17 and 0.35, being considerably lower than the values adopted by Heilos and McAdams. Comparably high exponents are only obtained for elevated Reynolds numbers. For the current set-up, the local Reynolds numbers at the thermocouples are however low, $8 < Re < 140$. As a consequence, the constant 2 in Eq. (4.17), which is related to heat conduction into the surrounding medium, gains relative influence, particularly for low flow velocities and high temperatures. This reduces the values for β.

From Figure 4.10, another conclusion can be drawn. Despite the values for β in Table 4.1 do noticeably vary, the consequences for the gas temperature reconstruction are relatively low. The relative deviation of $\bar{T}_g$ being reconstructed with $\beta = 0.4$ and $\beta = 0.2$, respectively, is lower than 8%. With respect to other measurement uncertainties, it

seems therefore justified to assume a constant β for all operating conditions. By choosing the intermediate value $\beta \equiv 0.3$, the uncertainty level can be restricted to 4%. The reconstruction equation (4.15) can now be specified to

$$\bar{T}_g = \bar{T}_1 + \frac{\bar{T}_1 - \bar{T}_2}{\left(\frac{d_2}{d_1}\right)^{0.7} \cdot \frac{\bar{T}_2^4 - \bar{T}_w^4}{\bar{T}_1^4 - \bar{T}_w^4} - 1}. \tag{4.18}$$

4.4.1.2 Geometry of the Thermocouples

In order to assess the assumption of spherical thermocouple geometries, the thermocouples have been investigated under the microscope.

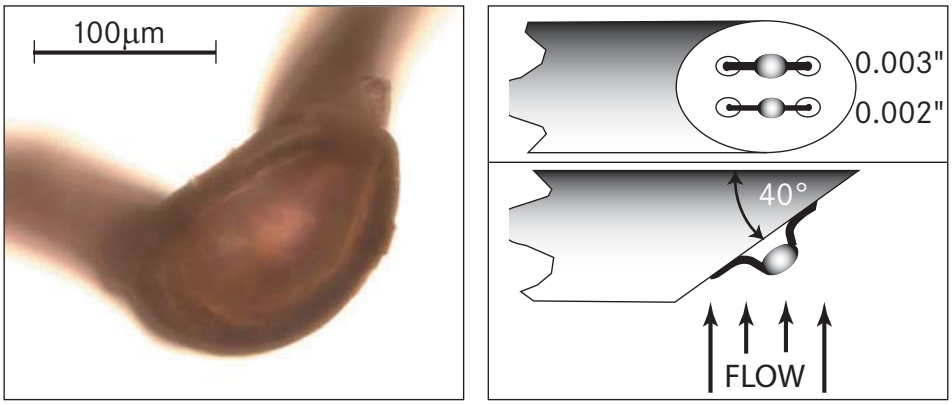

Fig. 4.11: Microscopic image of the welding point geometry of a 0.002"-thermocouple (left) and orientation of the ellipsoid thermocouples on the probe tip (right).

As shown in Figure 4.11, the thermocouple geometry rather resembles a rotational ellipsoid than a sphere. The axis ratio has been determined for both thermocouple sizes to 1:1.7. The semi-major axis always coincides with the connecting line between the wires, which leads to an identical orientation of both thermocouples on the probe head relative to the flow (see Figure 4.11, right). The implications of the non-spherical geometry on the heat transfer are thus the same for both thermocouples. Since only the diameter ratio is accounted for in Eq. (4.18), it therefore does not matter which axis is used for

referencing. The semi-minor axis was selected for that purpose, since it could be easily measured by means of a micrometre screw before thermocouple implementation on the probe.

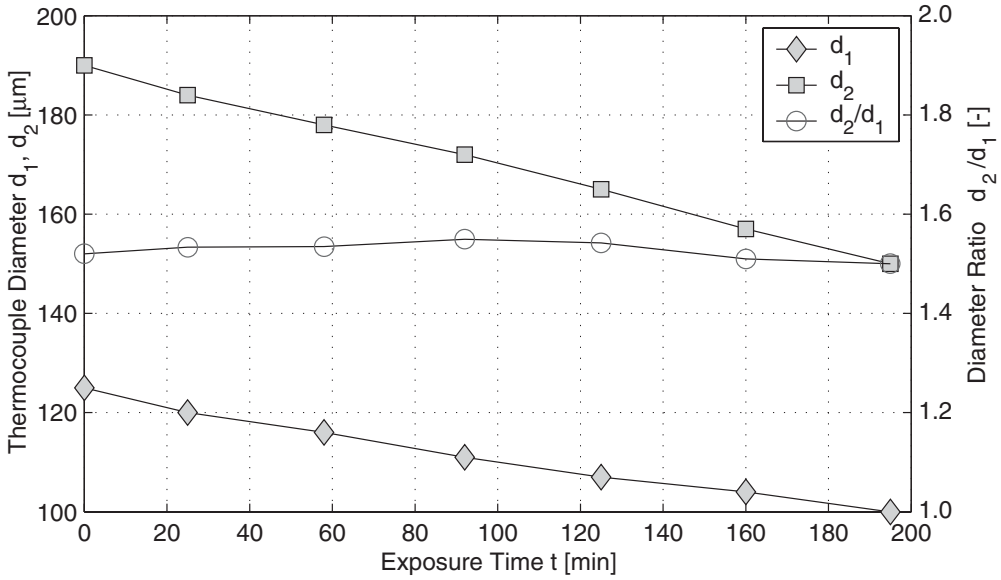

Fig. 4.12: Thermocouple diameters d_1, d_2 as a function of the flame exposure time t.

Despite the Pt/RhPt thermocouples are nominally operated below their allowable temperature of 1700 K, effects of unmixedness related to the spray flame and the strong combustion oscillations were found to enhance aging and surface degeneration, resulting in a decrease of the thermocouple diameter. For this reason, it had to be checked how the diameter changes with time and particularly if the initial d_1/d_2 is maintained. For that purpose, the probe was submitted to long-term exposure in the self-excited spray flame, being operated at $\phi = 0.7$. The diameters of the thermocouples were periodically protocolled, leading to the results of Figure 4.12.

During the 3 hours of flame exposure, both thermocouples were subject to a substantial diameter loss of roughly 20% of the initial values. However, the ratio d_2/d_1, immediately impacting the reconstruction, is only little affected, exhibiting a relative uncertainty margin of only 4%. This is very favourable, since the initial thermocouple diame-

ters remain representative for the evaluation of the gas temperatures throughout thermocouple lifetime. In order to minimise the impact of aging, the duration of use for the thermocouples on the probe was limited to 4 hours of flame exposure in total.

4.4.1.3 Radiative Heat Losses to the Wall

The reconstruction of the steady gas temperature requires the quantification of the radiative heat losses to the confining combustor walls and the determination of the wall temperatures $\bar{T}_w$ in the combustor. $\bar{T}_w$ was captured locally by a set of thermocouples being soldered into pocket holes which were drilled into the combustor side plates. These measurement points were located in the primary zone and in the dilution zone of the combustor, 50 mm and 100 mm downstream of the injector exit. Depending on the burning conditions of the flame, the local temperature was ranging between $430\ \mathrm{K} < \bar{T}_{w,prim} < 640\ \mathrm{K}$ and $600\ \mathrm{K} < \bar{T}_{w,dil} < 790\ \mathrm{K}$. The wall temperature in the dilution zone $\bar{T}_{w,dil}$ was commonly exceeding the temperature in the primary zone by about 150 K due to the elevated flame burn-out. Reconstruction is based on the average value

$$\bar{T}_w = \frac{1}{2}(\bar{T}_{w,dil} + \bar{T}_{w,prim}). \tag{4.19}$$

The error induced by this simplification is small. In Figure 4.13, temperature reconstructions have been performed on the basis of the measured data sets $\bar{T}_1$ and $\bar{T}_2$ for $\bar{T}_w = [500\ \mathrm{K}, 650\ \mathrm{K}, 800\ \mathrm{K}]$, covering the range of typical wall temperatures in the tests. The relative error $\Delta\bar{T}_g/\bar{T}_g$ does not exceed 6% even though the wall temperature varies by 60%. The reconstruction error induced by taking the average according to Eq. (4.19) can therefore be estimated below 3%.

4.4.1.4 Calibration in a Premixed Flame

Calibration of the thermocouple probe was done with a premixed 60 kW methane-air flame in a separate test rig under steady flow

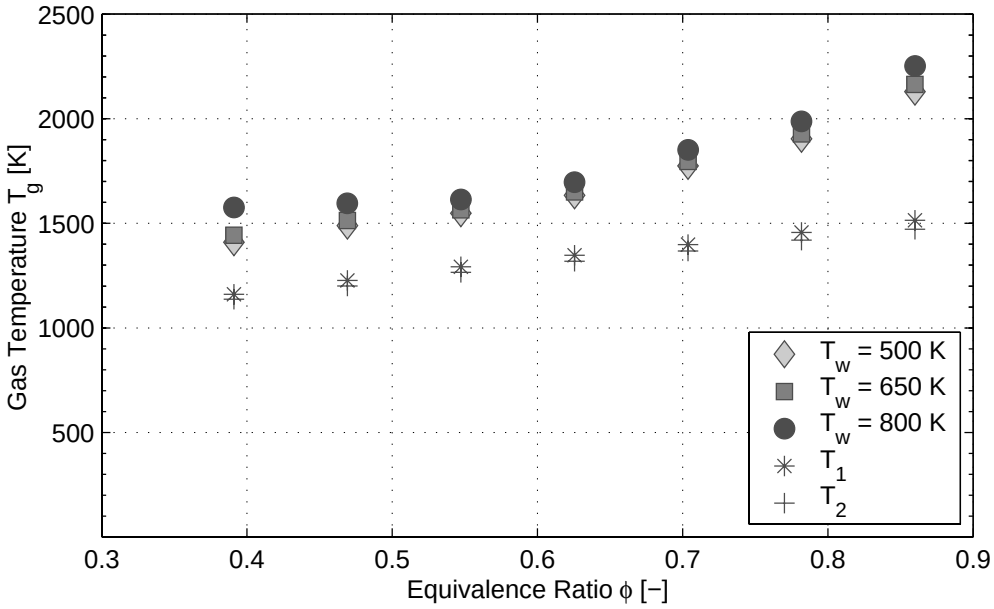

Fig. 4.13: Reconstructed gas temperature as a function of $\bar{T}_w$.

conditions. A description of the rig and of the premix burner can be found in [PFHS03, Fis04]. The flame was enclosed by a combustion chamber being of identical dimensions as the RQL-type used for the investigations of rumble. The combustion chamber cooling was minimised to obtain burning conditions near adiabacy. The thermal power output of the flame and the air mass flows for calibration were adapted to produce similar flow velocities and equivalence ratios as for the kerosene flames investigated.

The probe was placed on the central axis of the combustion chamber in downstream vicinity to the main reaction zone. Two independent measurement sequences (A, B) of 50000 samples each were taken at a sampling rate of 10 kHz for equivalence ratios ranging between $0.6 < \phi < 1.0$. Temperature reconstruction was done using Eq. (4.18). The reconstruction results for both measurement sequences $\bar{T}_{gA}$, $\bar{T}_{gB}$ are plotted together with the adiabatic flame temperatures $T_{ad}(\phi)$ in Figure 4.14.

The adiabatic flame temperature is approximated well for overall lean conditions ($\phi < 0.7$). The reconstructed temperature lies about 80 K

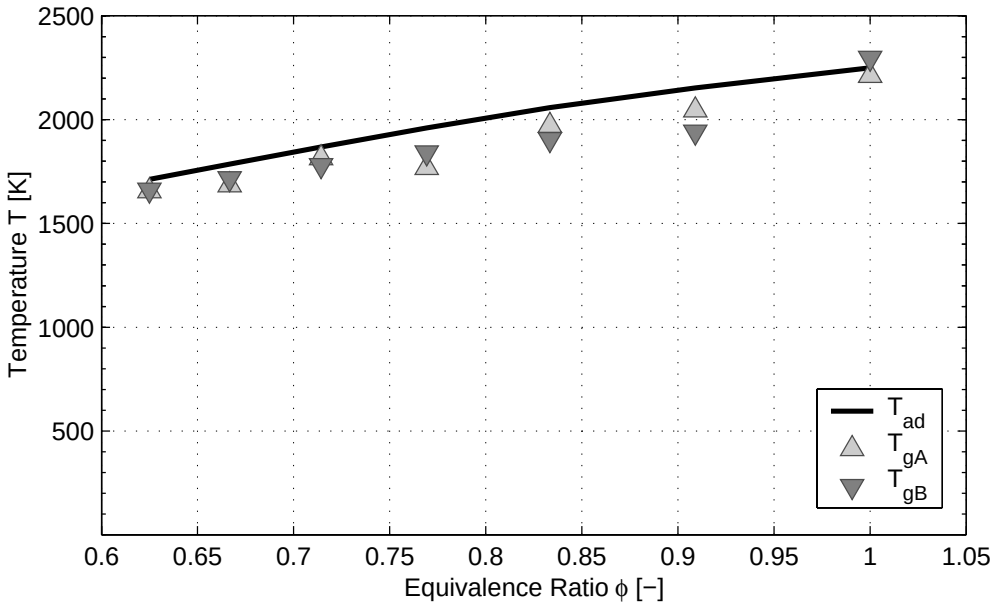

Fig. 4.14: Probe calibration with a premixed 60 kW methane-air flame.

(5%) below the adiabatic value and repeatability is good (< 50 K). For $\phi > 0.7$, the deviations of the reconstructed temperatures become more pronounced. This might be related to dissociation in the exhaust gas, to an increasingly non-adiabatic behaviour of the combustion chamber and to higher radiative losses by the probe, which can not be sufficiently captured by the assumption of a uniform average wall temperature. Repeatability decreases, too, and the results differ by up to 150 K ($\approx 7.5\%$ of the measured temperature) for same operating conditions. Under near-stoichiometric conditions, the relative contribution of radiative heat losses of the probe becomes important and temperature reconstruction reacts very sensitively to small deviations in the measured thermocouple voltage. However, with respect to the overall lean test conditions at which rumble will be investigated ($\phi < 0.8$), the double thermocouple probe method produces reliable temperature results within an estimated error margin of $\pm 4\%$.

4.4.2 Dynamic Temperature Reconstruction

With the mean temperatures $\bar{T}_{1,2}$ and the diameters $d_{1,2}$ of the thermocouples being known, the energy balance Eq. (4.11) can be used to specify the fluctuations of the local gas temperature T'_g. However, the unknown value for α_c in Eq. (4.11) impedes an immediate reconstruction. Equation (4.11) applied to both thermocouples thus results in 2 equations for 3 unknowns, namely the two local convective heat transfer numbers $\alpha_{1,2}$ and the common gas temperature fluctuation T'_g.

Nevertheless, T'_g can be reconstructed with good success from the two measured thermocouple signals $T'_{1,2}$ using their response-compensated Fourier spectra. For this, the Fourier transform of each of the measured temperature perturbations are multiplied with the inverted transfer functions Eq. (4.14)

$$\mathscr{F}(T'_{g,1}) = \hat{H}_1^{-1} \cdot \mathscr{F}(T'_1) \tag{4.20}$$

$$\mathscr{F}(T'_{g,2}) = \hat{H}_2^{-1} \cdot \mathscr{F}(T'_2), \tag{4.21}$$

where

$$\mathscr{F}(T'_{g,1}) \equiv \mathscr{F}(T'_{g,2}) \tag{4.22}$$

since the gas temperature perturbation is common to both thermocouples. Equation (4.22) represents the required third equation for the reconstruction of the dynamic gas temperature.

However, practical difficulties arise, since the application of $\hat{H}_{1,2}$ in Eqs. (4.20), (4.21) requires again the explicit knowledge of $\alpha_{1,2}$ and therefore of the local gas velocities $u_{1,2}$. A common method to overcome this problem is to determine the cut-off frequencies $f_{c1,2}$ of the thermocouple responses experimentally, which, according to Eq. (4.12), implicitly contain $\alpha_{1,2}$. This is usually accomplished by analysing the cooling curve of an electrically overheated thermocouple being exposed to the flow at operating conditions

[Wit80, Koh88, Hei02]. This in-situ calibration is however not applicable here, since the presence of the flame and the sonic nozzle would have immediately induced heavy combustion oscillations, unsuitable for calibration.

Another possibility to determine the transfer functions $\hat{H}_{1,2}$ is numerical optimisation, iterating the cut-off frequencies and using Eq. (4.22) as optimisation criterion. According to Eqs. (4.14), (4.12) and (4.13), the convective heat transfer numbers $\alpha_{1,2}$ impact the respective transfer functions $\hat{H}_1$ and $\hat{H}_2$ by influencing the initial gains $K_{1,2}$ and the cut-off frequencies $f_{c1,2}$. For a given cut-off frequency, say f_{c2}, α_2 can be calculated from Eq. (4.12) since σ_B, ρ_t, c_t, $\bar{T}_2$ and the initial thermocouple diameter d_2 are known and ε is obtained using Eq. (4.8) on the basis of $\bar{T}_2$. With α_2 being determined, the value for K_2 can be quantified using Eq. (4.13). Assuming $u_1 \equiv u_2$, the convective heat transfer numbers $\alpha_{1,2}$ of both thermocouples are linked by the convective heat transfer characteristics, derived in section 4.4.1.1:

$$\frac{\alpha_1}{\alpha_2} = \left(\frac{d_2}{d_1}\right)^{0.7}. \tag{4.23}$$

As a consequence, with α_2 being known, α_1, and also f_{c1} and K_1 of the other thermocouple can be determined. Corresponding pairs of transfer functions $\hat{H}_1(f_{c2})$, $\hat{H}_2(f_{c2})$ can thus be calculated as a function of f_{c2}. Optimisation now aims at finding the right value for $f_{c2,opt}$ for which Eq. (4.22) is fulfilled; i.e., where the difference in the reconstructed gas temperatures $T'_{g,1}$ and $T'_{g,2}$ is minimum. The reconstruction approach is summarised in Figure 4.15.

During the iteration, f_{c2} is estimated to be part of the frequency interval 1 Hz $< f_{c2} <$ 30 Hz, which is a conservative approximation for thermocouples of that size. The chosen frequency range also accounts for possible diameter losses of the thermocouple during flame exposure, which tend to increase f_c. The P-T1 compensated Fourier spectra $\mathscr{F}(T'_{g,1}), \mathscr{F}(T'_{g,2})$ are subsequently reconstructed as a function of f_{c2}.

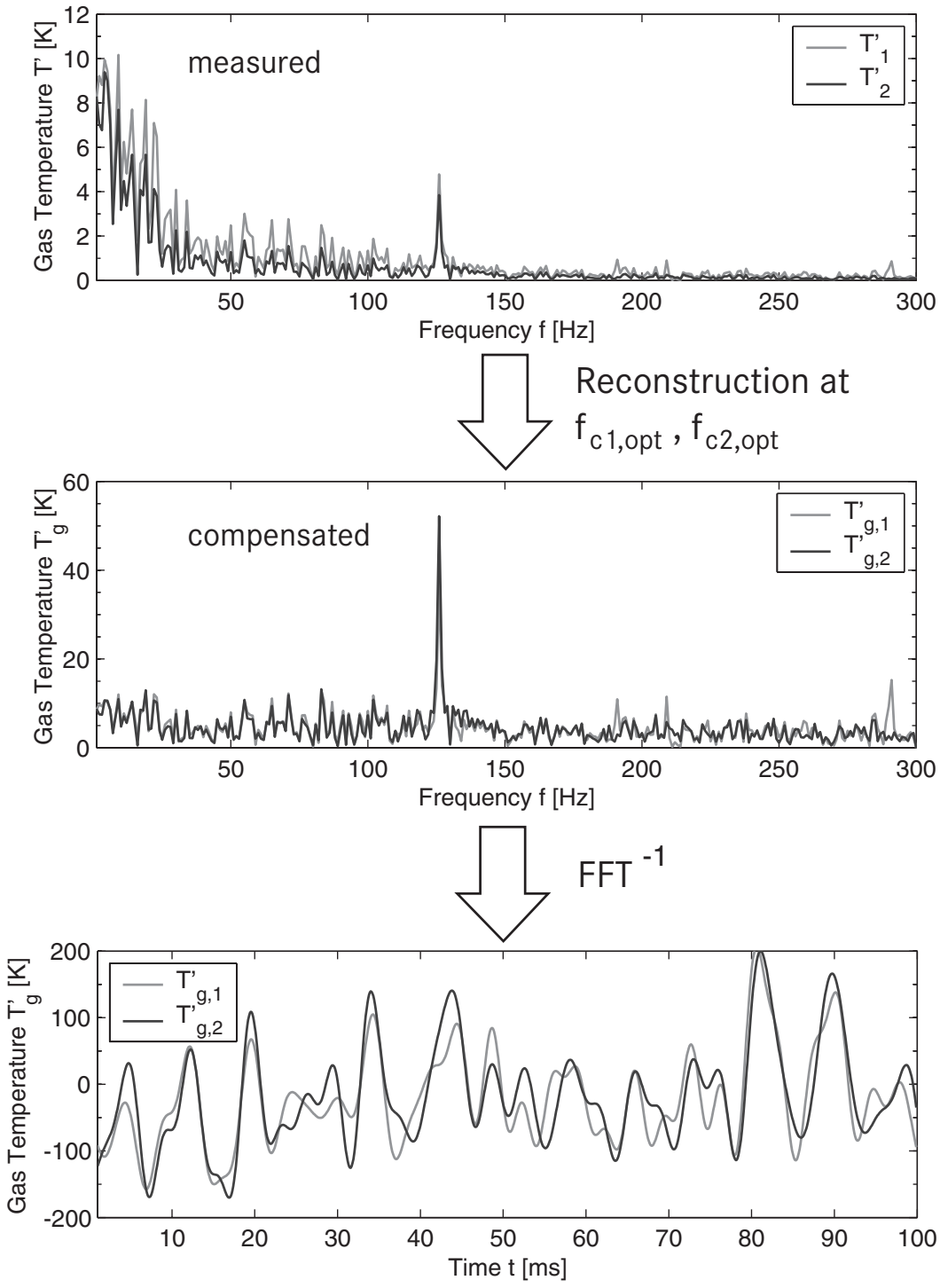

Fig. 4.15: Phase-optimised reconstruction of the temperature perturbations.

Comparison of the Fourier phases has shown to produce the most stable optimisation results. The absolute phase differences of the reconstructed temperature perturbations in the frequency domain are calculated according to

$$\Delta\varphi(f, f_{c2}) = \| \arg(\mathscr{F}(T'_{g,2})) - \arg(\mathscr{F}(T'_{g,1})) \|. \tag{4.24}$$

Care has to be taken not to overestimate the contribution of amplified high frequency noise in the spectrum. Therefore, phase optimisation and signal reconstruction in the frequency domain was bound to the frequency interval 1 Hz $< [f] <$ 300 Hz. The error function χ consists of the accumulated phase deviations of the reconstructed signals and must be minimised:

$$\chi(f_{c2,opt}) = \sum_{[f]} \Delta\varphi(f, f_{c2,opt}) \stackrel{!}{=} \min. \tag{4.25}$$

In order to get an estimate of the reliability of the reconstruction, measurements sequences were recorded under self-excitation at identical nominal operating conditions and the reconstructed gas temperatures were compared. For measured signals with a signal-to-noise ratio above 6, as encountered under heavy rumble, the quality of the amplitude reconstruction was acceptable, showing relative deviations of the reconstructed oscillation amplitudes below $\pm 11\%$. It should be noted that this relatively high margin is not exclusively related to the uncertainties of the reconstruction method since the self-excited combustor flow is also subject to non-deterministic changes. The reconstruction of the signal phases proved to be better, since the expected oscillation frequencies lie remarkably above the cut-off frequencies of the thermocouple response, inducing a phase shift of nearly 90° to the measured phase, according to the P-T1 behaviour shown in Figure 4.9. Phase deviations are therefore bound to $\pm 5°$.

Since the temperature reconstruction according to Eqs. (4.20), (4.21) is conducted with complex-valued transfer functions, the measured FFT-phases are corrected accordingly. With respect to the low reconstruction uncertainties for the phase, the reconstruction approach is

therefore particularly reliable for phase-related analysis, such as the evaluation of Rayleigh's integral Eq. (1.1) or the determination of entropy wave propagation speeds in the combustor.

4.4.3 Measurement Locations

Single-point measurements were conducted at the axial locations in the combustor shown in Figure 4.16 and Table 4.2.

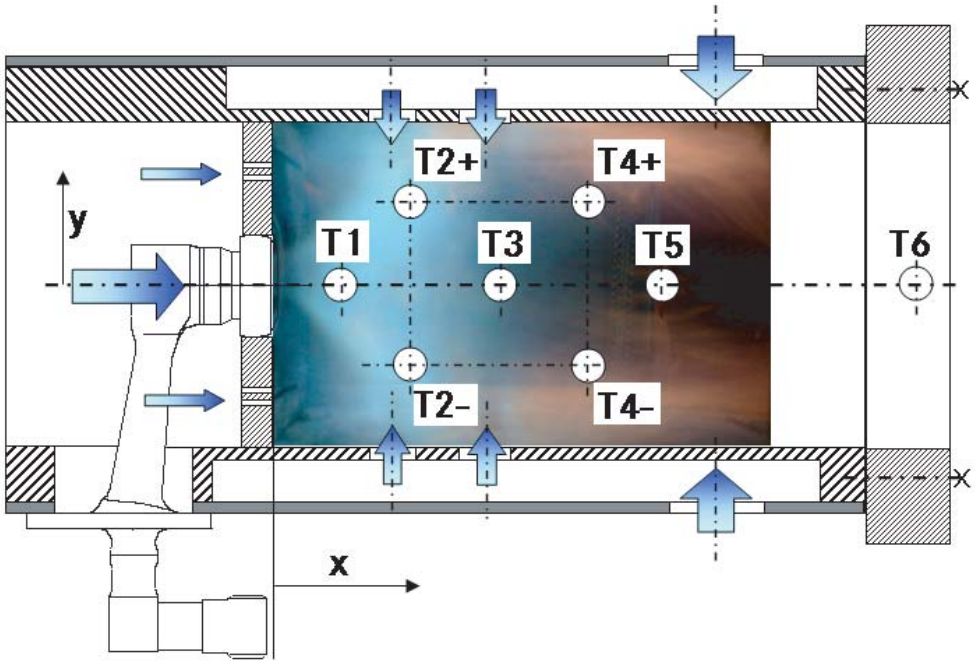

Fig. 4.16: Thermocouple positions (∘) in the combustor.

The positions T1, T3, T5 and T6 were used to determine the generation and convection of the entropy wave along the centre line of the combustor. T1 and T3 correspond to positions in immediate up- and downstream vicinity of the main heat release zone. T5 is located in the dilution sector of the combustor where the burnout of the flame is nearly completed. T6, at the inlet plane of the choked nozzle, is used to quantify the effective amplitude of the entropy perturbations for pressure feedback. The probe located at T6 was also used at

selected radial positions to determine the spatial dispersion of entropy waves arriving at the nozzle, an aspect which also motivated the measurements at the positions T2+/- and T4+/-.

Position	x [mm]	y [mm]	z [mm]
T1	20	0	0
T2+	45	21	0
T2-	45	-21	0
T3	75	0	0
T4+	105	21	0
T4-	105	-21	0
T5	120	0	0
T6	275	0	variable

Tab. 4.2: Coordinates of the thermocouple positions in the combustion chamber.

4.5 Malvern Particle Sizing

The Malvern Particle Sizer is used to determine the droplet size distribution at the injector exit under non-ignited conditions. The underlying measurement principle refers to Fraunhofer diffraction of a monochromatic light beam by a moving drop.

The optical setup is shown in Figure 4.17. When an particle with diameter d is illuminated by monochromatic light of the wavelength λ with $\lambda \ll d$, a Fraunhofer diffraction pattern is generated at infinity, with an intensity distribution being given as

$$I = I(0) \left(\frac{2J_1(X)}{X} \right)^2 . \tag{4.26}$$

In Eq. (4.26) J_1 is the first-order spherical Bessel function and $I(0)$ is the intensity at the centre of the diffraction pattern. X is a dimensionless size parameter being defined as

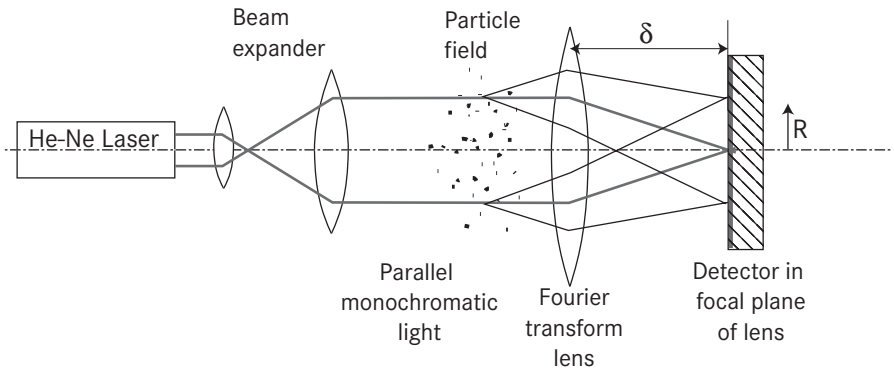

Fig. 4.17: Optical setup of the laser diffraction technique, used for particle sizing [CL83].

$$X = \frac{dR\pi}{\lambda\delta}. \tag{4.27}$$

δ is the focal length of the collector lens and R is the radial coordinate in the detector plane, starting from the optical axis of the system according to Figure 4.17. The diffraction pattern is thus unique for a given particle diameter. As a consequence, a cluster of particles will produce a particular light intensity distribution on the collector plane of the particle sizer, which can be used for the determination of the particle size spectrum. The range of detectable particle sizes is a function of the focal length δ of the collector lens. The Malvern sizer contains a set of 31 concentric photo-detector rings to collect the diffracted light intensity distribution. The output of the photo-detector rings is multiplexed and immediately evaluated by a measurement computer to specify the droplet size distribution and the droplet number density.

Of primary interest for the current investigation is the determination of the droplet size distribution of the injected fuel spray close to the burner outlet for both steady and forced conditions. The measurement volume in the combustor is defined by the expanded Helium-Neon laser beam (wavelength 670 nm) with a diameter of 15 mm. It was located at a distance of 12 mm downstream of the injector exit in the horizontal centre plane as shown in Figure 4.18. The receiver

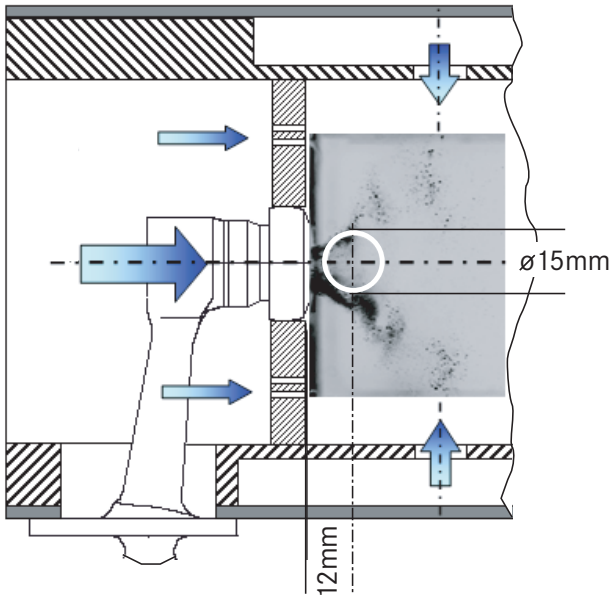

Fig. 4.18: Positioning of the laser beam in the combustor.

lens had a focal length of $\delta = 200$ mm, such that droplet diameters between 3 μm and 400 μm were captured. A measurement sequence usually consisted of 1250 samples which were acquired at a sampling frequency of 2.5 kHz. For dynamic measurements, the recordings were initiated phase-triggered. Figure 4.19 shows a typical droplet spectrum obtained. The measured droplet spectra did commonly agree with a Rosin-Rammler distribution

$$Q = 1 - e^{-(d/X)^q}, \tag{4.28}$$

where $Q(d)$ is the cumulative liquid volume contained in drops of diameter less than d, and X and q are constants. From the droplet size distribution, the Sauter mean diameter D_{32} was calculated according to

$$D_{32} = \frac{\sum n_i d_i^3}{\sum n_i d_i^2} = \frac{X}{\Gamma\left(1 - \frac{1}{q}\right)}, \tag{4.29}$$

where n_i denotes the number of droplets contained in the i-th size

range and Γ is the gamma function [Lef89]. D_{32} was employed in the subsequent analysis as the representative diameter of the distributions.

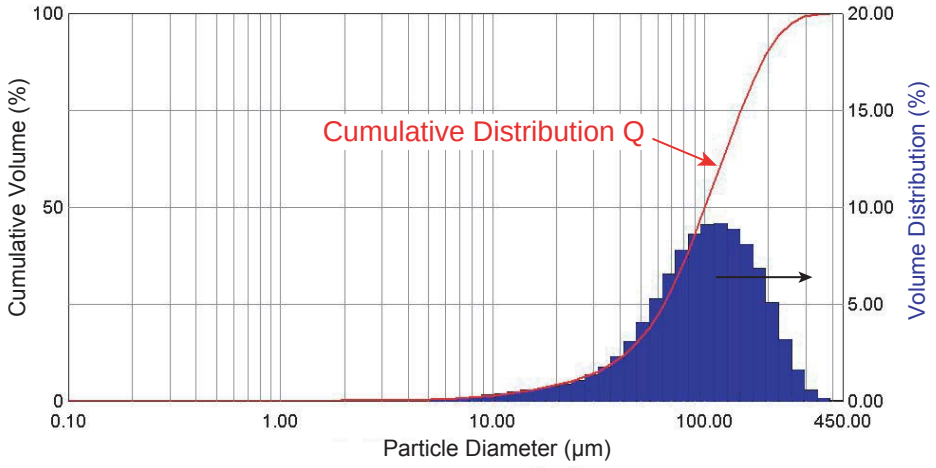

Fig. 4.19: Measured droplet spectrum.

For the spray measurements conducted at ambient air temperature, repeatability and consistency checks proved the reliability of the SMD measurements. The measurements were performed without mixing air injection in order to minimise the recirculation of droplets into the measurement volume. From the typical data scatter obtained, an error bar of $\pm 5\%$ can be deduced for the SMD.

4.5.1 Surrogate Fuel

For the spray investigations in the absence of a flame, kerosene was replaced for safety reasons by a surrogate fuel with similar atomisation properties. The key figures describing the atomisation properties are the Weber number We and the Ohnesorge number Oh [Lef89]. The Weber number is defined as

$$We = \frac{\rho_a u_{rel}^2 d}{\sigma}, \tag{4.30}$$

and relates the disruptive aerodynamic forces and the consolidating surface tension. We thus determines the breakup behaviour and the maximum stable droplet size. Oh accounts for the resistance to spray disintegration induced by the liquid viscosity ν_l

$$Oh = \frac{(We)^{0.5}}{Re} = \frac{\nu_l}{(\rho_l \sigma d)^{0.5}}. \tag{4.31}$$

The droplet acceleration by the surrounding gas flow is influenced by the density ratio ρ_l/ρ_a, as shown in section 5.2.2. ρ_l has therefore been explicitly taken into consideration to account for similar transport properties of the droplets in the primary zone.

An investigation of data bases [Arn01] has shown that a binary mixture of 90% (by weight) ethanol and 10% water matches the properties of kerosene [Rac98] rather well. Ethanol is easy to procure and does not discharge aromatic vapours. The key figures of the mixture deviate within acceptable limits from kerosene, as shown in Table 4.3. The differences are predominantly related to the higher surface tension of kerosene. As a consequence, the measured droplet sizes of the replacement fluid tend to be smaller. The SMD obtained are therefore scaled by the ratio of Weber numbers $We_{Eth.}/\,We_{Ker.} = 1.113$ when being evaluated in the context of kerosene combustion to preserve the Weber number.

90% Ethanol + 10% Water			
Property	Value (300 K)		Difference to Kerosene
σ	0.0234	N/m	−11.1%
ν_l	$1.983 \cdot 10^{-6}$	m/s^2	−0.86%
ρ_l	811.9	kg/m^3	+1.48%
We			+11.32%
Oh			+5.29%

Tab. 4.3: Properties of the surrogate fuel at 300 K.

4.6 Data Acquisition and Triggering

The time-resolved acquisition of the acoustic data was controlled by a multichannel-I/O-Board (333 kHz, 12 Bit)[19]. Eight measurement channels were available for capturing the dynamic data. Each of the measurement channels was sampled at 10 kHz. The recorded time-domain sequences usually contained 10000 samples. The same I/O-board was used to control the process parameters of the rig. The air mass flow, fuel mass flow, air temperature, static pressures and the siren rotation speed (see Figure 3.2) were monitored at a lower sampling rate of about 1 Hz.

Test rig control and data acquisition were performed on the same computer[20]. The corresponding routines were being programmed using the commercial software package *LabVIEW*. Emphasis was placed on a highly automated execution of the dynamic data acquisition. The flow chart of the measurement procedures is shown in Figure 4.20.

Before starting the measurements, the steady process parameters of the rig are acquired and written in a separate protocol file. The recording of the dynamic data is organised in loops performing n individual recordings for a given operating point. n is set by the user. Under conditions of acoustic forcing, the online data acquisition can optionally be phase-triggered which is useful for synchronising external measurement systems with independent data acquisition and analysis (i.e., PIV, high-speed camera and Malvern Particle Sizer). The trigger signal is delivered by an external signal converter, presented in section 4.6.1.

In the case of deterministic forcing by the siren, the measurement procedure contains an outer loop which optionally executes a list of m nominal excitation frequencies f_{nom}, which are also user-set.

The dynamic data can be directly saved as time-domain sequences.

[19] Type Meilhaus ME2600i PCI
[20] AMD Duron 700MHz processor

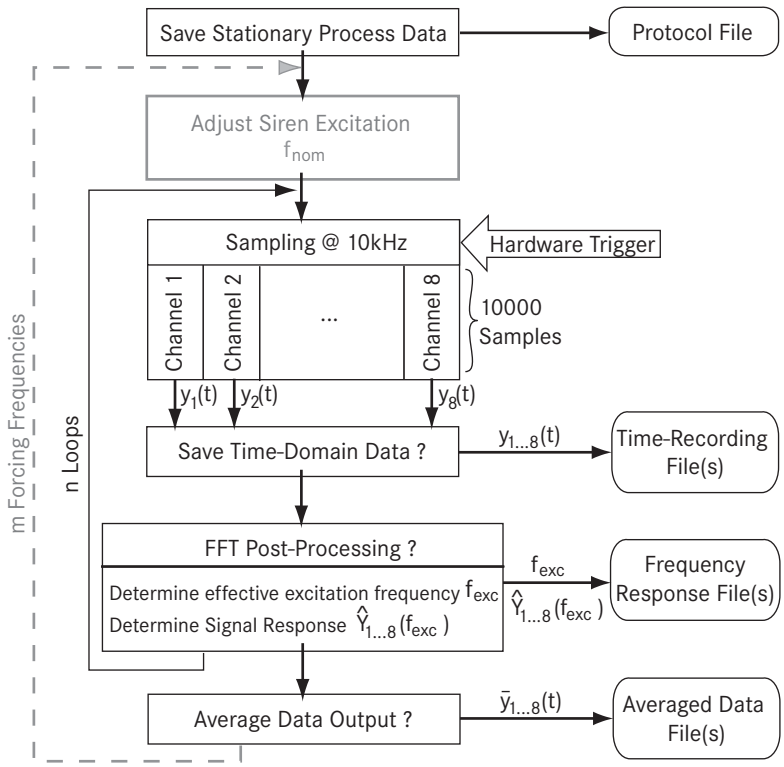

Fig. 4.20: Flow chart of the dynamic measurements.

Optionally, they can be submitted to online post-processing tools to perform averaging or a Fourier analysis. The Fourier analysis contains the application of the Fast-Fourier Transformation (FFT) to the signals in the time-domain and the identification of the dominating oscillation frequency f_{exc} [Fis04]. Hence, the amplitude and phase responses to acoustic forcing can be immediately identified from the Fourier spectrum and separately stored without further post-processing to reduce the amount of data produced. The usual bin size selected for the FFT was 1 Hz.

4.6.1 Hardware Trigger

As mentioned above, a major requirement for the current experiments lies in the synchronisation of external optical measurement systems (ICCD-camera, PIV, Malvern sizer) to obtain phase-resolved

data. A reference signal is therefore generated for the purpose of triggering, which stays in a fixed phase relationship with the forced or self-excited pressure oscillations in the combustor.

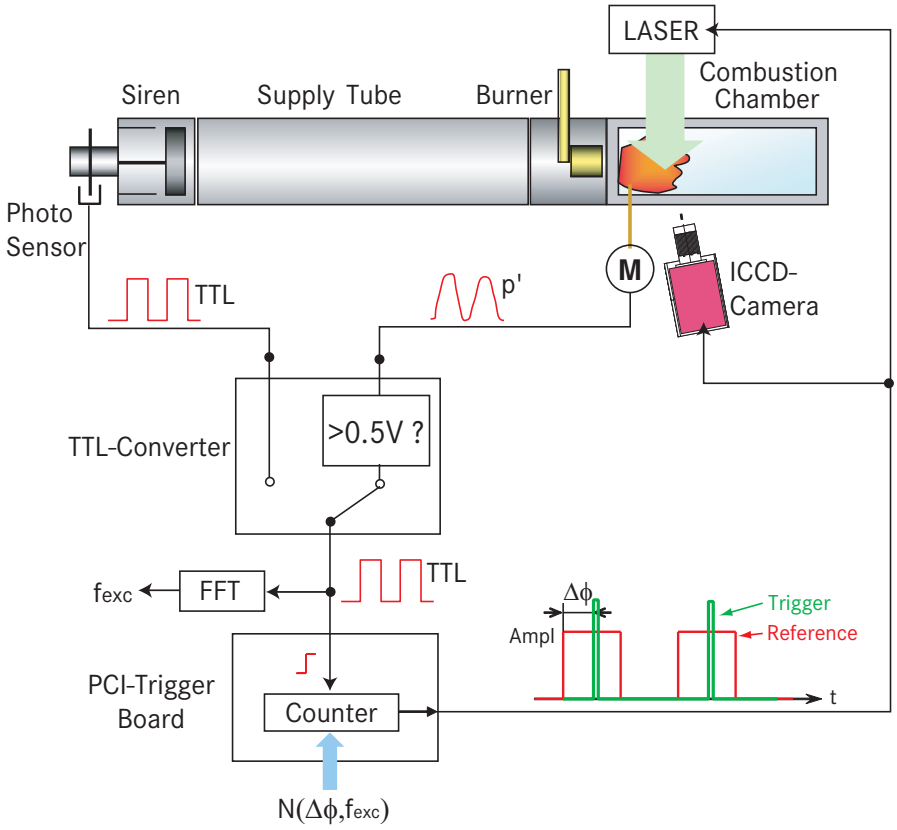

Fig. 4.21: Generation of the trigger pulse.

The principle of trigger pulse generation is outlined in Figure 4.21. Under conditions of external forcing, the phase-resolved measurements are referenced to a periodic TTL-signal which is generated by a profiled disk, being mounted on the siren shaft, and a photo sensor. The trigger unit of the siren is shown in Figure 4.22.

For the measurements under self-excitation, the siren is not used. A corresponding reference signal is obtained on the basis of dynamic pressure measurements in the combustion chamber itself. The amplified microphone signal is connected to a subsequent voltage comparitor switch with a threshold level of 0.5 V. The TTL status will be high as long as the microphone output voltage exceeds 0.5 V.

As a consequence, the obtained phase reference will be subject to a certain scattering, depending on the deterministic character and the amplitude of the referencing pressure signal, but the resulting phase uncertainties of the reference phase do usually not exceed ±10°.

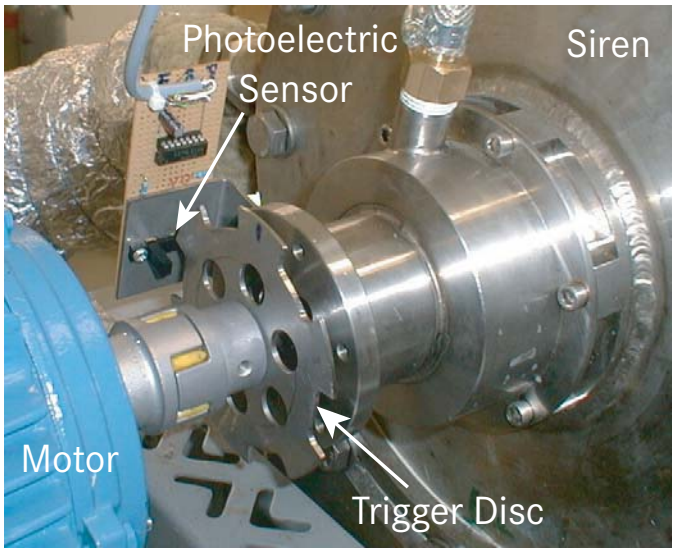

Fig. 4.22: Trigger unit on the siren shaft for phase-referencing measurements under external forcing.

The rectangular reference signal is used to start a programmable 16 bit counter on a PCI-board[21], which triggers the measurement devices on completion of a preselected countdown. The starting value N of the countdown is determined on the basis of the selected phase shift $\Delta\phi$, taking into account the oscillation frequency f_{exc}. f_{exc} is determined from the TTL-reference signal by Fast Fourier Transformation. The phase resolution of the trigger board is 0.86°.

[21] Type Meilhaus ME1400B PCI

5 Atomiser Performance

In the introductory section 1.4, it was shown that the following subprocesses are of particular interest for understanding the excitation of rumble:

- **Primary zone aerodynamics**: The transport processes in the primary zone are influenced by the response of the burner to acoustic perturbations. The dynamic velocity field and the generated droplet sizes will vary. The time delay for spray convection to the flame determines whether the Rayleigh criterion Eq. (1.1) for a pure thermoacoustic mode is fulfilled or not.
- **Combustion**: The oscillating heat release of the flame is the driver for the low-frequency instability. However, it is not yet clear whether the pure thermoacoustic mode or the entropy mode is effecting the closure of the feedback loop leading to self-excitation.
- **Dilution zone aerodynamics**: A dispersive aerodynamics of the dilution zone of the combustor can significantly influence the amplitude of entropy waves and the pressure feedback at the nozzle.

These aspects will be discussed in chapters 5 and 6 on the basis of the measured data.

In this chapter, experimental results of atomiser performance tests are presented both for steady conditions and with external excitation. For that purpose, the combustor is operated open-ended. The investigation of the droplet size distribution is performed without combustion, using the surrogate fuel of ethanol and water introduced in section 4.5.1. The index 'Eth.' refers to the data obtained for the ethanol-water mixture. Conversion to the properties of kerosene is being done assuming Weber number equivalence (see section 4.5.1), and the converted data will be indexed with 'Ker.'.

For the purpose of convenience, the overbar, previously denoting the average quantities, will be omitted in the following, e.g. $\bar{p} \equiv p$.

5.1 Injector Aerodynamics

5.1.1 Steady Velocity Field

The characteristic instantaneous air velocity field in the primary zone without spray is shown in Figure 5.1. The relative pressure loss is $\Delta p/p = 2.3\%$. In the vector map, mixing air originating from the first injection row enters the combustor at about half the image length.

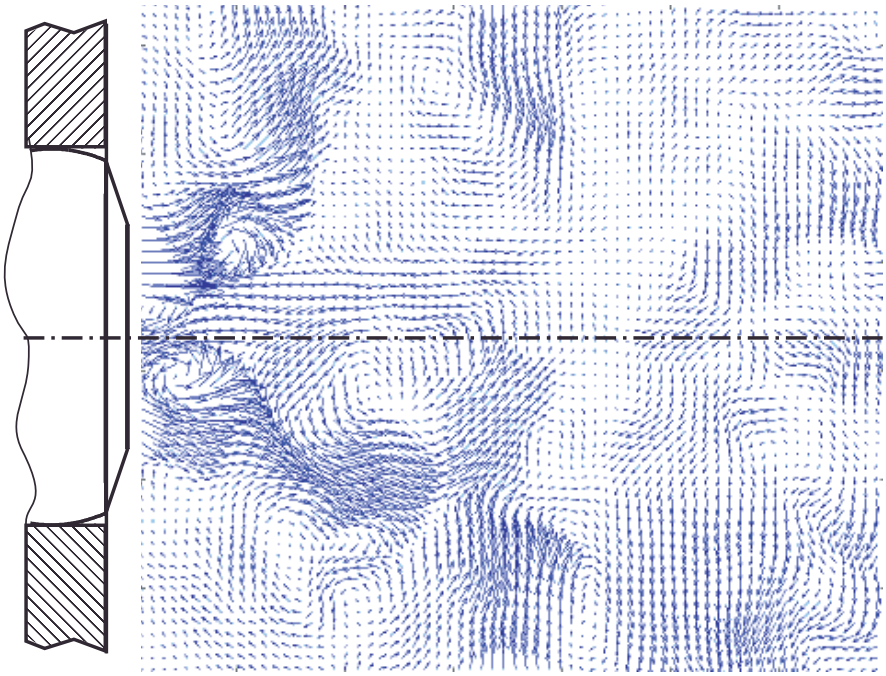

Fig. 5.1: Instantaneous PIV-vector maps of the air velocity field in the primary zone in the absence of a flame for $T_a = 300$ K, $\Delta p/p = 2.3\%$.

The flow field is turbulent. Vortices are periodically generated in the shear layer between the swirled air cone and the inner recirculation zone and are convected downstream. Corresponding vortex pairs are also encountered in the shear layer of the corner recirculation zo-

nes. Coherent structures were observed for all operating points. The vortex shedding obtained at $\Delta p/p = 3.3\%$ is shown in Figure 5.2.

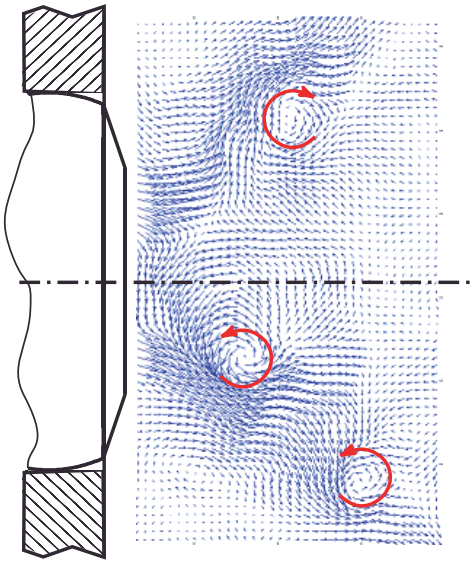

Fig. 5.2: Helical vortex structure in the instantaneous air velocity field at $\Delta p/p = 3.3\%$.

From the diameter of the nozzle d, the axial separation of the vortex cores in the PIV images and the average injection velocity of the air u_a, an approximate Strouhal number $Sr = f \cdot d/u_a = 0.26$ of the vortex shedding is obtained. The vortex shedding frequency in Figure 5.2 is approximately 430 Hz, thus significantly above the typical rumble frequencies. The vortex structure in Figure 5.2, particularly the periodic and alternating occurrence in the upper and lower lobes, indicates a helical vortex structure originating from a circumferentially rotating separation point at the prefilmer lip or within the annular air ducts of the injector. Helical shear-layer instabilities have also been reported for other configurations, e.g. [PGW00, GGDL02], being a common source for instability, particularly for premixed combustion.

The interaction between the swirling air jet and the first row of mixing air injection can be strong, as seen in the vector map, Figure 5.1. The corresponding vector map for $\Delta p/p = 2.3\%$ after averaging 100 instantaneous vector maps is shown in Figure 5.3. Here again, the swirling air cone, the centre recirculation zone and the first row

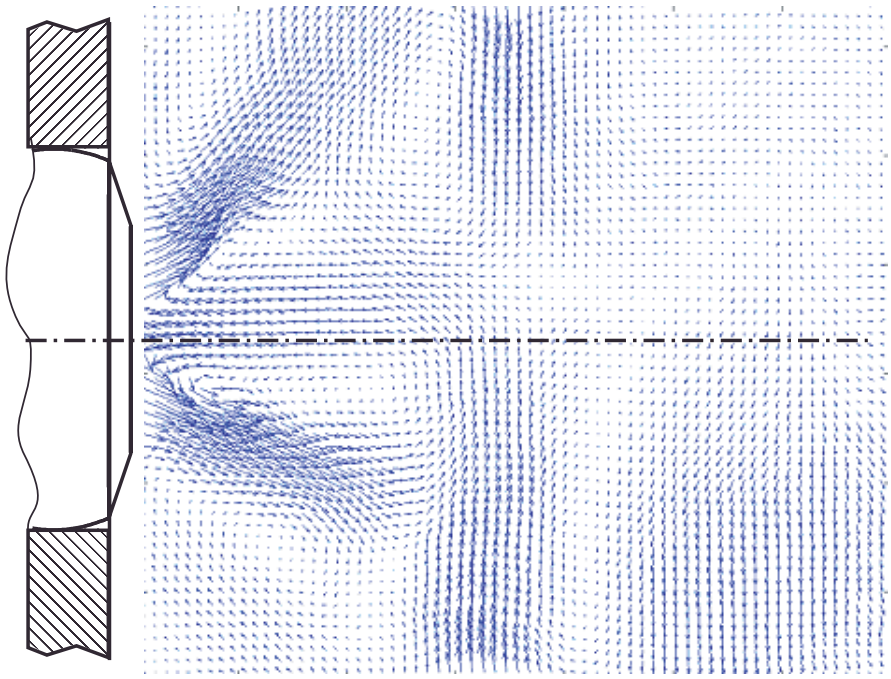

Fig. 5.3: Averaged air velocity field in the primary zone without flame for $T_a = 300$ K, $\Delta p/p = 2.3\%$.

of mixing air injection can be seen. In Figure 5.1 and Figure 5.3, asymmetries in the flow field are obtained which are primarily related to the interaction of the swirled air cone and the central lower jet of the first mixing row shown in Figure 3.8. As a consequence, the air cone angle decreases to 72° compared to 88° for the isolated burner, without the mixing flow. The effective area of the mixing orifices is rather low and the mixing air enters the generic combustor at injection velocities up to 70 m/s, being comparable to the burner exit velocities. Although the identical pattern of mixing orifices according to Figure 3.8 was applied on the combustor top and bottom plate, minor geometrical asymmetries in the set-up were practically unavoidable; e.g., resulting from the PIV light sheet access (Figure 4.2). The unequal momentum balance of the opposed mixing jets is amplified by the swirling core flow, leading to the observed asymmetries of the flow field in the primary zone.

5.1.2 Pressure-Velocity Coupling under Forcing

Figure 5.4 shows the colour plots of the phase averaged air velocities in the centre plane of the combustor. The velocity magnitude corresponds to the absolute value of the two-component velocity vectors $\sqrt{u^2 + v^2}$ in the centre plane of the combustor. The injector is operated at $T_a = 300$ K, $\Delta p/p = 3.3\%$, without fuel and under siren forcing at 90 Hz. The relative forcing amplitude $p'/\Delta p$ at the burner inlet is 13% and the phase angle φ is given relative to the minimum pressure phase at the burner inlet. Since the open combustion chamber is operated without extension, the static pressure in the combustor is nearly constant. As a consequence, minimum dynamic pressure at the injector inlet corresponds to minimum effective pressure drop across the burner which produces the low air velocities encountered in Figure 5.4 at $\varphi = 0°$. For $\varphi > 0°$, a global rise in velocity amplitude is observed due to the increasing upstream pressure, featuring maximum values at a relative phase angle $\varphi \approx 180°$. Subsequently, the velocities decay again. For the frequency range associated with rumble, no vortex shedding is observed in the phase-averaged flow fields, indicating negligible influence of forced coherent flow structures mentioned in section 1.2.

The PIV flow field suggests that the burner response to the forcing is quasi-steady in the low frequency range investigated. For verification, the quasi-steady relation between the amplitudes of burner velocity and pressure drop is derived from a perturbation expansion using the perturbations of pressure and velocity in the steady Bernoulli equation. Due to the very large area ratio between the supply tube and the burner channels (about 1:90), the supply tube may be treated as a plenum chamber, neglecting the contribution of the air velocity to the total pressure. For a low Mach number flow from a plenum through the burner channels, the total pressure balance from the plenum to the burner exit is then given by

$$\Delta p = \frac{\rho_a}{2} u_a^2 (1 + \zeta_{inj}). \tag{5.1}$$

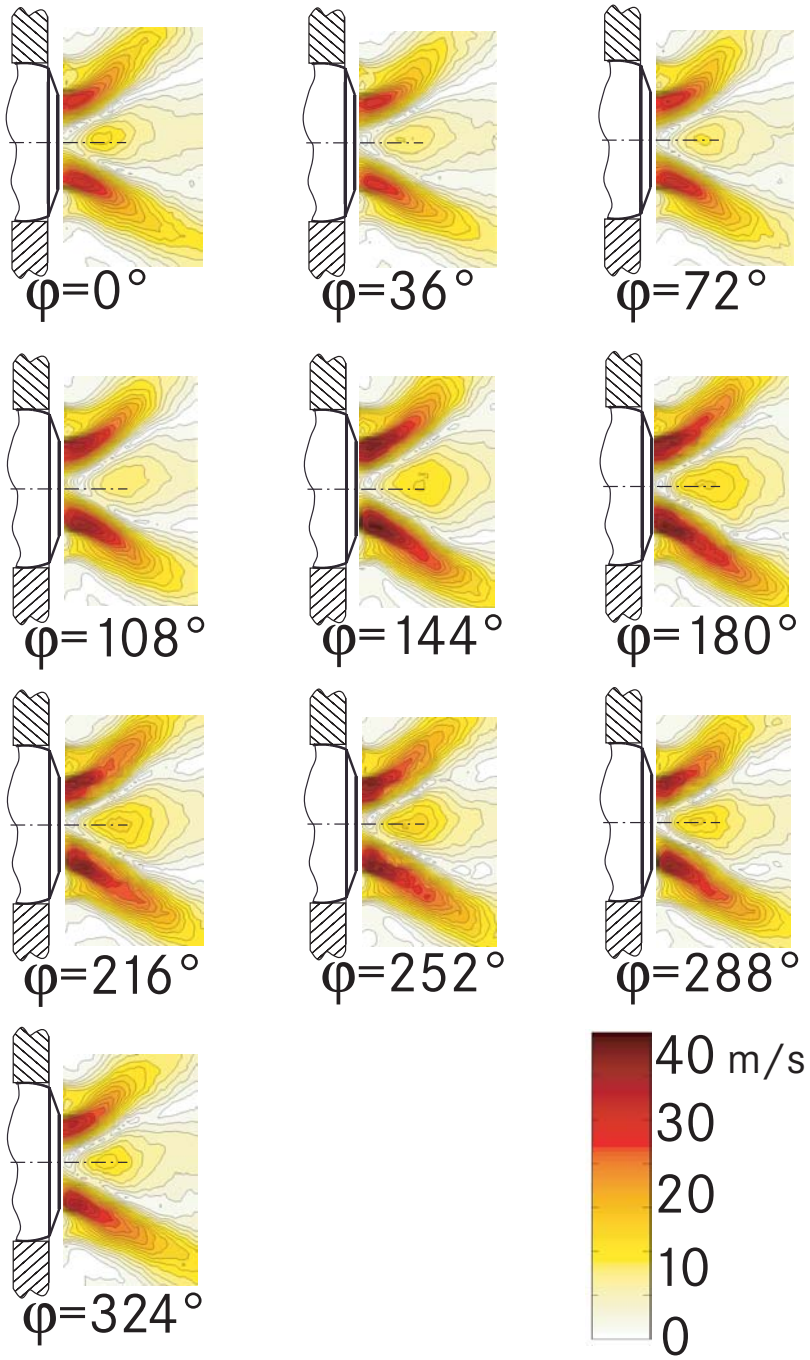

Fig. 5.4: Averaged phase-locked air velocity field under forcing at 90 Hz without combustion. The given velocity magnitude corresponds to $\sqrt{u^2 + v^2}$. The mean operating parameters are $T_a = 300$ K, $\Delta p/p = 3.3\%$.

ζ_{inj} is the pressure loss coefficient of the injector. According to section 2.1, the following perturbation equation is obtained

$$\Delta p' = \rho_a u_a u'_a (1 + \zeta_{inj}) \tag{5.2}$$

after linearisation and subtraction of the equation for the time mean values. The quasi-steady relation of relative pressure and velocity perturbations is

$$\frac{1}{2}\frac{\Delta p'}{\Delta p} = \frac{u'_a}{u_a}. \tag{5.3}$$

Equation (5.3) indicates that for a quasi-steady burner response the relative velocity amplitude will be half the amplitude of the relative pressure drop.

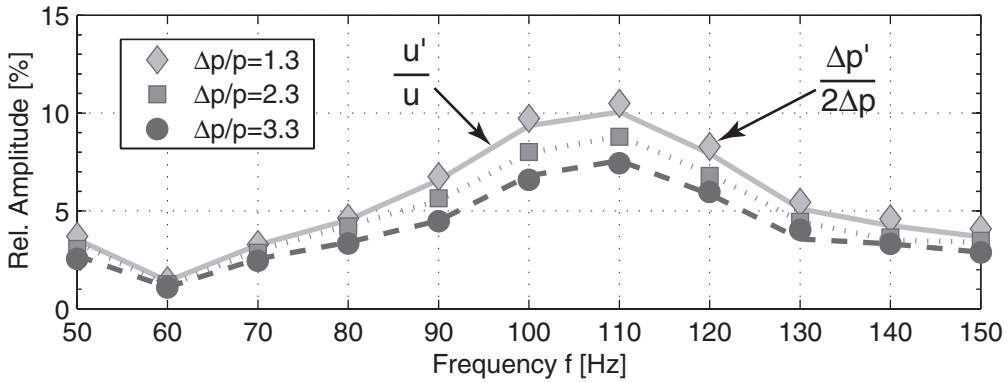

Fig. 5.5: Comparison of the measured pressure amplitudes (symbols) and air velocities (lines) over frequency for three static injector pressure drops in a non-combusting environment.

In Figure 5.5, the oscillation amplitudes of half the relative pressure drop $\Delta p'/2\Delta p$ are compared with the relative velocity oscillation u'_a/u_a of the air. u'_a/u_a was measured with the CTA. The correlation of the data, plotted for three static pressure drops $\Delta p/p$, is very good.

This reveals that the burner flow responds quasi-steadily to the low frequency forcing. Small differences are observed between velocity and pressure amplitudes for the higher frequencies for $\Delta p/p = 1.3\%$. These deviations decrease with increasing air flow rates and $\Delta p/p$, due to the higher signal to noise ratio of the CTA. For increasing flow rate, the relative amplitudes obtained at the burner are seen to decrease, because the rising burner back pressure reduces the relative forcing amplitude of the siren.

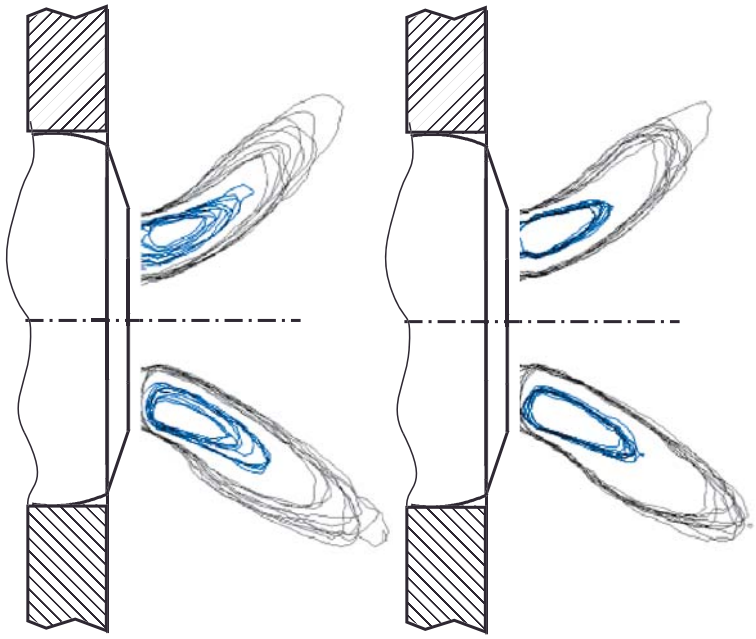

Fig. 5.6: Phase-locked velocity field taken from Figure 5.4. The left image shows two contour levels of velocity magnitude for all 10 phase angles. The right image shows the same field scaled with the phase-resolved average velocity at the burner exit.

Figure 5.6 shows a superposition of the phase-resolved velocities of Figure 5.4. In the left image, the contour lines represent two fixed levels of air velocity magnitude at the 10 measured phase angles. The spread of the contours gives an impression of the injector's velocity response and shows how the swirling jet velocity grows and shrinks during the forcing period. The right image in Figure 5.6 shows the contour lines of equal relative velocity. These are obtained by norma-

lising the phase-averaged velocity field with the injector exit velocity at the respective phase angles. The contours coincide, meaning that the velocity field is invariant during the forcing cycle. Furthermore, no change in the injection angle is observed. Therefore, it can be concluded that the aerodynamic behaviour of the injector is quasi-steady for the low-frequency range, which is in line with the pressure-velocity coupling discussed above.

5.2 Atomisation and Droplet Dynamics

5.2.1 Steady Atomisation Behaviour

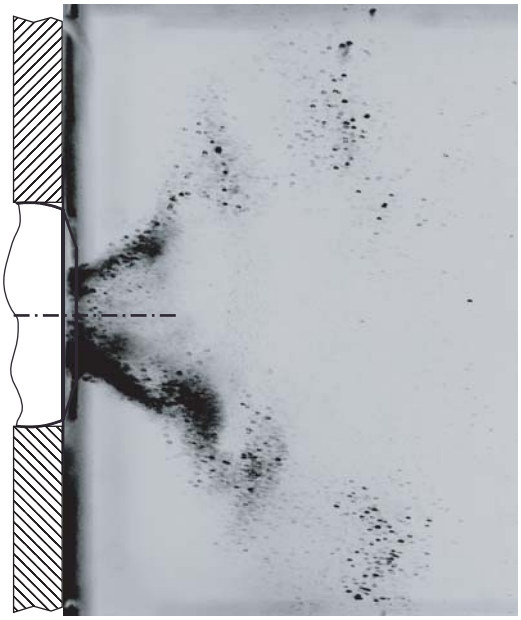

Fig. 5.7: Mie scattering of the instantaneous spray cone with combustion ($\Delta p/p = 2.3\%$, $\dot{m}_f$ =1.2 g/s.)

The instantaneous spray pattern in the centre plane of the combustor in the absence of external excitation is shown in Figure 5.7. The spray features a rather heterogeneous distribution, typical for airblast devices that are operated under low air pressures [ZJL97]. The shear-layer instabilities, which were already observed for the air flow without spray, impose a wavy structure on the instantaneous droplet

distribution. The average spray cone angle is 74°. Under conditions of very low fuel and air flow rates ($\Delta p/p < 2.0\%$, $\dot{m}_f < 1.2$g/s), the circumferential fuel distribution on the prefilmer lip tends to be increasingly irregular, leading to elevated rates of injected fuel on the lower side of the prefilmer lip under the impact of gravity.

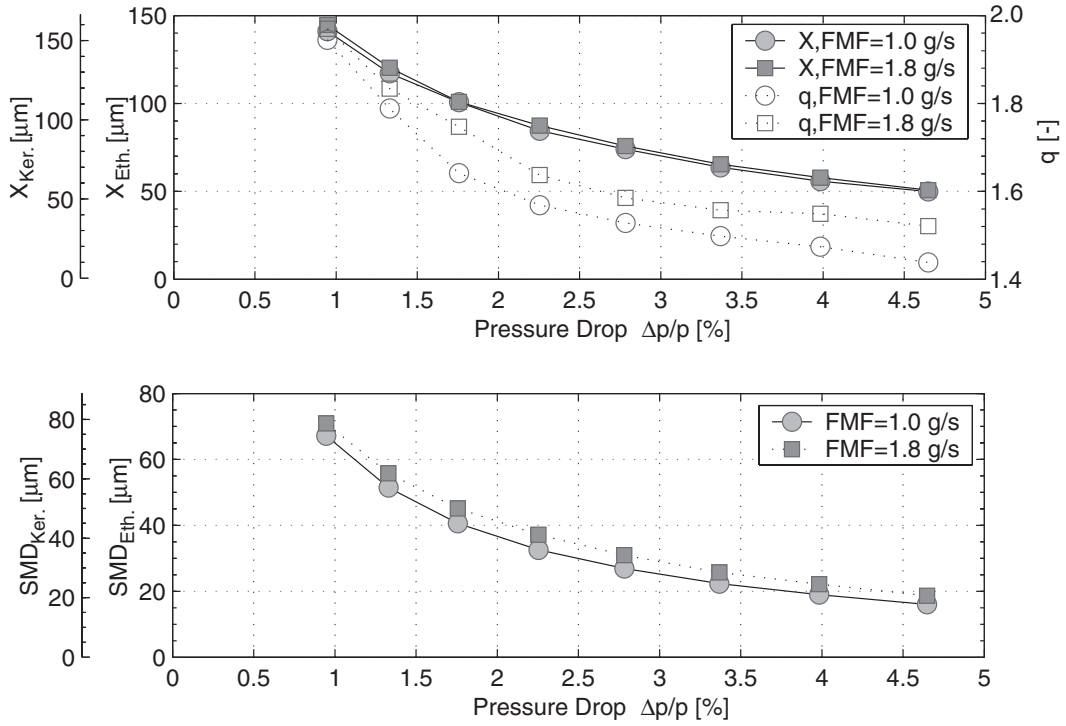

Fig. 5.8: Characteristic Rosin-Rammler parameters X and q (upper graph) and SMD (lower graph) over relative injector pressure drop for different fuel mass flows in the steady, non-combusting case.

The upper graph in Figure 5.8 shows the parameters X and q of the measured Rosin-Rammler distributions, according to Eq. (4.28). X and q are given as a function of $\Delta p/p$ and for two characteristic fuel mass flows. The measured values for the exponent q range between $2 > q > 1.4$, which indicates a relatively broad spectrum of droplet sizes, however lying within the usual performance range of airblast injectors [Lef89]. For rising pressure drops, the spray becomes increasingly polydisperse due to the influence of the smaller droplet sizes while considerable fractions of large droplets are still produced.

The corresponding variation of the SMD with $\Delta p/p$ is plotted in the lower graph of Figure 5.8. Typical for air-blast atomisers, the SMD is dominated by the relative air velocities at the atomiser lip, being proportional to Δp according to Eq. (5.1). For low viscosity fuels such as kerosene or ethanol, the atomisation process is governed by the Weber number We. Referring to the relation given in [Lef99]:

$$\frac{D_{32}}{L_c} \propto \left(1 + \frac{\dot{m}_f}{\dot{m}_a}\right) We^{-x} \tag{5.4}$$

the current data exhibits an exponent $x \approx 0.8$ with respect to the AMF variation. This corresponds to the characteristic values for airblast atomisers found in literature, e.g. [Sat85]. According to the steady curves, the SMD is fairly insensitive to changing fuel mass flows (FMF), resulting in a diameter increase of approximately 10% for doubled fuel flow rate. For low pressure drops $\Delta p/p < 3.0\%$, the steady atomiser characteristics exhibits an increasing sensitivity of the droplet sizes to changing air supply conditions. Considerable changes in absolute droplet size are already obtained for small perturbations of the air flow.

5.2.2 Droplet Motion Timescale

The dynamic behaviour of the spray is characterised by the timescale of droplet motion. An estimate for this timescale can be obtained from the equation of motion for a simple spherical droplet at constant air velocity. The frequency limits of the quasi-steady behaviour of the spray in an unsteady air flow can be assessed in this manner. This information is necessary for interpreting the forced spray measurements presented in section 5.2.3. Following Hinze [Hin75] the equation of motion of a spherical particle reduces to the balance of inertia and drag force:

$$\rho_f \frac{\pi d^3}{6} \frac{du_f}{dt} = -\frac{\rho_a}{2} c_D \frac{\pi d^2}{4} (u_f - u_a)|u_f - u_a| \tag{5.5}$$

For a droplet Reynolds number in the range $1 < Re < 1000$, the drag coefficient c_D is well approximated by an extended Stokes-type law [Krä88]

$$c_D = \frac{24}{Re}(1 + 0.15Re^{0.68}) \tag{5.6}$$

with

$$Re = \frac{d|u_f - u_a|}{\nu_a}. \tag{5.7}$$

Inserting Eq. (5.6) into Eq. (5.5), the following nonlinear ordinary differential equation for the droplet velocity is obtained:

$$\frac{du_f}{dt} = -18\frac{\nu_a}{d^2}\frac{\rho_a}{\rho_f}(1 + 0.15Re^{0.68})(u_f - u_a) \tag{5.8}$$

Solving this equation for characteristic droplet diameters obtained, it is found that the deviation from the Stokes drag relation is only relevant during the initial acceleration of the droplet, when the slip velocity is large. A characteristic timescale τ can be defined analogously to the linear case, yielding

$$\frac{1}{\tau} = 18\frac{\nu_a}{d^2}\frac{\rho_a}{\rho_f}, \tag{5.9}$$

which will scale the solutions of Eq. (5.8) for zero initial droplet velocity. Applying the measured Sauter diameters in Eq. (5.9), the τ represents a characteristic time delay of the spray. τ is shown in Figure 5.9.

In the linear case, τ gives the time in which the droplet has accelerated to 63% of the gas velocity, whereas in the nonlinear case 63% of the gas velocity are reached earlier after about $1/3\tau$.

5.2.3 Spray Behaviour under Forcing

The Sauter mean diameters of the forced spray, measured with the Malvern particle sizer, are shown in Figure 5.10 for fuel flow rates of

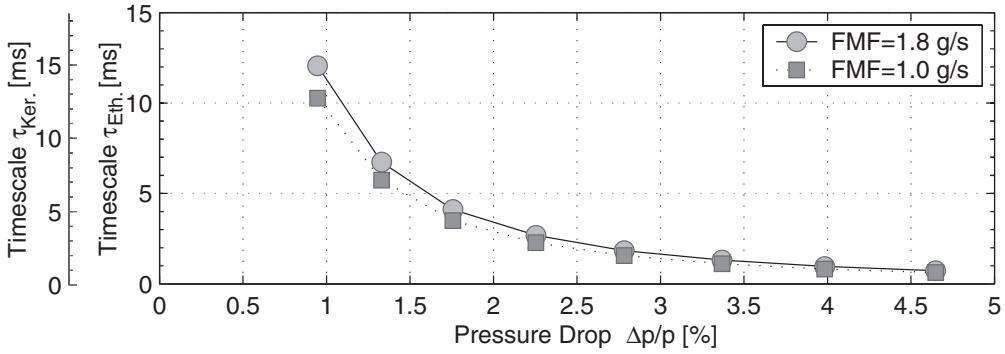

Fig. 5.9: Characteristic timescales of droplet acceleration τ as a function of the pressure drop across the injector.

1 g/s (upper graph) and 1.8 g/s (lower graph), mean pressure drops of $\Delta p/p = 1.3\%$ (diamonds) and 3.0% (circles), and excitation frequencies ranging between 50 and 150 Hz. From the measured time series of the oscillating SMD, the mean diameter d and the amplitude of the perturbation d' at the forcing frequency were extracted using FFT. For comparing the dynamic measurements with the steady case, the SMD values at the maximum and the minimum velocity phase ($d_{min} = d - d'$ and $d_{max} = d + d'$, respectively) are plotted in Figure 5.10 together with the steady SMD curves.

For the higher air mass flow rates corresponding to $\Delta p/p = 3.0\%$, the agreement between the dynamic and steady data is good, proving quasi-steady behaviour of the atomiser. For lower air flow rates of $\Delta p/p = 1.3\%$, the droplet SMD and thus its motion time scale (Figure 5.9) increases to the same magnitude as the forcing period. Now, convection will bias the drop size distribution in the measurement volume towards larger droplets, as discussed in the previous section, since larger droplets from the low velocity phase still continue to reach the measurement volume during the high velocity phase. Therefore, the time series of drop size becomes asymmetric between the low and high velocity phases. As a consequence, the measured mean diameter d and the amplitudes d', obtained from FFT, are shifted towards higher values, particularly deviating the values for d_{max}. For the 1.0 g/s fuel flow rate, the consistency with the steady

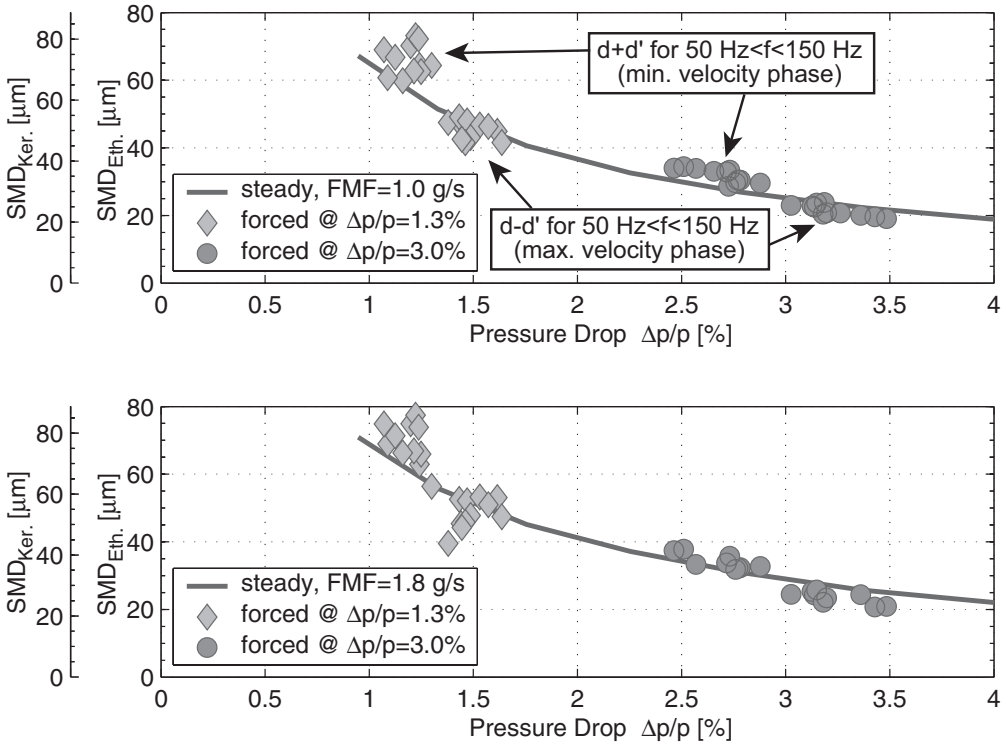

Fig. 5.10: Comparison of unsteady SMD (symbols) data with the steady atomisation curve for $\dot{m}_f$ =1.0 g/s (top) and $\dot{m}_f$ =1.8 g/s (bottom).

curve at lower pressure drop is better than for the case with 1.8 g/s fuel, which is related to the lower characteristic time scale in Figure 5.9. Therefore, it seems that the deviations seen in Figure 5.10 are mainly an intrinsic problem related to the measurement technique employed [WASS84].

In order to assess the applicability of the forced spray behaviour under non-ignited conditions to the case with combustion, the spray cone in the combusting environment was analysed by means of Mie-scattering. The intensity of the PIV-light sheet was held constant throughout the cycle. Figure 5.11 shows two phase-averaged pictures at minimum and maximum velocity phases with constant levels of Mie-scattering intensity. The intensity of the scattered light varies during the period due to the variation of droplet number and size with the air velocity as seen by the fixed contour lines. But the

crown lines on the intensity contours of both phase angles coincide, showing that the underlying spray geometry does not vary with the periodic velocity oscillation.

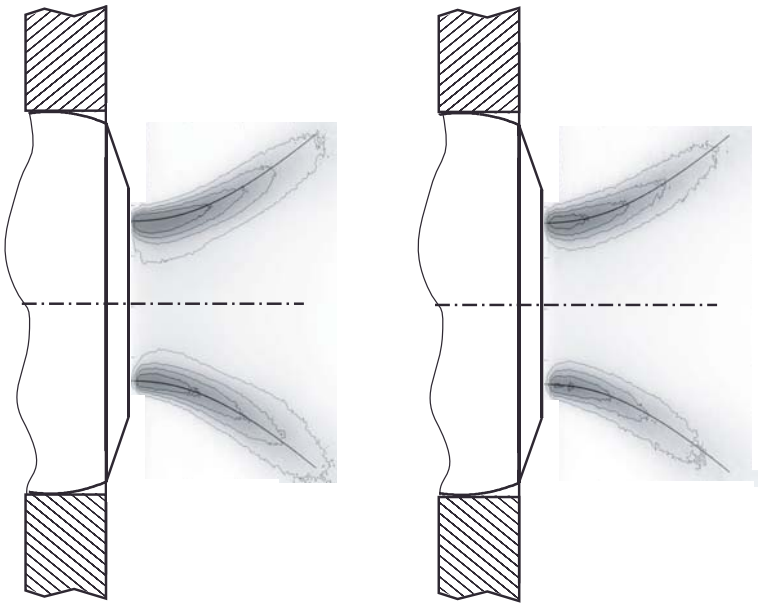

Fig. 5.11: Mie scattering images of the spray cone with combustion at $\Delta p/p = 3.3\%$, $\dot{m}_f$ =1.3 g/s, and $f = 130$ Hz. The contours show constant levels of scattered intensity. Left image: maximum velocity phase; right image: minimum velocity phase. Crown lines show constant spray geometry.

In addition to extracting the spray geometry from phase locked averages of the Mie scatter, the intensity oscillation itself is of interest. In dilute sprays, the average intensity observed from Mie scattering depends on droplet diameter and number density approximately as

$$\frac{I}{I_0} = \left(\frac{d}{d_0}\right)^2 \frac{N}{N_0} \overset{\dot{m}_f=\text{const.}}{\approx} \left(\frac{d}{d_0}\right)^2 \left(\frac{d}{d_0}\right)^{-3} = \frac{d_0}{d}. \tag{5.10}$$

For a constant fuel mass flow, the ratio of the particle number densities in the second term of Eq. (5.10) can be expressed in terms of the droplet diameter. For the current atomiser under steady-state

conditions, the droplet diameter and air velocity correlate well with

$$\frac{d}{d_0} = \left(\frac{u_{a,0}}{u_a}\right)^{\xi} \ , \ \xi > 0. \tag{5.11}$$

The velocity exponent ξ can be deduced from the static atomisation curves in Figure 5.8 to $\xi = 1.6$. ξ describes the sensitivity of the atomiser to changing air velocities and therefore is a central parameter for characterising the atomiser performance.

Given Eq. (5.11) and Eq. (5.10), the measured intensity amplitude can then be transformed into a velocity amplitude

$$\frac{u_a'}{u_{a,0}} = \frac{1}{\xi}\frac{I'}{I_0}. \tag{5.12}$$

With this equation and given the steady atomiser characteristics, relative velocity amplitudes are calculated from the relative Mie intensity amplitudes for the quasi-steady behaviour of the atomiser. This procedure provides a second proof for the quasi-steady spray behaviour.

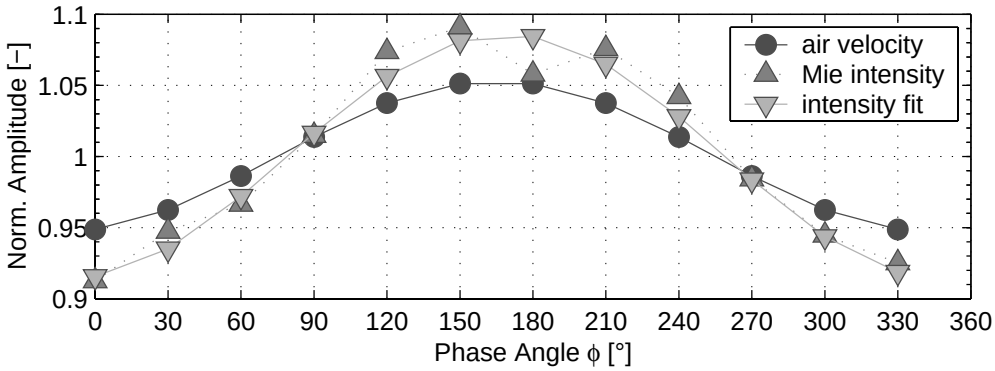

Fig. 5.12: Air velocity and Mie scattering intensity fluctuation for the spray at 130 Hz excitation.

Figure 5.12 shows the comparison of the relative burner air velocity and the mean Mie scattering intensity oscillation for the same operation point taken from phase-locked PIV measurements. To obtain the intensity amplitude, a sinusoidal fit was used, which is also

shown. Taking into account the average convective time delay of the spray ($\approx 10^\circ$ at 130 Hz), the net phase angle difference between the scattering intensity and velocity trace is negligible, which means that the spray response to velocity forcing is in phase. Using Eq. (5.12) with $\xi = 1.6$, the quasi-steady velocity amplitude is calculated from the Mie intensity amplitude. A relative velocity amplitude of 5.4% results, which compares well with 5.3% measured velocity amplitude, shown in Figure 5.12. The validity of Eq. (5.12) implies that quasi-steady atomisation behaviour is also found under combustion and that the momentary fuel mass flow rate in the spray is constant.

5.3 Conclusions

From the investigation of the atomiser performance of the rumble-prone airblast atomiser design, the following conclusions can be drawn:

- At low-frequencies, the atomiser exhibits a quasi-steady behaviour, both for the velocity field and for the spray, under combusting and non-combusting conditions. A linear stability analysis focussing on rumble can therefore apply the steady atomiser characteristics.
- For decreasing injector pressure drops, the atomiser response is increasingly sensitive to varying air mass flows. The sensitivity can be characterised by the velocity exponent ξ. The changes in the droplet sizes not only alter the droplet number density, but also impose a considerable spread of the convective delay times in the primary zone.
- The generation and convection of vortex structures in the shear-layer of the injected air cone impacts the instantaneous spray distribution. The vortex shedding frequencies however lie distinctively above the frequency range of rumble such that a destabilising effect can be excluded.

6 Experimental Investigation of Rumble

In this chapter, the measurement results under self-excitation are presented and the influencing parameters are analysed. As in the previous chapter, the investigation is focussed on the narrow-cone injector design, which has been introduced at the beginning of chapter 4. The extensions at the combustor exit were varied to separate the destabilising effect of entropy waves from the pure thermoacoustic mode, as discussed in section 3.3.3. The impact of the primary zone aerodynamics is assessed by replacing the narrow-cone injector by the highly dispersive wide-cone design.

In the following section 6.1, the mechanism of the self-excited oscillation is investigated for an operating point being characterised by a mean injector pressure drop of $\Delta p/p = 2.3\%$, no air preheating ($T_a = 300$ K), and an overall equivalence ratio $\phi = 0.55$. This operating point is highly unstable, producing elevated oscillation amplitudes at a constant limit frequency, which are particularly suitable for triggering the external PIV system [EFHS04].

The instability characteristics for changing operating conditions is presented in section 6.2 on the basis of a parametric variation of the air and the fuel mass flows. The air temperature is maintained at $T_a = 300$ K for all measurements.

The steady temperature distribution in the staged combustor and the dispersion of entropy waves under self-excitation are discussed in section 6.3. A comparative analysis of the different injector designs and the influence of the primary zone aerodynamics is conducted in section 6.4. In section 6.5, the experimental findings of this chapter are summarised.

6.1 Phenomenological Description

6.1.1 Choked Combustor Exit

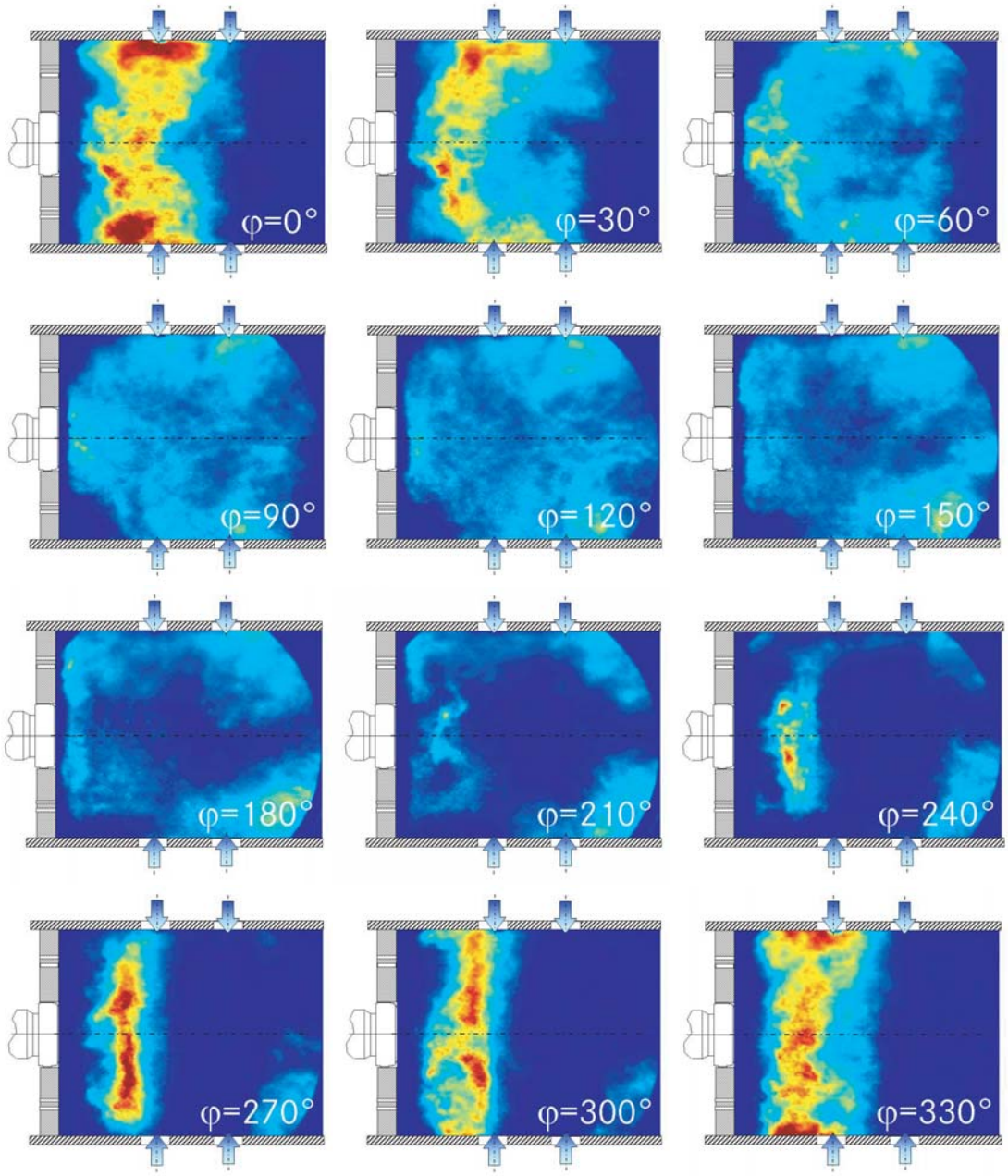

Fig. 6.1: High speed camera recording of the flame OH*-chemiluminescence during one combustion oscillation cycle at 126 Hz.

Figure 6.1 shows one period of the self-excited combustion oscillation at 126 Hz limit frequency obtained with the choked exit nozzle. The images are taken from the high speed video sequence capturing the OH*-chemiluminescence of the flame. The relative phase angle φ refers to the phase with maximum OH*-radiation (φ=0°). The corresponding time trace of the combustor pressure is plotted together with the flame OH*-chemiluminescence recorded by the photomultiplier in Figure 6.2.

The chemiluminescence and the acoustic pressure shown in Figure 6.2 are strongly pulsating. High OH*-intensities are mainly observed in the primary zone near the inlets of the mixing air, as seen from Figure 6.1. The pressure rise inside the combustion chamber, immediately following the high reaction rates in Figure 6.2, leads to periodic build-up and decay of the main reaction zone. A Fourier analysis of the results shown in Figure 6.2 reveals that the OH*-signal leads the pressure signal by 53°. The time-resolved signals indicate a very stable phase relationship between the signals. Furthermore, the time trace reveals a synchronised modulation of the amplitudes.

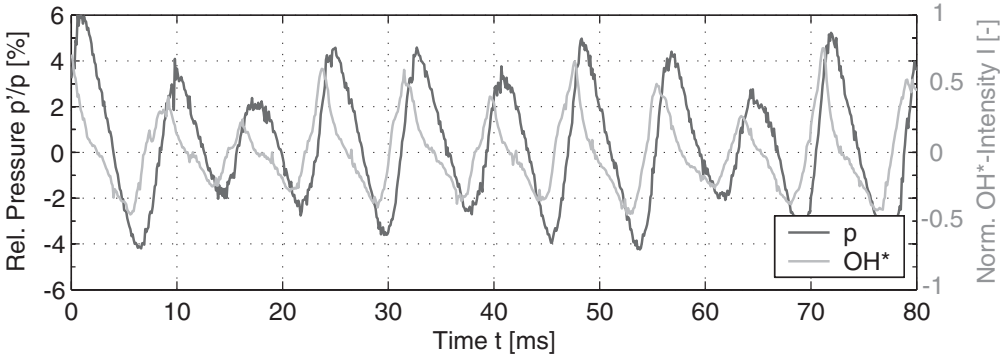

Fig. 6.2: Time traces of the relative combustor pressure p'/p (black) and the normalised OH*-chemiluminescence (grey) obtained with the sonic nozzle.

The pressure amplitudes in the range of 2 to 5% of the static combustor pressure partly exceed the pressure drop of the nozzle for this operating point. As a consequence, the flow velocity from the injector decreases strongly and occasionally the flame propagates towards the

nozzle ($\varphi = 60°$ in Figure 6.1). In the dilution zone, i.e., downstream of secondary air injection, lower levels of OH*-radiation are detected. In this region with an overall lean mixture, periodic detachment of zones of locally increased reaction rate can be observed, which originate from the primary reaction zone and which are subsequently convected towards the combustor outlet.

The oscillating combustor pressure alters the fuel spray characteristics, as shown in section 5.1: Rising combustor pressure reduces the available air momentum for atomisation, shifts the droplet size distribution towards larger droplets and increases the convective delay times of the spray from the injector to the flame [EFH$^+$03].

The impact of the pressure fluctuations on the injector and on the transport properties of the spray can be seen in Figure 6.3 and Figure 6.4. The reference phase is the same as for Figure 6.1. Figure 6.3 exhibits highest Mie intensities at an approximate phase angle of $\varphi = 144° \ldots 216°$, i.e. when the combustor pressure is minimum and highest injection velocities of the air are obtained. As a consequence, minimum average droplet size and maximum droplet number density N are expected at these phase angles, following Eq. (5.10). Maximum penetration depth of the spray is found at the same phases, correlating with the injection velocities of the air. From the phase-resolved spray velocities shown in Figure 6.4, it can be seen that the elevated combustor pressure at $\varphi < 90°$ leads to a rapid breakdown of spray injection. The recovery of adequate spray velocities is encountered for $\varphi > 144°$. The droplet peak velocities in the centre plane of the combustor vary between 8 m/s for $\varphi \approx 72°$ and 32 m/s for $\varphi \approx 252°$.

The maximum droplet velocities in the cycle are obtained approximately 72° after the generation of the minimum droplet sizes by the injector. This phase shift is related to the time scales of droplet acceleration, discussed in section 5.2.2. From the phase shift and the oscillation frequency (126 Hz), a characteristic delay time $\tau_{acc} \approx 1.5$ ms can be deduced. According to Figure 5.9, the measured time delay is associated with an effective pressure drop $\Delta p/p \approx 4.5\%$. This value

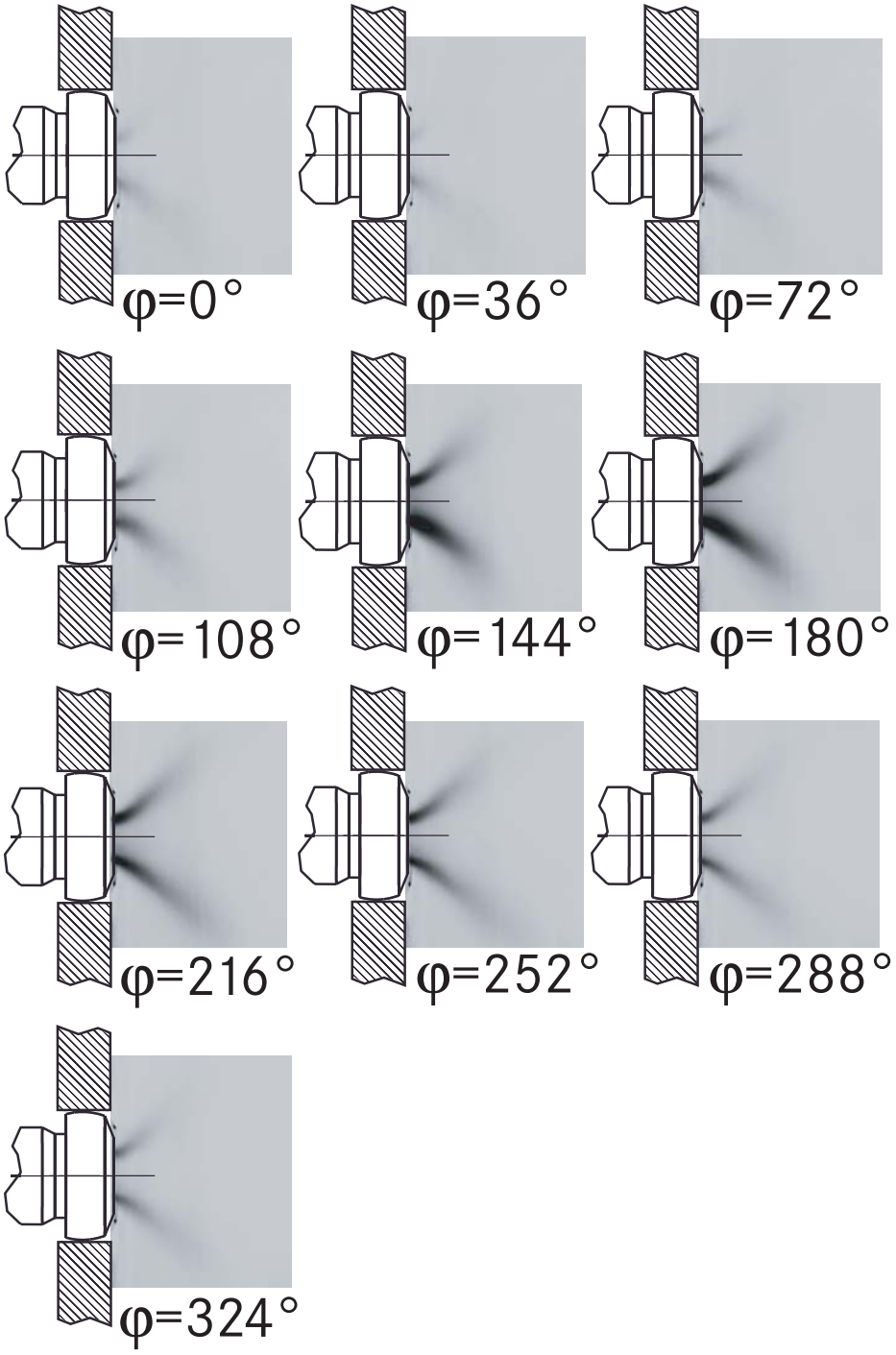

Fig. 6.3: Phase-resolved droplet Mie-scattering at the injector outlet obtained from the PIV images for one oscillation cycle at 126 Hz.

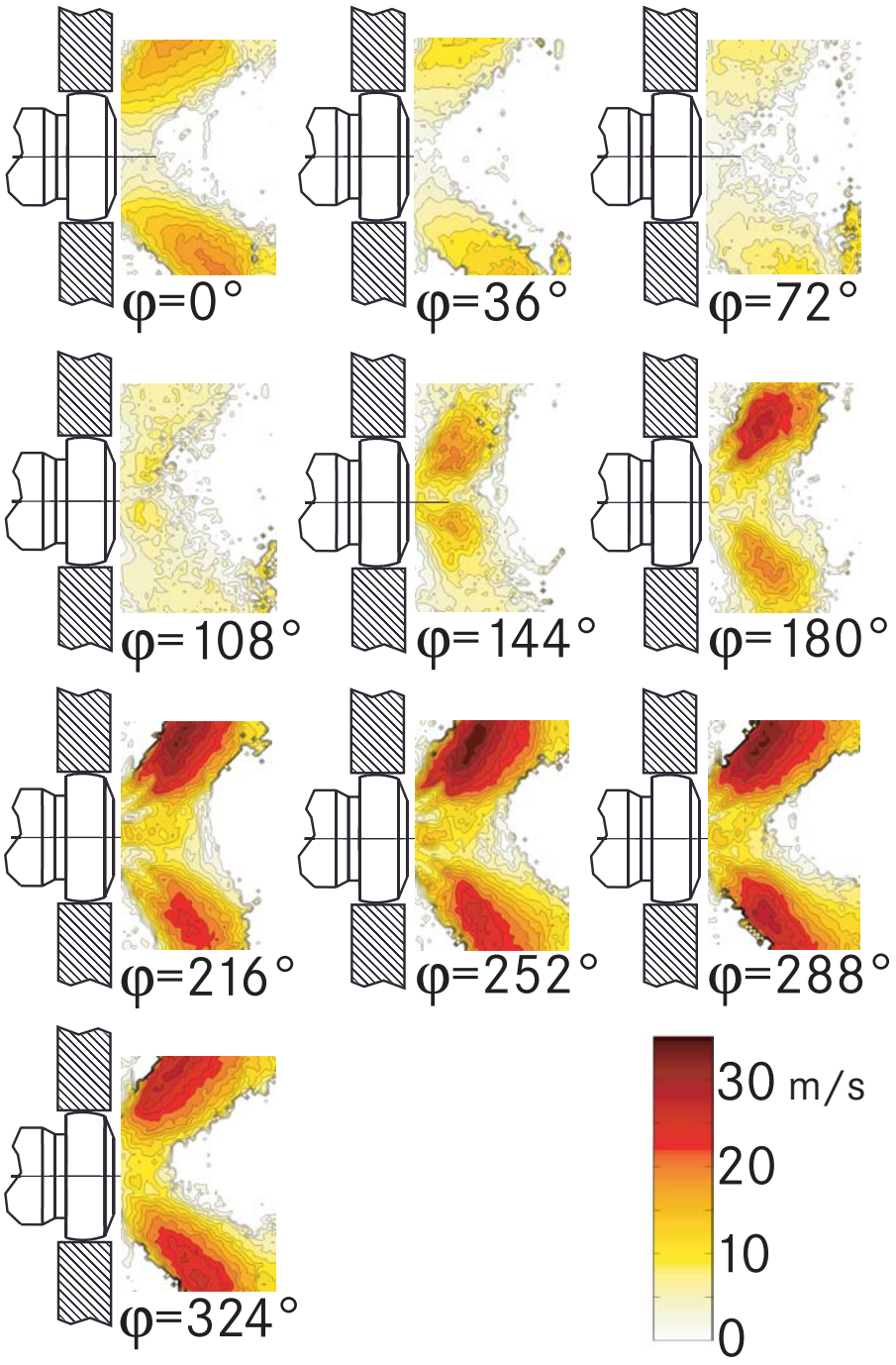

Fig. 6.4: Phase-resolved, averaged droplet velocities at the injector outlet measured by PIV for one oscillation cycle at 126 Hz. The velocity magnitude refers to the absolute value of the two-component velocity vectors $\sqrt{u^2 + v^2}$.

approximately corresponds to the maximum driving pressure drop during the oscillation cycle, leading to the generation of the smallest droplets.

In order to investigate the impact of the combustor aerodynamics on the entropy wave produced by the flame, dynamic temperature measurements have been performed at different axial locations of the combustor at the positions shown in Figure 4.16. Figure 6.5 shows the recorded time domain data of the combustor pressure (grey) and the reconstructed gas temperature at the inlet of the choked nozzle (Pos. T6 in Table 6.1, black).

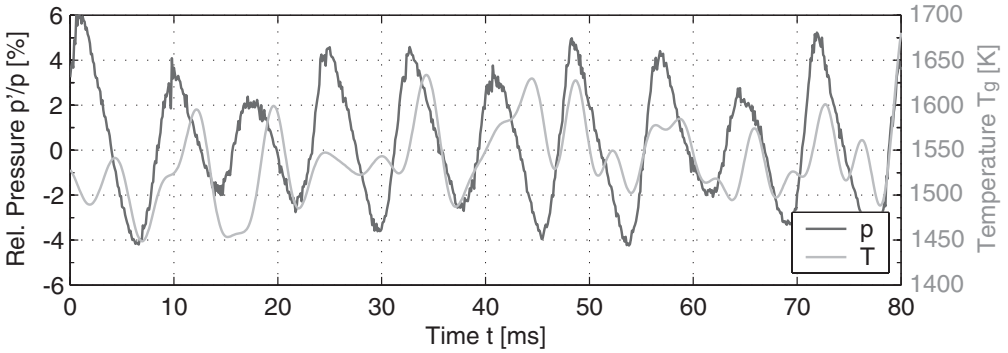

Fig. 6.5: Time traces of the relative combustor pressure p'/p (black) and the gas temperature near the nozzle inlet (Pos. T6 in Figure 4.16, grey).

The reconstructed mean temperature is 1545 K and deviates by about 2% from the adiabatic flame temperature for the overall equivalence ratio set ($\phi = 0.55, T_{ad} \approx 1580$ K). The oscillations of combustor pressure and temperature are nearly in phase, the temperature lags the pressure by 17°. The amplitude of the temperature fluctuation varies significantly from cycle to cycle, which can be attributed to the influence of wave dispersion induced by the combustor aerodynamics. The average amplitude of the temperature disturbance is 31 K.

In Table 6.1, the temperature perturbations are characterised by their Fourier amplitudes at the dominating oscillation frequency. Table 6.1 also shows the phase difference to the synchronously measured

Pos.	x [mm]	y [mm]	T'_g [K]	$\Delta\varphi_{OH*,T}$ [°]
T1	20	0	161	104
T3	75	0	102	109
T5	120	0	47	-120
T6a	275	0	31	123
T6b	275	15	38	89

Tab. 6.1: Propagation of the temperature waves in the combustor.

OH*-signal at the respective frequency. The y-coordinate is the distance from the centre axis of the combustor. T1 and T3 correspond to thermocouple positions directly up- and downstream of the main reaction zone, which is bound to the interval 30 mm $> x_f >$ 50 mm, as seen from Figure 6.1. At the nozzle inlet, two radial positions have been investigated, denoted by T6a and T6b.

A first important conclusion can be drawn from Table 6.1 with respect to the significance of the measured OH*-chemiluminescence as indicator for the heat release: The signal phases obtained for T1 and T2 in immediate vicinity up- and downstream to the reaction zone show that the temperature lags the OH*-chemiluminescence by about 105°. Taking into account minor phase delays due to convection between flame and thermocouples, the measured phase shift agrees with the expected relationship between harmonic fluctuations of the volumetric heat release $\dot{q}'$ and the temperature T'_g under isobaric conditions:

$$\dot{q}' e^{i\omega t} = \rho c_p \frac{d(T'_g e^{i\omega t})}{dt} = i\omega \rho c_p T'_g e^{i\omega t} \Rightarrow \arg(\dot{q}') - \arg(T'_g) = 90°. \tag{6.1}$$

For the diffusion flames investigated, it can now be concluded that the detected OH*-chemiluminescence gives significant phase information about the local heat release oscillation of the flame, $\dot{q}'$. This is helpful for the further evaluation, since the phase information is required for the assessment of the Rayleigh integral Eq. (1.1).

From Table 6.1 it can be further concluded that the dispersion of the entropy wave in the combustor is important. In vicinity of the flame, temperature pulsations of 161 K and 102 K are obtained. T3 is located between the two rows of mixing air injection, which explains the lower temperature amplitudes measured at this location. The entropy waves produced by the flame decay rapidly when travelling towards the combustor outlet. At the outlet, approximately 80% of their measured initial strength is dispersed. Comparing the phase shifts between the positions T2 and T6a, a convective time delay τ_s =8.3 ms from the flame to the nozzle can be deduced for the entropy wave. The resulting travelling speed is $u_s = 25$ m/s, which is close to the nominal bulk velocity of the gas in the combustor. This finding confirms the convective character of the waves.

The chemiluminescence recorded in Figure 6.1 reveals an inhomogeneous heat release over the combustion chamber height featuring increasing intensities near the combustor walls. Due to the highly inhomogeneous velocity field inside the combustor, a phase dispersion of the entropy waves is expected at the sonic nozzle. In order to assess the effective temperature inhomogeneity at the nozzle inlet, a measurement of the dynamic temperature has been conducted 15 mm off the centre axis, corresponding to about half the distance towards the upper rim of the convergent nozzle inlet (Pos. T6b). Under the influence of the hot spots near the combustor walls, the temperature amplitude increases by 20% compared to the value at the centre line (Pos. T6a). The relative phase difference of 34° between T6a and T6b is another indicator for the highly dispersed entropy wave at the combustor exit.

The theoretical value for the entropy-induced pressure amplitudes at the compact nozzle is given by Eq. (2.77). The measured temperature fluctuation at the nozzle inlet is too low to produce the pressure amplitudes of Figure 6.5. Furthermore, the pressure and temperature perturbations near the choked outlet in Figure 6.5 oscillate nearly in phase, which disagrees with the theory predicting an expansion wave and therefore a phase shift of 180° between T' and p'.

6.1.2 Flame Tube Extension

In order to decouple the influence of entropy waves on the combustor acoustics, the choked nozzle at the combustor outlet was replaced by the open-ended resonance tube, imposing a comparably high outlet impedance on the combustion chamber exit. Figure 6.6 shows the amplitude spectrum of the occurring instability mode.

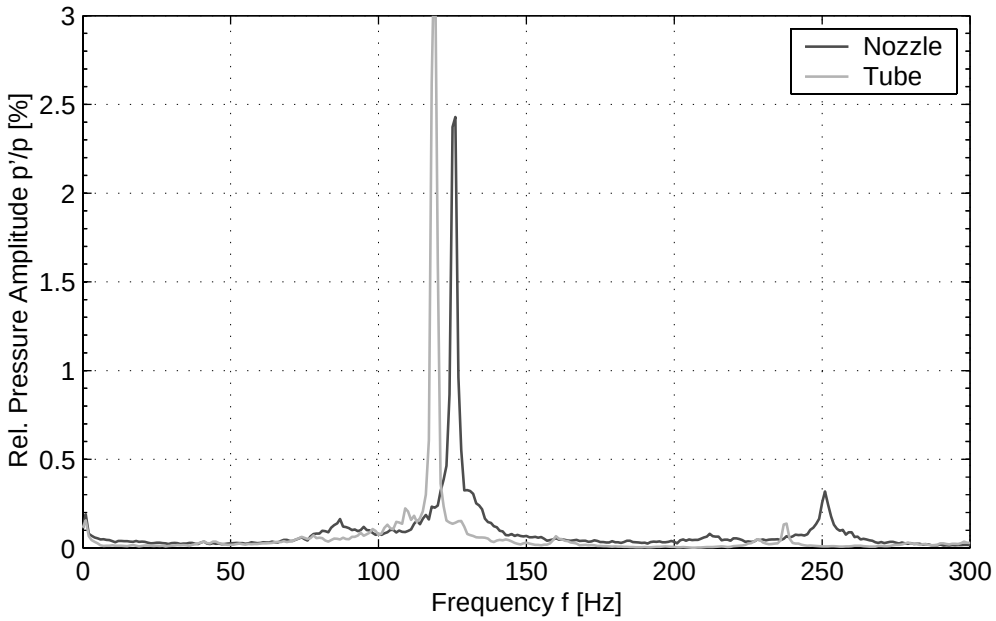

Fig. 6.6: Fourier spectra of the relative pressure amplitudes obtained for operation with Venturi nozzle (black) and resonance tube (grey).

The relative pressure amplitude with resonance tube (grey) rises to about 3% of the static combustor pressure, being about 0.6 percentage points higher than the oscillation obtained in the presence of the nozzle (black). The peak frequency is 118 Hz, which is only 8 Hz below the instability frequency of the choked case. Both amplitudes are nominally higher than the static pressure drop across the injector, which is 2.3%. When taking the pressure fluctuations upstream of the injector into account, which oscillate in phase, the maximum effective oscillation amplitude across the burner reduces to 2.2% and thus falls below the static value.

The time traces of pressure and OH*-chemiluminescence are plotted in Figure 6.7. The oscillatory behaviour is very similar to the case with nozzle (Figure 6.2). The heat release of the flame leads the combustor pressure by 62°, such that the Rayleigh criterion Eq. (1.1) is fulfilled. However, the oscillations exhibit a lower beat compared to Figure 6.2.

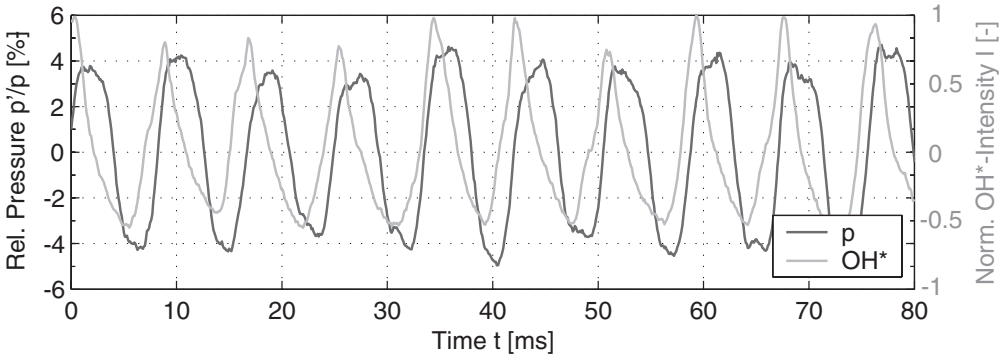

Fig. 6.7: Time traces of the relative combustor pressure p'/p (grey) and the normalised OH*-chemiluminescence (black) obtained with the resonance tube.

6.1.3 Consequences for the Excitation Mechanism

A pressure feedback by the reflection of entropy waves at the nozzle can be excluded for the resonance tube. The similarity of the results proves that entropy waves do not play a significant role for the occurrence of the low-frequency combustion instability observed. It can thus be concluded that the dominant mode encountered is purely thermoacoustic. The measured phase shifts $\Delta\varphi$ between heat release and pressure are 62° for the flame tube and 53° for the choked nozzle, thus lying within the limits for driving given by the Rayleigh criterion.

For both test configurations, $\Delta\varphi$ is thus very similar for comparable injector pressure drops and identical equivalence ratios. With respect to the limit frequencies, a time delay τ_d between the pressure minimum and the heat release maximum can be calculated, which is

almost identical. τ_d, as illustrated in Figure 6.8, becomes 2.8 ms for the configuration with nozzle and 2.78 ms for that with flame tube.

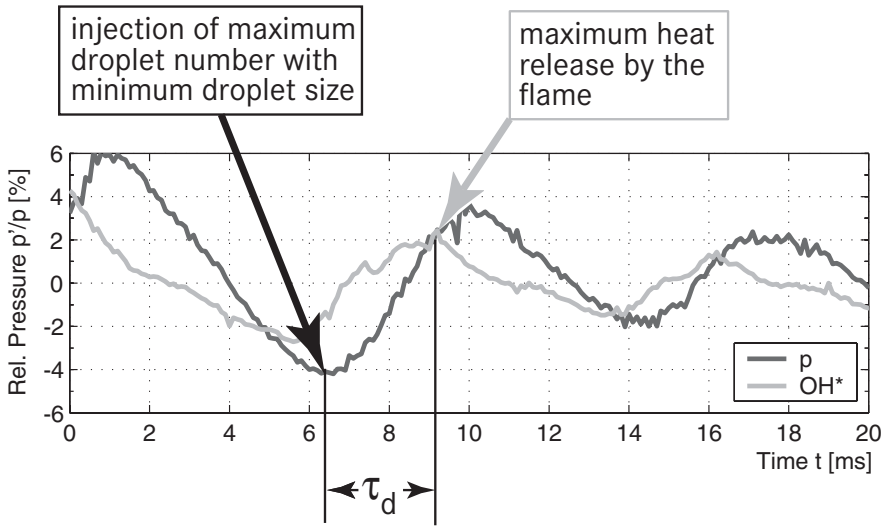

Fig. 6.8: Interpretation of the dependency between combustor pressure and heat release with respect to the time scales of droplet convection. Figure 6.8 is a close-up view of Figure 6.2.

As shown above, the point of minimum combustor pressure coincides with the generation of the smallest SMD in the oscillation cycle. The associated droplet number must be maximum, since for negligible admittance of the fuel side, the fuel mass flow rates remain constant. Estimations on the basis of the PIV-measurements in Figure 6.4 have shown that τ_d represents a measure for the average delay time of the droplet cluster with minimum SMD, required for the convection of the droplets from the injector to the flame.

As a consequence, the sensitivity of the atomiser to changing air velocities impacts the heat release by producing a higher number of smaller droplets with correspondingly faster burnout times, as already discussed in context of Eq. (5.11). The global heat release rate will thus rise with the finer spray obtained for low dynamic pressures in the combustion chamber. The height of the heat release peak for each oscillation cycle is then intrinsically related to the depth of the preceding drop of the dynamic combustor pressure. This explains the

similarity of the amplitude modulation of p' and $\dot{q}'$ encountered in Figure 6.2.

It follows that the injector and in particular the convective delay times in the primary zone determine the tendency for self-excitation. The necessary condition for the instability is a high impedance Z_{cc} at the combustion chamber outlet. It is imposed by both the sonic nozzle and the flame tube, as illustrated in Figure 6.9. The acoustic wavelengths associated with rumble are several metres and exceed by far the length l of the unextended combustion chamber. Hence, the low-frequency oscillations of the combustor pressure take place in the bulk mode. A high value for Z_{cc} will therefore imply a high impedance at the injector Z_{inj}. In this case, the elevated pressure amplitudes at the injector outlet considerably modulate the injection velocity and the droplet size.

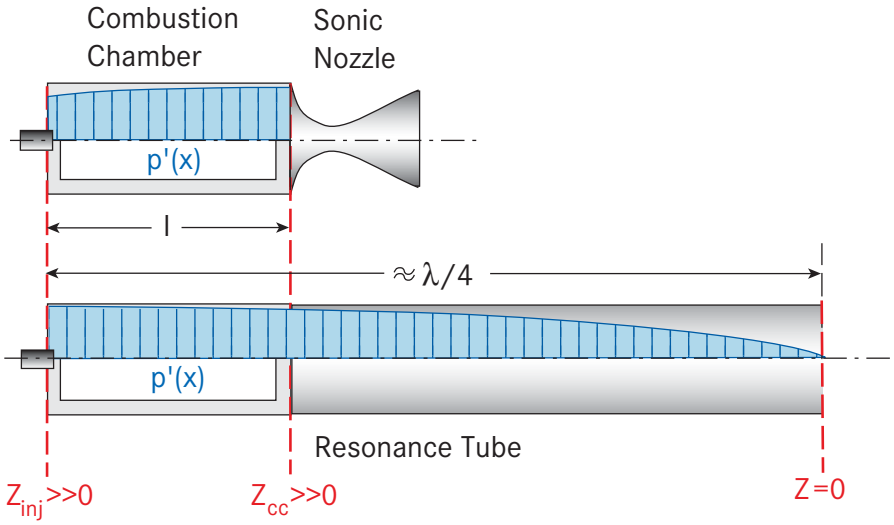

Fig. 6.9: Bulk mode pressure oscillations in the combustion chamber.

For the test configuration with nozzle, the reflected pressure disturbance related to the entropy wave interferes with the self-excited thermoacoustic mode. This explains the beat obtained in the pressure trace of Figure 6.2, which leads to a relative variation of the amplitudes by about 1.5 to 2 percentage points. In the Fourier spectrum for the nozzle shown in Figure 6.6, a minor pressure peak at

85 Hz is found, which does not appear for the resonance tube and which is likely to be related to the influence of entropy waves.

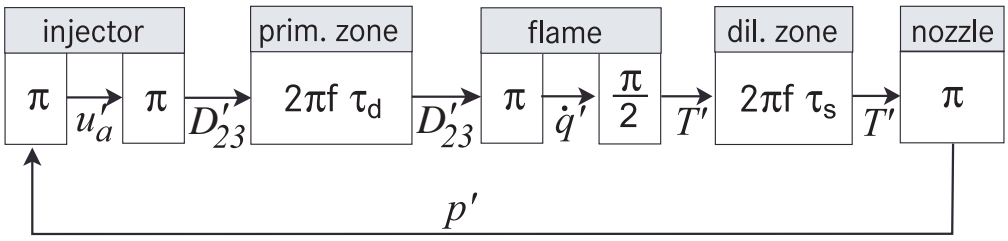

Fig. 6.10: Schematic of the feedback cycle for entropy waves including the phase relations between the parameters that influence the combustion process.

Figure 6.10 shows a schematic of the feedback cycle for the entropy waves and the phase relationships between the impacting parameters. Following Eq. (5.11), the air velocity perturbations at the burner u_a' inversely alter the SMD, inducing a phase-shift of π. The droplet delay time in the primary zone results in a frequency dependent phase delay $\Delta\varphi = 2\pi f \tau_d$, as previously discussed. Accounting for the experimental findings that (1) the heat release rate increases with smaller droplet diameters and that (2) a 90°-phase shift between heat release and temperature is obtained, the flame turns the total phase by $3/2\pi$. Similar to the droplet delay times in the primary zone, the convection of the resulting entropy waves in the dilution zone lead to a phase shift of $2\pi f \tau_s$. At the nozzle, the reflected pressure wave lags the impinging entropy disturbance by π, according to Eq. (2.77), and alters the injector pressure drop with negligible time and phase delay. The pressure drop again inversely modulates the injection velocities, closing the feedback loop.

For the measured τ_d =2.8 ms and τ_s =8.3 ms, the matching condition

$$\sum_i \Delta\varphi_i = n \cdot 2\pi \qquad (n = 1, 2, 3, \ldots) \tag{6.2}$$

is fulfilled for f_s =68 Hz. It has been shown in section 2.4.2 that the entropy-related instability frequency is prone to rise under effects of distributed heat release [Dow95]. With respect to the model

simplifications, the above schematic provides a suitable explanation and shows that the oscillation of the entropy can indeed be expected in the frequency range of the second peak at 85 Hz (Figure 6.6). The relative strength of the entropy peak in the pressure spectrum is small as a consequence of phase dispersion of the entropy waves. This proves that the flow conditions in the combustor are far from being one-dimensional.

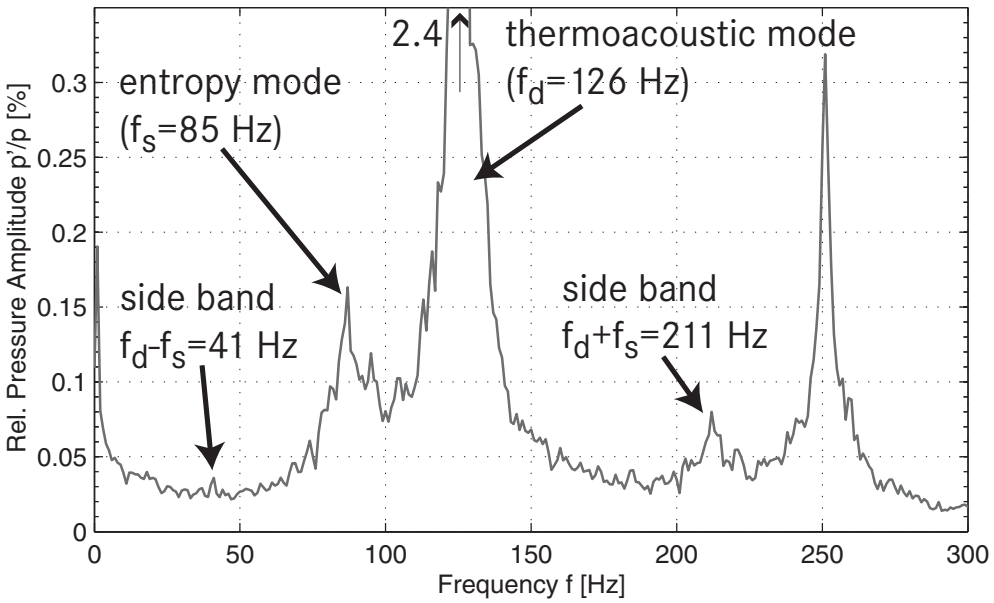

Fig. 6.11: Side bands of the relative pressure amplitude for the limit cycle of the self-excited oscillation with Venturi. The graph is a close-up view of Figure 6.6.

As shown in Figure 6.11, the fundamental thermoacoustic mode at 126 Hz and its first harmonic at 252 Hz are dominating the pressure spectrum. The separate pressure peak at 85 Hz indicates that the entropy-related pressure perturbations coexist with the thermoacoustic oscillations in the combustion chamber.

The weaker entropy wave is coupled with the dominating thermoacoustic mode by the oscillating heat release of the flame. The side bands that can be found in the amplitude spectrum (Figure 6.11) are a result of the non-linearity of the limit cycle. The peak frequencies

of the side bands at 211 Hz and 41 Hz correspond to the combination frequencies of the entropy and the thermoacoustic oscillation, leading to the amplitude modulation in Figure 6.2.

6.2 General Instability Behaviour

In this subsection, the limit cycle properties of the self-excited oscillation are analysed, based on a parametric variation of the fuel and the air mass flow. The relative air distribution in the combustor is maintained. The time-domain recordings of the pressure limit cycle are characterised by the dominant oscillation frequency f and the amplitudes of the dynamic pressure drop fluctuations $\Delta p'$ across the burner. The data shown are averaged over 15 independent measurement sequences with 10000 samples each. The dynamic pressure drop was obtained by subtracting the measured pressure oscillations at the injector inlet from the dynamic combustor pressure. In general, both pressures were oscillating in phase and the upstream pressure did not exceed 25% of the corresponding pressure amplitude in the combustor.

The limit cycle properties are influenced by the acoustic system as a whole, comparable to that shown in Figure 1.4. The nominal operating parameters will influence the system as follows:

- **Overall equivalence ratio** ϕ: impacts the flame stability, the temperature rise across the flame and the speed of sound downstream of the flame according to Eq. (2.16).

- **Relative pressure drop across the injector** $\Delta p/p$: determines the air injection velocities u_a. Using the steady state equation of the ideal gas

$$\rho = \frac{p}{RT}, \tag{6.3}$$

Eq. (5.1) becomes

$$u_a = \sqrt{\frac{2}{1+\zeta_{inj}} R_a T_a \frac{\Delta p}{p}}. \tag{6.4}$$

- **Absolute pressure drop across the injector** Δp: is related to the specific momentum flux $\rho_a u_a^2$ of the atomising air by Eq. (5.1). $\rho_a u_a^2$ is part of the Weber number and thus influences the droplet sizes produced following Eq. (5.4).

Using the sonic nozzle, a pressure rise inside the combustor could not be avoided under varying air and fuel mass flows. For the open flame tube, the static combustor pressure was maintained at atmospheric conditions.

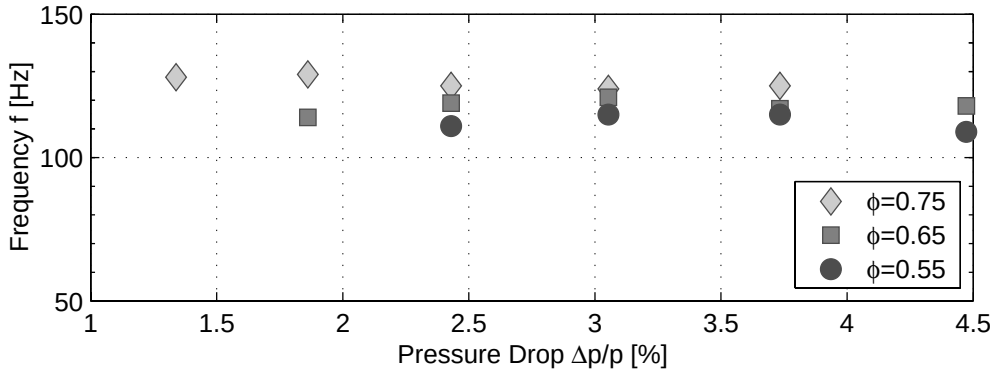

Fig. 6.12: Limit cycle frequencies of the combustion oscillations with extended flame tube as a function of the normalised static pressure drop $\Delta p/p$ of the injector.

Figure 6.12 shows the limit cycle frequencies f for the experiments with open flame tube, being parameterised with the overall equivalence ratio ϕ. f ranges between 108 Hz and 131 Hz. The general dependence of f on $\Delta p/p$ is small. For air-fuel ratios approaching stoichiometry ($\phi = 0.75$), the limit frequencies obtained are highest which can be explained with the higher speed of sound in the flame tube acting as a resonator. In accordance with Eq. (2.16), the measured limit frequencies scale fairly well with the square

root of the adiabatic flame temperatures: Comparing the values for $\phi = 0.75$ ($T_{ad} = 2287$ K, $f \approx 131$ Hz) and $\phi = 0.55$ ($T_{ad} = 1614$ K, $f \approx 109$ Hz), a temperature and frequency ratio of 1.42 and 1.2, respectively, is obtained. For the combustor with flame tube extension, the flame is small compared to its axial length. The thermoacoustic properties of the flame tube thus dominate the overall system, and the oscillation frequency is mainly determined by the flue gas temperature.

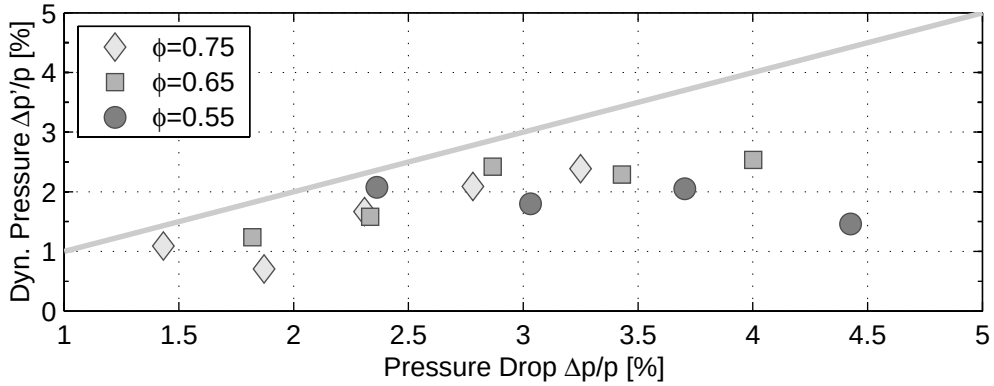

Fig. 6.13: Amplitude of the dynamic pressure drop fluctuations $\Delta p'/p$ as a function of the normalised static pressure drop of the injector. The grey line indicates the identity $\Delta p'/p = \Delta p/p$.

Figure 6.13 shows the oscillation amplitudes of the limit cycle. The grey line delimits the region where dynamic pressure oscillations would exceed the static pressure drop across the injector, leading to flow reversal through the burner. According to Figure 6.13, the oscillation amplitudes lie below this line. The static pressure loss characteristics of the injector thus provides an upper limit for the attainable oscillation amplitudes. In chapter 1.2, the non-linear effects limiting self-excited combustion oscillations were discussed. The measurement data indicate that the break-down of the air injection and the deceleration of fuel transport to the flame under conditions of rising combustor pressures controls the rumble amplitudes attainable in the limit cycle.

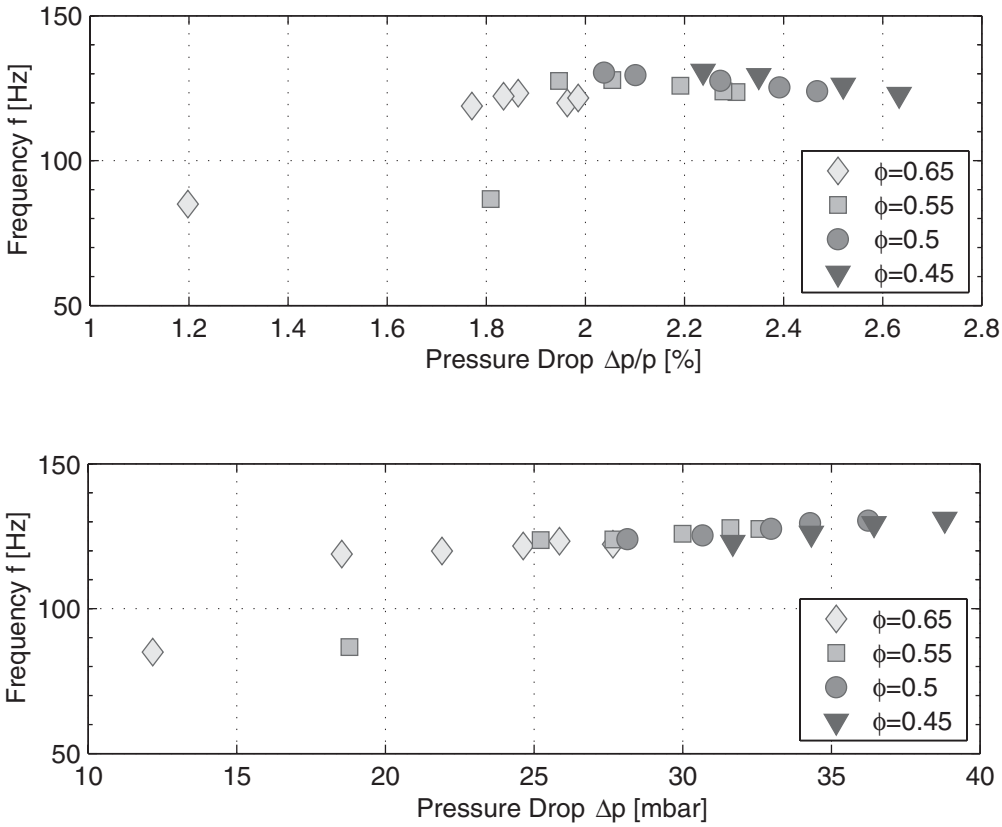

Fig. 6.14: Limit cycle properties of the combustion oscillations with Venturi. Limit cycle frequencies over the static pressure drop $\Delta p/p$ of the injector (top) and over the absolute pressure drop over the injector Δp (bottom).

The limit cycle frequencies for the injector with the sonic nozzle are shown in Figure 6.14. Similar to the flame tube experiments, the limit frequency ranges between 113 Hz and 131 Hz for $\Delta p/p > 1.8\%$. Soot deposition was observed at the water-cooled nozzle, which indicates local quenching and incomplete spray combustion, becoming particularly important under conditions of low Δp. As a consequence, the influence of ϕ and the exhaust gas temperature on the limit frequencies are low. More specifically, richer mixtures do not lead to higher limit frequencies, and varying frequencies can also be observed for constant equivalence ratios, as shown in the upper graph of Figure 6.14.

It can be seen from Figure 6.14 that for the investigated operating conditions the limit frequency is essentially determined by the *absolute* pressure drop of the injector Δp and thus by the average droplet size D_{32} produced. D_{32} again is linked with the time scales for fuel transport, evaporation and combustion, which in turn influence the flame position and the flame length. The work of SUJITH ET AL. [SWJZ00] has shown that the presence of an acoustic field enhances the evaporation rates by providing relative motion between gas phase oscillations and the liquid phase. Droplet burning rates are further known to increase by up to 20% in an acoustic velocity antinode [DMJ98, GSK01]. Both effects particularly enhance the consumption of the smallest droplets and the heat released by the flame. The dominating influence of D_{32} and Δp encountered in the experiments is another indicator for the significance of the processes in the primary-zone on the overall acoustic behaviour. Entropy-related instabilities would have been expected to scale with the flow velocity in the combustor and thus rather with $\Delta p/p$. This also confirms the interpretation given in section 6.1.3 for a wider range of operating conditions.

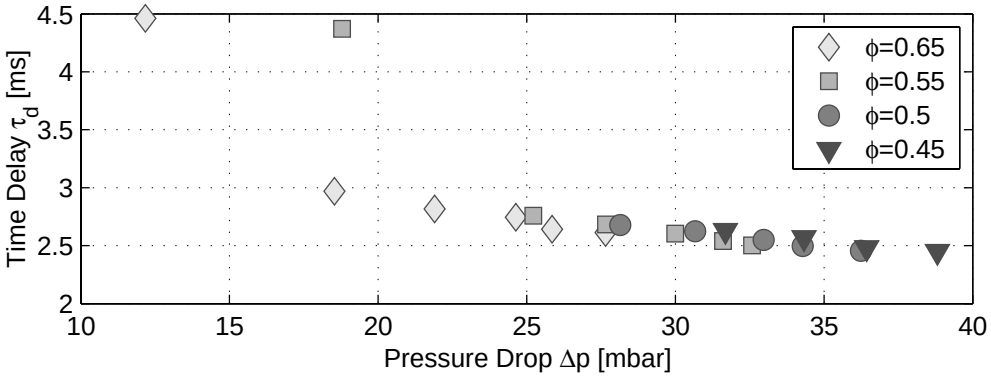

Fig. 6.15: Limit cycle properties of the combustion oscillations with Venturi. Convective time delay τ_d as a function of the static pressure drop Δp of the injector.

Figure 6.15 shows the convective time delays τ_d in the primary zone as a function of Δp. The values for τ_d are obtained by evaluating the phase shift between the measured pressures and heat release rates

according to Figure 6.8. τ_d continuously decreases by approximately 20% from 3 ms to 2.4 ms with rising pressure drop, which agrees with the expectations. For leaner mixtures, the time delays tend to be higher under the influence of rising flame stand-off distances and lower temperatures of the recirculating gas.

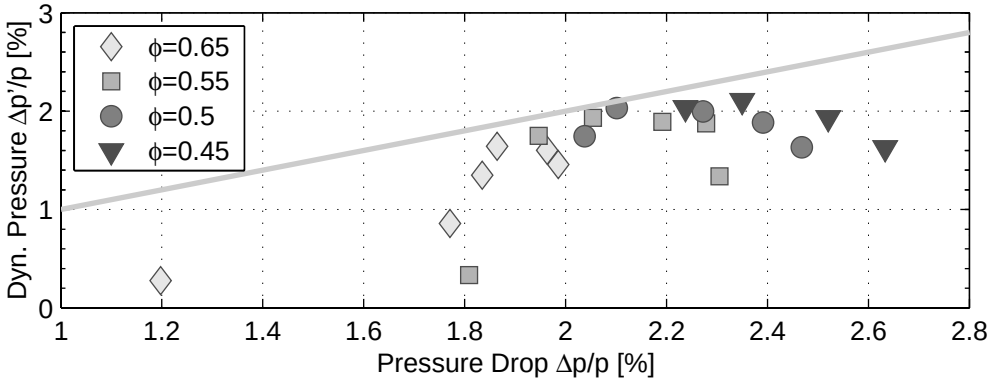

Fig. 6.16: Normalised pressure amplitude $\Delta p'/p$ over the normalised static pressure drop $\Delta p/p$.

The instability amplitude observed is comparable to the configuration with flame tube. Figure 6.16 shows the limit imposed on the pulsation amplitude by the static pressure loss characteristics of the burner and the impact of the fuel transport on the attainable instability amplitude.

6.2.1 Operation under Low Static Pressure Drops

In Figure 6.14, a sudden decrease in the limit frequency is observed for very low pressure drops ($\Delta p < 20$ mbar), being characterised by limit cycle frequencies below 90Hz and very low limit cycle amplitudes below $\Delta p'/p < 0.5\%$ (Figure 6.16). Figure 6.17 shows an image of a spray flame being operated at $\Delta p = 12$ mbar[22]. The large droplet sizes produced by the injector at these pressure drops lead to an asymmetric flame. It predominantly burns at the upper rim of the combustion chamber and extends over the entire combustor length.

[22] A picture of the flame at higher pressure drops ($\Delta p = 32$ mbar) is shown in Figure 4.16.

The flame asymmetry is related to the low fuel flow rates, causing an inhomogeneous fuel distribution on the circumferential prefilmer lip of the injector. Due to the long flame, the quenching by the mixing air is ineffective.

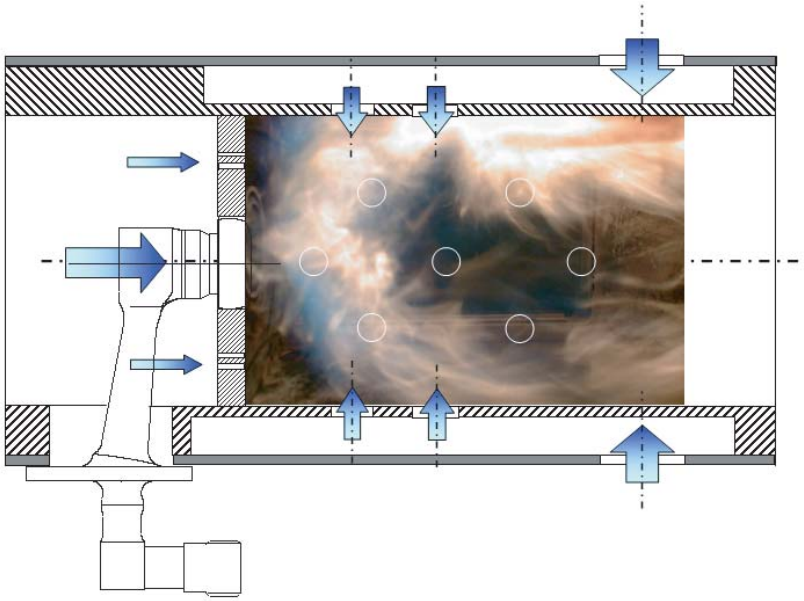

Fig. 6.17: Typical asymmetrical spray flame obtained for low pressure drops ($\Delta p = 12$ mbar) at $\phi = 0.65$. The measurement positions of the thermocouple probes (see section 6.3) are indicated by the white circles.

Figure 6.18 shows the OH*-chemiluminescence for an oscillation period at $\Delta p = 12$ mbar. The phase angle φ again refers to the phase of maximum heat release. The reaction zone is asymmetric, primarily burning on the upper side of the combustor in the vicinity of the walls. The heat release fluctuations are not bound to the primary zone of the combustor but gradually develop all along the combustion chamber, including the dilution zone. A flame propagation towards the injector can not be observed, due to the lower pressure amplitudes, but a modulation in fuel injection exists.

The amplitude spectrum of the oscillating combustor pressure is plotted in Figure 6.19 (black line). The energy of the self-excited oscillation is distributed within a broad frequency band between 50 Hz and

120 Hz. Two peaks can be discerned at 87 Hz, which is the global maximum, and at 107 Hz. For higher pressure drops, the dominating pressure peak was associated with the typical convective delay times

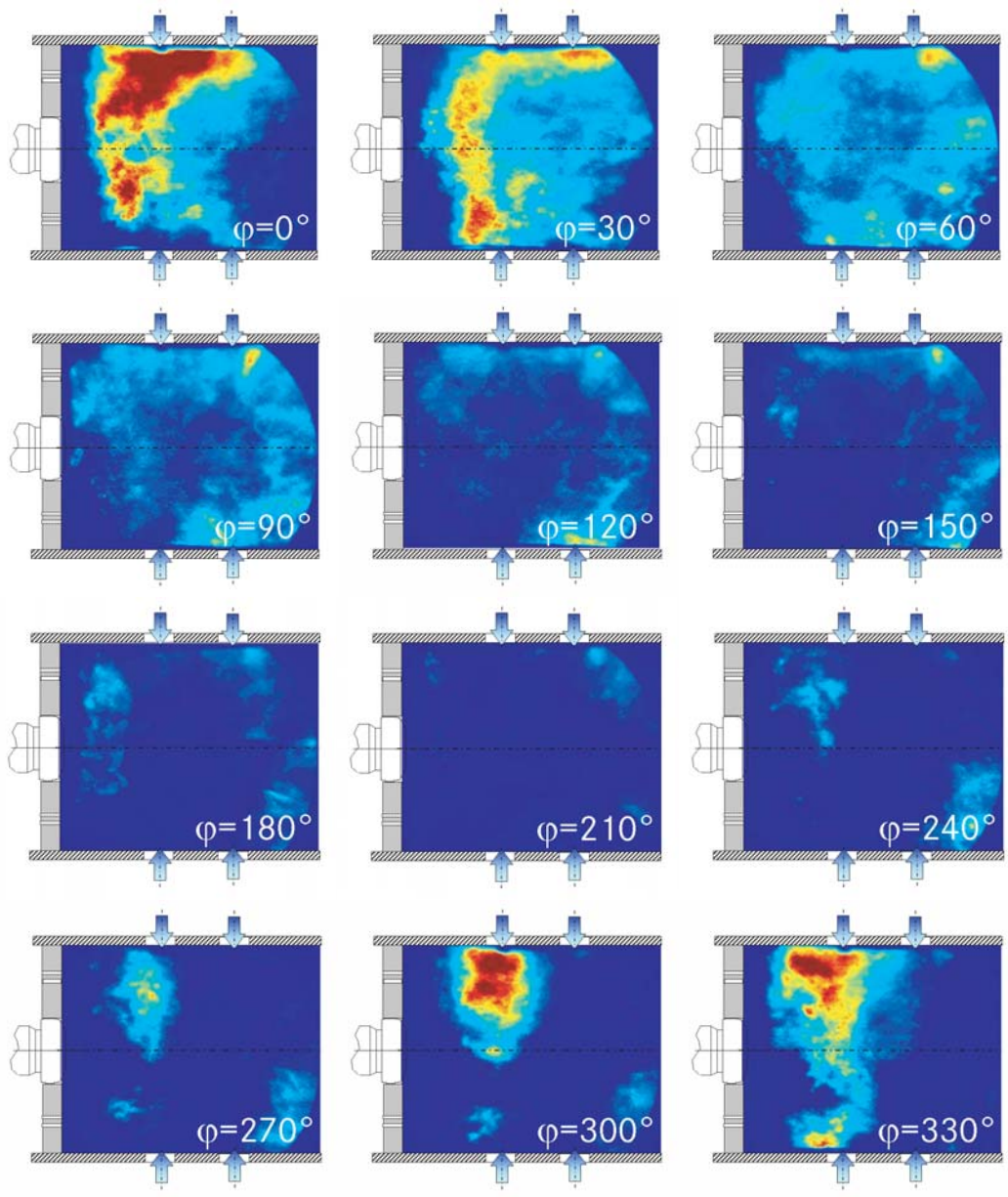

Fig. 6.18: High speed camera recording of the flame OH*-chemiluminescence during one combustion oscillation cycle at 87 Hz under very low pressure drop conditions ($\Delta p = 12$ mbar).

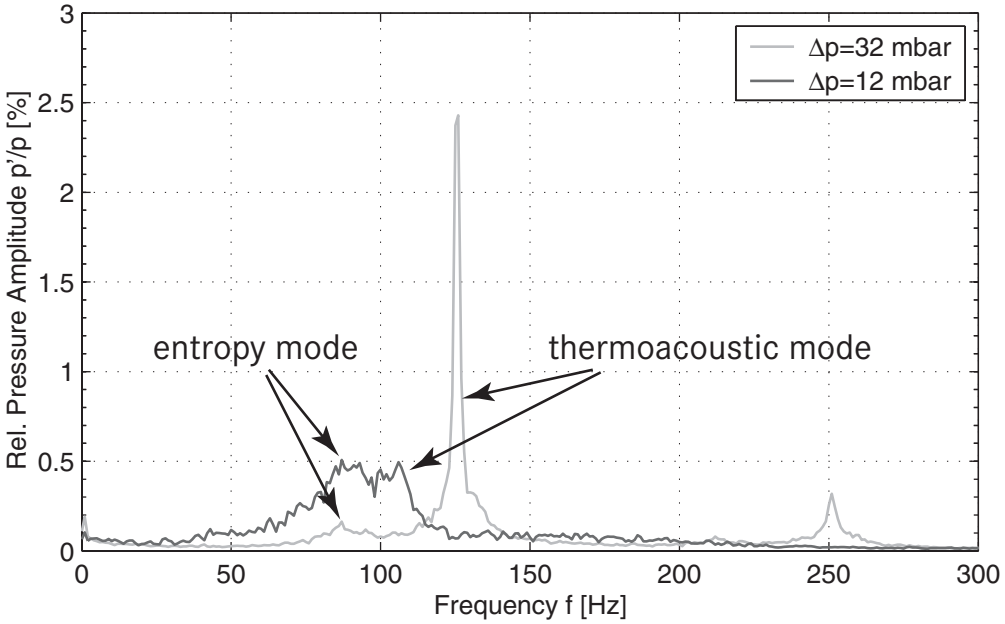

Fig. 6.19: Amplitude spectra of the relative pressure amplitudes obtained for the operation with choked nozzle for a pressure drop over the burner of $\Delta p = 12$ mbar (black) and $\Delta p = 32$ mbar (grey).

of the smallest droplets. As a consequence, the flat and broad amplitude spectrum for low Δp indicates a larger spread of droplet sizes, which contributes to the relatively weak self-excited combustion oscillation. This complies with the extended reaction zone observed in Figure 6.18. Comparing the amplitude spectra for different pressure drops (Figure 6.19), the peak at 85 Hz for $\Delta p = 12$ mbar coincides with the sub-peak for $\Delta p = 32$ mbar, which was found to be entropy induced (section 6.1.3). On the other hand, the second pressure peak at 107 Hz for $\Delta p = 12$ mbar coincides with a frequency which would be expected to dominate when extrapolating the thermoacoustic modes in Figure 6.14 towards lower pressure drops, as shown in Figure 6.20.

The logical explanation for this behaviour is a mode shift. For elevated pressure drops and compact flames, entropy waves are negligible for instability (section 6.1). For very low pressure drops however, larger droplets and longer flames are obtained and entropy waves may

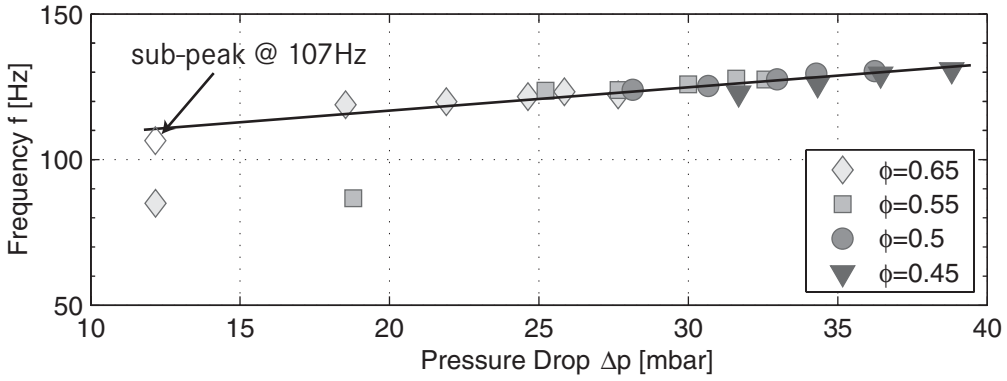

Fig. 6.20: Reproduction of Figure 6.14, taking into account the sub-peak encountered in Figure 6.19.

thus play a more pronounced role. This makes sense when taking into consideration that the dispersion induced by the opposing mixing air jets is probably smaller near the combustor walls, where the majority of the fuel burns off under those conditions. This hypothesis will be further assessed in the following chapter on the basis of the temperature measurements.

6.3 Entropy Waves

6.3.1 Mean Temperature Distribution

Figures 6.21 – 6.23 show the mean gas temperatures, which were obtained in the RQL-combustor at the measurement locations shown in Table 4.2. The measurements were conducted in the open combustion chamber without extension in the absence of self-excitation. The mean gas temperature T_g is given for different injector pressure drops Δp. ϕ is the overall equivalence ratio, taking into account the primary and the mixing air.

The mean temperatures on the combustor axis are shown in Figure 6.21. The temperatures at T3 immediately downstream of the flame are considerably lower than the adiabatic temperature, particularly for $\phi > 0.4$. A considerable deviation is obtained for $\phi > 0.45$: For

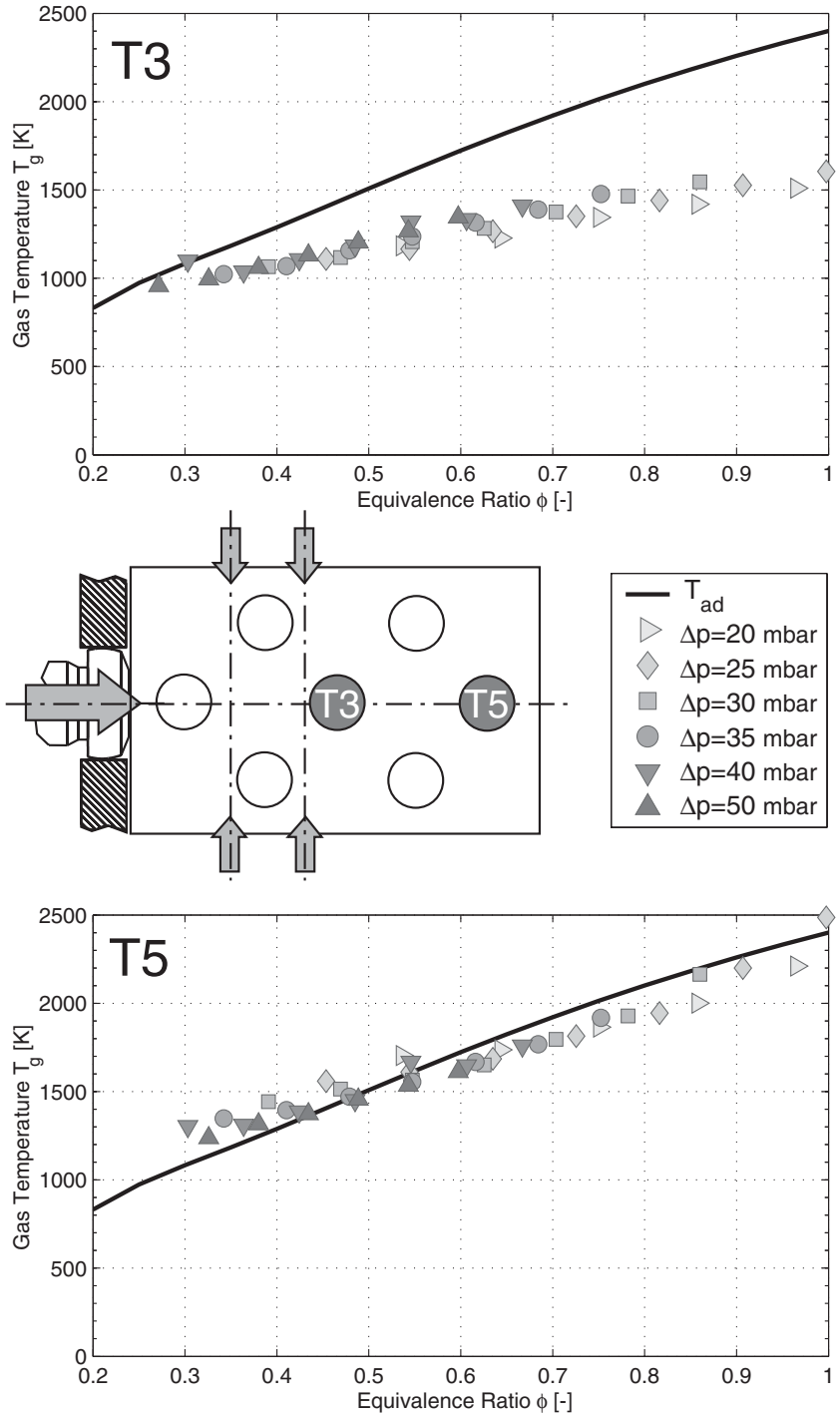

Fig. 6.21: Mean gas temperatures in the centre plane of the combustor at Pos. T3 and T5 as a function of the overall equivalence ratio ϕ and the static pressure drop Δp.

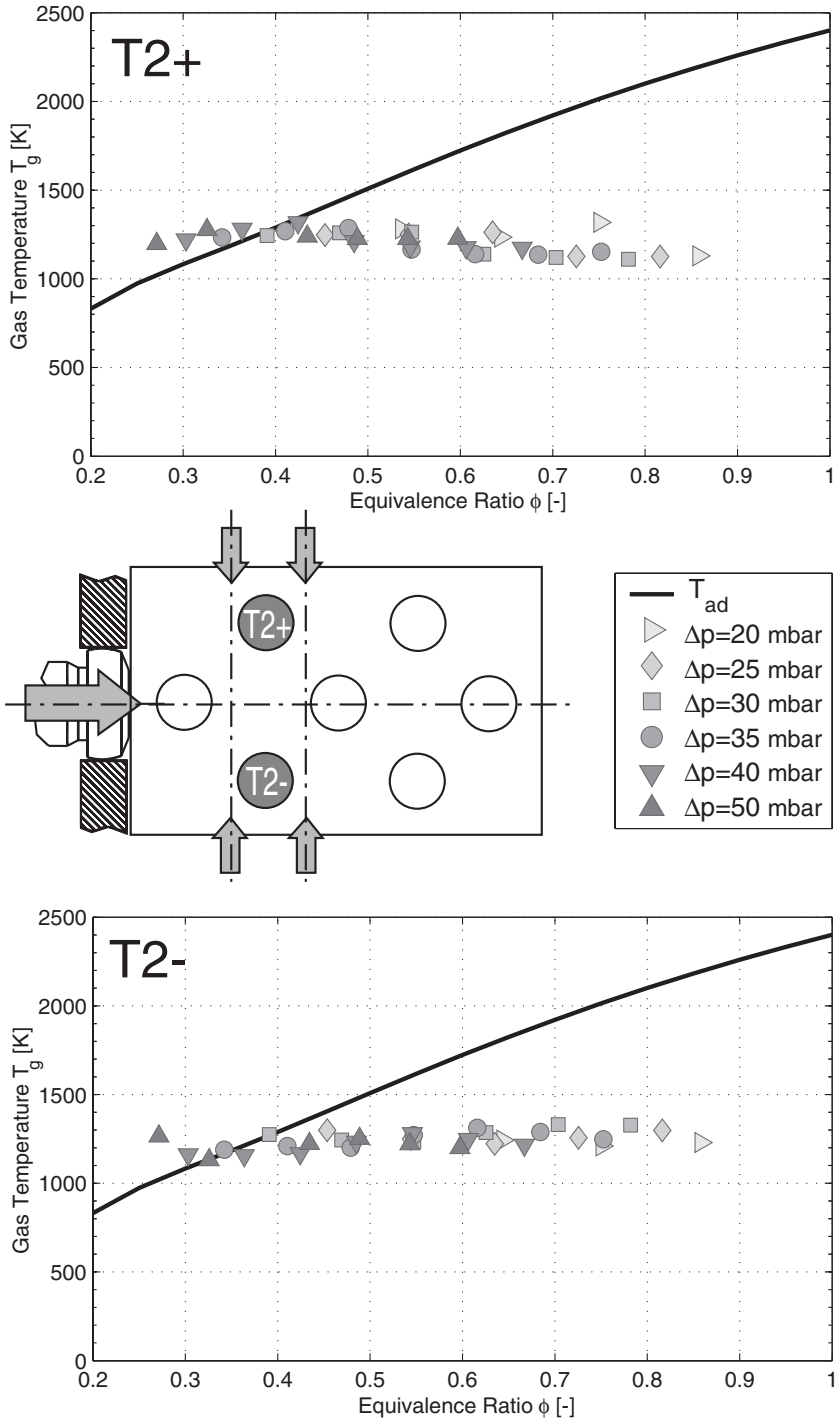

Fig. 6.22: Mean gas temperatures in the centre plane of the combustor at Pos. T2+ and T2– as a function of the overall equivalence ratio ϕ and the static pressure drop Δp.

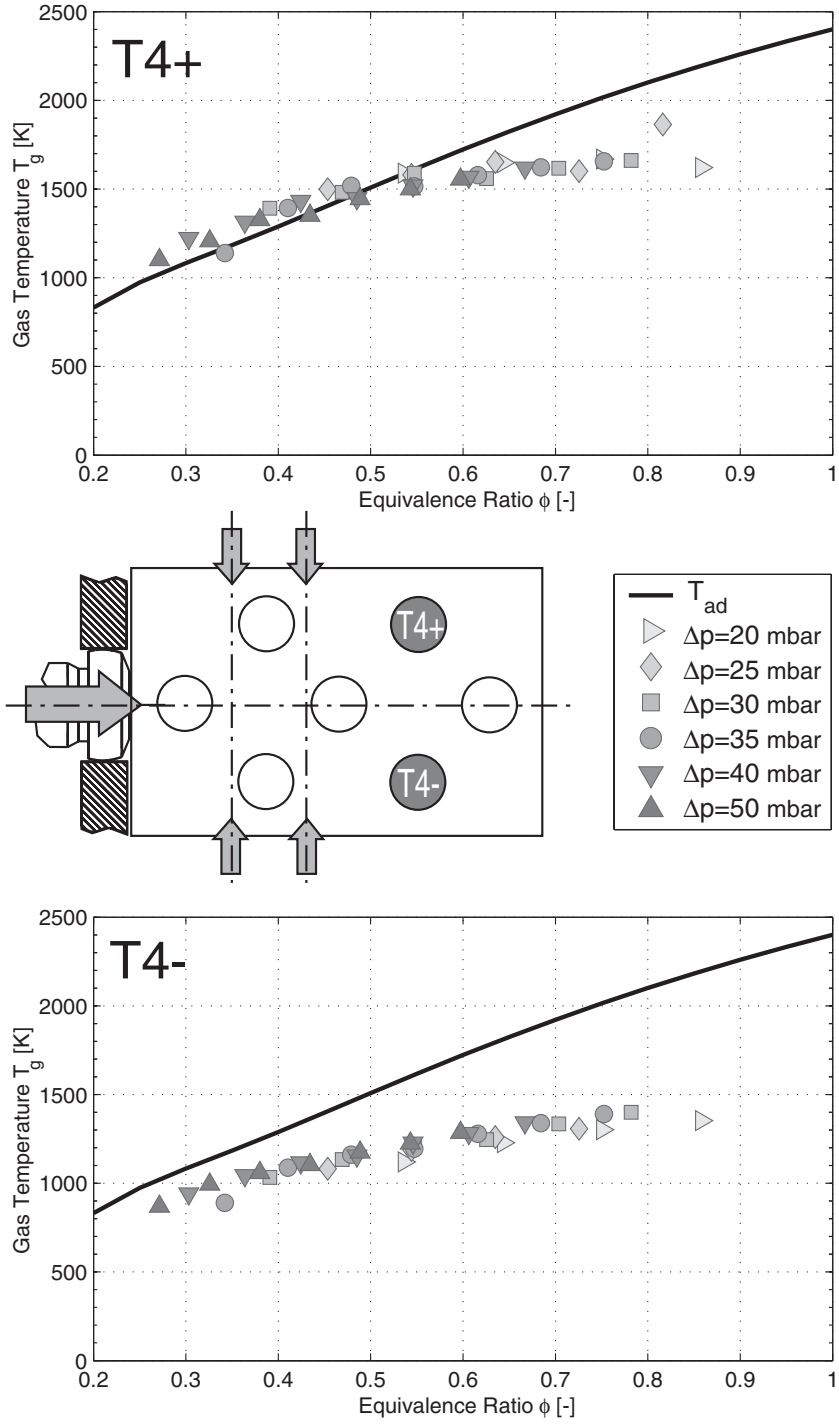

Fig. 6.23: Mean gas temperatures in the centre plane of the combustor at Pos. T4+ and T4– as a function of the overall equivalence ratio ϕ and the static pressure drop Δp.

rising Δp, the measured mean temperatures increase by approximately 250 K. This dependency of the local gas temperature is primarily influenced by the droplet size which in turn determines the local fuel evaporation and combustion rates. For larger droplets (i.e. lower Δp) less fuel is consumed up to that point. A second reason for the dependency of T_g on Δp can be found in the inhomogeneous distribution of the heat release zones in the combustor. As discussed in section 6.2.1, the flame burns closer to the combustor walls for decreasing Δp (Figure 6.17). Thus, decreasing temperatures are obtained on the central axis for lower pressure drops. A substantial increase of the gas temperature is obtained in downstream direction at the measurement location T5. Located 45 mm downstream of T3, the measured gas temperatures have approached the adiabatic flame temperature. For lower values of Δp, the attainable temperature again tends to be lower, particularly for ϕ approaching unity.

The temperatures at positions T2+ and T2– are shown in Figure 6.22. The measurement points are directly located in the cone of the burning spray (Figure 4.16), approximately 5 mm downstream of the first row of mixing air injection. Nearly identical temperatures are obtained for both measurement locations, corresponding to the adiabatic flame temperature for $\phi \approx 0.4$. The air distribution obtained in section 3.3.2 has shown that 43% of the air enters the combustor through the front panel. An overall equivalence ratio of $\phi = 0.43$ thus nominally equals stoichiometric conditions in the primary zone $\phi_{prim} = 1$, when neglecting the contribution of the mixing air. As a consequence, the measured temperature distribution can be understood as rapid quenching of a stoichiometric spray flame in the primary zone by the mixing air.

The temperature at the measurement points T4+/– in the dilution sector of the combustor is shown in Figure 6.23. As can be seen from Figures 6.23 and 6.22, a gradual adaptation of the gas temperature to the adiabatic value is encountered with increasing downstream position. This effect is clearly visible for operating conditions featuring overall equivalence ratios above 0.43, which corresponds to a nomi-

nally rich primary zone with $\phi_{prim} > 1$. In Figure 6.23, asymmetries of the local temperature distribution are observed between T4+ and T4–: Higher temperatures are obtained on the upper combustor side at T4+, exceeding the temperatures at T4– by up to 300 K. This behaviour can be explained by the tendency for asymmetrical flames with lower fuel and air flow rates, as discussed in sections 5.2.1 and 6.2.1. Figure 6.17 has shown that for low Δp, rising combustion rates are obtained near the upper combustion chamber wall, resulting in locally higher temperatures. Increasing flame asymmetry also tends to lower the gas temperatures at T4– for decreasing Δp.

6.3.2 Entropy Waves under Self-Excitation

The generation of the entropy waves in the combustor was investigated for the following operating conditions:

1. $\Delta p = 12$ mbar, $\phi = 0.55$
2. $\Delta p = 32$ mbar, $\phi = 0.55$
3. $\Delta p = 42$ mbar, $\phi = 0.44$

The first operating condition represents the very low pressure drops discussed in section 6.2.1, where the entropy wave are prone to dominate the overall pressure response. The second case corresponds to the test condition of section 6.1.1. The last operating point was introduced to investigate the oscillations at high pressure drop and lean equivalence ratio, featuring a very compact flame.

In Figure 6.24, the mean temperatures are given, which were captured at the measurement points T1 to T6. T6,0 corresponds to the measurement location at the nozzle inlet, on the centre axis, whereas T6,15 was measured with 15 mm offset. The upper graph shows the absolute temperature values, while in the lower graph the measured temperatures were normalised with the adiabatic flame temperature, determined by the equivalence ratio ϕ.

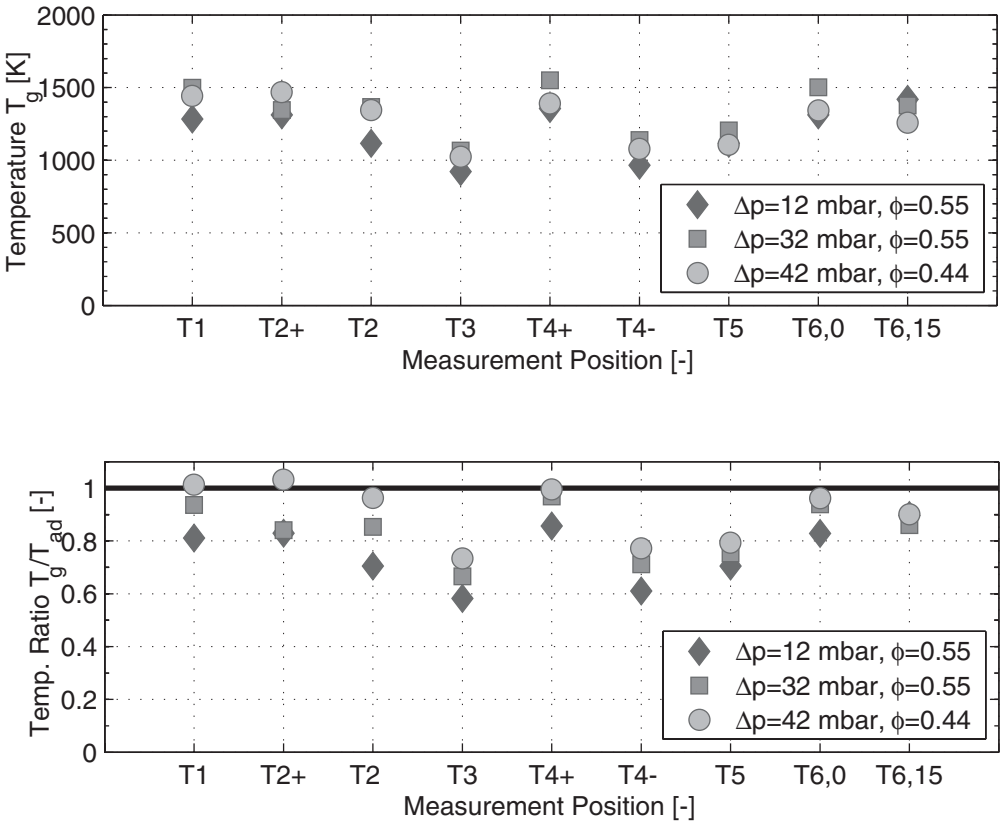

Fig. 6.24: Mean gas temperatures T_g obtained at the different measurement points under self-excitation. Absolute values (upper graph) and temperature ratio T_g/T_{ad} with the adiabatic temperature at the respective operating condition (lower graph).

The measured data agree well with the steady temperature characteristics: For $\phi = 0.44$, stoichiometric temperatures are obtained in the primary zone (T1, T2). T3 reveals a reduced temperature level, being directly influenced by the mixing air. Temperature differences are encountered between T4+ and T4– corresponding to Figure 6.23. The dilution zone T5 features slightly lower mean temperatures compared to the steady case. Near the nozzle, the temperature level is again near-adiabatic. The temperature rise between T3 and T6 indicates an inhomogeneous temperature distribution and a non-homentropic dilution zone of the combustor. For the other operating conditions, a similar behaviour is observed. However, with decreasing pressure

drop, the temperatures in the primary zone are successively lowered down to 80% of the adiabatic value, since a considerable fraction of the droplets burns in the dilution zone. Close to the nozzle, a temperature level of nearly 90% of the adiabatic temperature is encountered, being common to all investigated operating points.

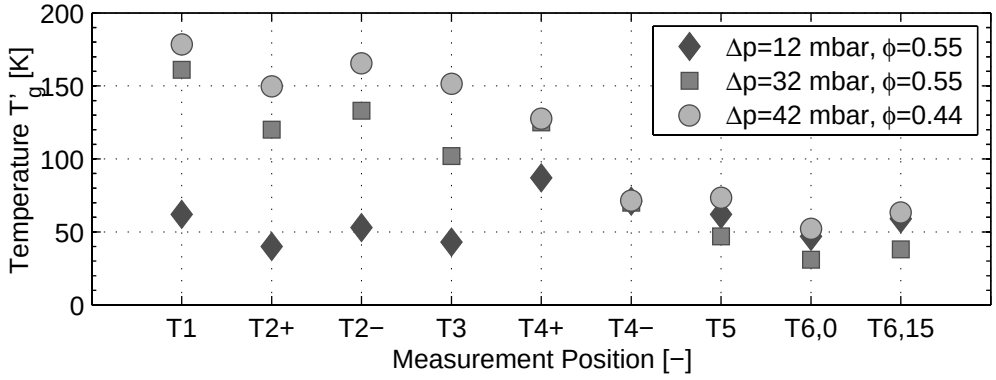

Fig. 6.25: Amplitudes of the gas temperature fluctuations T_g' at the different measurement points in the combustor.

The amplitude of the dynamic gas temperature fluctuations T_g' is shown in Figure 6.25. Depending on the pressure drop, a different behaviour can be seen. For the elevated Δp of operating points 2 and 3, high oscillation amplitudes are encountered in the primary zone, successively decaying towards the nozzle. The oscillations are strongest for $\Delta p = 42$ mbar, exhibiting amplitudes up to 180 K at T1. A substantial decrease in amplitude is obtained between operating points T3 and T5 in the wake of the secondary air injection, where only half the temperature amplitude is conserved. The decrease in amplitude is accompanied by an increase of the mean temperature ($\Delta T \approx 75$ K, Figure 6.24), which illustrates the intensity of homogenisation taking place in the burn-out zone. Despite the rather symmetric flame for $\Delta p = 42$ mbar, the oscillations at the upper wall of the combustion chamber (T4+) are more pronounced than for T4–, probably due to unequal mixing air injection. At the nozzle (T6), the entropy wave has lost about 70% to 80% of its initial strength.

For very low pressure drops, the temperature fluctuations in the primary zone are relatively low, amounting to approximately 50 K. A

substantial increase of the oscillation amplitude by a factor 2 is obtained at T4+, coinciding with a region where strong flame oscillations are encountered (Figure 6.18). Compared to the cases with higher pressure drop, the amplitude of the entropy wave decays less when propagating towards the combustor exit, and similar values are obtained at the nozzle for all pressure drops. This proves the lower dispersion rates at the combustor walls encountered for extended flames at low Δp.

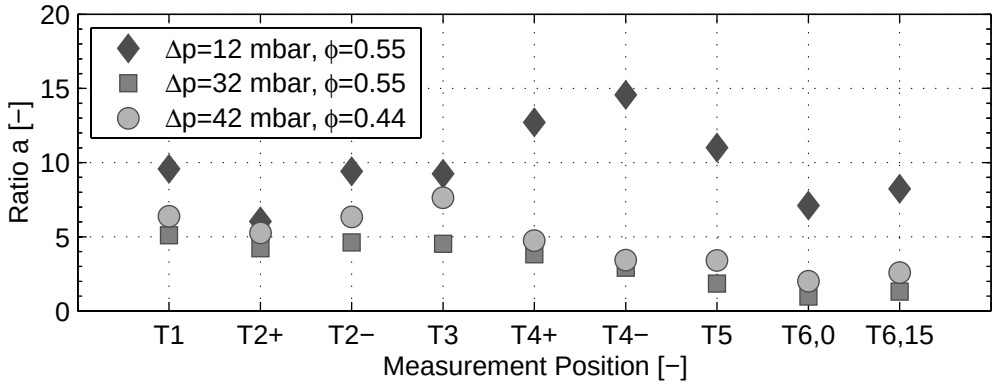

Fig. 6.26: Relative gas temperature fluctuations $T_g'/\bar{T}_g$ at the different measurement points in the combustor, being normalised by the relative pressure oscillations in the combustor p'/p.

The amplitude of the temperature oscillation depends on pressure oscillations in the combustor, since the fluctuating pressure effects the modulation of the droplet sizes and the heat release. Therefore, an amplification factor is defined

$$a := \frac{T_g'}{T_g} \cdot \frac{p}{p'}, \tag{6.5}$$

describing the specific temperature amplitude related to the pressure fluctuation in the combustor. a, which also measures the relative influence of the entropy waves on the instability observed, is shown in Figure 6.26. From Figure 6.26 can be seen that a is globally higher for test case 1 than for the operating points 2 and 3, due to the

overall lower pressure amplitudes. In the dilution zone (T4 – T6), a lies between 8 and 15, indicating that the local relative temperature fluctuations are 8 to 15 times higher than the relative pressure fluctuations. At the choked nozzle (T6,0; T6,15), a exceeds the values for higher pressure drops by a factor of 3.5. This explains the increasing importance of the entropy waves for low pressure drops, leading to a higher magnitude of the entropy-related pressure peak at 87 Hz in the amplitude spectrum shown in Figure 6.19.

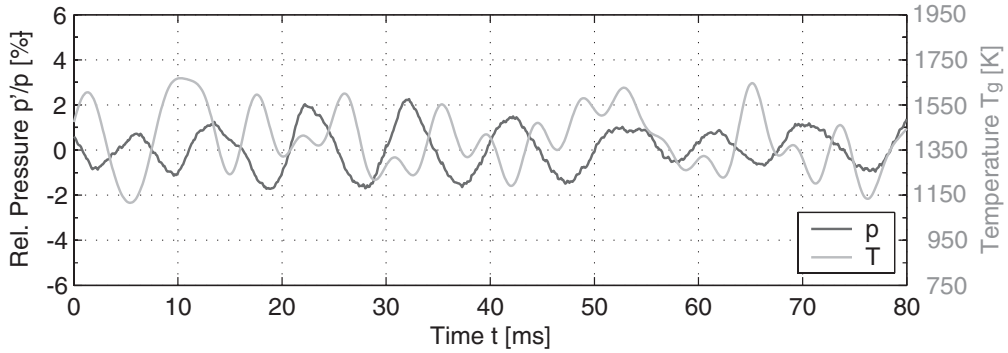

Fig. 6.27: Time traces of the relative combustor pressure p'/p (black) and the gas temperature near the nozzle inlet at Pos. T6,0 (grey) for $\Delta p = 12$ mbar, $\phi = 0.55$.

The corresponding time traces of the pressure and temperature fluctuations measured for $\Delta p = 12$ mbar at T6,0 are shown in Figure 6.27. Referring to the time-traces for $\Delta p = 32$ mbar in Figure 6.5, the phase shift between p' and T_g' was small (17°). The phase shift in Figure 6.27 however is oscillating nearly out of phase at an average $\Delta\varphi = 154°$, coinciding with the expectations on the basis of Eq. (2.77). This proves once more that the instability modes found at $\Delta p < 20$ mbar are essentially entropy-driven.

6.4 Primary Zone Aerodynamics

The preceding chapter has shown that entropy waves can contribute to instability as long as the dispersion in the combustor is low. The contribution of the fuel transport processes in the primary zone to self-excitation is investigated in this chapter. For this purpose, the set-up was modified using a different airblast injector, producing a higher effective swirl, a wider angle of the injected air cone and a stronger aerodynamic dispersion in the primary zone. In the following, this injector is called 'wide cone injector'. The different aerodynamics are mainly attributed to a higher swirl vane angle in the outer air circuit of the three stream atomiser. The other parameters of the injector, particularly the angles of the remaining swirl vanes and the effective burner area are identical to the rumble-prone 'narrow cone'-design which was subject to investigation in the preceding chapters. The combustion chamber was again operated under choked exit conditions.

Figure 6.28 gives a comparison of the injector aerodynamics, recorded by PIV. The flow field of the cold air in the non-combusting case is given in the upper images, being characterised by the vector plot of the velocities and the resulting streamlines. The averaged and the instantaneous spray cones obtained using Mie scattering of the laser light-sheet are also given. In case of the narrow-cone design, the streamlines coincide with the spray cone, thus promoting the droplet transport in direction of the main reaction zone. The wide-cone injector deflects the burner air almost radially outwards, immediately after exiting the injector. The influence of the mixing jets on the primary zone velocity field is stronger, leading to an extended recirculation zone. The streamlines are oriented in counter-direction to the injected spray. As shown in the instantaneous spray images in Figure 6.28, the droplets in the spray cone are subject to an intense dispersion. The stabilisation of the spray cone by corner recirculation zones in the combustor is reduced and the smaller droplets follow the air flow, resulting in a wider spray cone angle as shown in the

instantaneous spray images of Figure 6.28.

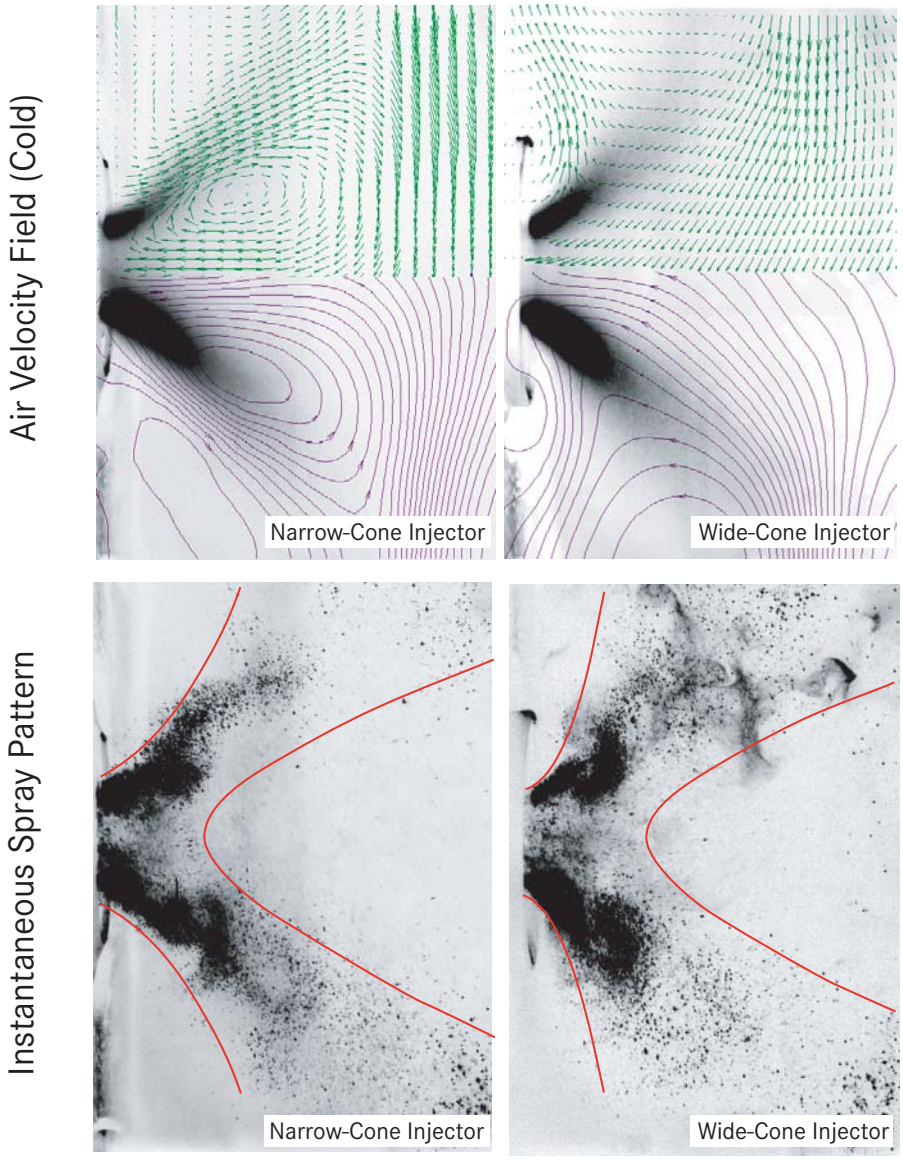

Fig. 6.28: Comparison of the primary zone aerodynamics of the narrow-cone injector(left) and the wide-cone injector (right). The upper graphs show the averaged spray cones and the non-combusting air flow field, represented by averaged vector maps and stream lines. The lower graphs show the instantaneous spray patterns of the burners [Laz04].

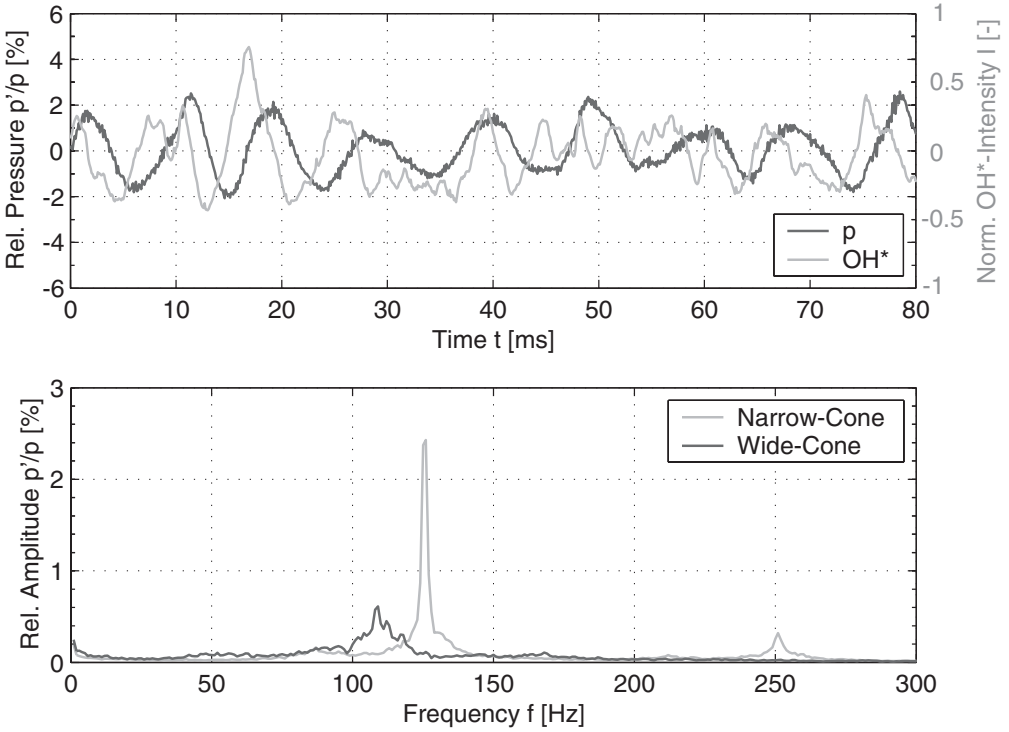

Fig. 6.29: Self excited combustion oscillation of the wide-cone burner for $\Delta p/p = 2.3\%$, $\phi = 0.55$. Upper graph: Time traces of the pressure (black) and the OH*-chemiluminescence (grey). Lower graph: Amplitude spectra of the combustor pressure fluctuations for the wide-cone injector (black) and the narrow-cone design (grey).

In Figure 6.29, the time-resolved fluctuations of the combustor pressure and of the OH*-chemiluminescence are plotted for the same operating condition ($\Delta p/p = 2.3\%$, $\phi = 0.55$) at which rumble was studied for the narrow-cone design in section 6.1. The limit cycle of the self-excited oscillation is peaking at 109 Hz, being 17 Hz lower than for the narrow-cone design at the same operating point. Considerably lower limit amplitudes of $\Delta p'/p = 0.6\%$ are obtained. The chemiluminescence signal is noisier than for the narrow-cone injector and the strong correlation between pressure and heat release, observed in Figure 6.2, is not found any more. The pressure spectrum for the wide-cone injector (Figure 6.29) is relatively broad compared to the peak height, due to the impact of dispersion in the primary zone.

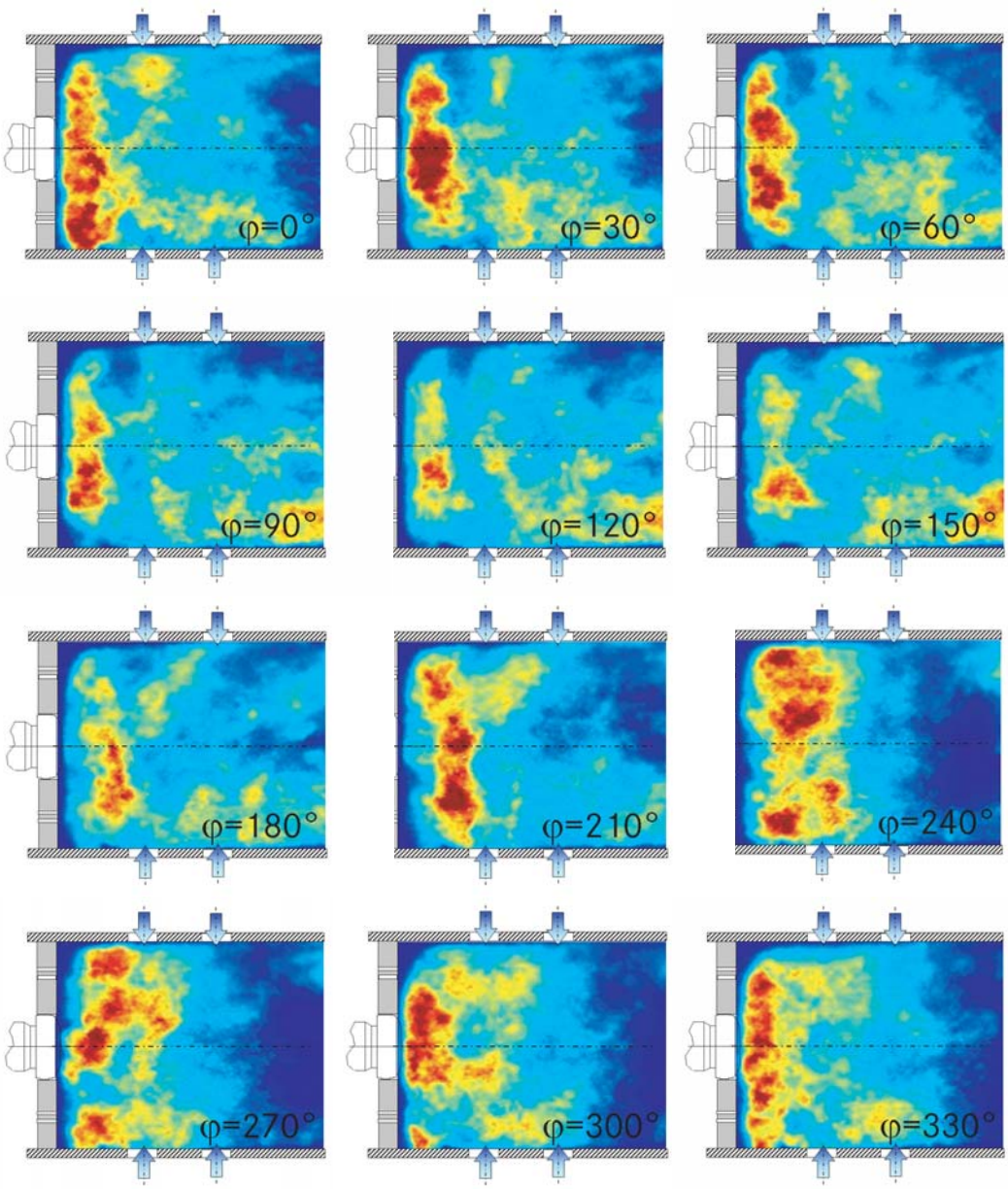

Fig. 6.30: High speed camera recording of the heat release pulsations of the flame for the wide-cone injector at $\Delta p/p$=2.3%, $\phi = 0.55$.

The phase-resolved ICCD-recordings of the chemiluminescence in the combustor are shown in Figure 6.30. The reference phase $\varphi = 0°$ coincides with the phase of maximum chemiluminescence intensity observed in the combustor. The intensity fluctuation exhibits a more

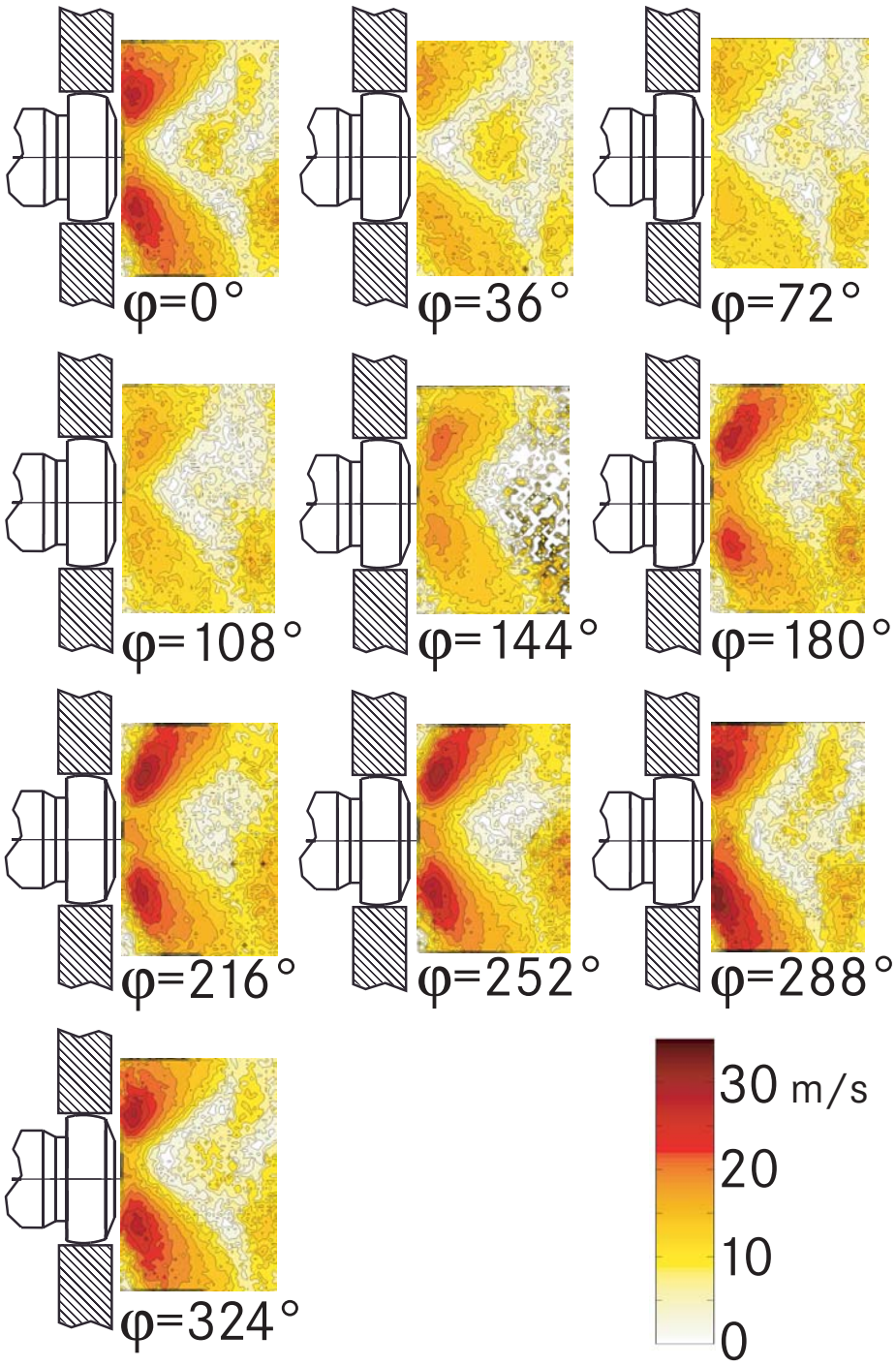

Fig. 6.31: Phase-resolved, averaged droplet velocities in the primary zone of the wide cone injector for one oscillation period ($\Delta p/p = 2.3\%$, $\phi = 0.55$).

random character while pronounced oscillations of the axial flame position are seen. The main reaction zone at $\varphi = 0°$ is located further upstream compared to Figure 6.1 and moves downstream for $\varphi > 150°$ under the influence of rising combustor pressures, lower injection velocities and larger droplet sizes. It returns to the combustor front at increasing effective pressure drops ($\varphi > 300°$) due to the influence of the smaller droplets, which better follow the strongly deviated air flow. A strong flame propagation in upstream direction suppressing the air injection and the fuel delivery is not observed. Regions of strong heat release are encountered throughout the oscillation cycle.

Figure 6.31 shows the corresponding phase-resolved 2-D droplet velocities in the centre plane of the primary zone during an oscillation cycle. The average velocity is about 12% lower than for the narrow-cone design under the influence of the counter-flowing air and the higher swirl. A stronger recirculation region can be found. The general decrease in average droplet velocity correlates fairly well with the limit frequency being about 15% lower than for the narrow-cone injector. A velocity minimum is obtained for a relative phase between 72° and 108°, affecting the convective fuel transport only little. The injection angle of the spray cone varies. It widens for high pressure

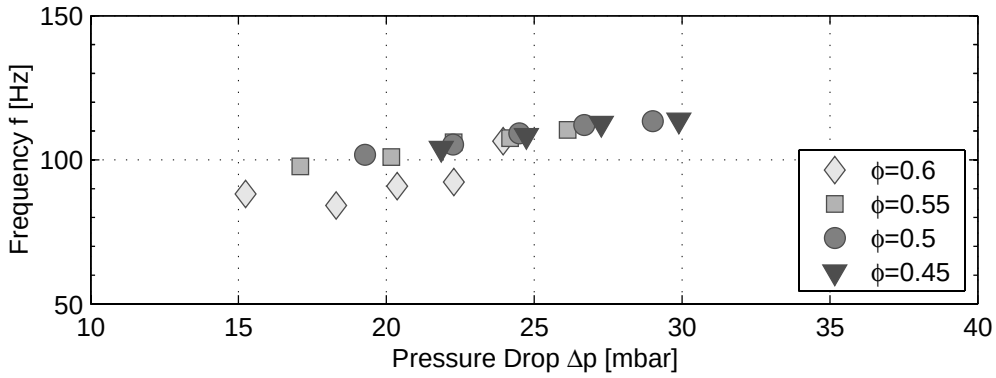

Fig. 6.32: Limit cycle properties for the wide-cone injector with sonic nozzle. Limit frequencies as a function of the absolute static pressure drop Δp.

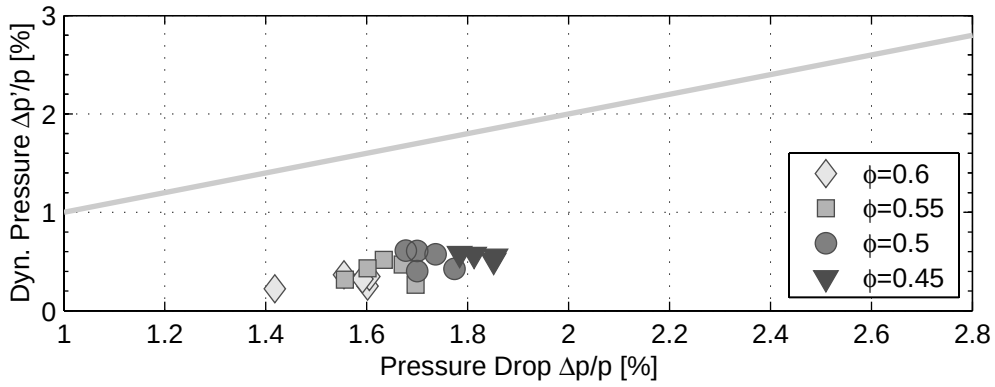

Fig. 6.33: Limit cycle properties for the wide-cone injector with sonic nozzle. Normalised amplitude of the dynamic pressure drop $\Delta p'/p$ over the normalised static pressure drop. The grey line in the lower graph indicates $\Delta p'/p = \Delta p/p$.

drops ($\varphi \approx 288°$) due to the increasing ability of the smaller droplets to follow the flow.

The properties of the limit cycle for varying pressure drops Δp and overall equivalence ratios ϕ are shown in Figures 6.32 and 6.33. As for the narrow cone design, a dominating dependency of f on Δp is found, being almost insensitive to changing equivalence ratios. Again, the droplet dynamics in the primary zone determine the limit frequency and the conclusions of chapter 6.2 also apply to the wide-cone injector. The limit frequencies lie approximately 15% below the values for the narrow-cone design, under the influence of the lower velocities in the primary zone. The limit cycle amplitudes amount to only 40% of the values found for the narrow-cone injector.

As shown in Figure 6.34, the measured phase shift $\Delta\varphi$ between the dynamic pressure and the heat release in the combustor is larger for the wide-cone injector, indicating smaller τ_d according to Figure 6.8. For the narrow-cone injector, the phase differences range between -40° and -60°, being only governed by Δp. For the wide-cone burner however, the phase shifts reveal a stronger data scatter, also depending on ϕ. The values are close to the thermoacoustic stability limit $\Delta\varphi_{crit}$ =-90°, imposed by the Rayleigh criterion Eq. (1.5), which also

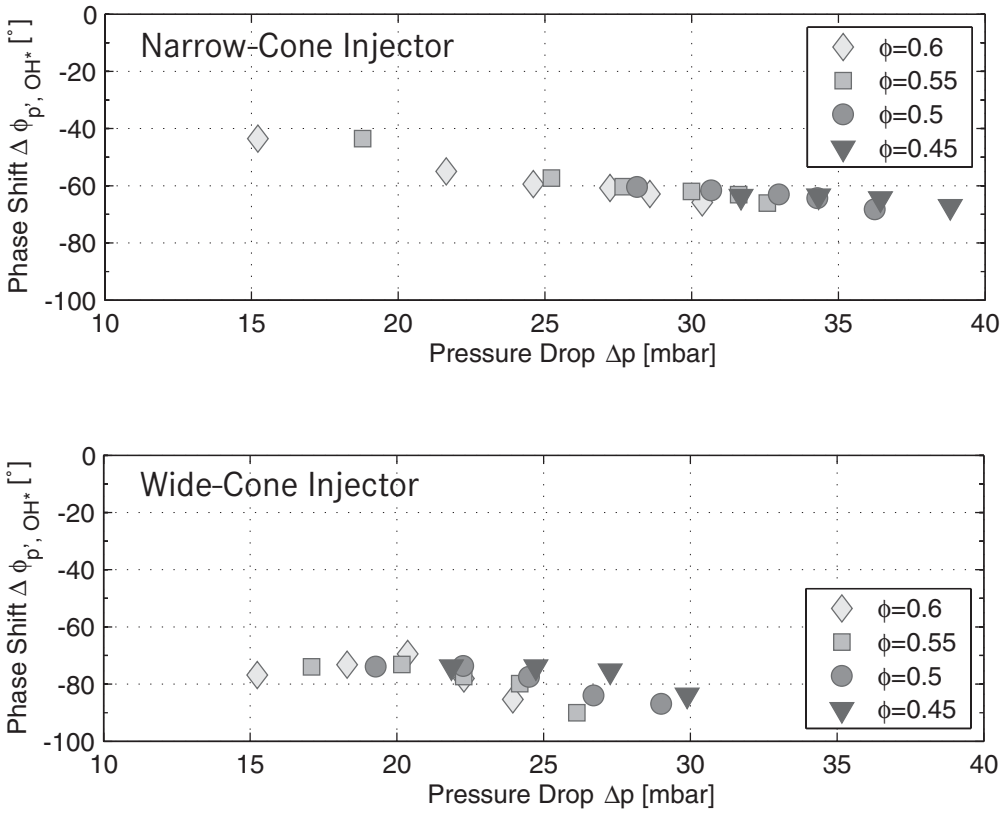

Fig. 6.34: Phase shift between chemiluminescence and pressure signal as a function of Δp measured for the narrow-cone (upper graph) and the wide-cone injector (lower graph).

explains the lower tendency for strong instabilities.

6.5 Conclusions

In this chapter, the RQL-combustor was investigated under self-excitation. The analysis of the limit cycles has shown the following results:

- The self-excited flame oscillations are accompanied by the formation of entropy waves which are convected with approximately bulk velocity towards the combustor outlet.

- Self-excited flame oscillations are also obtained under non-choked exit conditions, for high outlet impedances of the combustion chamber. Entropy waves thus are not a prerequisite for the occurrence of the low-frequency combustion oscillations.

- Unsteady heat release, which proved to oscillate in phase with the OH*-chemiluminescence of the flame, primarily stems from the atomisation characteristics of the airblast atomiser and its sensitivity to pressure perturbations.

- The measurement of the average droplet velocities has shown that the coupling between the pressure and the heat release rate is primarily influenced by the characteristic convection time scales of the smallest fuel droplets from the atomiser lip to the flame. The oscillation frequencies are dominated by the absolute pressure drop across the injector and thus by the average droplet size produced.

- The entropy waves are subject to aerodynamic dispersion in the dilution zone of the combustor, related to the staged injection of air. For moderate and high injector pressure drops ($\Delta p < 20$ mbar), the entropy waves are too weak to alter the dominating thermoacoustic mode. For lower pressure drops, longer flames are obtained with a dominating entropy mode. The corresponding instability amplitudes are low. Compared to the model combustor, where internal cooling of the combustor walls was omitted, film or effusion cooling will probably increase the aerodynamic dispersion in real combustors, which further reduces the impact of entropy waves on instability.

- The attainable pressure amplitudes are limited by the static pressure drop across the injector. Comparison with a different injector design has shown that the limit cycle amplitudes can be considerably reduced by a highly dispersive primary zone, which enhances the mixing of the droplet clusters.

7 Linear Stability Analysis

In the preceding chapter it was found that the occurrence of low-frequency instabilities in the investigated RQL-combustor is predominantly influenced by the atomiser characteristics and the aerodynamics of the primary zone. Heat release fluctuations are mainly attributed to changing droplet number densities, impacting the number of droplets which simultaneously burn in the flame. Entropy waves were observed, but their influence is comparably small as long as dispersion, induced by the mixing air, is high.

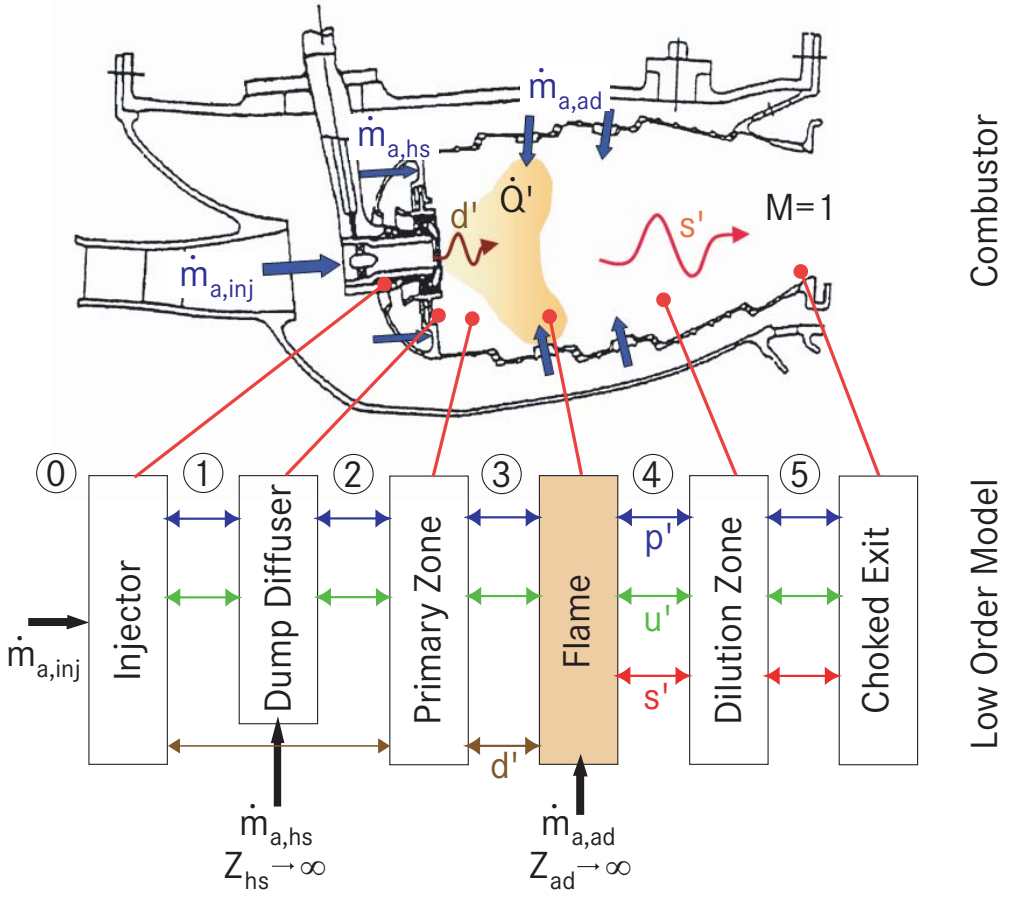

Fig. 7.1: RQL-combustor and low order model.

A low order model (LOM) was formulated for the RQL-configuration aiming at a linear stability analysis of the system and for the theore-

tical reproduction of the experimental findings. This linear network model describes the onset of instabilities by determining the unstable eigenfrequencies ω_e of the acoustic system. The experiments have shown that the variables impacting the overall system stability are the acoustic pressure p' and velocity u', the droplet size fluctuations d' in the primary zone and the entropy waves s' in the dilution sector. For theoretical analysis, the overall system is decomposed into separate acoustic multi-ports, each representing the physical processes in a specific sector of the combustor. According to Figure 7.1, the following elements are derived for the RQL-combustor:

- **Injector** 0-1: determines the p'-u'-coupling at the upstream boundary of the system and the production of droplet clusters d' according to the atomiser characteristics.
- **Dump Diffuser** 1-2: takes into account the acoustic coupling over the area jump at the combustor front panel and the accompanying acoustic losses.
- **Straight Ducts** 2-3,4-5: consider the sound propagation in the primary and the dilution zone, including the effects of aerodynamic dispersion of the droplet clusters d' and the entropy wave s'.
- **Flame** 3-4: is the acoustic driver and describes the heat release by the flame as a function of the incoming fuel droplets, the coupling of the acoustic properties under the influence of the fluctuating heat release and the generation of entropy waves.
- **Sonic Nozzle** 5: incorporates the acoustic boundary conditions at the downstream end of the combustor including the interaction between entropy waves s' and combustor acoustics.

Following Figure 7.1, the vector of variables $\mathbf{v}$ of the network model contains 14 elements, $\mathbf{v} := [p'_1 \dots p'_5, u'_1 \dots u'_5, d'_1, d'_3, s'_4, s'_5]$. The coupling between the vector elements is given by a 14×14 system matrix

$\hat{\mathbf{C}}$, describing the properties of the network elements. $\hat{\mathbf{C}}$ is in general complex and a function of the excitation frequency ω.

The system response to external forcing is described by

$$\hat{\mathbf{C}}(\omega) \cdot \mathbf{v} = \mathbf{e}, \tag{7.1}$$

where $\mathbf{e}$ is the vector of excitation. Performing an eigenmode analysis of the system, only the homogeneous solution of the set of linear equations Eq. (7.1) is considered and the vector of excitation is set to zero $\mathbf{e} \equiv \mathbf{0}$

$$\hat{\mathbf{C}}(\omega) \cdot \mathbf{v} = \mathbf{0}. \tag{7.2}$$

Equation (7.2) yields non-trivial solutions only for

$$\det[\hat{\mathbf{C}}(\omega)] = 0. \tag{7.3}$$

Eq. (7.3) defines the characteristic equation of the system which is usually non-linear in frequency. The complex-valued roots of Eq. (7.3) are the eigenfrequencies ω_e. For a harmonic time-dependence $e^{i\omega t}$ with $\omega_e = \Re(\omega_e) + i\Im(\omega_e)$, one obtains

$$e^{i\omega_e t} = e^{i\Re(\omega_e)t} \cdot e^{-\Im(\omega_e)t}. \tag{7.4}$$

The real part of the eigenfrequency $\Re(\omega_e)$ thus determines the frequency of oscillation, while the imaginary part $\Im(\omega_e)$ specifies the growth behaviour of the corresponding eigenmode in time. Negative $\Im(\omega_e)$ indicate instability, since the resulting exponent of the second term in Eq. (7.4) is positive, indicating exponential growth. Positive values for $\Im(\omega_e)$ are associated with decaying eigenmodes and hence with stability. The growth rate of an eigenmode is described by the amplitude ratio Ξ of two successive oscillation cycles and follows

$$\Xi = \frac{e^{-\Im(\omega_e)(t+T)}}{e^{-\Im(\omega_e)(t)}} = e^{-\Im(\omega_e)T} = e^{-2\pi\frac{\Im(\omega_e)}{\Re(\omega_e)}}. \tag{7.5}$$

The growth rate thus depends on the ratio $\Im(\omega_e)/\Re(\omega_e)$ of the eigenfrequency.

7.1 Key Elements of the Combustor Model

One unique feature of the investigated combustor is the staged injection of the air. As indicated in Figure 7.1, the overall air mass flow is separately fed into the combustion chamber through the injector $\dot{m}_{a,inj}$, the heat shield $\dot{m}_{a,hs}$ and mixing orifices in the quenching zone $\dot{m}_{a,mix}$. However, as was mentioned in section 3, the area ratio between the cooling holes of the heat shield and the combustion chamber is very high. Furthermore, the mixing orifices were acoustically decoupled by perforated plates inducing considerable pressure loss. Closed end conditions were thus assumed for both inlets, $Z_{hs} \rightarrow \infty$, $Z_{ad} \rightarrow \infty$, suppressing any modulation of the velocities of the entering air. The impact of $\dot{m}_{a,hs}$, $\dot{m}_{a,mix}$ on the overall system stability has therefore to be seen primarily in context with

- increasing the mean volume fluxes and the mean velocities of the gas downstream of the respective inlets
- inducing aerodynamic dispersion in the primary and the dilution zone of the combustor
- increasing the turbulent mixing in the spray flame
- homogenising the average temperatures up- and downstream of the flame.

The only acoustically 'active' inlet thus remains the airblast atomiser.

7.1.1 Airblast Injector

The airblast injector is considered as a compact element which imposes the acoustic boundary conditions on the system inlet.

The measurements conducted in section 5.1 have shown that the pressure-velocity coupling of the injector in the low-frequency domain is quasi-steady, being characterised by the Bernoulli equation for the linearised perturbations

$$\frac{1}{2}\frac{p_0' - p_1'}{\Delta\bar{p}} = \frac{u_1'}{\bar{u}_1}. \tag{7.6}$$

Since the area change at the burner inlet is very large (about 1:90) and no external forcing is applied, plenum conditions are assumed at the upstream end of the injector

$$p_0' = 0. \tag{7.7}$$

Equation (7.6) then becomes

$$\frac{-p_1'}{2\Delta\bar{p}} = \frac{u_1'}{\bar{u}_1}. \tag{7.8}$$

For $\bar{u}_0 \rightarrow 0$ (plenum condition), the static pressure drop and the average air velocity in the burner are correlated by Eq. (5.1)

$$2\Delta\bar{p} = \rho_a(1 + \zeta_{inj})\bar{u}_1^2. \tag{7.9}$$

ζ_{inj} is the static pressure loss coefficient of the injector ducts. The average air velocity can be calculated on the basis of the burner area A_{inj}

$$\bar{u}_1 = \frac{\dot{m}_{a,inj}}{\rho_a A_{inj}} \tag{7.10}$$

Using Eqs. (7.9) and (7.10), $\zeta_{inj} = 6.4\%$ was obtained from static pressure drop measurements. With Eqs. (7.8), (7.9) and (7.10), the coupling of the acoustic pressure and velocity at the injector outlet is finally given by

$$u_1' = \frac{-A_{inj}}{(1 + \zeta_{inj})\dot{m}_{a,inj}} \cdot p_1'. \tag{7.11}$$

In the model, the polydisperse spray generated by the injector is assumed to be adequately represented by the SMD. Resuming the quasi-steady atomiser performance Eq. (5.11) in section 5.2

$$\frac{d}{d_0} = \left(\frac{u}{u_0}\right)^{-\xi} \;,\; \xi > 0, \tag{7.12}$$

the sensitivity of the generated droplet sizes to the injector air velocity is characterised by the exponent ξ. A rising ξ indicates stronger dependencies. Linearisation yields

$$\frac{d_1'}{\bar{d}_1} = -\xi \left(\frac{u_1'}{\bar{u}_1}\right). \tag{7.13}$$

For the narrow-cone injector, ξ has been experimentally determined to $\xi = 1.6$. Equation (7.13) is used to model the spray-velocity coupling of the injector. While using Eqs. (7.11) and (7.13), it should be noted that the underlying assumption of a quasi-steady injector response has been experimentally proven only for the low frequency domain, which restricts the applicability of the low-order model to that frequency range.

7.1.2 Compact Dump Diffuser

The transfer function approach, which has already been introduced in the context of flame modelling in section 2.3.2, can be used to describe the properties of any acoustic element, such as the sudden area change downstream of the injector exit:

$$\begin{pmatrix} \frac{p'}{\bar{\rho}c} \\ u' \end{pmatrix}_2 = \hat{\mathbf{D}} \cdot \begin{pmatrix} \frac{p'}{\bar{\rho}c} \\ u' \end{pmatrix}_1 \tag{7.14}$$

An analytical formulation of the matrix elements for the compact

dump diffuser with acoustic loss is given in [GFEP03]:

$$\hat{\mathbf{D}} = \begin{pmatrix} 1 & \left[1 - \zeta - \left(\frac{A_1}{A_2}\right)^2\right] M_1 - i\frac{\omega}{c} l_{eff} \\ -i\frac{\omega}{c} l_{red} & \frac{A_1}{A_2} \end{pmatrix}. \tag{7.15}$$

ζ represents the acoustic loss across the area change, l_{eff} is the effective and l_{red} is the reduced length of the compact element. All parameters are essentially determined by the properties of the moving medium and the adjacent duct geometries that build the sudden change. ζ is a function of ω. l_{eff} and l_{red}, respectively, represent inductance and capacitance effects of the sudden change. According to [GFEP03], $l_{eff} = 8.7\,\text{mm}$ and $\zeta = 4.1 \cdot 10^{-5}\sqrt{\omega}$ is obtained for the current geometry. l_{red} is usually very small for low Mach number flows and can be set to zero in the scope of this work [Pol04].

7.1.3 Dispersion Function Θ

As discussed in the preceding chapters, the dispersion induced by the aerodynamics in the combustor considerably alters the global instability behaviour. The temperature measurements in section 6.3.2 have proven that the amplitude decay of the entropy wave travelling in the dilution zone is important and cannot be neglected in the instability analysis. In addition, the tests with both injector designs have shown that a highly dispersive flow field in the primary zone can contribute to overall stability. As a consequence, spatial dispersion is an indispensible feature the low order model must account for.

A 1-D model for the aerodynamic dispersion of a fluctuating scalar Ψ' in a duct is proposed in [Sat03]. The underlying idea is shown in Figure 7.2: A perturbation pulse Ψ' of the scalar is applied uniformly over the inlet area of the duct. Ψ' is subject to dispersion, since the convective delay times, imposed by a non-uniform flow profile inside the duct, vary over the cross-section of the duct. A "smeared" profile of the dispersed scalar will therefore be obtained at the

duct outlet after an average convection time $\bar{\tau}$. Based on the analysis of the probability density distribution of the delay times, the following coupling condition is obtained:

$$\begin{aligned} \Theta(i\omega) \;&:=\; \frac{\Psi'_{outlet}(i\omega)}{\Psi'_{inlet}(i\omega)} = \frac{1}{2\Delta\tau(i\omega)^2}\cdot e^{-i\omega\overline{\tau}}\cdot \\ &\cdot\quad \left[\left(\frac{\Delta C}{C}+i\omega-\frac{\Delta C}{C}i\omega\Delta\tau\right)\cdot e^{i\omega\Delta\tau}\right. \\ &-\quad \left.\left(\frac{\Delta C}{C}+i\omega+\frac{\Delta C}{C}i\omega\Delta\tau\right)\cdot e^{-i\omega\Delta\tau}\right] \end{aligned} \tag{7.16}$$

The function $\Theta(i\omega)$ in Eq. (7.16) describes the dispersion of Ψ' as a function of the oscillation frequency ω. As shown in Figure 7.2, the profile of the dispersed scalar can be idealised as a trapezoid. The transfer characteristics of the duct is thus essentially given by the mean convection time $\bar{\tau}$, and by the time spread $\Delta\tau$ which is a measure for the non-uniformity of the flow and the strength of the dispersion. $\Delta\tau/\bar{\tau}$ is a measure for the *dispersion rate*.

For the special case of $\Delta C/C = 0$, Eq. (7.16) simplifies to

$$\Theta(i\omega) = \underbrace{e^{-i\omega\overline{\tau}}}_{\text{time lag}}\cdot\underbrace{\frac{e^{i\omega\Delta\tau}-e^{-i\omega\Delta\tau}}{2i\omega\Delta\tau}}_{\text{dispersion}} \tag{7.17}$$

$\Theta(i\omega)$ in Eq. (7.17) is composed of a convective time lag (first term) and an integrator term (second term), which introduces a frequency-dependent damping of the scalar fluctuations. This dispersive term is plotted in Figure 7.3.

For the limiting case $\Delta\tau \to 0$, it can be shown by series expansion that

$$\lim_{\Delta\tau\to 0}\left(\frac{e^{i\omega\Delta\tau}-e^{-i\omega\Delta\tau}}{2i\omega\Delta\tau}\right) = 1; \tag{7.18}$$

i.e., the dispersion function $\Theta(i\omega)$ reduces to a simple convective time lag.

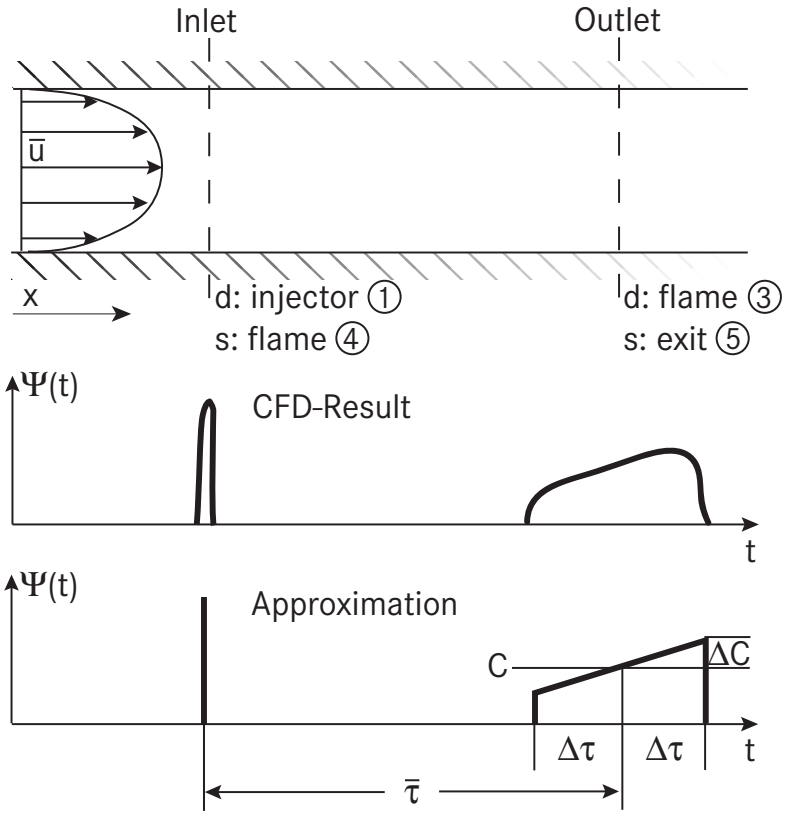

Fig. 7.2: Dispersion of the perturbation of a scalar Ψ' in a duct [Sat03].

Equation (7.17) is used to model the dispersion of the droplet clusters in the primary zone and the entropy wave in the dilution sector of the combustor:

$$d'_3 = \Theta_d d'_1 \tag{7.19}$$

$$s'_5 = \Theta_s s'_4. \tag{7.20}$$

The convective time delay of the droplets $\bar{\tau}_d$ includes the subprocesses of droplet acceleration and convection. From Figure 6.15, $2\ \text{ms} < \bar{\tau}_d < 3\ \text{ms}$ can be determined for the test rig. In the linear stability analysis, only very small deviations of the droplet diameter from its mean value are considered. $\bar{\tau}_d$ is therefore assumed independent of the droplet size variations during the oscillation cycle.

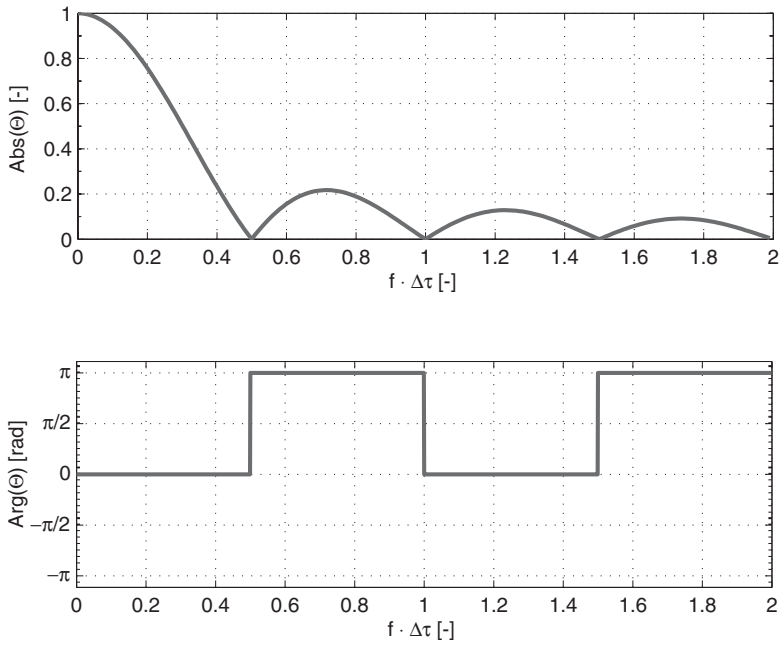

Fig. 7.3: Dispersion function $\Theta(i\omega)$ for $\overline{\tau} = 0$.

It has further been found in section 6.1.1 that the entropy wave travels approximately with bulk velocity in the combustor. As a consequence, the delay time $\bar{\tau}_s$ can generally be calculated by

$$\bar{\tau}_s = \frac{l_4}{\bar{u}_4}. \tag{7.21}$$

Referring to the notation introduced in Figure 7.1, l_4 is the length of the dilution zone and $\bar{u}_4$ is the corresponding bulk velocity. The time spreads $\Delta\tau_d$ and $\Delta\tau_s$, respectively, will be varied as part of the parametric analysis in section 7.2.

7.1.4 A Simple Transfer Function for Spray Combustion

In the case of premixed flames, velocity changes which alter the flame surface area are one important source for heat release fluctuations [HD98, Dow99, Lie03]. In addition, equivalence ratio waves contribute to the fluctuating heat release by altering the laminar flame speed and the adiabatic flame temperature. In the case of diffusion flames

however, no uniform equivalence ratio distribution in the flame can be presumed. The experimental results revealed a strong dependency of the limit cycle properties on Δp, via the droplet size. This suggests that, in the case of spray flames, the heat release as acoustic driver should be expressed as a function of the droplet size modulations (d'/d) which enter the reaction zone:

$$\frac{\dot{Q}'}{\bar{\dot{Q}}} = f\left(\frac{d'}{\bar{d}}\right) \tag{7.22}$$

To model the transfer function of the spray flame, the following assumptions are made:

- The impact of prevaporisation is negligible; i.e., the droplet diameters remain unaffected during the convection to the flame. This assumption is justified by the low temperatures of the carrier air (300 K) and the moderate convective time scales in the primary zone, leading to low prevaporisation.
- The properties of the burning spray is appropriately represented by the Sauter mean diameter.
- Combustion is controlled by droplet evaporation. Due to staged air injection with high turbulence levels, turbulent mixing and reaction are infinitely fast. Negligible interaction between the burning droplets is assumed. Each droplet burns close to its spherical surface at stoichiometric conditions ($\phi = 1$). Under these conditions, the heat released by a single droplet is proportional to the instantaneous fuel evaporation rate. The evaporation process in the flame is assumed to follow the D^2-law [Law82, Tur00].
- The time-dependent combustion rate of a burning droplet can be appropriately represented by the average heat release over the burning time τ_b

$$\dot{Q}_{eff} := \frac{1}{\tau_b}\int_0^{\tau_b} \dot{Q}_d(t)dt. \tag{7.23}$$

- The heat release fluctuations can be attributed exclusively to the droplet cluster arriving in the flame. This is a simplification since the integrator effect of finite droplet burning times τ_b is not explicitly accounted for. However, for the low frequencies range considered, it is justified as long as the droplet burning time is small compared to the oscillation period: $\tau_b \ll 1/f$.
- The impedance of the fuel supply is infinite $Z_f \rightarrow \infty$; i.e., the total fuel flow rate $\dot{m}_f$ is constant.
- The length of the flame is small compared to the occurring wavelengths; i.e. the flame is compact.

The overall heat release of the flame $\dot{Q}$ is then the product of the average heat released by a single droplet $\dot{Q}_{eff}$ and the droplet number density N. Both N and $\dot{Q}_{eff}$ are functions of the droplet diameter. Linearisation yields:

$$\frac{\dot{Q}'}{\bar{\dot{Q}}} = \frac{(N\dot{Q}_{eff})'}{(\overline{N\dot{Q}_{eff}})} = \frac{N'}{\bar{N}} + \frac{\dot{Q}'_{eff}}{\bar{\dot{Q}}_{eff}} \tag{7.24}$$

In order to obtain a dependency according to Eq. (7.22), both terms in Eq. (7.24) have to be expressed as a function of the incremental diameter change $(d'/\bar{d})$.

Under conditions of constant fuel mass flow and monodisperse spray, the droplet number density in a unit volume is coupled with the droplet diameter by Eq. (7.25)

$$\dot{m}_f = \frac{d}{dt}\left(N\frac{\pi}{6}\rho_f d^3\right) = \text{const.} \tag{7.25}$$

Linearising Eq. (7.25) yields the required function for the first term in Eq. (7.24)

$$\frac{N'}{\bar{N}} = -3\frac{d'}{\bar{d}}. \tag{7.26}$$

For the second term, the average heat release of a single droplet (Eq. (7.23)) has to be calculated, which requires detailed knowledge of the underlying burning behaviour. Following the D^2-law, the square of droplet diameter decreases linearly in time

$$d(t)^2 = d_0^2 - K \cdot t. \tag{7.27}$$

$d_0 = d(t = 0)$ is the initial droplet diameter and K is the burning rate constant, which is entirely determined by the thermodynamic properties of the reacting oxidiser-fuel combination. Following the methodology given in [Tur00], K becomes

$$K \;=\; 6.022 \cdot 10^{-7} \;\frac{m^2}{s}$$

for the reacting kerosene-air mixture[23]. As a consequence of the above assumption about the governing effect of evaporation, the instantaneous heat release of the fuel droplet is the product of the fuel evaporation rate of the spherical droplet $\dot{m}_d$ and the specific enthalpy of reaction of the fuel h_b

$$\dot{Q}_d(t) = h_b \cdot \dot{m}_d = h_b \cdot -\frac{\pi}{6}\rho_f \frac{d}{dt} d^3 = -h_b \cdot \frac{\pi}{2}\rho_f d^2 \frac{d}{dt} d. \tag{7.28}$$

Inserting Eq. (7.27) in Eq. (7.28) yields

$$\dot{Q}_d(t) = h_b \frac{\pi}{4}\rho_f K \sqrt{d_0^2 - Kt}. \tag{7.29}$$

The droplet burning time τ_b follows from Eq. (7.27)

$$\tau_b = \frac{d_0^2}{K}. \tag{7.30}$$

Figure 7.4 shows the calculated values for τ_b as a function of the initial droplet diameter. The values in Figure 7.4 are conservative, since the underlying value for the burning rate constant K refers to

[23] Initial fuel temperature: T_f=300 K

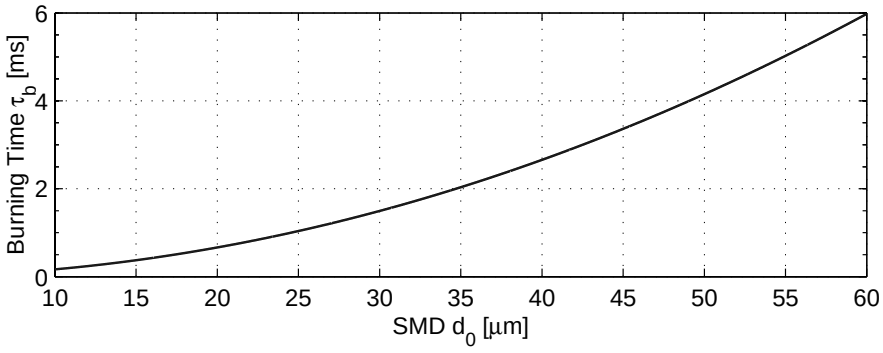

Fig. 7.4: Time scales of droplet combustion τ_b as a function of the initial droplet diameter according to the D^2-law.

a quiescent environment. The highly turbulent environment under the influence of the mixing air will considerably enhance the local mass transfer rates and practically lead to lower τ_b. With Eq. (7.30), integrating Eq. (7.29) according to Eq. (7.23) yields

$$\dot{Q}_{eff} = \frac{\pi}{6} h_b \rho_f K d_0. \tag{7.31}$$

The average heat release rate of droplet combustion thus depends linearly on the initial droplet diameters

$$\frac{\dot{Q}'_{eff}}{\bar{\dot{Q}}_{eff}} = \frac{d'}{\bar{d}}. \tag{7.32}$$

Combining Eq. (7.26), Eq. (7.32) and Eq. (7.24), the following transfer function can be finally composed, adopting the notation of Figure 7.1

$$\frac{\dot{Q}'}{\bar{\dot{Q}}} = -3\left(\frac{d'_3}{\bar{d}_3}\right) + 1\left(\frac{d'_3}{\bar{d}_3}\right) = -2\left(\frac{d'_3}{\bar{d}_3}\right). \tag{7.33}$$

The expression Eq. (7.33) is simple and reflects the dominating effect of the droplet number on the heat release, observed in the experiments. The simplicity, particularly the independence from the fre-

quency, is a result of neglected burning times τ_b, as discussed above. Eq. (7.24) is therefore only applicable in the low frequency domain.

$(d'/\bar{d})$ and $(u'/\bar{u})$ are coupled via the linearised atomiser characteristics Eq. (7.13). The flame transfer function in Eq. (2.55), based on the relative velocity fluctuations $(u'/\bar{u})$, can therefore be obtained by backtracking the droplet path from the flame across the dispersive primary zone to the injector. Combining Eqs. (7.33), (7.17) and (7.13) yields

$$\frac{\dot{Q}'}{\bar{\dot{Q}}} = 2\ \xi\ \Theta_d(i\omega) \cdot \left(\frac{u_1'}{\bar{u}_1}\right), \tag{7.34}$$

making the heat release fluctuations in the spray flame depend on the atomiser performance, the velocity fluctuations encountered by the atomiser and the aerodynamic features of the primary zone.

The coupling of the acoustic variables over the flame front is given by the Rankine-Hugoniot relations Eqs. (2.53), (2.54), derived in section 2.3. In Eq. (2.54), the heat release per unit area $\dot{Q}_A$ is used. With $\bar{\dot{Q}}_A = \dot{m}_f h_b / A_{cc}$, where A_{cc} is a representative cross-section of the combustion chamber, the following matching conditions are finally obtained

$$p_4' = p_3' \tag{7.35}$$

$$u_4' = u_3' - 2\frac{\dot{m}_f h_b}{A_{cc}} \frac{\gamma - 1}{c_3^2 \bar{\rho}_3} \left(\frac{d_3'}{\bar{d}_3}\right). \tag{7.36}$$

The generated entropy wave s_4' can be calculated using Eq. (2.61)

$$s_4' = -2c_p \left(1 - \frac{\bar{T}_3}{\bar{T}_4}\right) \frac{d_3'}{\bar{d}_3}. \tag{7.37}$$

s_4' thus depends on the static temperature rise across the flame and the strength of the droplet size fluctuations, entering the flame.

7.1.5 System Equations

The primary zone 2-3 and the dilution zone 4-5 of the combustor are modelled as straight ducts. The mathematical relations describing the propagation of the acoustic variables p', u' in these sectors are obtained by inserting Eqs. (2.25), (2.26) into Eqs. (2.37), (2.38):

$$p'_{3,5} = \bar{\rho}_{3,5} c_{3,5} \left[\frac{u'_{2,4}}{2} \left(e^{-i\omega k_+ l_{2,4}} - e^{i\omega k_- l_{2,4}} \right) + \right. \\ \left. + \frac{p'_{2,4}}{2\bar{\rho}_{2,4} c_{2,4}} \left(e^{-i\omega k_+ l_{2,4}} + e^{i\omega k_- l_{2,4}} \right) \right] \qquad (7.38)$$

$$u'_{3,5} = \frac{u'_{2,4}}{2} \left(e^{-i\omega k_+ l_{2,4}} + e^{i\omega k_- l_{2,4}} \right) + \\ + \frac{p'_{2,4}}{2\bar{\rho}_{2,4} c_{2,4}} \left(e^{-i\omega k_+ l_{2,4}} - e^{i\omega k_- l_{2,4}} \right) \qquad (7.39)$$

With respect to the dimensions of the generic combustion chamber and the approximate flame position encountered, e.g. in Figure 6.1, the sector lengths are set to $l_2 = 40$ mm, $l_4 = 260$ mm. Applying Eqs. (7.38) and (7.39) to the primary and the dilution zone of the combustor results in the first 4 system equations for the low order model. The remaining equations are:

5.	u'_1	$=$	$\dfrac{-A_{inj}}{(1+\zeta_{inj})\dot{m}_{a,inj}} \cdot p'_1$	Eq. (7.11)
6.	p'_2	$=$	$\bar{\rho}_2 c_2 \left(\hat{D}_{11} \dfrac{p'_1}{\bar{\rho}_1 c_1} + \hat{D}_{12} u'_1 \right)$	Eq. (7.15)
7.	u'_2	$=$	$\hat{D}_{21} \dfrac{p'_1}{\bar{\rho}_1 c_1} + \hat{D}_{22} u'_1$	Eq. (7.15)
8.	p'_4	$=$	p'_3	Eq. (7.35)
9.	u'_4	$=$	$u'_3 - 2\dfrac{\dot{m}_f h_b}{A_{cc}} \dfrac{\gamma - 1}{c_3^2 \bar{\rho}_3} \left(\dfrac{d'_3}{\bar{d}_3} \right)$	Eq. (7.36)

10.	u'_5	$=$	$\frac{\gamma-1}{2}M_5\frac{p'_5}{\bar{\rho}_5 c_5}+M_5\frac{c_5}{2}\frac{s'_5}{c_p}$	Eq. (2.76)
11.	d'_1	$=$	$-\xi\frac{\bar{d}_1}{\bar{u}_1}u'_1$	Eq. (7.13)
12.	d'_3	$=$	$\Theta_d d'_1$	Eq. (7.19)
13.	s'_4	$=$	$-2c_p\left(1-\frac{\bar{T}_3}{\bar{T}_4}\right)\frac{d'_3}{\bar{d}_3}$	Eq. (7.37)
14.	s'_5	$=$	$\Theta_s s'_4$	Eq. (7.20)

Concerning the average gas temperature, the combustor is considered being separated into two temperature zones up- and downstream of the flame. The upstream temperature is approximated by the inlet air temperature, which was kept constant at 300 K during the experiments. The measurement of the static combustor temperature in section 6.3.1 indicates a rapid increase of the average flue gas temperature to the adiabatic temperature. The downstream temperature was therefore set to the adiabatic value:

$$\bar{T}_{up} = \bar{T}_1 = \bar{T}_2 = \bar{T}_3 = 300\ \text{K} \tag{7.40}$$

$$\bar{T}_{down} = \bar{T}_4 = \bar{T}_5 = T_{ad}(\phi). \tag{7.41}$$

The corresponding sound propagation speeds c_1 to c_5 are calculated using Eq. (2.16).

The mean velocities influence the local Mach numbers and the convective wave numbers. The average air velocity at the injector $\bar{u}_1$ is given by Eq. (7.10). Accounting for the staged air injection in the combustor, the other mean velocities are obtained by

$$\bar{u}_2 = \bar{u}_3 = \frac{\dot{m}_{a,inj}+\dot{m}_{a,hs}}{\rho_{up}A_{cc}} \tag{7.42}$$

$$\bar{u}_4 = \bar{u}_5 = \frac{\dot{m}_{a,inj}+\dot{m}_{a,hs}+\dot{m}_{a,mix}}{\rho_{down}A_{cc}}. \tag{7.43}$$

For evaluating Eqs. (7.42) and (7.43), the internal air distribution in the combustor, specifying $\dot{m}_{a,inj}$, $\dot{m}_{a,hs}$ and $\dot{m}_{a,mix}$ for a given overall air mass flow $\dot{m}_{a,tot}$, was determined by the pressure loss measurements in section 3.3.2.

The complex eigenfrequencies for the system matrix were calculated numerically, using the software package *Mathematica*.

7.2 Model Results

7.2.1 Instability behaviour in the absence of entropy waves

In this section, the stability behaviour of the model combustor in the absence of entropy waves is discussed. The contribution of the entropy waves to the exit nozzle impedance is neglected by setting $s'_4 \equiv 0$. Using Eq. (2.76), an outlet impedance

$$Z_5 = \frac{p'_5}{u'_5} = \frac{2\bar{\rho}_5 c_5}{(\gamma - 1)M_5} \tag{7.44}$$

is then obtained, which is high, since $c_5 \gg 1$, $M_5 \approx 0.05$. This setting thus resembles the conditions obtained with the flame tube being attached to the combustion chamber exit.

In Figure 7.5, the growth rate Ξ according to Eq. (7.5) is plotted versus the eigenfrequencies $f_e = \omega_e/2\pi$. The droplet dispersion rate $\Delta\tau_d/\bar{\tau}_d$ is used as parameter. The bold black line at $\Xi = 1$ separates the instability region ($\Xi > 1$) from the stable modes ($\Xi < 1$). The combustor exhibits a highly unstable eigenfrequency at 126 Hz $< f <$ 140 Hz, depending on the dispersion rate, and a second mode at higher frequencies above 250 Hz. The frequency of the lower unstable mode tends to increase with rising $\Delta\tau_d/\bar{\tau}_d$. Particularly for low dispersion rates $\Delta\tau_d/\bar{\tau}_d < 0.3$, the eigenfrequency agrees very well with the experimental data in section 6.2, deviating by max. 12 Hz from the limit cycle frequency obtained for a compa-

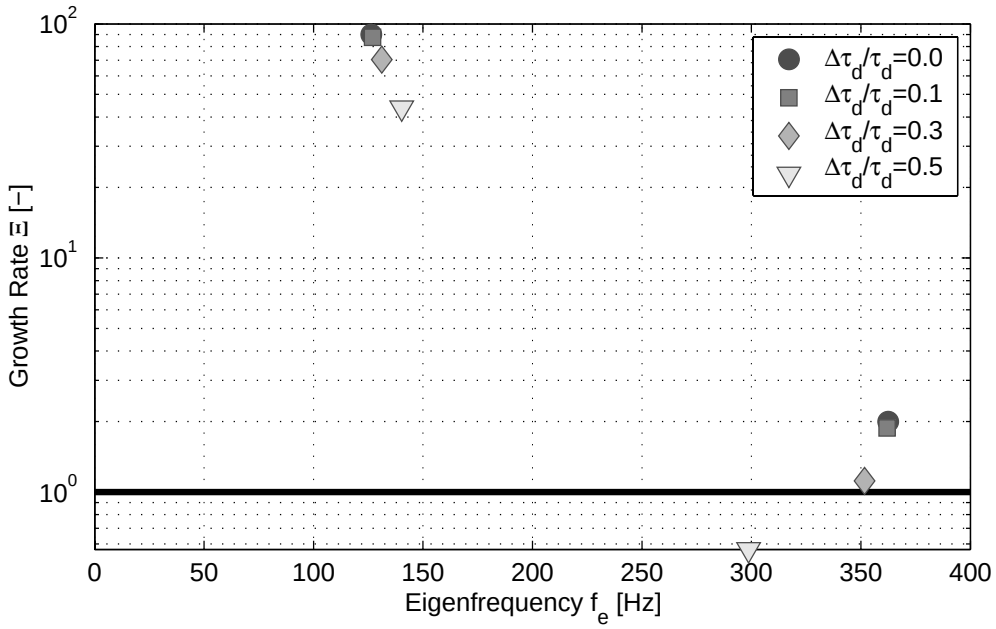

Fig. 7.5: Eigenfrequencies of the combustor for different dispersion rates of the fuel droplets $\Delta\tau_d/\bar{\tau}_d$ ($\phi = 0.77$, $\bar{\tau}_d$=3 ms, ξ =1.6). Entropy waves are neglected.

rable droplet delay time of $\bar{\tau}_d = 3$ ms. This is a very good agreement considering the model simplifications implied. The second eigenmode at higher frequencies grows less, attaining stability for $\Delta\tau_d/\bar{\tau}_d > 0.3$. Figure 7.5 proves that instability at characteristic rumble frequencies is obtained even without entropy perturbations. This result strongly supports the experimental findings about the critical role of the primary zone for self-excitation, as discussed in section 6.1.3. Increasing dispersion of the droplet clusters tends to lower the growth rates. Following Figure 6.28, a considerable increase of dispersion can be achieved by reducing the support of the carrier air for fuel transport; i.e., by detuning the air injection such that the streamlines of the air do not coincide with droplet trajectories in the primary zone. Instead, the shear layers towards the central recirculation zone and the counterflow of the central recirculation zone can be used to disperse and to mix the droplet clusters on their way to the flame. For the fuel mass flows investigated it is however impossible to stabilise the system only by increasing the dispersion. This is con-

firmed by the measurements where instability was also obtained in a highly dispersive environment (section 6.4), albeit at lower limit amplitudes. It should be kept in mind that the linear model does only provide information about potentially unstable frequencies of the system, but not about the resulting limit cycle amplitudes due to the non-linearities involved. The model results in Figure 7.5 show the importance of the droplet size fluctuations for destabilising the combustor and the effect of dispersion on reducing the tendency to instability.

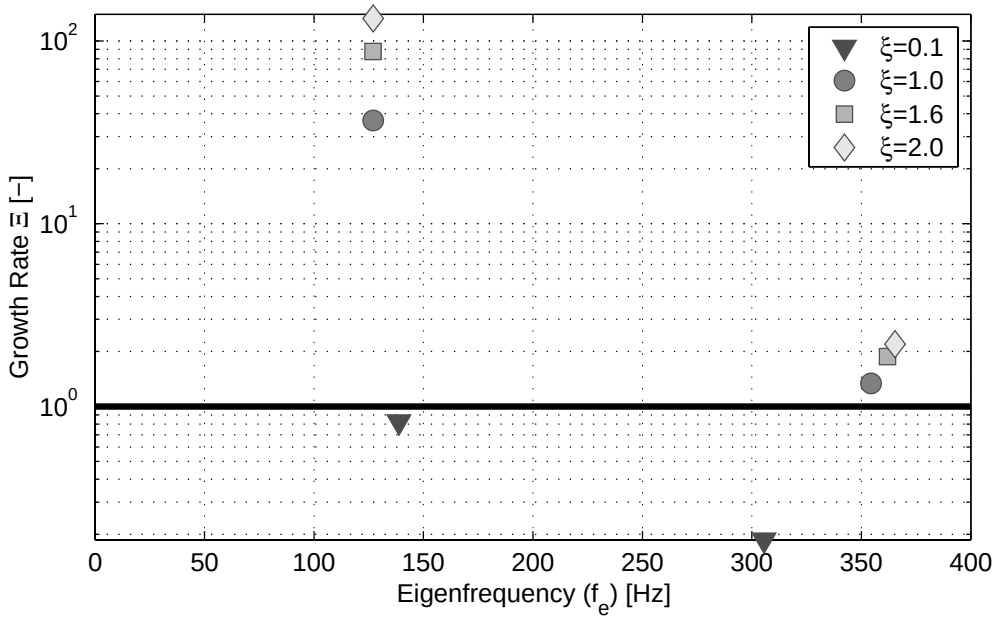

Fig. 7.6: Eigenfrequencies of the combustor for different atomiser sensitivities ξ, neglecting entropy waves ($\phi = 0.77$, $\bar{\tau}_d$=3 ms, $\Delta\tau_d/\bar{\tau}_d = 0.1$).

A more effective option than increasing the dispersion is to use an injector design which is less sensitive to changing air velocities. Figure 7.6 shows the instability behaviour of the combustor for varying atomiser sensitivities ξ, defined in Eq. (5.11). The frequency of the instability is hardly affected. For the unstable narrow-cone injector design, $\xi = 1.6$ was obtained in the measurements of section 5.2. Highly sensitive injectors with elevated values for ξ are prone to produce instabilities at higher growth rates. For a more robust injector

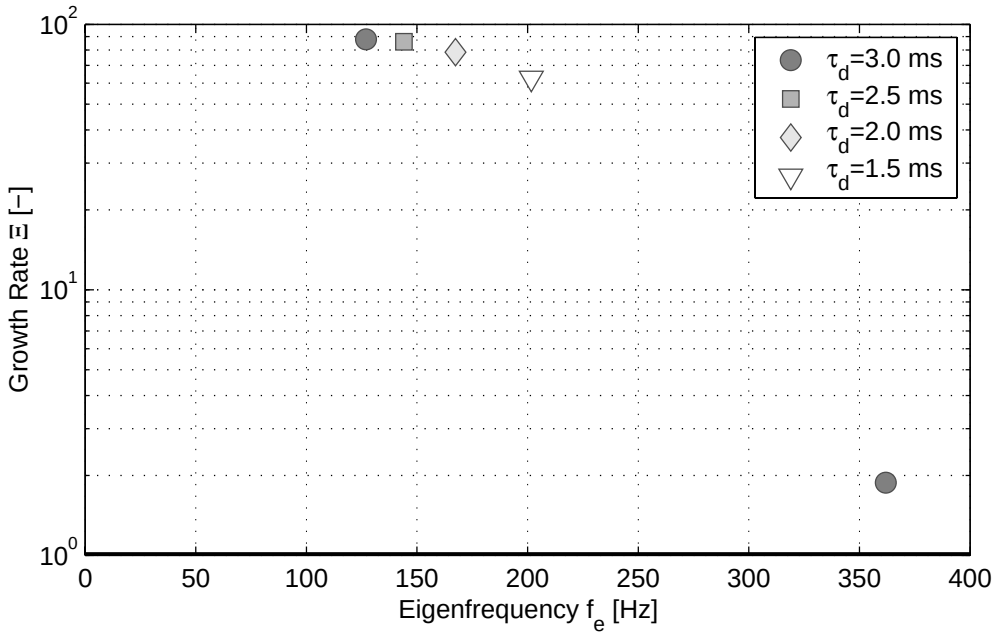

Fig. 7.7: Eigenfrequencies of the combustor as a function of τ_d, neglecting entropy waves ($\phi = 0.77$, $\Delta\tau_d/\bar{\tau}_d = 0.1$, $\xi = 1.6$).

design, tending to lower ξ, the tendency to instability decreases. The stability limit is achieved for $\xi_{crit} = 0.1$, which is very low from a design point of view. However, ξ_{crit} is a function of the volume increase by the flame and thus of $\dot{m}_f$ according to Eq. (7.36). Lower fuel mass flows generally lead to rising ξ_{crit}.

The frequencies of the dominating unstable mode are seen to be primarily influenced by the characteristic droplet delay times in the primary zone, as seen in Figure 7.7. $\bar{\tau}_d$ is varied within the range of characteristic time delays in the measurements (Figure 6.15). As expected, higher time delays lead to decreasing eigenfrequencies, ranging between 126 Hz for $\bar{\tau}_d = 3$ ms and 202 Hz for $\bar{\tau}_d = 1.5$ ms. An inversely proportional frequency rise is however not obtained. This illustrates that despite $\bar{\tau}_d$ is the most influencing factor, the combustor instability remains to be determined by the acoustics of the entire system. The growth rates are found to decrease for lower $\bar{\tau}_d$. This stabilising effect stays in agreement with the experimental observations for the wide-cone burner in section 6.4.

7.2.2 Instability behaviour in the presence of entropy waves

The investigation is now extended to include entropy waves, which influence the acoustic boundary conditions at the combustor outlet. Figure 7.9 shows the eigenfrequencies of the system for different entropy dispersion rates $\Delta\tau_s/\bar{\tau}_s$ in the dilution sector of the combustor. Compared to Figure 7.5, neglecting entropy waves, the presence of temperature perturbations in the system leads to an increasing number of eigenfrequencies in the low-frequency regime.

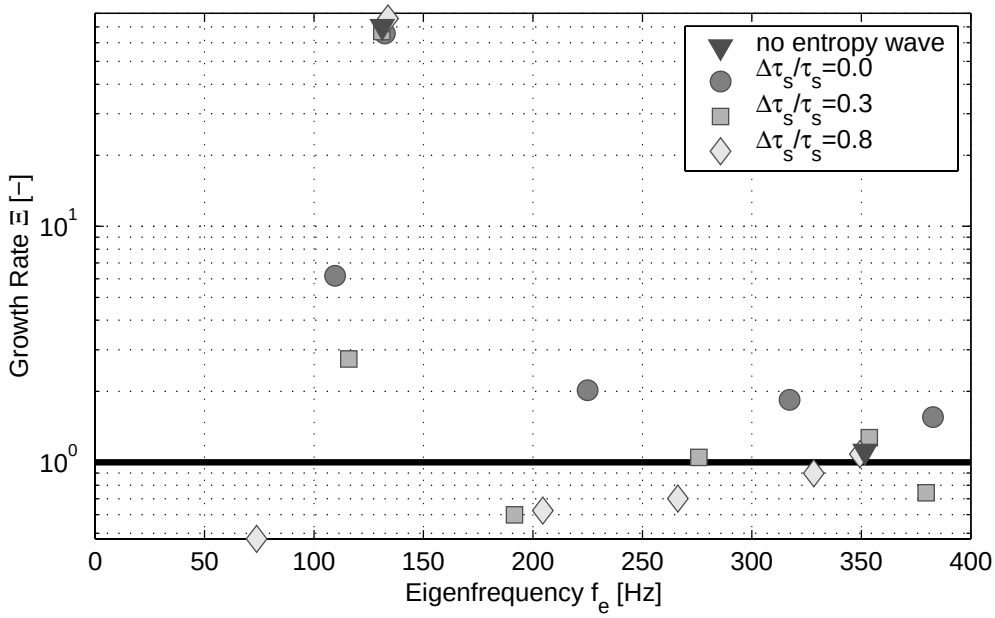

Fig. 7.8: Eigenfrequencies of the combustor for different dispersion rates of the entropy wave $\Delta\tau_s/\bar{\tau}_s$ ($\phi = 0.77$, $\dot{m}_f$=1.8 g/s, $\bar{\tau}_d$=3 ms, $\Delta\tau_d/\bar{\tau}_d = 0.3$, $\xi = 1.6$).

In the absence of dispersion ($\Delta\tau_s/\bar{\tau}_s = 0$), all eigenfrequencies are unstable. The lowest unstable eigenmode at 109 Hz is related to entropy, which can be concluded from its amplitude dependency on the dispersion rate. This entropy mode is found at a higher frequency than in the measurements with nozzle, where the sub-peak was encountered at 87 Hz. In general, the limit cycle frequencies can deviate from the initial values during linear growth of the pulsation due to the

non-linearities involved. Higher order entropy modes can be found at $f_e = 224$ Hz, 317 Hz and 382 Hz. Increasing dispersion rates of $\Delta\tau_s/\bar{\tau}_s = 0.3$ and $\Delta\tau_s/\bar{\tau}_s = 0.8$ lead to a general shift of the eigenfrequencies towards stability and to a selective stabilisation of eigenmodes. The dominating instability mode is found at 130 Hz. The comparison with the data in the preceding section for the open flame tube shows that this mode is purely thermoacoustic, which agrees with the experimental observations in section 6.3. The eigenfrequency and the growth rate of this thermoacoustic mode is altered only little by the dispersion of the entropy waves. Low dispersion rates tend to lower the growth rates while for $\Delta\tau_s/\bar{\tau}_s = 0.8$ the instability is slightly increased. If dispersion is low, the lowest entropy mode might contribute to the self-excitation driven by the thermoacoustic mode, due to the elevated growth rates observed. This stays in agreement with the experimental findings in Figure 6.11.

From the model equations in section 7.1.5 can be seen that the relative strength of the entropy and the thermoacoustic mode strongly depends on the operating conditions of the combustion chamber. The strength of the generated entropy wave is mainly influenced by the temperature ratio across the flame according to Eq. (7.36) and thus by the equivalence ratio ϕ. On the other hand, the volume increase by the flame as the driver of the thermoacoustic mode is, among others, a function of the fuel mass flow $\dot{m}_f$; see Eq. (7.37). In the first phase of engine start-up, immediately after ignition, $\dot{m}_f$ is low and the AFR is near-stoichiometric, potentially favouring the entropy mode. During engine acceleration, $\dot{m}_f$ increases considerably, successively leading to a prevailing thermoacoustic mode as seen in Figure 7.8 and in the experiments. For this reason, it is interesting to extend the investigation to the conditions of low fuel mass flows and the interaction of the modes found there. The eigenfrequencies for varying dispersion rates are shown in Figure 7.9 after the fuel mass flow in the model was reduced to $\dot{m}_f = 0.5$ g/s.

Contrary to Figure 7.8, the entropy modes are found to dominate the instability behaviour for negligible dispersion $\Delta\tau_s/\bar{\tau}_s = 0.0$. The

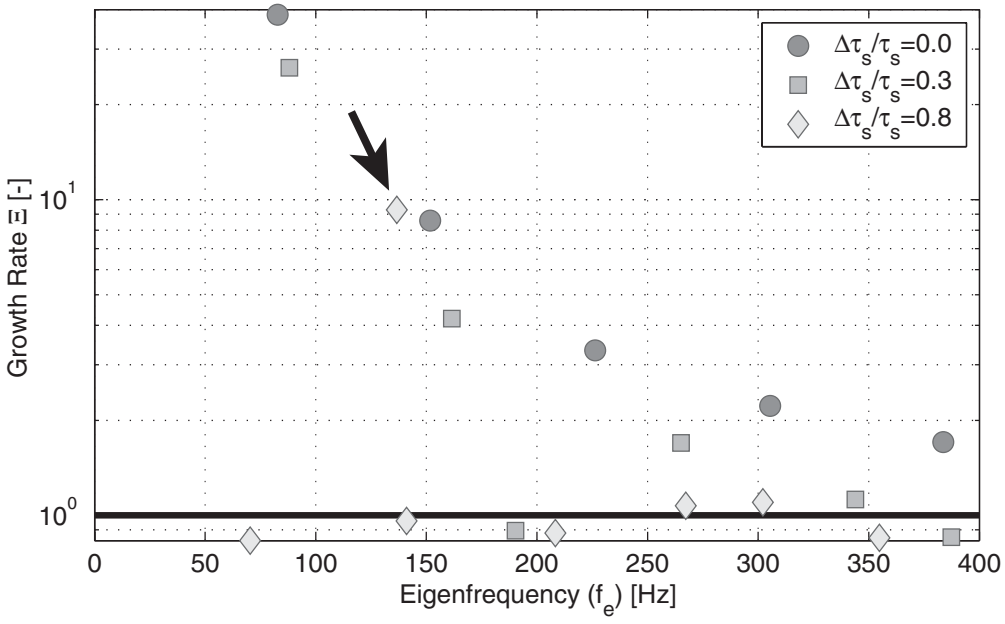

Fig. 7.9: Eigenfrequencies of the combustor for different dispersion rates of the entropy wave $\Delta\tau_s/\bar{\tau}_s$ and low fuel flow rates ($\phi = 0.77$, $\dot{m}_f$=0.5 g/s, $\bar{\tau}_d$=3 ms, $\Delta\tau_d/\bar{\tau}_d = 0.1$, $\xi = 1.6$).

lowest eigenmode is obtained at 82 Hz. As in Figure 7.8, this mode is associated with the lowest entropy mode, featuring a feedback loop over the entire system according to Figure 6.10. The eigenfrequency lies considerably closer to the value of 87 Hz, found experimentally. Increasing dispersion again results in a global decrease of the growth rates and in a selective stabilisation of formerly unstable modes. For high entropy dispersion $\Delta\tau_s/\bar{\tau}_s = 0.8$, almost all eigenmodes are stabilised or near stability except the one, which is marked with the black arrow in Figure 7.9. This one is of particular interest, since it represents the dominating instability mode for this operating point, exhibiting high growth rates comparable to the undispersed entropy modes at $\Delta\tau_s/\bar{\tau}_s = 0$. It further has a very similar eigenfrequency to the thermoacoustic modes observed above for identical $\bar{\tau}_d$.

Figure 7.10 shows the instability behaviour of the system at high dispersion rates of the entropy wave ($\tau_s/\bar{\tau}_s$=0.8) for a varying equivalence ratio ϕ. The equivalence ratio has been modified in the model by changing the overall air mass flow and maintaining the low fuel

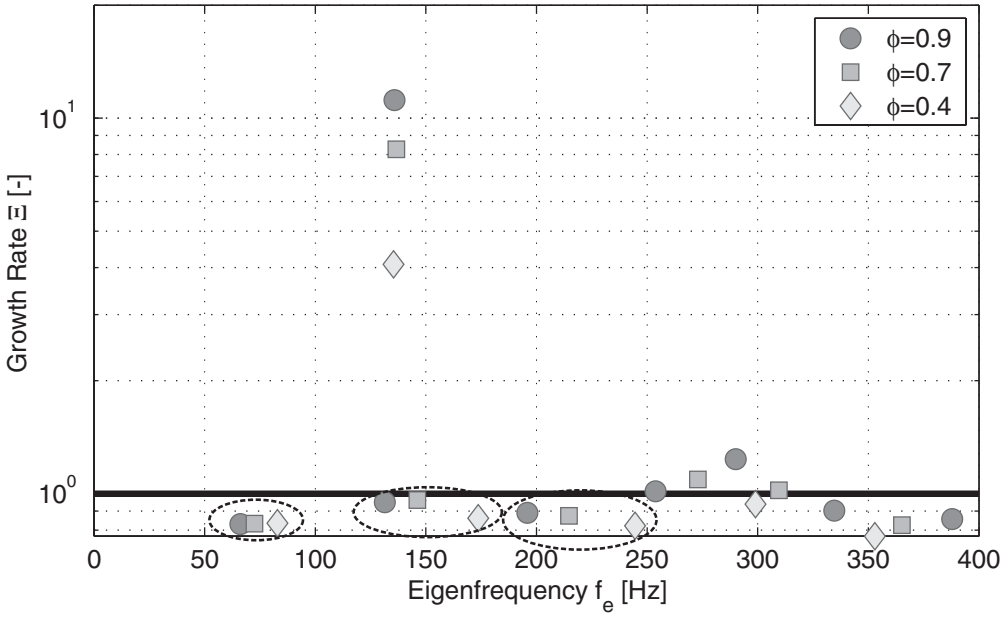

Fig. 7.10: Eigenfrequencies of the combustor for different equivalence ratios ϕ and low $\dot{m}_f$, produced by varying the overall air mass flow ($\bar{\tau}_d$=3 ms, $\dot{m}_f$=0.5 g/s, $\Delta\tau_d/\bar{\tau}_d = 0.1$, $\Delta\tau_s/\bar{\tau}_s = 0.8$, $\xi = 1.6$).

mass flow. The overall instability behaviour of the system will then be influenced by two factors: First, decreasing ϕ by increasing air mass flows will increase the average bulk velocity in the combustor and decrease the average residence times in the dilution zone. Second, due to the overall leaner mixture, the temperature ratio over the flame $\bar{T}_3/\bar{T}_4$ will increase and the entropy waves produced will become weaker, following Eq. (7.37).

The entropy modes in Figure 7.10 are affected by changes in ϕ, tending to higher eigenfrequencies for lower ϕ due to decreasing convective delay times $\bar{\tau}_s$. Corresponding eigenmodes for different ϕ are encircled in Figure 7.10. The frequency of the dominating unstable mode does however not respond to changes in $\bar{\tau}_s$, indicating a purely thermoacoustic excitation. The influence of the entropy waves is nevertheless remarkable and much more developed than for higher fuel mass flows (e.g. Figure 7.8), since the growth rates decrease for leaner mixtures and weaker entropy waves.

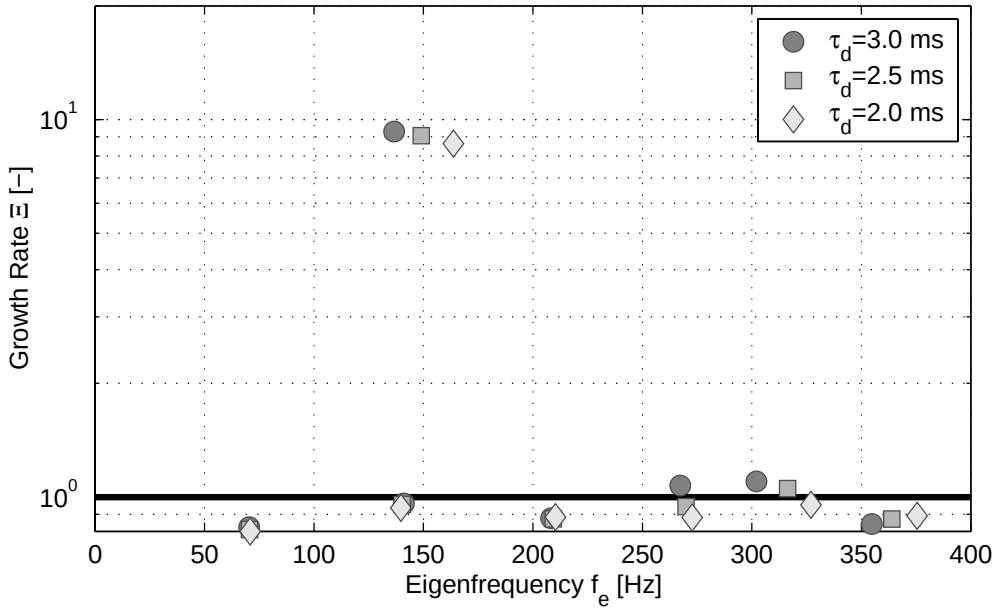

Fig. 7.11: Eigenfrequencies of the combustor as a function of $\bar{\tau}_d$ (ϕ=0.77, $\bar{\tau}_d$ =3 ms, $\dot{m}_f$=0.5 g/s, $\Delta\tau_d/\bar{\tau}_d$ = 0.1, $\Delta\tau_s/\bar{\tau}_s$=0.8, ξ = 1.6).

A contrary behaviour to Figure 7.10 can be seen for varying droplet delay times in the primary zone $\bar{\tau}_d$ in Figure 7.11. Changing droplet transport properties in the primary zone only influence the eigenfrequencies of the thermoacoustic mode without major impact on the entropy modes. The dominating instability mode thus exhibits the same characteristic features and frequencies as the purely thermoacoustic mode discussed in section 7.2.1.

Hence, the fairly simple low order model is able to replicate the rather complex instability behaviour of the test combustor (sections 6.1.1 and 6.2.1): For the majority of operating conditions, the low-frequency self-excitation is associated with a purely thermoacoustic mode, which is barely influenced by the presence of entropy waves. For low air and fuel mass flows however[24], the instability behaviour can successively shift into an entropy-driven mode, particularly if the dispersion rates are low as observed for the side-wall bound flame at low pressure drops (section 6.2.1). With rising dispersion rates

[24]or equivalently, for low combustion efficiencies

of the entropy wave, a *mode shift* can be expected from the entropy dominated combustor response back to the thermoacoustic mode. For lower fuel mass flows, the entropy waves can considerably influence the growth rates of this thermoacoustic mode. This interaction of the modes will be analysed in the next section, based on the equations of the low order model.

7.3 Mode shifting under the influence of entropy waves

The downstream boundary condition, determining the coupling between the entropy waves and the combustor acoustics, is given by Eq. (2.76):

$$u'_5 = \frac{\gamma - 1}{2} M_5 \frac{p'_5}{\bar{\rho}_5 c_5} + \frac{\bar{u}_5}{2} \frac{s'_5}{c_p} \tag{7.45}$$

Re-formulating Eq. (7.45), using Eq. (2.64), $c^2\bar{\rho} = \gamma\bar{p}$ and $\gamma = 1.4$ gives

$$2\frac{u'_5}{\bar{u}_5} = \frac{\gamma - 1}{\gamma}\frac{p'_5}{\bar{p}_5} + \frac{T'_5}{\bar{T}_5} = 0.29\frac{p'_5}{\bar{p}_5} + \frac{T'_5}{\bar{T}_5} \tag{7.46}$$

In section 6.2 it has been shown that the upper limit of the pressure oscillations $p'_5/\bar{p}_5$ is bound by the static pressure loss characteristics of the injector. At start-up conditions, $p'_5/\bar{p}_5$ will hardly exceed 5%. Relative temperature fluctuations have been measured in Table 6.1, varying between 10% and 2%, depending on dispersion. As a consequence, the contribution of the entropy term to u'_5 will usually dominate the response, particularly under conditions of low entropy dispersion. Equation (7.45) can therefore be simplified to the second

term for the sake of straightforwardness:

$$u'_5 \approx \frac{\bar{u}_5}{2}\frac{s'_5}{c_p} \tag{7.47}$$

The velocity fluctuations at the outlet can then be obtained as a function of the relative droplet size fluctuations $d'_3/\bar{d}_3$ by combining Eqs. (7.47), (7.17) and (2.76):

$$u'_5 \approx -\Theta_s \bar{u}_5 \left(1 - \frac{\bar{T}_3}{\bar{T}_4}\right)\frac{d'_3}{\bar{d}_3} \tag{7.48}$$

The temperature measurements in section 6.1.1 have indicated an approximate travelling time of the entropy wave of $\bar{\tau}_s$ =8.3 ms. This corresponds to $f_s = 1/\bar{\tau}_s = 120$ Hz which lies close to the unstable eigenfrequencies f_e encountered in both the measurements and the low order model. The phase difference of the (undispersed) entropy wave at the flame s'_4 and the nozzle s'_5 can therefore be assumed to vanish with good accuracy, which considerably simplifies the interpretation. Under these conditions, the time delay function $e^{-i\omega\overline{\tau}}$ in the dispersion function Θ_s, Eq. (7.17), can be omitted $e^{-i\omega\overline{\tau}} = e^{-2\pi i} = 1$ and only the dispersive part, plotted in Figure 7.3, influences the result.

On the other side, the velocity fluctuations downstream of the flame are given by Eq. (7.36)

$$u'_4 = u'_3 - 2\frac{\dot{m}_f h_b}{A_{cc}}\frac{\gamma - 1}{c_3^2 \bar{\rho}_3}\left(\frac{d'_3}{\bar{d}_3}\right) \tag{7.49}$$

The impact of the droplet size fluctuations $d'_3/\bar{d}_3$ on the acoustic velocities u'_4 at the flame and u'_5 at the combustor outlet can now be assessed from Eqs. (7.48) and (7.49). The phase difference between u'_4 and u'_5 is neglected, since the dilution zone is small compared to the acoustic wavelength. For the conditions summarised in Figure 7.12, the following behaviour is obtained:

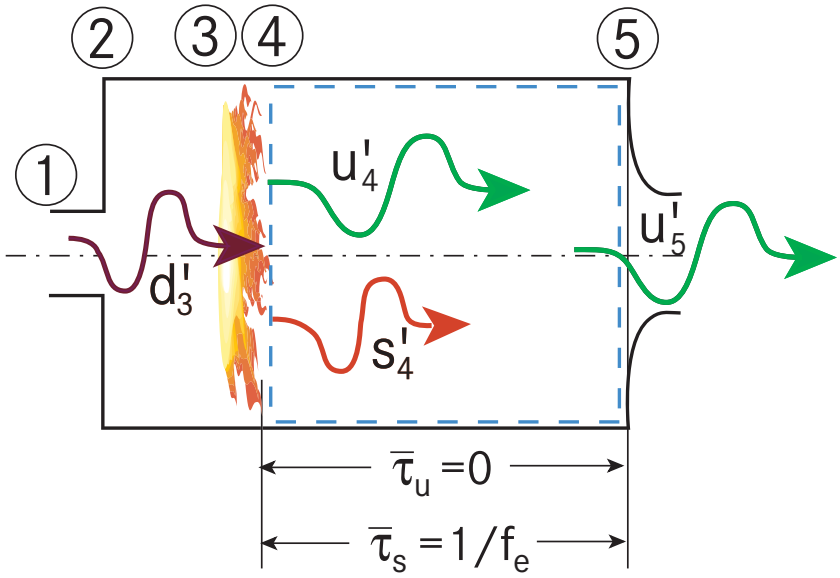

Fig. 7.12: Simplified interaction between entropy waves and thermoacoustics in the dilution sector of the combustor.

- **Vanishing entropy wave** $s'_4 \equiv 0$: The combustor outlet impedance Z_5 is high, as shown in context of Eq. (7.44), and u'_5 will nearly vanish. The volume production by the flame, being associated with decreasing droplet sizes $d'_3/\bar{d}_3$, leads to increasing u'_4. The air volume in the dilution zone will thus be compressed inducing rising combustor pressures. For this reason, the pressure maximum immediately follows the maximum heat release as seen in Figure 6.7. Since the wavelength of the acoustic pressure exceeds the overall combustor length by one order, the combustor pressure oscillates in the bulk mode (Figure 6.9). The rising pressure immediately impedes the fuel injection, which sustains the instability as observed in section 7.2.1.

- **Low entropy dispersion rates** $\Delta\tau_s/\bar{\tau}_s$: For low values of $\Delta\tau_s/\bar{\tau}_s$, the phase of the dispersion function in Figure 7.3 is zero. As a consequence, decreasing droplet sizes $d'_3/\bar{d}_3$ entering the flame will increase the acoustic velocities at the flame u'_4 (Eq. (7.48)), *but also* lead to an in-phase modulation of the acoustic velocities at the nozzle u'_5 (Eq. (7.49)). Thermoacoustic eigenmodes, originating from the volume expansion of the flame

are therefore *attenuated* (as in Figure 7.8) or even *compensated* (as in Figure 7.9) under the impact of entropy, depending on the relative strength. Under the latter conditions, the pressure fluctuations induced by the entropy waves themselves according to Eq. (2.77) will dominate.

- **High entropy dispersion rates** $\Delta\tau_s/\bar{\tau}_s$: For high values of $\Delta\tau_s/\bar{\tau}_s$ exceeding $f_e \cdot \Delta\tau_s/\bar{\tau}_s = 0.5$, the phase of the dispersion function Figure 7.3 is shifted by 180°. The velocity u'_5 at the nozzle oscillates 180° out of phase with u'_4. The entropy wave therefore *amplifies* the thermoacoustic mode of the flame by supporting the compression of the enclosed air in the dilution zone from the downstream side.

This behaviour coincides with the theoretical considerations in [PPD01] about the constructive and destructive interference between entropy and (thermo-)acoustic waves in combustors.

In the context of the experimental results, it is worth noting that for high dispersion rates, entropy waves do not *generate* the dominating mode in the low frequency regime, but they may *amplify* the instability of an existing eigenmode. The unstable eigenfrequency remains to be intrinsically tied with the features of the primary zone, as encountered for the absence of entropy waves.

8 Conclusions

In the scope of this thesis, the excitation mechanisms of low-frequency instabilities in aero-engine combustors were investigated experimentally and by linear stability analysis. This type of instability, also known as 'rumble', predominantly occurs in the start-up cycle of aero-engines, when the air side is operated at low pressure and low temperature conditions. The experiments were conducted in a single-sector RQL-combustor without internal film cooling, using a generic three-stream airblast atomiser with a design typical for aero-engines.

The following results were obtained from the experiments:

- The occurrence of self-excited combustion instabilities is intrinsically tied to the atomiser's sensitivity towards changing air mass flows. For the operation at low injector pressure losses during engine start-up, even small fluctuations of the air velocity remarkably alter the average droplet size and the droplet number density. Both parameters in turn strongly influence the combustion rates and the heat release of the flame.

- Self-excited instability modes were observed within a frequency band between 80 Hz and 135 Hz. The oscillatory heat release of the flame was accompanied with the formation of entropy waves, which were convected with approximately bulk velocity towards the combustor outlet. However, their strength diminished quickly in the highly dispersive environment of the combustor, being induced by the staged injection of mixing air.

- The dominant instability mode showed to be purely thermoacoustic. Oscillations, similar in amplitude and frequency, were also obtained for an open combustor exit, where an entropy-related pressure feedback can be excluded. A high combustor outlet impedance has shown to be the key requirement for low-frequency instabilities instead. Under those conditions strong

pressure oscillations at the injector exit induce a considerable modulation of the injector pressure drop.

- The strength of the entropy mode was usually too weak to significantly alter the dominating thermoacoustic mode of the primary zone. The reflected pressure waves at the choked nozzle, originating from entropy non-uniformities, rather lead to an amplitude modulation of the combustor pressure in the limit cycle.
- The oscillation frequency was dominated by the transport and the combustion time scales of the droplets in the primary zone. The low limit cycle frequencies, being typical for rumble, are related to the low Mach number of the combustor flow and the extended time scales for transport and combustion of the generally larger fuel droplets.
- Large amplitude oscillations of the combustor pressure showed to suppress the air flow through the burner and thus the fuel transport to the flame. The amplitude of the pressure oscillations was therefore limited by the static pressure loss of the injector. The limit cycle amplitudes could be considerably reduced using an injector design with higher swirl and improved mixing of the droplet clusters generated in the primary zone.

A linear network model of the staged combustor was formulated to investigate the conditions for the onset of low-frequency instabilities. The model takes into consideration the effects of aerodynamic dispersion on overall system stability. Furthermore, a simple spray flame model was implemented, which accounts for the dominating influence of droplet size variations on the heat release fluctuations, as observed in the experiments. The model results confirmed the experimental findings and showed that

- the system is unstable in the low-frequency domain, even without the contribution of entropy waves.
- entropy waves and thermoacoustic waves can interfere both constructively and destructively in the combustor. For low fuel mass

flows and low dispersion, the entropy waves can considerably influence the instability behaviour in the low frequency domain. At elevated fuel mass flows and dispersion rates however, the purely thermoacoustic mode is dominating, being hardly influenced by entropy.

- the key parameters influencing combustor instability are the atomisation characteristics of the injector and the aerodynamics of the primary zone, both influencing the droplet size variations and the droplet number densities arriving at the flame.

As a consequence, a primary measure for reducing or suppressing rumble consists in an atomiser design which is insensitive towards changing air mass flows. In the low-frequency domain, the atomiser performance can be practically described by the steady atomisation characteristics. As a secondary measure, the tendency for instability can be significantly reduced by a highly dispersive primary zone aerodynamics of the injector. The droplet size fluctuations generated by the injector are dampened this way before entering the flame.

A goal for future work is the extension of the rumble investigations towards elevated pressures, since rumble practically occurs at operating pressures up to 4 bar (absolute). The pressure dependence of the underlying instability mechanisms is of practical interest for the formulation of scaling laws, which account for the entire range of operating conditions during engine start-up.

Thermoacoustic modelling requires the use of appropriate combustion models. The simplicity of the spray combustion model derived in this thesis stems from the assumption of negligible droplet burning times. It was shown that the model sufficiently explains the mechanisms of the low-frequency oscillations. For general use, it is however desirable to improve this model by including aspects of droplet prevaporisation and finite time scales of droplet combustion.

With the dynamic temperature probe, a method was developed which can be used to investigate the nature of OH*-chemiluminescence in

more detail. In this thesis, the determination of the phase correlation between the OH*-emissions and heat release was of primary interest, being used for evaluating Rayleigh's criterion. Future research should aim at deriving quantitative relationships. In this framework, the thermocouple method can serve as the reference.

References

[Arn01] A.S. Arnesen. Report on the search of alternatives to kerosine for the use in spray investigations. Unpublished, September 2001.

[Aue99] M. Auer. Wegweiser zur Konzepterstellung für Versuchsstände zur Untersuchung von periodischen Verbrennungsinstabilitäten. Master's thesis, Lehrstuhl A für Thermodynamik, Technische Universität München, 1999.

[Bal76] H.P. Baltes. On the validity of Kirchhoff's law of heat radiation for a body in a nonequilibrium environment. In Inc. American Elsevier Publishing Co., editor, *Progress in optics*, volume 13, pages 1–25, 1976.

[Bau04] H.-J. Bauer. New low emission strategies and combustor designs for civil aeroengine applications. *Progress in Computational Fluid Dynamics, An International Journal*, 4(3/4/5):130–142, 2004.

[Büc92] H. Büchner. *Experimentelle und theoretische Untersuchungen der Entstehungsmechanismen selbsterregter Druckschwingungen in technischen Vormisch-Verbrennungssystemen.* PhD thesis, Universität Karlsruhe (TH), 1992.

[Bee92] H. Beer. *Vorlesung Thermodynamik III.* Vorlesungsumdruck, Fachgebiet Technische Thermodynamik, TU Darmstadt, 1992.

[BKHD99] M. Blomeyer, B. Krautkremer, D.K. Hennecke, and T. Doerr. Mixing zone optimization of a Rich-Burn/Quick-Mix/Lean-Burn combustor. *Journal of Propulsion and Power*, 15(2):288–295, 1999.

[Bra91] H. Braun. *Experimentelle Untersuchungen zur dynamischen Druck- und Temperaturmessung in einer*

Hubschrauber-Gasturbine. PhD thesis, Technische Universität München, 1991.

[CHP+00] J.M. Cohen, J.R. Hibshman, W. Proscia, T.J. Rosfjord, B.E. Wake, J.B. McVey, J. Lovett, M. Ondas, J. DeLaat, and K. Breisacher. Experimental replication of an aeroengine combustion instability. *ASME-Paper 2000-GT-0093*, 2000.

[Chu53] B.-T. Chu. On the generation of pressure waves at a plane flame front. *Fourth Symposium (International) on Combustion/The Combustion Institute*, pages 603–612, 1953.

[CL83] J.S. Chin and A.H. Lefebvre. Steady-state evaporation characteristics of hydrocarbon fuel drops. *AIAA Journal*, 21(10):1437–1443, 1983.

[CM77] N.A. Cumpsty and F.E. Marble. The interaction of entropy fluctuations with turbine blade rows; a mechanism of turbojet engine noise. *Proceedings of the Royal Society London*, 357:323–344, 1977.

[CMF+04] E. Canepa, P. Di Martino, P. Formosa, M. Ubaldi, and P. Zunino. Unsteady aerodynamics of an aeroengine double swirler lpp burner. *ASME-Paper GT-2004-54212*, 2004.

[Cor92] S. Correa. A review of NOx formation under gas-turbine combustion conditions. *Combustion Science and Technology*, 87(1-6):329–362, 1992.

[Cro65] L. Crocco. Theoretical studies on liquid-propellant rocket instability. *Tenth Symposium (International) on Combustion*, (1101-1128), 1965.

[CRS01] H. Cohen, G.F.C. Rogers, and H.I.H. Saravanamuttoo. *Gas Turbine Theory*. Prentice Hall, 5th edition, 2001.

[CS91] P. Clavin and E.D. Siggia. Turbulent premix flames and sound generation. *Combustion Science and Technology*, 78:147–155, 1991.

[CSC+03] W.S. Cheung, G.J.M. Sims, R.W. Copplestone, J.R. Tilston, C.W. Wilson, S.R. Stow, and A.P. Dowling. Measurement and analysis of flame transfer function in a sector combustor under high pressure conditions. *ASME-Paper GT-2003-38219*, 2003.

[Cul88] F.E.C. Culick. Combustion instabiltites in liquid-fueled propulsion systems- an overview. *AGARD Conference Proceeding No.450*, 1988.

[Cul94] F.E.C. Culick. Some recent results for nonlinear acoustics in combustion chambers. *AIAA Journal*, 32(1):146–169, 1994.

[Dan00] Dantec Dynamics A/S. *FlowMap Particle Image Velocimetry Instrumentation- Installation and User's Guide*, 5th edition, 2000.

[Dip72] D.F. Dipprey. Liquid propellant rockets. In R.F. Landel and A. Rembaum, editors, *Chemistry in Space Research*. American Elsevier Publishing, Inc., 1972.

[DMJ98] R.K. Dubey, M.Q. McQuay, and J.A. Carvalho Jr. An experimental and theoretical investigation on the effects of acoustics on spray combustion. *Twenty-Seventh Symposium (International) on Combustion/The Combustion Institute*, 2:2017–2023, 1998.

[Dow95] A.P. Dowling. The calculation of thermoacoustic instabilities. *Journal of Sound and Vibration*, 180(4):557–581, 1995.

[Dow99] A.P. Dowling. A kinematic model of a ducted flame. *Journal of Fluid Mechanics*, 394:51–72, 1999.

[DV92] D.S. Dandy and S.R. Vosen. Numerical and experimental studies of hydroxyl radical chemiluminescence in methane-air flames. *Combustion Science and Technology*, 82:131–150, 1992.

[EFH+03] J. Eckstein, E. Freitag, C. Hirsch, T. Sattelmayer, R. von der Bank, and T. Schilling. Forced low-frequency spray characteristics of a generic airblast swirl diffusion burner. *ASME Paper GT-2003-38646*, 2003.

[EFHS04] J. Eckstein, E. Freitag, C. Hirsch, and T. Sattelmayer. Experimental study on the role of entropy waves in low-frequency oscillations for a diffusion burner. *ASME-Paper GT-2004-54163*, 2004.

[Fin01] Rainer Fink. *Untersuchungen zu LPP-Flugtriebwerksbrennkammern unter erhöhtem Druck*. PhD thesis, Technische Universität München, 2001.

[Fis04] A. Fischer. *Hybride, thermoakustische Charakterisierung von Drallbrennern*. PhD thesis, Technische Universität München, 2004.

[Gay74] A.G. Gaydon. *The spectroscopy of flames*, pages 210–213. John Wiley and Sons, New York, 1974.

[GC86] N.L. Garland and D.R. Crosley. On the collisional quenching of electronically excited OH, NH and CH in flames. *Twenty-first Symposium (International) on Combustion/The Combustion Institute*, (21):1693–1702, 1986.

[GFEP03] A.M.G. Gentemann, A. Fischer, S. Evesque, and W. Polifke. Acoustic transfer matrix reconstruction and analysis for ducts with sudden change of area. *AIAA 2003-3142, 9th Aeroacoustics Conference and Exhibit, Hilton Head, South Carolina*, 2003.

[GGDL02] F. Giuliani, P. Gajan, O. Diers, and M. Ledoux. Characterisation of an air-blast injection device with forced

periodic entries. In A. Pollard and S. Candel, editors, *IUTAM Symposium on Turbulent Mixing and Combustion*, pages 327–336. Kluwer Academic Publishers, 2002.

[GSK01] C. Ghenai, O.I. Smith, and A. R. Karagozian. Acoustical excitation of burning fuel droplets. *AIAA 2001-0328, 39th Aerospace Sciences Meeting and Exhibit, Reno, Nevada*, 2001.

[Hab00] L.C. Haber. An investigation into the origin, measurement and application of chemiluminescent light emissions from premixed flames. Master's thesis, Virginia Polytechnic Institute and State University, 2000.

[HCF+98] C. Hassa, M. Carl, M. Frodermann, T. Behrendt, J. Heinze, I. Röhle, N. Brehm, T. Schilling, and T. Doerr. Experimental investigation of an axially staged combustor sector with optical diagnostics at realistic operating conditions. *RTO MP-14, RTO AVS Symposium on Gas Turbine Engine Combustion, Emissions and Alternative Fuels, 12.-16. Oktober 1998, Lissabon, Portugal*, 1998.

[HD98] S. Hubbard and A.P. Dowling. Acoustic instabilities in premix burners. *AIAA 98-2272, 4th AIAA/CEAS Aeroacoustics Conference, Toulouse, France*, 1998.

[Hei02] A. Heilos. Spektrale Analyse der thermischen Strahlungswechselwirkung in Kohlenwasserstoffflammen. *Berichte aus der Energietechnik, Shaker Verlag*, 2002.

[Hin75] J.O. Hinze. *Turbulence*. McGraw-Hill, 2nd edition, 1975.

[HV02] C.C. Hanschk and D. Vortmeyer. Numerical simulation of self-excited combustion oscillations in a non-premixed burner. *Combustion Science and Technology*, 174:189–204, 2002.

[HV03] L.C. Haber and U. Vandsburger. A global reaction model for OH* chemiluminescence applied to a laminar

flat-flame burner. *Combustion Science and Technology*, 175:1859–1891, 2003.

[HZGV95] J. Hermann, P. Zangl, S. Gleis, and D. Vortmeyer. Untersuchung der Anregungsmechanismen selbsterregter Verbrennungsschwingungen an einem Verbrennungssystem für Flüssigkraftstoff. *VDI-Berichte Nr. 1193*, 251-260, 1995.

[ID96] F.P. Incropera and D.P. DeWitt. *Fundamentals of Heat and Mass Transfer*. John Wiley and Sons, 4th edition, 1996.

[JDG02] M.C. Jermy, W.G. Doherty, and D.A. Greenhalgh. The response of fuel injector sprays to acoustic perturbation and their role in combustion instability. *11th Int. Symp. Applications of Laser Tech. to Fluid Mech., 8-11th July 2002, Lissabon, Portugal*, 2002.

[JHG03] M.C. Jermy, M. Hussain, and D.A. Greenhalgh. Operating liquid-fuel airblast injectors in low pressure test rigs: Strategies for scaling down the flow conditions. *Measurement Science and Technology*, 14:1151–1158, 2003.

[Jør02] F.E. Jørgensen. *How to measure turbulence with hot wire anemometers- A practical guide*. Dantec Dynamics, 1st edition, 2002.

[KB61] S. Krishnamahari and H. Broida. Effect of molecular oxygen on the emission spectra of atomic oxygen-acetylen flames. *Journal of Chemical Physics*, 34(5):1709–1711, 1961.

[KBK+98] W. Konrad, N. Brehm, F. Kameier, C. Freeman, and I.J. Day. Combustion instability investigations on the BR710 jet engine. *Journal of Engineering for Gas Turbines and Power*, 120(39):34–40, 1998.

[KEH85] J.J. Keller, W. Egli, and J. Hellat. Thermally induced low-frequency oscillations. *Journal of Applied Mathematics and Physics (ZAMP)*, 36:250–274, 1985.

[Kel95] J.J. Keller. Thermoacoustic oscillations in combustion chambers of gas turbines. *AIAA Journal*, 33(12):2280–2287, 1995.

[KHS04] K. Kunze, C. Hirsch, and T. Sattelmayer. Transfer function measurements on a swirl stabilized premix burner in an annular combustion chamber. *ASME-Paper GT2004-53106*, 2004.

[KK99] S.A. Klein and J.B.W. Kok. Acoustic instabilities in syngas fired combustion chambers. *ASME-Paper 99-GT-355*, 1999.

[Kle00] S.A. Klein. *On the Acoustics of Turbulent Non-Premixed Flames*. PhD thesis, University of Twente, 2000.

[Koc72] G. Kochen. *Praxis der Duchflussmessung von Gasen, Dampf und Flüssigkeiten.* Hartmann und Braun AG, 6th edition, 1972.

[Koh88] W. Kohler. *Turbulenz und Turbulenzstruktur in freien und eingeschlossenen Flammen*. PhD thesis, Universität Karlsruhe (TH), 1988.

[Krä88] M. Krämer. *Untersuchungen zum Bewegungsverhalten von Tropfen in turbulenter Strömung im Hinblick auf Verbrennungsvorgänge*. PhD thesis, TH Karlsruhe, 1988.

[Kun04] K. Kunze. *Untersuchung des thermoakustischen Flammenübertragungsverhaltens in einer Ringbrennkammer*. PhD thesis, Technische Universität München, 2004.

[Law82] C.K. Law. Recent advances in droplet vaporization and combustion. *Progress in Energy and Combustion Science*, 8:171–201, 1982.

[Law00] C.J. Lawn. Distributions of instantaneous heat release by the cross-correlation of chemiluminescent emissions. *Combustion and Flame*, 123:227–240, 2000.

[Laz04] A. Lazaridis. Experimentelle Untersuchung des Mischungsverhaltens thermoakustisch instabiler Diffusionsflammen. Master's thesis, TU München, Lehrstuhl für Thermodynamik, 2004.

[Lef89] A.H. Lefebvre. *Atomization and Sprays*. Hemisphere Publishing, 1989.

[Lef95] A.H. Lefebvre. The role of fuel preparation in low-emission combustion. *Journal of Engineering for Gas Turbines and Power*, 117:617–655, 1995.

[Lef99] A.H. Lefebvre. *Gas Turbine Combustion*. Taylor and Francis, 2nd edition, 1999.

[Len80] W. Lenz. *Die dynamischen Eigenschaften von Flammen und ihre Einfluss auf die Entstehung selbsterregter Brennkammerschwingungen*. PhD thesis, Engler Bunte Institut, Universität Karlsruhe (TH), 1980.

[LG81] W. Lenz and R. Günther. Der einfluss von Flammen auf die Entstehung selbsterregter Brennkammerschwingungen. *VDI-Berichte*, 423:111–118, 1981.

[Lie03] T. Lieuwen. Modeling premixed combustion- acoustic wave interactions: A review. *Journal of Propulsion and Power*, 19(5):765–781, 2003.

[LZ98] T. Lieuwen and B.T. Zinn. The role of equivalence ratio oscillations in driving combustion instabilities in low NOx gas turbines. *Twenty-Seventh Symposium (International) on Combustion/The Combustion Institute*, pages 1809–1816, 1998.

[LZ00] T. Lieuwen and B.T. Zinn. Application of multipole expansions to sound generation from ducted unsteady

combustion processes. *Journal of Sound and Vibration*, 235(3):405–414, 2000.

[MC77] F.E. Marble and S.M. Candel. Acoustic disturbance from gas non-uniformities convected through a nozzle. *Journal of Sound and Vibration*, 55(2):225–243, 1977.

[MDL98] R. Mongia, R. Dibble, and J. Lovett. Measurement of air-fuel ratio driven fluctuations caused by combustor driven oscillations. *ASME Paper 98-GT-304*, 1998.

[MSW+01] M.R. Morrell, J.M. Seitzman, M. Wilensky, E. Lubarsky, J. Lee, and B.T. Zinn. Interpretation of optical emissions for sensors in liquid fueled combustors. *AIAA-01-0787, 39th AIAA Aerospace Sciences Meeting and Exhibit, Reno (NV), USA*, 2001.

[Mun87] M.L. Munjal. *Acoustics of Ducts and Mufflers*. John Wiley and Sons, 1987.

[MW70] J. Mathews and R.L. Walker. *Mathematical Methods of Physics*. Benjamin/Cummings, 2 edition, 1970.

[NPMW98] H.N. Najm, P.H. Paul, C.J. Mueller, and P.S. Wyckoff. On the adequacy of certain experimental observables as measurement of flame burning rate. *Combustion and Flame*, 113:312–332, 1998.

[Pan04] C. Pankiewitz. *Hybrides Berechnungsverfahren für thermoakustische Instabilitäten von Mehrbrennersystemen*. PhD thesis, Technische Universität München, 2004.

[PFHS03] C. Pankiewitz, A. Fischer, C. Hirsch, and T. Sattelmayer. Computation of transfer matrices for gas turbine combustors including acoustics/flame interaction. *9th AIAA/CEAS Aeroacoustics Conference and Exhibit, AIAA-2003-3295, Hilton Head, SC, USA*, 2003.

[PGW98] C.O. Paschereit, E. Gutmark, and W. Weisenstein. Structure and control of thermoacoustic instabilities in

a gas-turbine combustor. *Combustion Science and Technology*, 138:213–232, 1998.

[PGW00] C.O. Paschereit, E. Gutmark, and W. Weisenstein. Excitation of thermoacoustic instabilities by interaction of acoustics and unstable swirling flow. *AIAA Journal*, 38(6):1025–1034, 2000.

[PHS68] R. Price, I. Hurle, and T. Sugden. Optical studies of the generation of noise in turbulent flames. *Proceedings of the Combustion Institute*, 12:1093–1102, 1968.

[PHW98] H. Pak, E. Hassel, and H.B. Weyer. Stabile, schadstoffarme Magerverbrennung im nationalen Luftfahrtforschungsprogramm (KEROMIX). *DGLR-Jahrestagung JT98-024*, 1998.

[PLG+99] J.E. Penner, D.H. Lister, D.J. Griggs, D.J. Dokken, and M. McFarland. Aviation and the global atmosphere. Technical report, Intergovernmental Panel on Climate Change (WMO and UNEP), 1999.

[Pol04] W. Polifke. Personal communication, 2004.

[PP98] C.O. Paschereit and W. Polifke. Investigation of the thermoacoustic characteristics of a lean premixed gas turbine burner. *ASME-Paper 98-GT-582*, 1998.

[PPD99] W. Polifke, C.O. Paschereit, and K. Döbbeling. Suppression of combustion instabilities through destructive interference of acoustic and entropy waves. *6th International Congress on Sound and Vibration, Copenhagen*, 1999.

[PPD01] W. Polifke, C.O. Paschereit, and K. Döbbeling. Constructive and destructive interference of acoustic and entropy waves in a premixed combustor with a choked exit. *International Journal of Acoustics and Vibration*, 6(3):135–146, 2001.

[PS02] C. Pankiewitz and T. Sattelmayer. Time domain simulation of combustion instabilities in annular combustors. *ASME-Paper GT-2002-30063*, 2002.

[PTV+87] T. Poinsot, A. Trouvé, D. Veynante, S. Candel, and E. Esposito. Vortex driven acoustically coupled combustion instabilities. *Journal of Fluid Mechanics*, 177:265–292, 1987.

[Rac98] M. Rachner. Die Stoffeigenschaften von Kerosin Jet A-1. *Mitteilung 98-01, Institut für Antriebstechnik (Köln), DLR*, 1998.

[Ray26] J.W.S. Lord Rayleigh. *The Theory of Sound*. Macmillan an Co. Ltd., 2nd edition, 1926.

[RM56] D.E. Rogers and F.E. Marble. A mechanism for high frequency oscillations in ramjet combustors and afterburners. 26, 1956.

[RWK98] M. Raffel, C. Willert, and J. Kompenhans. *Particle Image Velocimetry: A Practical Guide*. Springer, 1998.

[Sat85] T. Sattelmayer. *Zum Einfluss der ausgebildeten, turbulenten Luft-Flüssigkeitsfilm-Strömung auf den Filmzerfall und die Tropfenbildung am Austritt von Spalten geringer Höhe*. PhD thesis, Universität Karlsruhe (TH), 1985.

[Sat03] T. Sattelmayer. Influence of the combustor aerodynamics on combustion instabilitites from equivalence ratio fluctuations. *Journal of Engineering for Gas Turbines and Power*, 125(1):11–19, 2003.

[SG92] K.C. Schadow and E. Gutmark. Combustion instability related to vortex shedding in dump combustors and their passive control. *Progress in Energy and Combustion Science*, 18:117–132, 1992.

[SP99] B.B.H. Schuermans and W. Polifke. Modeling transfer matrices of premixed flames and comparison with experimental results. *ASME Paper 99-GT-132*, 1999.

[SP03] T. Sattelmayer and W. Polifke. Assessment of methods for the computation of the linear stability of combustors. *Combustion Science and Technology*, 175(3):477–497, 2003.

[Spu87] J.H. Spurk. *Strömungslehre*. Springer, 3rd edition, 1987.

[SRBS01] D.L. Straub, G.A. Richards, W.T. Baumann, and W.R. Saunders. Measurement of dynamic flame response in a lean premixed single-can combustor. *ASME-Paper 2001-GT-0038*, 2001.

[SSL01] P.B. Subrahmanyam, R.I. Sujith, and T.C. Lieuwen. A family of exact transient solutions for acoustic wave propagation in inhomogeneous, non-uniform area ducts. *Journal of Sound and Vibration*, 240(4):705–715, 2001.

[Sta71] W.C. Stahle. On combustion generated noise. *Journal of Fluid Mechanics*, 49:399–414, 1971.

[Sum51] M. Summerfield. A theory of unstable propulsion in liquid propellant rocket systems. *ARS Journal*, 21(5):108–144, 1951.

[SWJZ00] R.I. Sujith, G.A. Waldherr, J.I. Jagoda, and B.T. Zinn. Experimental investigation of the evaporation of droplets in axial acoustic fields. *Journal of Propulsion and Power*, 16(2):278–285, 2000.

[SWZ95] R.I. Sujith, G.A. Waldherr, and B.T. Zinn. An exact solution for one-dimensional acoustic fields in ducts with an axial temperature gradient. *Journal of Sound and Vibration*, 184(3):389–402, 1995.

[SZ85] D.A. Smith and E.E. Zukoski. Combustion instability sustained by unsteady vortex combustion. *AIAA 85-1248, AIAA/SAE/ASME/ASEE 21th Joint Propulsion Conference, Monterrey, CA*, 1985.

[SZ87] J.D. Sterling and E.E. Zukoski. Longitudinal mode combustion instabilities in a dump combustor. *AIAA-Paper 87-0220, AIAA 25th Aerospace Sciences Meeting*, 1987.

[TH96] T. Terasaki and S. Hayashi. The effects of fuel-air mixing on NOx formation in non-premixed swirl burners. *Twenty-Sixth Symposium (International) on Combustion/The Combustion Institute*, pages 2733–2739, 1996.

[Tur00] S. Turns. *An Introduction to Combustion: Concepts and Applications*. McGraw-Hill Series in Mechanical Engineering, second edition, 2000.

[Umu99] O.M. Umurhan. Exploration of fundamental matters of acoustic instabilities in combustion chambers. *Center for Turbulence Research- Annual Research Briefs*, pages 85–98, 1999.

[vdBS03] R. von der Bank and T. Schilling. Development of an Ultra-Low NOx LP(P) Burner. *ASME-Paper GT2004-53341*, 2003.

[WASS84] S. Wittig, M. Aigner, K. Sakbani, and T. Sattelmayer. Optical measurements of droplet size distributions: Special considerations in the parameter definition for fuel atomizers. *AGARD-Conference Proceedings No. 353, Paper 13*, 1984.

[Wit80] V. Wittmer. *Geschwindigkeit und Temperatur in einer turbulenten Freistrahldiffusionsflamme*. PhD thesis, Universität Karlsruhe (TH), 1980.

[WKHJ99] G. Walz, W Krebs, S. Hoffmann, and H. Judith. Detailed analysis of the acoustic mode shapes of an annular combustion chamber. *ASME Paper 99-GT-113*, 1999.

[YPW+96] K.H. Yu, T.P. Parr, K.J. Wilson, K.C. Schadow, and E.J. Gutmark. Active control of liquid-fueled combustion using periodic vortex-droplet interaction. *Twenty-Sixth Symposium (International) on Combustion/The Combustion Institute*, pages 2843–2850, 1996.

[Zar97] N. Zarzalis. NOx-Emissionsminderung bei Flugtriebwerksbrennkammern nach dem Konzept der Fett-Mager Verbrennung. *DGLR-Jahrestagung JT97-107*, 1997.

[ZDB99] M. Zhu, A.P. Dowling, and K.N.C. Bray. Combustion oscillations in burners with fuel spray atomizers. *ASME Paper 99-GT-302*, 1999.

[ZDB00] M. Zhu, A.P. Dowling, and K.N.C. Bray. Self-excited oscillations in combustors with spray atomizers. *ASME Paper 2000-GT-0108*, 2000.

[ZJL97] Q.P. Zheng, A.K. Jasuja, and A.H. Lefebvre. Structure of airblast sprays under high ambient pressure conditions. *Journal of Engineering for Gas Turbines and Power*, 119:512–518, 1997.